DISSERTATION

submitted to the

Combined Faculties for the Natural Sciences and for Mathematics

of the Ruperto-Carola University of Heidelberg, Germany

for the degree of

Doctor of Natural Sciences

Put forward by

Simon Reichert, M. Sc.

born in Dresden, Germany

Oral examination: February 1, 2024

Advancing Sodium Triple Quantum (TQ) Nuclear Magnetic Resonance (NMR) Spectroscopy and Imaging

Simon Reichert

First reviewer Prof. Dr. Lothar R. Schad
Computer Assisted Clinical Medicine
Ruperto-Carola University of Heidelberg

Second reviewer Prof. Dr. Tristan A. Kuder
Medizinische Physik in der Radiologie
Deutsches Krebsforschungszentrum

Advancing Sodium Triple Quantum (TQ) Nuclear Magnetic Resonance (NMR) Spectroscopy and Imaging

Slow interactions of sodium ions with macromolecules result in a sodium triple quantum (TQ) signal. This TQ signal is intracellularly sensitive and promises to be a valuable biomarker for cell viability. However, a deeper understanding of the sodium molecular environment and the detected TQ signal as well as substantial reduction in measurment time are necessary to leverage the full potential of the sodium TQ signal in clinical applications. As a first step of this thesis, a simulation framework for sodium nuclear magnetic resonance (NMR) dynamics was implemented, including a refined motion model for simultaneous compatibility with T_1 and T_2 relaxation times. For both the TQ time proportional phase intrement (TQTPPI) and the inversion recovery TQTPPI (IRTQTPPI) sequences, the simulation showed good agreement with the experimental data. In a second step, the sodium molecular environment was further investigated by using globular proteins of different sizes with different sodium binding affinities. TQ signal increased with protein size. However, a strong sodium binding affinity and the structure of the protein hydration shell had a stronger influence than the protein size. In a third step, a novel IRTQTPPI sequence was proposed to investigate the TQ signal and thus the sodium molecular environment on a different time scale. This sequence allows for a reliable and simultaneous quantification of T_1 relaxation times and TQ signal. Measurements at 9.4 T and 21.1 T showed a separation of T_1 relaxation times of at least 15 ms and a strong T_1-TQ signal for agar samples. The separation in T_1 relaxation time and T_1-TQ signals were smaller than their T_2 counterparts, indicating a unique sensitivity of the T_1-TQ signal to a molecular environment on a different time scale. In the last part of this thesis, a novel and fast TQ acquisition method using only a single pulse sequence was proposed. The TQ signal of this method was in close agreement with the TQTPPI sequence and the theoretical prediction. Furthermore, the method reproduced the expected TQ signal behavior even for multi-compartment systems and in the presence of noise. This approach, combined with multi-echo ultra-short echo time (UTE) imaging, provides an efficient method to extract the sodium TQ signal in vivo without increasing acquisition time compared to SQ sequences and a dramatically reducing scan time compared to conventional phase cycling sequences. The proposed NMR techniques are a promising research tool to obtain a deeper understanding of the sodium molecular environment and thus leverage the full potential of the sodium TQ signal in vivo.

Weiterentwicklung der Natrium Triple-Quanten (TQ) Nuklearer Magnetresonanz (NMR) Spektroskopie und Bildgebung

Langsame Wechselwirkungen von Natriumionen mit Makromolekülen führen zu einem Natrium-Triple-Quantum (TQ)-Signal. Dieses TQ-Signal ist intrazellulär empfindlich und verspricht, ein wertvoller Biomarker für die Lebensfähigkeit von Zellen zu sein. Allerdings sind ein tieferes Verständnis der molekularen Natriumumgebung und des nachgewiesenen TQ-Signals sowie eine erhebliche Verkürzung der Messzeit erforderlich, um das volle Potenzial des Natrium-TQ-Signals in klinischen Anwendungen zu nutzen. Als erster Schritt dieser Arbeit wurde ein Simulationsframework für die Dynamik der Natrium-Kernspinresonanz (NMR) implementiert, einschließlich eines verfeinerten Bewegungsmodells für die gleichzeitige Kompatibilität mit T_1 und T_2 Relaxationszeiten. Sowohl für die TQ time proportional phase increment (TQTPPI) Sequenz als auch für die Inversion Recovery TQTPPI (IRTQTPPI) Sequenz zeigte die Simulation eine gute Übereinstimmung mit den experimentellen Daten. In einem zweiten Schritt wurde die molekulare Umgebung der Natriumionen weiter untersucht, indem globuläre Proteine verschiedener Größe mit unterschiedlichen Natriumbindungsaffinitäten verwendet wurden. Das TQ-Signal nahm mit der Größe des Proteins zu. Allerdings hatten eine starke Natriumbindungsaffinität und die Struktur der Proteinhydratationshülle einen stärkeren Einfluss als die Proteingröße. In einem dritten Schritt wurde eine neuartige IRTQTPPI-Sequenz vorgeschlagen, um das TQ-Signal und damit die molekulare Natriumumgebung auf einer anderen Zeitskala zu untersuchen. Diese Sequenz ermöglicht eine zuverlässige und gleichzeitige Quantifizierung der T_1-Relaxationszeiten und des TQ-Signals. Messungen bei 9.4 T und 21.1 T zeigten eine Trennung der T_1-Relaxationszeiten von mindestens 15 ms und ein starkes T_1-TQ-Signal für Agarproben. Der Abstand zwischen den T_1-Relaxationszeiten und den T_1-TQ Signalen war kleiner als die T_2 Relaxationszeiten und TQ Signale, was auf eine einzigartige Empfindlichkeit des T_1-TQ-Signals gegenüber der molekularen Umgebung auf einer anderen Zeitskala hinweist. Im letzten Teil dieser Arbeit wurde eine neuartige und schnelle TQ-Akquisitionsmethode mit nur einer Singlepulssequenz vorgeschlagen. Das TQ-Signal dieser Methode hat gut mit der TQTPPI-Sequenz und der theoretischen Vorhersage übereingestimmt. Darüber hinaus reproduzierte die Methode das erwartete TQ-Signalverhalten auch bei Systemen mit mehreren Kompartimenten und für verrauschte Daten. Dieser Ansatz stellt in Verbindung mit einer Multiecho Ultra-short (UTE) Bildgebungsequenz eine effiziente Methode zur Extraktion des Natrium-TQ-Signals in vivo dar, ohne dass die Messzeit im Vergleich zu SQ-Sequenzen verlängert und die Messzeit im Vergleich zu herkömmlichen Phasenzyklus-Sequenzen drastisch reduziert. Die vorgeschlagenen NMR-Techniken sind ein vielversprechendes Forschungsinstrument, um ein tieferes Verständnis der molekularen Umgebung von Natrium zu erlangen und so das volle Potenzial des Natrium-TQ-Signals in vivo zu nutzen.

Acknowledgement

The pursuit of a PhD is a journey that relies on the unwavering support and guidance of many people, each playing a crucial role in shaping the path to success. I am sincerely grateful to the support of everyone who played a part in this journey.

Foremost, my deepest appreciation goes to Prof. Dr. Lothar Schad for not only providing me with the invaluable opportunity to work in his research group but also for entrusting me with the freedom to explore the exciting world of sodium triple quantum coherences under his expert guidance. I am also thankful for the friendly and supportive atmosphere he cultivated within the research group.

Moreover, I appreciate Prof. Dr. Tristan Kuder for serving as the second referee for my thesis.

A special acknowledgment is reserved for Dr. Victor Schepkin from the National High Magnetic Field Laboratory. His generosity in welcoming me to Tallahassee and facilitating my work at 21.1 T, coupled with his invaluable assistance with the scanner, has left an permanent mark on my academic journey. I am thankful for the enlightening discussions, new perspectives on the TQ signal, and the detailed corrections and comments on my papers and abstracts.

I express my appreciation to Prof. Dr. Frank Zöllner for his valuable assistance with the HCC project, his unwavering support, and his open-door policy for addressing any challenges.

Felix Hörner from the Central Institute for Mental Health deserves my heartfelt thanks for his consistent support in navigating all the challenges crashes posed by the 9.4 T MRI scanner, even during late evening hours.

Dennis, I cannot thank you enough for all the hard work, time, energy and blood you put in the proof-reading of my papers, abstracts, applications, proposals and my thesis. I am indebted to you for introducing me to the sodium TQ signal, adopting me in the X-nuclei group and for your mentorship, which continues to enrich my academic journey. Your support, extending to both work and personal discussions, laughs, hikes, and other activities, has been instrumental.

The CKM always had a great and supportive atmosphere. To all its members, thank you for the enjoyable activities, shared lunch breaks, conferences, and bouldering and gym sessions. A special mention goes to Safa, my wonderful office mate, for the laughter, memes, and the kindness of offering your place in my time of need. I am also grateful to the X-nuclei group members, particularly Christian L. and Dominik, for the dicussions about the TQ signal, imaging and k-space trajectories (Cartesian sampling ftw!), and relieving me from grant writing pressures when I was busy

with my thesis. Dennis, Christian, and Steffen, your proofreading contributions and thoughtful suggestions are deeply appreciated.

Last but not least, to my parents and sisters, your unwavering support and encouragement have been my anchor. Without you, none of my achievements would have been possible. Special thanks to Luca for the emotional support and culinary skill that definitely saved me from an unbalanced diet.

Contents

List of Abbreviations

ADC	Analog-to-Digital Converter.
BSA	Bovine Serum Albumin.
DQ	Double Quantum.
DQF	Double Quantum Filtering.
EFG	Electric Field Gradient.
FID	Free Induction Decay.
FT	Fourier Transform.
IR	Inversion Recovery.
IRTQTPPI	Inversion Recovery Triple Quantum Time Proportional Phase Increment.
ISTO	Irreducible Spherical Tensor Operator.
MA	Magic Angle.
MCS	Multi Compartment System.
MQ	Multiple Quantum.
MQF	Multiple Quantum Filtering.
MR	Magnetic Resonance.
MRI	Magnetic Resonance Imaging.
NMR	Nuclear Magnetic Resonance.
RF	radio-frequency.
SAR	Specific Absorption Rate.
SE	Spin Echo.
SNR	Signal to Noise Ratio.
SP	Single-Pulse.
SQ	Single Quantum.
TPPI	Time Proportional Phase Increment.
TQ	Triple Quantum.
TQF	Triple Quantum Filtering.
TQTPPI	Triple Quantum Time Proportional Phase Increment.
TSC	Tissue Sodium Concentration.

UTE	Ultra-Short Echo Time.
ZQ	Zero Quantum.

1 Introduction

Nuclear Magnetic Resonance (NMR) has become a powerful and indispensable tool in materials science, chemistry and medicine. In medicine in particular, NMR-based Magnetic Resonance Imaging (MRI) is widely used for non-invasive diagnostics. Compared to other medical imaging modalities such as computed tomography (CT) and positron emission tomography (PET), it produces images with high soft tissue contrast without the use of ionizing radiation. Nuclear spins, $^{1}\mathrm{H}$ in most applications, align in an external magnetic field resulting in a macroscopic magnetization. This magnetization can be manipulated with radio-frequency (RF) pulses and spatially encoded with gradient fields in MRI. Besides protons, any nucleus with a non-zero nuclear spin, so-called X-nuclei, can be used to generate the Magnetic Resonance (MR) signal. One of the most important and most studied X-nuclei is $^{23}\mathrm{Na}$. The sodium nucleus has not only the second strongest biological MR signal, but also attractive NMR and MRI properties from both a physical and a biomedical point of view [1, 2].

Sodium ions are involved in multiple vital cell processes, such as membrane transport processes and electric signaling between neurons [3]. The sodium-potassium pump maintains a large concentration gradient between intra- and extracellular space by constantly pumping sodium ions out of the cell and potassium ions into the cell [4, 5]. The energy consumption of this process is up to two thirds of the cells total energy. This combined with the crucial involvement of the sodium concentration gradient in cellular transport processes and electric signaling between cells demonstrate the vital importance of the sodium-potassium pump for cell viability [2, 3]. Insufficient energy supply leads to a failure of the sodium-potassium pump followed by an influx of water and sodium ions into the cell. Thus, changes in the intracellular sodium concentration correlate with early pathophysiological changes.

The $^{23}\mathrm{Na}$ nucleus has a spin of $3/2$ and therefore the sodium electrical quadrupole moment interacts with surrounding Electric Field Gradient (EFG)s created by the molecular environment [6, 7]. In the case of a slowly fluctuating EFG as for instance during ion interactions with proteins and other macromolecules, these electric quadrupole interactions cause bi-exponential relaxation and allow the formation of Triple Quantum (TQ) coherences subsequent to the Single Quantum (SQ) coherence [6–11]. The weighted mean value of the intra- and extracellular sodium concentrations, the Tissue Sodium Concentration (TSC) can be determined from the sodium SQ signal to gain valuable non-invasive information about cell viability and physiology [1, 2, 6, 12, 13]. However, the SQ signal does not allow the differentiation between increased intracellular sodium concentration and increased extracellular volume [14]. On the other hand, the TQ signal has been shown to have a higher weighting towards the intracellular sodium content than the SQ

signal [15–22]. Both sodium signals are potential valuable biomarkers for cell viability [23–28]. A combined measurement of SQ and TQ signals [29–31] might provide more insights into cellular processes. Several studies with perfused rat heart systems [15, 20, 32–35], brain ischemia [36] and tumors [37, 38] and in-vitro experiments using an MR-compatible bioreactor systems [39–42] have demonstrated a correlation of the TQ signal with cell viability. The TQ signal increases with the intracellular sodium concentration [20] and depends on the sodium [15, 34] and protein [15, 19] concentrations as well as the folding state of proteins [43]. Thus, the TQ signals increases the value of sodium MRI as a valuable biomarker for cell viability [15, 16, 19, 33, 34, 36, 39, 41, 42].

Proteins play a crucial role in a variety of biological processes [44], increasing the significance of exploring them with NMR techniques. Slow interactions of sodium ions with proteins, especially with negatively charged groups on the protein surface, are one of the major contributors to the TQ signal in biological tissues. This is due to the high abundance of proteins in cells of 20-35 % w/v [44] and the availability of negatively charged groups at cellular pH [43]. Most studies of the sodium NMR signal have focused on the protein Bovine Serum Albumin (BSA) and investigated the dependence of the TQ signal on the pH value and the protein concentration [9, 43, 45, 46]. BSA is a relatively large globular protein with 100 negatively charged groups. Nevertheless, sodium ions have a very low binding affinity for BSA [47]. As a result, the sodium TQ signal of BSA is a strong pH dependent TQ signal which is weaker than that of cells [9, 43, 45, 46]. Proteins differ in terms of size, sodium binding affinity, which influences the correlation time. The impact of these protein properties on the TQ signal remains unexplored, yet it is an essential aspect for achieving a more profound understanding of the sodium TQ signal.

Besides the investigation of different model systems for a deeper understanding of the molecular environment, also different relaxation pathways can be utilized. Previous studies [7, 20, 21, 29, 39, 41, 43, 45, 48–52] mainly investigated the T_2 relaxation pathway, which is sensitive to slow interactions. Contrary, the rarely investigated T_1 relaxation pathway of the TQ signal has a unique sensitivity to the intermediate regime [6, 10, 53]. Hence, the combination of both pathways allows to obtain a better characterization of the molecular environment. Interaction durations in the few ns range dominate the T_1-TQ signal and longer interactions do not influence the signal. In contrast, the latter longer interactions dominate the T_2-TQ signal. Thus, the T_1-TQ signal has a unique sensitivity and can provide valuable information to better characterize sodium-protein interactions. These interactions are characterized by a wide range of correlation times. Hence, the investigation of T_1- and T_2-TQ signals can advance our understanding on the TQ signal formation in biological environments. However, only a few studies have been able to detect bi-exponential T_1 relaxation and/or a T_1-TQ signal [54–56], as the fast T_{1f} relaxation time component contributes only 20 % to the overall signal. In general, reliable quantification of bi-exponential T_1 relaxation times is difficult using current techniques. Therefore, a reliable technique for the investigation of the T_1-TQ signal and the bi-exponential T_1 relaxation times is necessary to better characterize sodium interactions in biological tissue.

In summary, previous studies of the sodium TQ signal [7, 29, 39, 41–43, 48] laid the basis of the TQ signal as a biomarker using optimized T_2 sequences and similar model systems. For a deeper understanding of the TQ signal as a biomarker for cell viability, a better characterization of the TQ signal using a large variety of model systems and different TQ relaxation pathways is necessary. Therefore, the first objective of this thesis was to increase preclinical techinques for the detection of TQ signal and deepen the understanding of the molecular origin of the TQ signal using different techniques for a better characterization of the molecular environment.

MR systems are only capable to detect the SQ signal and thus the TQ signal can only be detected indirectly. For this purpose, complicated phase-cycled multi-pulse sequence are necessary [7, 45, 50, 52, 53]. The conventional Triple Quantum Filtering (TQF) sequence uses three RF pulses and two evolution periods between the pulses with an optional additional 180° refocusing pulse during the first evolution period [6]. These sequences are based on the principle that different coherence orders accumulate phase shifts differently, i.e. TQ coherences three times faster than SQ coherences. Therefore, phase alterations in the pulse sequence provide a tool for selection of the desired signal. The first 90° RF pulse creates $\hat{T}_{11}$ SQ coherences that are converted to $\hat{T}_{31}$ SQ coherences during the first evolution period τ_{evo}. The second 90° pulse transforms the $\hat{T}_{31}$ coherences to $\hat{T}_{33}$ TQ coherences, which accumulate phase shifts three times quicker than SQ coherneces. The mixing time (τ_{mix}) is usually selected as short as possible to avoid MR signal decay. At the end, a third 90° RF pulse transforms the $\hat{T}_{33}$ coherences back to $\hat{T}_{31}$, which later evolve into observable $\hat{T}_{11}$ MR signal. The phases of all three RF pulses are incremented in every scan and the signals are summed or processed independently. In the conventional TQF sequence, only the TQ signal passes the above phase filter. More advanced phase cycles help to reduce the impact of B_1 and B_0 inhomogeneities [29, 48, 51, 57] or filter out unwanted echoes [29, 30, 51]. Another way to detect TQ signal is the Triple Quantum Time Proportional Phase Increment (TQTPPI) [7, 58]. This sequence is very similar to the TQF sequence as described above with the evolution time being incremented in every phase step. It simultaneously detects both the SQ and TQ signals at distinct frequencies and therefore simplifies the TQ signal quantification by normalizing it to the SQ signal [7].

The requirement of a phase cycling scheme combined with multiple RF pulses results in a long scan time and a high Specific Absorption Rate (SAR). Furthermore, $\hat{T}_{33}$ coherences are prone to B_0 and B_1^+ inhomogeneities[59]. B_0 inhomogeneities have a three times larger effect on $\hat{T}_{33}$ state than on SQ coherences. Additionally , the TQ signal has a $\sin^5\theta$ dependency on the RF flip angle θ compared to $\sin^3\theta$ dependency of the SQ signal [49]. These drawbacks togehter with the low Signal to Noise Ratio (SNR) of the TQ filtered signal currently prevent a clinical application of the TQ signal. Hence, the second objective of this thesis was to optimize the TQ sequence such that it allows a clinical application, i.e., low scan time without phase-cycling and a low SAR value without complicated multi-pulses.

In summary, the two main aims of this thesis were (i) to investigate the molecular origin of the sodium TQ signal in a preclinical setting, using model systems and

advanced TQ techniques, and (ii) to accelerate the acquisition of the sodium TQ signal for clinical application. These two objectives were achieved in four parts.

In the first part, a simulation framework for the NMR dynamics of spin-3/2 nuclei was implemented and investigated. Sodium NMR dynamics is a combination of various coherences from multiple relaxation pathways, which complicates the signal interpretation. Hence, a simulation framework of spin-3/2, sodium, NMR dynamics provides a unique tool to characterize and quantify signal components in more detail. Simulation frameworks for sodium NMR pulse sequences have been already proposed [30, 53, 60–62]. However, these simulation frameworks are not optimized for fast computation of arbitrary phase cycles with multiple iterations and varying time delays. This thesis presents a computationally efficient modular simulation framework for spin-3/2, sodium, NMR dynamics for biological environments using hard RF pulses. This simulation framework provides a complete description of all signal components for arbitrary pulse sequences. Moreover, the framework was veryfied using experimental data from the TQTPPI and Inversion Recovery Triple Quantum Time Proportional Phase Increment (IRTQTPPI) sequences. Hence, pulse sequences can be optimized and the influence of sequence and sample parameters on the signal can be quantitatively evaluated.

In the second part, several other proteins were investigated in this thesis with two main objectives to obtain a deeper understanding of the sodium molecular environment. First, the TQ and relaxation behavior of BSA was compared with the TQ and relaxation behavior of a form of bovine hemoglobin, methemoglobin, a similar sized paramagnetic protein with a similar sodium binding affinity as BSA. Second, the TQ signal and relaxation behavior of several globular proteins of different sizes were studied to determine the dependence of the TQ signal on protein size.

In the third part the T_1 and T_2 relaxation times and T_1- and T_2- TQ signals were compared using the TQTPPI and IRTQTPPI sequences. The detection of the T_1-TQ signal requires a modified pulse sequence and phase cycling. Jaccard et al. [53] already proposed an inversion recovery TQ filtration (Inversion Recovery (IR)-TQF) pulse sequence using the T_1 relaxation pathway. In the case of imperfect inversion, both the $\hat{T}_{1\pm1} \rightarrow \hat{T}_{3\pm1}$ and the $\hat{T}_{10} \rightarrow \hat{T}_{30}$ pathways indistinguishably contribute to the TQ signal [6]. Moreover, unwanted signal contributions, e.g. double quantum (Double Quantum (DQ)) signals, may overlap with the TQ signal making its quantification a difficult task. Therefore, methods that suppress unwanted signal contributions may improve the quantification of the T_1 relaxation times and the T_1-TQ signal. Based on the sequence of Jaccard et al. [53], this thesis proposes an IRTQTPPI sequence, which allows a simultaneous quantification of bi-exponential T_1 relaxation times and T_1-TQ signal similar to the TQTPPI sequence. To reliably detect the T_1 relaxation times and the T_1-TQ signal, three different double quantum (DQ) suppression methods were evaluated using a simulation framework and experiments. Using the optimized IRTQTPPI sequence, T_1 and T_2 TQ signals were compared between 9.4 T and 21.1 T for agar tissue model systems. The local motional environment was characterized by evaluating the correlation time and quadrupole interaction strength. The results of this part were submitted

for publication in [63]. The results of this part were submitted for publication in [63].

In the final part, a novel method to acquire the sodium TQ signal using only a single-pulse sequence was introduced. The evolution of the $\hat{T}_{31}$ coherences after the first RF pulse already encode the relevant TQ state [6, 10, 11]. The other parts of the conventional TQ pulse sequences have the sole purpose of making the creation of the $\hat{T}_{31}$ state detectable. A direct extraction of $\hat{T}_{31}$ coherences has a huge potential to simplify and accelerate the detection of sodium TQ signals. Based on this idea, this thesis presents a novel method to extract the TQ signal using only Free Induction Decay (FID) from a Single-Pulse (SP) sequence or a Spin Echo (SE) sequence. The TQ signal was compared with theory and the TQ signal from the state-of-the-art TQTPPI sequence using agarose as a tissue model system. The performance of the method was investigated in multi-compartment systems and in the presence of noise using simulated data. As a proof-of-concept, this method was also combined with a multi-echo radial Ultra-Short Echo Time (UTE) sequence to demonstrate the applicability of this approach for sodium MR imaging in-vitro. The results of this part were submitted for publication in [64].

2 Theoretical Background

This chapter covers a brief overview of basic concepts and physics of Nuclear Magnetic Resonance (NMR) with a focus on spin-3/2 systems. Relaxation and the effect of radio frequency pulses on nuclear spins and the signal detection, the key components of every NMR experiment, are introduced with the intention to provide a brief overview that supports the understanding of the subsequent work.

2.1 Nuclear Magnetic Resonance

NMR has become a powerful and indispensable tool for the material sciences, chemistry and medicine. Rabi et al. [65] first described and measured nuclear precession in marking the discovery of nuclear magnetic resonance and received the 1944 Nobel Prize in Physics. His experiment was an extension of the famous Stern-Gerlach experiment by Gerlach and Stern [66], who first showed quantification of the spatial orientation of angular momentum. Otto Stern was awarded the 1943 Nobel Prizes in Physics. In 1946, Bloch [67] and Purcell et al. [68] were the first to detect NMR signals of solid and liquid samples marking the start of NMR spectroscopy. For their contribution, they shared the shared the 1952 Nobel Prize in Physics.

After that, NMR developed to be an important tool for structural analysis of molecules which led to two further Chemistry Nobel prizes for Richard Robert Ernst in 1991 and for Kurt Wüthrich in 2002. In the 70's Mansfield and Grannell [69] and Lauterbur [70] extended NMR spectroscopy with spatial encoding. For their discoveries concerning the development of Magnetic Resonance Imaging (MRI), Paul Christian Lauterbur and Peter Mansfield were awarded the 2003 Nobel Prize in Physiology or Medicine.

This chapter discusses the basic principles of NMR including the Zeeman splitting, macroscopic magnetization and the detection of the NMR signal. The discussion is based on the books of Abragam [71], Slichter [72], Levitt [73], Haacke et al. [74], and Graaf [75].

2.1.1 Nuclear Spin and the Nuclear Zeeman Effect

Atoms consist of an electron shell and the nucleus, made of two types of nucleons, protons and neutrons. Protons carry a positive electric charge and neutrons do not carry electric charge. Thus, the nucleus as a whole is positively charged with the charge being determined by the number of protons. The nucleons are held together

by the strong force. Moreover, the nucleus posses a nuclear spin $\hat{\boldsymbol{I}}$, a quantum mechanical property that behaves like an angular momentum. As a quantum mechanical angular momentum, the spin $\hat{\boldsymbol{I}}$ with the spin components $\hat{I}_x$, $\hat{I}_y$ and $\hat{I}_z$ satisfies the angular momentum algebra defined by the commutator relations

$$\left[\hat{I}_i, \hat{I}_j\right] = i\hbar\epsilon_{ijk}\hat{I}_k, \tag{2.1}$$

with $\hat{I}_i$ being the components of the angular momentum operator $\hat{\boldsymbol{I}}$, the Levi-Civita symbol ϵ_{ijk} and the reduced Planck constant $\hbar = h/2\pi = 1.0545 \times 10^{-34}\,\mathrm{J\,s}$. As can easily be verified, the angular momentum operator additionally satisfies the commutator relaxation

$$\left[\hat{I}_i, \hat{\boldsymbol{I}}^2\right] = 0. \tag{2.2}$$

Per convention and without loss of generality, the z-axis is usually chosen as the quantization axis. The eigenstates $|I, m\rangle$ of $\hat{I}_z$ are described by two quantum numbers, the nuclear spin quantum number I and the magnetic quantum number $m = -I, -I+1, \ldots, I-1, I$ and follow the eigenvalue equations

$$\hat{\boldsymbol{I}}^2\,|I,m\rangle = \hbar^2 I(I+1)\,|I,m\rangle \qquad \text{and} \qquad \hat{I}_z\,|I,m\rangle = \hbar m\,|I,m\rangle\,. \tag{2.3}$$

Thus, the eigenstates are $(2I+1)$-fold degenerated. It is also useful to define the angular momentum ladder operators

$$\hat{I}_\pm = \hat{I}_x \pm i\hat{I}_y. \tag{2.4}$$

The total spin quantum number I of the nucleus, or simply nuclear spin, is the vector sum of the spins of the protons and neutrons, which are both spin $s = 1/2$ fermions and an additional orbital momentum of the nucleons, $j = |l \pm 1/2|$. In contrast to the total angular momentum of the electron shell, the calculation of the nuclear spin is much more difficult. In a few cases the nuclear shell model, the nuclear analogue to the atomic shell model, correctly predicts the spin. In general, all nuclei with odd number of protons and/or neutrons possess a non-vanishing nuclear spin. If either the number of protons or the number of neutrons is odd, the nuclear spin is a half-integer, while it is an integer if both the number of protons and neutrons is odd.

The nuclear spin is connected with a nuclear magnetic moment

$$\boldsymbol{\mu}_I = \frac{g\mu_N}{\hbar}\hat{\boldsymbol{I}} = \gamma\hat{\boldsymbol{I}} \tag{2.5}$$

where g is the Landé-factor, a nucleus-specific constant, $\mu_N = 5.05 \times 10^{-27}\,\mathrm{J/T}$ is the nuclear magneton and $\gamma = g\mu_N/\hbar$ is the the gyromagnetic ratio, a nucleus specific constant. Like a classical magnetic moment, the nuclear magnetic moment interacts with magnetic fields.

Nuclear Zeeman Effect

In an NMR experiment, the probe is placed in a static magnetic field, $\boldsymbol{B}_0$, also known as magnetic flux density. Per convention, the direction of the magnetic field $\boldsymbol{B}_0 = (0, 0, B_0)^T$ is the z-axis. The resulting nuclear Zeeman Hamiltonian $\hat{\mathcal{H}}_Z$ is

$$\hat{\mathcal{H}}_Z = -\boldsymbol{\mu}_I \boldsymbol{B}_0 = -\gamma B_0 \hat{I}_z \tag{2.6}$$

Using the eigenvalue equations Equation (2.3), it follows for the stationary Schrödinger equation

$$\hat{\mathcal{H}}_Z \left| I, m \right\rangle = E_m \left| I, m \right\rangle \tag{2.7}$$

with the energy eigenstates E_m

$$E_m = -\hbar m \gamma B_0. \tag{2.8}$$

Therefore, the Zeeman effect removes the eigenstate degeneracy with equidistantly spaced energy levels with a spacing of

$$\Delta E = \hbar \gamma B_0 \hbar \omega_0 \tag{2.9}$$

and the Lamor frequency

$$\omega_0 = \gamma B_0, \tag{2.10}$$

i.e., the spins are precessing around the quantization axis z with the Lamor frequency ω_0, which is proportional to the magnetic field. In Figure 2.1, this splitting is shown for hydrogen, ^{1}H and sodium, ^{23}Na, nuclei at a magnetic field strength of 9.4 T and 21.1 T. For his 1896 discovery of the Zeeman effect, a splitting of atomic spectral lines in a magnetic field, Pieter Zeeman received the Physics Nobel Prize in 1902.

The NMR experiment is based on the nuclear Zeeman effect and the manipulation of the spins with additional time-dependent magnetic fields $\boldsymbol{B}_1(t)$ that oscillate with the Lamor frequency ω_0 and being most effective when applied perpendicular to the main magnetic field $\boldsymbol{B}_0$. These additional magnetic fields $\boldsymbol{B}_1(t)$ are also called radio-frequency (RF) pulses.

NMR-Active Nuclei

Since the nuclear magnetic moment is only non-vanishing for a non-zero spin I, only spins with spin quantum number $I > 0$ are visible in NMR experiments. The NMR signal is given by the collective signal of a whole spin ensemble of identical nuclei, the macroscopic magnetization. Therefore, the concentration of the nuclei under investigation determines, among other factors like the isotope abundance and the gyromagnetic ratio γ, the NMR signal strength.

For spin-½ nuclei, the macroscopic magnetization can be thought of as a classical vector that can be manipulated by RF-pulses. The component perpendicular to

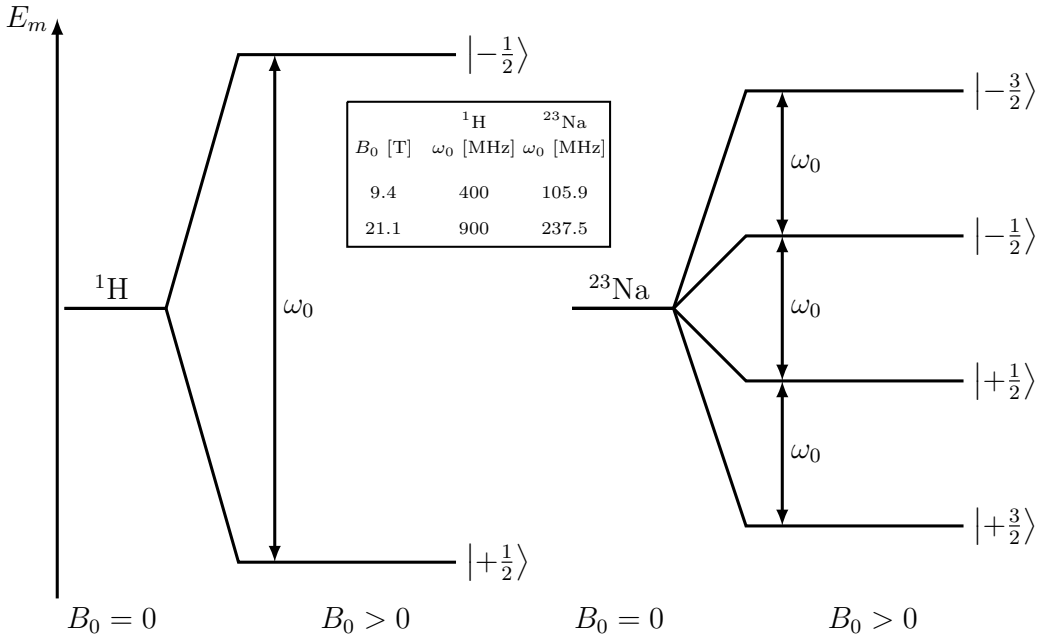

B_0 [T]	^{1}H ω_0 [MHz]	^{23}Na ω_0 [MHz]
9.4	400	105.9
21.1	900	237.5

Fig. 2.1.: Schematic depiction of the Zeeman splitting for ^{1}H (spin-½) and ^{23}Na (spin-3/2) nuclei. While at $B_0 = 0$, the energy levels are degenerated, they equidistantly split up at larger magnetic fields. The splitting is characterized by the Lamor frequency $\omega_0 = \gamma B_0$. Numeric values for ω_0 at $B_0 = 9.4\,\mathrm{T}$ and $B_0 = 21.1\,\mathrm{T}$ are given.

the magnetic field, the transversal magnetization, creates the NMR signal. The evolution of the magnetization vector can be described by the phenomenological Bloch-equations that also take into account relaxation effects, the longitudinal "T_1" and the transversal "T_2" relaxation. The hydrogen nucleus, ^{1}H, has a spin of $I = 1/2$ and creates the strongest NMR signal and is therefore the – by huge margin – most commonly investigated nucleus in NMR experiments. ^{1}H nuclei have a large biological and physical abundance and also a large gyromagnetic ratio γ. Other common spin-½ nuclei are e.g., ^{31}P phosphorous and ^{13}C carbon nuclei. All NMR-active nuclei other than ^{1}H are termed X-nuclei. Table 2.1 summarizes some of the most commonly investigated NMR-active nuclei. Nuclei with spin $I > 1/2$, also called quadrupole nuclei, can also be investigated with NMR and are discussed in the following chapters in more detail.

2.1.2 Formalism for Spin-3/2 Nuclei

Most NMR-active nuclei have a spin $I > 1/2$, the quadrupole nuclei. Examples are ^{23}Na and ^{39}K with spin $I = 3/2$, and ^{2}H and ^{14}N with spin $I = 1$. The description of quadrupole nuclei is more complicated for multiple reasons. Since there are additional Zeeman energy levels, the simple magnetization image is insufficient. Especially higher order coherences, the multiple quantum coherences, have interesting properties and encode information about the molecular environment

Tab. 2.1.: Properties of some of the most important NMR nuclei. Values are taken from [76]. The relative sensitivity only takes the physical abundance of the isotope into account and not the biological abundance c_{bio}.

Isotope	Spin	$\frac{\gamma}{2\pi}$ [MHz/T]	c_{phys} [%]	Relative sensitivity
^{1}H	1/2	42.58	99.985	1.0
^{2}H	1	6.54	0.015	4.8×10^{-3}
^{13}C	1/2	10.71	1.10	1.59×10^{-2}
^{17}O	5/2	5.77	0.038	2.91×10^{-2}
^{19}F	1/2	40.06	100	8.33×10^{-1}
^{23}Na	3/2	11.27	100	9.27×10^{-2}
^{31}P	1/2	17.25	100	6.65×10^{-2}
^{35}Cl	3/2	4.17	75.77	4.7×10^{-3}
^{39}K	3/2	1.99	93.26	4.8×10^{-4}

of the nuclei. The nuclear charge distribution is spherical for spin-1/2 nuclei and therefore rotations do not alter the electrostatic energy of the nucleus. Quadrupole nuclei, on the other hand, have an asymmetric charge distribution as depicted in Figure 2.2. Therefore, the nuclei posses an electric quadrupole moment that interacts with surrounding Electric Field Gradient (EFG) via the quadrupole interaction. In fact, the quadrupole interaction dominates relaxation for quadrupole nuclei such that magnetic interactions often can be neglected [77, 78].

Therefore, a more sophisticated formalism to describe the NMR dynamics of quadrupole nuclei is needed to account for the increased complexity. A similar formalism can also be used for a quantitative description of coupled spin-1/2 nuclei. This section introduces such a formalism for spin-3/2 that is used throughout this thesis. The description of the formalism is based on the work by [10, 11, 51, 71, 73], and own calculations [63].

Density Operator

A single nuclear spin i with $I = 3/2$ can be described in the angular momentum basis $|I = 3/2, m\rangle := |m\rangle$ by

$$|\psi_i\rangle = \sum_m c_m^i |m\rangle = c_{-3/2}^i |-3/2\rangle + c_{-1/2}^i |-1/2\rangle + c_{1/2}^i |1/2\rangle + c_{3/2}^i |3/2\rangle , \quad (2.11)$$

with complex time-dependent coefficients c_m^i that describe the amplitude of each basis element $|m\rangle$. Here, other quantum numbers than I and m describing the system are neglected. This also means that the influence of the fast moving electrons is averaged out and included in the the system Hamiltonian $\hat{\mathcal{H}}_{\text{spin}}$ instead using a full description of the atoms including the nucleus and electrons in a full wave

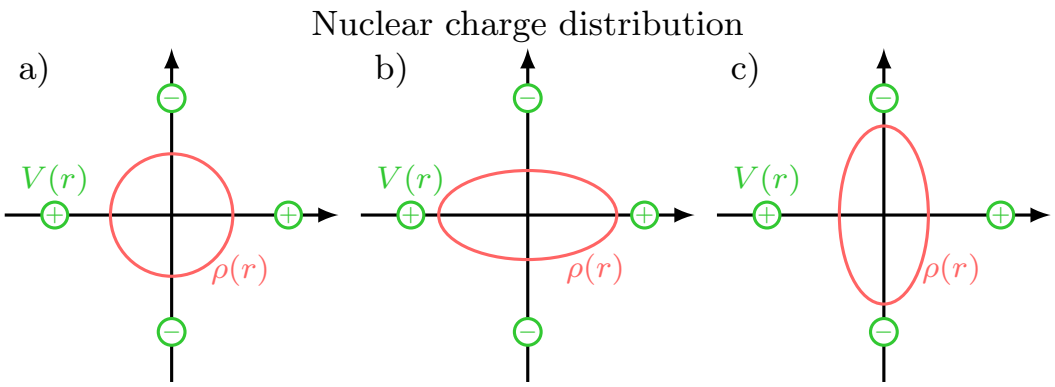

Fig. 2.2.: a) Spherical electrical charge distribution $\rho(\boldsymbol{r}) > 0$ of spin-½ nuclei in an electric potential $V(\boldsymbol{r})$ generated by two positive and two negative electric charges. There is no preferential orientation of the charge distribution due to the spherical symmetry. b) and c) Quadrupole nuclei with spin $I > 1/2$ have an asymmetric charge distribution $\rho(\boldsymbol{r}) > 0$. In the same electric potential as in a), the orientation in c) is energetically preferred, since it minimizes the distance of $\rho(\boldsymbol{r})$ to the negative charges and maximizes the energy to the positive charges. The quadrupole interaction is based on a similar consideration. The asymmetry of the charge distribution is exaggerated.

function $|\psi_{\text{full}}\rangle$. This assumption is also called spin Hamiltonian hypothesis. Since the time scales of motion of electrons and the nucleus is separated by several orders of magnitude and the nucleus influence on the electrons is small, this assumption is valid for NMR experiments with biological samples [73].

However, instead of single spins, NMR measures a whole spin ensemble of N spins and the states of the single spins are unknown. In quantum mechanics such an ensemble is described by the density operator $\hat{\sigma}$. The density operator is a positive ($\hat{\sigma} > 0$), normalized ($\mathrm{Tr}[\hat{\sigma}] = 1$), hermitian ($\hat{\sigma}^\dagger = \hat{\sigma}$) operator. If all spins of the ensemble are in the same state $|\psi_i\rangle$, the density operator is in the pure state

$$\hat{\sigma}_i = |\psi_i\rangle \langle\psi_i| \tag{2.12}$$

For a pure state it is

$$\mathrm{Tr}[\hat{\sigma}^2] = 1 \tag{2.13}$$

and $\hat{\sigma}$ is additionally a projection ($\hat{\sigma}^2 = \hat{\sigma}$) operator. In general and especially in NMR, the system is in a mixed state $\hat{\sigma}$, which is comprised of many pure state subsystems $\hat{\sigma}_i$. The density operator of a mixed state is defined by

$$\hat{\sigma} \coloneqq \sum_i p_i |\psi_i\rangle \langle\psi_i| = \sum_i p_i \hat{\sigma}_i \tag{2.14}$$

where $p_i = N_i/N$ is the probability of the system being in the one of the subsystems $\hat{\sigma}_i$ with N_i spins and it is $\sum_i p_i = 1$. For a mixed state it is

$$\mathrm{Tr}[\hat{\sigma}^2] < 1. \tag{2.15}$$

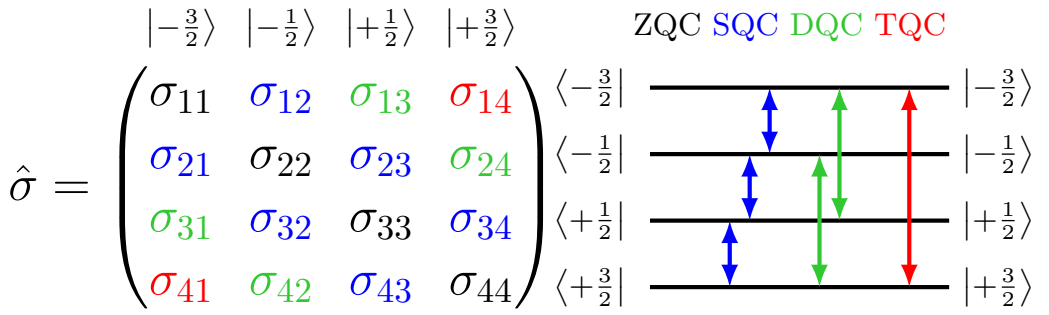

Fig. 2.3.: A matrix representation of the density operator with all components for spin-3/2 nuclei is shown on the left side and the corresponding Zeeman energy levels on the right. The diagonal elements describe the energy level populations, also called zero quantum (ZQ) coherences. The off-diagonal elements describe coherences between neighboring (single quantum (SQ) coherences), next-to-neighboring (double quantum (DQ) coherences) and the upper and lower energy levels (triple quantum (TQ) coherences), respectively as indicated by the arrows between the Zeeman levels.

The expectation value of an observable $\hat{A}$ for a state described by the density matrix $\hat{\sigma}$ is given by

$$\langle \hat{A} \rangle_{\hat{\sigma}} = \mathrm{Tr}[\hat{\sigma}\hat{A}]. \tag{2.16}$$

The matrix elements of the density operator in the angular momentum basis are given by

$$\sigma_{\alpha\beta} = \langle \alpha | \, \hat{\sigma} \, | \beta \rangle = \sum_i p_i \, \langle \alpha | \psi_i \rangle \, \langle \psi_i | \beta \rangle = \overline{c_\alpha c_\beta^*} \tag{2.17}$$

where the overbar over $\overline{c_\alpha c_\beta^*}$ indicates the ensemble average. The diagonal elements $\sigma_{\alpha\alpha} = \overline{c_\alpha c_\alpha^*} = p_\alpha > 0$ denote the occupation probability of the basis state $|\alpha\rangle$ and are also called population or Zero Quantum (ZQ) coherences. The off-diagonal elements $\sigma_{\alpha\beta} = \overline{c_\alpha c_\beta^*}$ (with $\alpha \neq \beta$) correspond to coherences between the states $|\alpha\rangle$ and $|\beta\rangle$ with coherence order $m = \alpha - \beta$ (note that here, m denotes the difference in magnetic quantum number, not the magnetic quantum number as above). For spin-3/2 nuclei, ZQ coherences, Single Quantum (SQ) coherences with $m = 1$, Double Quantum (DQ) coherences for $m = 2$ and Triple Quantum (TQ) coherences are possible. Figure 2.3 shows the 16 independent elements of the density operator and their connection to the coherences.

Tab. 2.2.: Normalized irreducible spherical tensor operators $\hat{T}_{lm}$ based on the definitions of [79, 80]. $[\hat{A}, \hat{B}]_+ = \hat{A}\hat{B} + \hat{B}\hat{A}$ is the anticommutator. For convenience, here and in the following, the angular momentum operators $\hat{I}_i$ are defined without the $\hbar$.

$\hat{T}_{lm}$	**Definition**	**Meaning**
$\hat{T}_{00}$	$\frac{1}{2}\mathbb{1}$	Identity
$\hat{T}_{10}$	$\frac{1}{\sqrt{5}}\hat{I}_z$	Longitudinal magnetization
$\hat{T}_{20}$	$\frac{1}{6}(3\hat{I}_z^2 - I(I+1)\mathbb{1})$	Quadrupole mangetization
$\hat{T}_{30}$	$\frac{1}{3\sqrt{5}}(5\hat{I}_z^3 - (3I(I+1)-1)\hat{I}_z)$	Octupole magnetization
$\hat{T}_{1\pm1}$	$\mp\frac{1}{\sqrt{10}}\hat{I}_\pm$	Rank 1 SQC
$\hat{T}_{2\pm1}$	$\mp\frac{1}{2\sqrt{6}}[\hat{I}_z, \hat{I}_\pm]_+$	Rank 2 SQC
$\hat{T}_{3\pm1}$	$\mp\frac{1}{4\sqrt{15}}[\hat{I}_z^2 - (I(I+1) - \frac{1}{2})\mathbb{1}, \hat{I}_\pm]_+$	Rank 3 SQC
$\hat{T}_{2\pm2}$	$\frac{1}{2\sqrt{6}}\hat{I}_\pm^2$	Rank 2 DQC
$\hat{T}_{3\pm2}$	$\frac{1}{2\sqrt{6}}[\hat{I}_z, \hat{I}_\pm^2]_+$	Rank 3 DQC
$\hat{T}_{3\pm3}$	$\mp\frac{1}{6}\hat{I}_\pm^3$	Rank 3 TQC

Irreducible Spherical Tensor Operators (ISTOs)

It is convenient to represent the density operator $\hat{\sigma}$ in the Irreducible Spherical Tensor Operator (ISTO) basis

$$\hat{\sigma} = \sum_{l,m} A_{lm}(t)\hat{T}_{lm} \tag{2.18}$$

where $\hat{T}_{lm}$ are the ISTO basis elements and the complex coefficients $A_{lm}(t)$ are time-dependent amplitudes. In general for nuclei with spin I, the ISTO basis consists of $(2I+1)^2$ tensors $\hat{T}_{lm}$ with ranks $l = 0, 1, \ldots 2I$ and coherence orders $m = -l, -l+1, \ldots, l-1, l$. For spin-3/2 this corresponds to 16 tensors and rank $l = 0, 1, 2, 3$. The $\hat{T}_{lm}$ are summarized in Table 2.2 with the definitions and normalization of Bowden and Hutchison [79]. Note that here and in the following, the angular momentum operators $\hat{I}_i$ are defined without the $\hbar$. The Hamiltonian $\hat{\mathcal{H}}$ is then given in units of [J/$\hbar$] and only in numerical calculations, the $\hbar$'s are added back where necessary.

In the literature, often symmetric and antisymmetric combinations of the ISTOs are defined

$$\begin{aligned}\hat{T}_{11}(s) &= \frac{1}{\sqrt{2}}(\hat{T}_{1-1} + \hat{T}_{11}) \\ \hat{T}_{11}(a) &= \frac{1}{\sqrt{2}}(\hat{T}_{1-1} - \hat{T}_{11}).\end{aligned} \tag{2.19}$$

$\hat{T}_{lm}(a)$ and $\hat{T}_{lm}(s)$ are both hermitian which reflects of the hermitian nature of the Hamiltonian and observables in quantum mechanics. Since always both the tensors with $+m$ and $-m$ are formed, this step is not necessary and in this thesis only the $\hat{T}_{l\pm m}$ are used. The dynamics of both pathways is analogous in most cases, and therefore, the second pathway with $-m$ is only explicitly mentioned if necessary.

The ISTOs are used to express the density operator and the Hamiltonian of the system due to their interesting rotation properties under the effect of hard RF-pulses and relaxation:

- Hard RF-pulses only change the coherence order m of the $\hat{T}_{lm}$ as shown in Subsection 2.1.5.
- Relaxation only changes the rank l of $\hat{T}_{lm}$ as shown in Subsection 2.1.6.

Dynamics

The dynamics of the density operator follow the Liouville equation

$$\frac{\mathrm{d}\hat{\sigma}}{\mathrm{d}t} = -\frac{i}{\hbar}[\hat{\mathcal{H}}, \hat{\sigma}] \tag{2.20}$$

where $\mathcal{H}$ is the Hamilton operator of the system. In NMR, the $\hbar$ of the Liouville equation is usually absorbed by the Hamiltonian $\mathcal{H}$, which is then given in units of $[\mathrm{J}/\hbar]$. The Liouville equation then becomes

$$\frac{\mathrm{d}\hat{\sigma}}{\mathrm{d}t} = -i[\hat{\mathcal{H}}, \hat{\sigma}]. \tag{2.21}$$

The formal solution of the Liouville equation is then given by

$$\hat{\sigma}(t) = \mathrm{e}^{-i\hat{\mathcal{H}}t}\hat{\sigma}(0)\mathrm{e}^{i\hat{\mathcal{H}}t} \tag{2.22}$$

with the initial state $\hat{\sigma}(0)$.

The Hamiltonian $\hat{\mathcal{H}}$ is the sum of the Hamiltonians of all interactions of the system. Two types of interaction of the nucleus with the environment are taken into account, interactions of the magnetic moment of the nucleus with magnetic fields and surrounding interactions of the nucleus charge distribution with surrounding electric fields. The interactions can be subdivided in two types that describe the origin of the surrounding fields.

On the one hand, internal interactions fields, originating from interactions of the nuclei with molecules and atoms in the sample itself, cannot be controlled and cause relaxation of the magnetization. Thus, investigating the relaxation dynamics reveal information about the molecular environment of the nuclei. The electric fields are internal in the standard NMR experiment and the corresponding interaction, called quadrupole interaction, leads to interaction of quadrupole nuclei ($I > 1/2$) with EFGs of the environment of the nuclear spin. Internal magnetic interactions are for example the dipole-dipole interaction, J-coupling and the chemical shift interaction.

Since in most cases internal magnetic interactions are much weaker than the electric quadrupole interaction, magnetic interactions can often be neglected for quadrupole nuclei.

On the other hand, external fields originate from the NMR apparatus, such as the static magnetic field, RF-pulses and gradient fields. They can be controlled with the purpose of manipulating the spins in a beneficial way for the NMR experiment. As introduced before, the static magnetic field B_0 causes a Zeeman splitting of the energy levels of the nucleus. The Zeeman Hamiltonian in Equation (2.6) can also be expressed in terms of the ISTO basis:

$$\hat{\mathcal{H}}_Z = -\omega_0 \hat{I}_z = -\omega_0 \sqrt{5} \hat{T}_{10}. \tag{2.23}$$

The Zeeman interaction is the dominating NMR interaction several orders of magnitude stronger than the other interactions. Neglecting all other contributions, the formal solution of the Liouville equation for the Zeeman Hamiltonian is

$$\hat{\sigma}(t) = \mathrm{e}^{-i\hat{\mathcal{H}}t} \hat{\sigma}(0) \mathrm{e}^{i\mathcal{H}t}. \tag{2.24}$$

Assuming, that $\hat{\sigma}(0) = \sum_{l,m} A_{lm} \hat{T}_{lm}$, i.e. that the density operator is given by an arbitrary state in the ISTO basis, and using the Baker–Campbell–Hausdorff formula and the commutator relations of the ISTO tensors, it can be easily shown, that

$$\hat{\sigma}(t) = \sum_{l,m} A_{lm} \hat{T}_{lm} \mathrm{e}^{-im\omega_0 t}. \tag{2.25}$$

This describes Lamor precession around the quantization axis z and reproduces the result from the phenomenological discussion regarding the Lamor frequency in Subsection 2.1.1.

Besides the Zeeman Hamiltonian, the total Hamiltonian $\hat{\mathcal{H}}$ is comprised of the Hamiltonian $\hat{\mathcal{H}}_{\mathrm{RF}}$ of RF-pulses, the internal Hamiltonian $\hat{\mathcal{H}}_{\mathrm{relax}}$, which describes relaxation, and potential other Hamiltonian resulting for example from a gradient field:

$$\hat{\mathcal{H}} = \hat{\mathcal{H}}_Z + \hat{\mathcal{H}}_{\mathrm{RF}} + \hat{\mathcal{H}}_{\mathrm{relax}} + \dots. \tag{2.26}$$

In the high field regime, with large B_0, the interaction with the external magnetic field is much stronger than the RF-fields and relaxation and therefore, $\hat{\mathcal{H}}_{\mathrm{RF}}$ and $\hat{\mathcal{H}}_{\mathrm{relax}}$ can be considered as a small perturbation.

The RF pulse Hamiltonian $\hat{\mathcal{H}}_{\mathrm{RF}}$ and the relaxation Hamiltonian $\hat{\mathcal{H}}_{\mathrm{relax}}$ are discussed in Subsection 2.1.5 and Subsection 2.1.6, respectively.

Interaction Picture and the Rotating Frame

As shown in Subsection 2.1.2, the Zeeman Hamiltonian $\hat{\mathcal{H}}_Z$ only leads to an oscillatory term in the dynamics of the density operator $\hat{\sigma}(t)$ without any further

dynamics, such as transitions between the tensors. It is convenient to switch into an rotating frame with the Lamor frequency ω_0, which removes $\hat{\mathcal{H}}_Z$ and hence the oscillatory term from the dynamics. In quantum mechanics, this is equivalent to switching into the interaction picture with $\hat{\mathcal{H}}_Z$ as $\hat{\mathcal{H}}_0$ and the other Hamiltonians, $\hat{\mathcal{H}}_{\text{RF}}$ and $\hat{\mathcal{H}}_{\text{relax}}$, as $\hat{\mathcal{H}}_1$. Operators and states in the interaction picture are denoted by an additional "$*$" as index and transform like

$$\begin{aligned} |\psi^*(t)\rangle &= \mathrm{e}^{i\hat{\mathcal{H}}_0 t}\,|\psi\rangle \qquad \text{and} \\ \hat{A}^* &= \mathrm{e}^{i\hat{\mathcal{H}}_0 t}\hat{A}\mathrm{e}^{-i\hat{\mathcal{H}}_0 t}. \end{aligned} \tag{2.27}$$

Consequently, the density operator in the interaction picture is given by

$$\hat{\sigma}^* = \mathrm{e}^{i\hat{\mathcal{H}}_0 t}\hat{\sigma}\mathrm{e}^{-i\hat{\mathcal{H}}_0 t} \tag{2.28}$$

and with $\hat{\mathcal{H}}_0^* = \hat{\mathcal{H}}_0$, the Liouville equation in the interaction picture is

$$\frac{\mathrm{d}\hat{\sigma}^*}{\mathrm{d}t} = -i\left[\hat{\mathcal{H}}_1^*, \hat{\sigma}^*\right] \tag{2.29}$$

with

$$\hat{\mathcal{H}}_1^* = \mathrm{e}^{i\hat{\mathcal{H}}_0 t}\hat{\mathcal{H}}_1\mathrm{e}^{-i\hat{\mathcal{H}}_0 t} = \hat{\mathcal{H}}_{\text{RF}}^* + \hat{\mathcal{H}}_{\text{relax}}^*. \tag{2.30}$$

In the following sections, the dynamics is described in the rotating frame rotating with the Lamor frequency.

2.1.3 Thermal Equilibrium and Macroscopic Magnetization

In this section, the thermal equilibrium density operator, starting point of every NMR experiment, and the macroscopic magnetization, which determines the strength of the NMR signal, are determined.

Without a magnetic field, all spins are in random super positions without a preferred direction. In a magnetic field, the Zeeman effect leads to a splitting of the energy levels and a preferred direction given by the quantization axis, the z-axis. The spin ensemble interacts with atoms and molecules of the sample, which can be interpreted as a thermal reservoir with exchange of energy but not particles. Hence, the systems thermal equilibrium of many nuclei can be described by the canonical ensemble and is given by

$$\hat{\sigma}_{\text{eq}} = \frac{1}{Z}\exp\left(-\hat{\mathcal{H}}_0/k_B T\right) \tag{2.31}$$

with $\hat{\mathcal{H}}_0 = \hat{\mathcal{H}}_Z$ in the high field regime, the Boltzmann constant $k_B = 1.38 \times 10^{-23}\,\text{J/K}$, the temperature T and the partition function

$$Z = \mathrm{Tr}\left(\exp\left(-\hat{\mathcal{H}}_0/k_B T\right)\right) \approx \mathrm{Tr}\left(\mathbb{1} - \hat{\mathcal{H}}_0/k_B T\right) \approx 2I + 1. \tag{2.32}$$

In the last two steps the high temperature approximation, $\Delta E = \hbar\omega_0 B_0 \ll k_B T$ was used to truncate the Taylor series. This approximation is justified since the temperature is in the range of 310 K and therefore the thermal energy in the range of 4.38×10^{-21} J, while at 9.4 T, the Zeeman energy splitting is in the range of 1.12×10^{-26} J for $^{23}\mathrm{Na}$, and thus much smaller than the thermal energy. Inserting Equation (2.32) into Equation (2.31) and Taylor expanding the equation gives

$$\hat{\sigma}_{\mathrm{eq}} = \frac{1}{2I+1}\left(\mathbb{1} - \frac{\hat{\mathcal{H}}}{k_B T}\right) = \frac{1}{2I+1}\left(\mathbb{1} + \frac{\gamma B_0}{k_B T}\hat{I}_z\right) \tag{2.33}$$

Since the identity operator $\mathbb{1}$ commutes with every other operator, this part of the density operator does not participate in NMR dynamics and is therefore dropped from the description for convenience. Furthermore, the equilibrium density operator can be expressed in terms of the ISTO basis such that it is

$$\hat{\sigma}_{\mathrm{eq}} = \frac{1}{2I+1}\left(\mathbb{1} - \frac{\hat{\mathcal{H}}}{k_B T}\right) = \frac{1}{2I+1}\frac{\gamma B_0}{k_B T}\hat{I}_z = \frac{\sqrt{5}\gamma B_0}{(2I+1)k_B T}\hat{T}_{10}. \tag{2.34}$$

The prefactor is called Boltzmann factor and is usually dropped from the density operator for simplicity. In thermal equilibrium there is only magnetization along the quantization axis z. This is also called longitudinal magnetization. By an RF-pulse the magnetization can be transferred into $\hat{T}_{1\pm1}$ coherences, which are also called transversal magnetization. Higher order and rank tensors do not have a spin-½ analogue.

The NMR signal results from the macroscopic magnetization, which is given by the sum over the expectation values of the magnetic moments $\boldsymbol{\mu}_I = \gamma\hat{\boldsymbol{I}}$ of all N spins with in a volume V:

$$\boldsymbol{M}_0 = \sum_{i=1}^{N}\frac{\langle\boldsymbol{\mu}_I\rangle}{V} = \frac{N}{V}\gamma\mathrm{Tr}(\sigma\hat{\boldsymbol{I}}) \tag{2.35}$$

The last step uses Equation (2.16) for the expectation value. For $B_0 = 0$, the expectation value of $\boldsymbol{\mu}_I$ is 0 and there is no NMR signal. For $B_0 > 0$ the macroscopic magnetization in thermal equilibrium density matrix $\hat{\sigma}_{\mathrm{eq}}$ from Equation (2.34) is determined by

$$\boldsymbol{M}_0 = \frac{N}{V}\gamma\mathrm{Tr}(\hat{\sigma}_{\mathrm{eq}}\hat{\boldsymbol{I}}) = \frac{N}{V}\frac{\gamma^2 B_0}{(2I+1)k_B T}\mathrm{Tr}(\hat{I}_z\hat{\boldsymbol{I}}) \tag{2.36}$$

Since $\mathrm{Tr}(\hat{I}_z\hat{I}_k) = 0$ for $k = y, x$ and $\mathrm{Tr}(\hat{I}_z^2) = \hbar^2 I(I+1)(2I+1)/3$, only the z component contributes to the macroscopic magnetization. The macroscopic magnetization in z direction is given by

$$M_{0,z} = \frac{N}{V}\frac{\gamma^2 B_0}{(2I+1)k_B T}\mathrm{Tr}(\hat{I}_z^2) = \frac{N}{V}\frac{\gamma^2\hbar^2 B_0 I(I+1)}{3k_B T} \tag{2.37}$$

For spin-½ nuclei, the time evolution of the magnetization vector

$$\boldsymbol{M}_0 = \frac{N}{V}\frac{\gamma^2 B_0}{3k_B T}\boldsymbol{z} \tag{2.38}$$

with $\boldsymbol{z}$ being the unit vector in z-direction, can be described classically by

$$\frac{\mathrm{d}}{\mathrm{d}t}\boldsymbol{M} = \gamma(\boldsymbol{M} \times \boldsymbol{B}) \tag{2.39}$$

where $\boldsymbol{B}$ is the the magnetic field that is comprised of the static magnetic field $\boldsymbol{B}_0$ and potential additional magnetic fields, like the magnetic field $\boldsymbol{B}_1(t)$ of RF-pulses. Together with an introduction of T_1 and T_2 relaxation, the resulting differential equations are called Bloch-equations [67]:

$$\begin{aligned} \mathrm{d}M_x/\mathrm{d}t &= \gamma(\boldsymbol{M} \times \boldsymbol{B})_x - M_x/T_2, \\ \mathrm{d}M_y/\mathrm{d}t &= \gamma(\boldsymbol{M} \times \boldsymbol{B})_y - M_y/T_2, \\ \mathrm{d}M_z/\mathrm{d}t &= \gamma(\boldsymbol{M} \times \boldsymbol{B})_z - (M_z - M_{0,z})/T_1 \end{aligned} \tag{2.40}$$

with the phenomenological relaxation times T_1 for longitudinal relaxation and T_2 for transversal relaxation. These equations are mentioned for completeness, but since this thesis is concerned with spin-3/2 nuclei, where this description is insufficient, they are only provided as a reference.

2.1.4 Sensitivity and the NMR Signal Detection

The thermal equilibrium density operator $\hat{\sigma}_{\mathrm{eq}}$ from Equation (2.34) can be flipped into the x, y-plane by an RF-pulse with phase ϕ (details are discussed in Subsection 2.1.5) and create perpendicular magnetization

$$\hat{\sigma}_\perp(t) = \frac{\sqrt{5}\gamma B_0}{(2I+1)k_B T}\frac{1}{\sqrt{2}}\mathrm{e}^{-i\phi}(\hat{T}_{11}\mathrm{e}^{-i\omega_0 t} + \hat{T}_{1-1}\mathrm{e}^{i\omega_0 t}). \tag{2.41}$$

that Lamor precesses in the laboratory frame. Levitt [73] shows in their book, that only one of the tensors $\hat{T}_{11}$ and $\hat{T}_{1-1}$ contribute to the signal. Per convention, $\hat{T}_{1-1} = -1/\sqrt{10}\hat{I}_-$ is defined as the detected coherence.

With an analogous calculation as for the macroscopic magnetization in the thermal equilibrium, the macroscopic magnetization for the system with the density operator $\hat{\sigma}_\perp$ can be calculated:

$$\begin{aligned} \boldsymbol{M}_{\perp,x} &= \frac{N}{V}\frac{\gamma^2 B_0}{(2I+1)k_B T}\frac{1}{\sqrt{2}}\mathrm{Tr}(\hat{I}_-\hat{I}_x)\mathrm{e}^{i(\omega_0 t-\phi)} = \frac{1}{\sqrt{2}}\frac{N}{V}\frac{\gamma^2\hbar^2 B_0 I(I+1)}{3k_B T}\mathrm{e}^{i(\omega_0 t-\phi)} \\ \boldsymbol{M}_{\perp,y} &= \frac{N}{V}\frac{\gamma^2 B_0}{(2I+1)k_B T}\frac{1}{\sqrt{2}}\mathrm{Tr}(\hat{I}_-\hat{I}_y)\mathrm{e}^{i(\omega_0 t-\phi)} = \frac{i}{\sqrt{2}}\frac{N}{V}\frac{\gamma^2\hbar^2 B_0 I(I+1)}{3k_B T}\mathrm{e}^{i(\omega_0 t-\phi)} \end{aligned} \tag{2.42}$$

Only the real part is detected and thus

$$\begin{aligned}\mathrm{Re}(\boldsymbol{M}_{\perp,x}) &= \frac{1}{\sqrt{2}}\frac{N}{V}\frac{\gamma^2\hbar^2 B_0 I(I+1)}{3k_B T}\sin(\omega_0 t+\phi)\\ \mathrm{Re}(\boldsymbol{M}_{\perp,y}) &= \frac{1}{\sqrt{2}}\frac{N}{V}\frac{\gamma^2\hbar^2 B_0 I(I+1)}{3k_B T}\cos(\omega_0 t+\phi)\end{aligned} \tag{2.43}$$

Thus there is macroscopic x and y magnetization with a phase shift of $\pi/2$ that is precessing around the z-axis. This oscillating magnetic field induces a voltage U_{ind} in the receiver RF-coil according to Faraday's law of induction:

$$U_{\mathrm{ind}} = -\frac{\mathrm{d}\Phi(t)}{\mathrm{d}t} \tag{2.44}$$

with the magnetic flux given by the surface integral

$$\Phi = \int_S \boldsymbol{B}\mathrm{d}S. \tag{2.45}$$

With a short calculation it follows for the induce voltage U_{ind}

$$U_{\mathrm{ind}} = -\frac{\mathrm{d}}{\mathrm{d}t}\int_V \mathrm{d}\boldsymbol{r}\boldsymbol{M}_{\perp}(\boldsymbol{r},t)\boldsymbol{B}_1^-(\boldsymbol{r}) \tag{2.46}$$

where $\boldsymbol{B}_1^-(\boldsymbol{r})$ is the receive field of the RF coil. Using that $U_{\mathrm{ind}} \propto \gamma M_{\mathrm{eq,z}}$ as shown by Haacke et al. [74] the sensitivity is proportional to

$$S \propto U_{\mathrm{ind}} \propto \gamma^3 I(I+1)c_{\mathrm{phys}}c_{\mathrm{bio}}. \tag{2.47}$$

Here, c_{phys} is the relative abundance of the detected isotope ($c_{\mathrm{phys}} = 1$ for $^{23}\mathrm{Na}$) and c_{bio} is the biological abundance of the nuclei. Note the γ^3 dependence, one of the reasons why the NMR signal of most X-nuclei is weak compared to the $^1\mathrm{H}$ NMR signal. $^1\mathrm{H}$ has a high γ and c_{bio}, which leads to the strongest NMR signal. $^{23}\mathrm{Na}$ yields the second strongest NMR signal in biological tissue, which is, however, around 20 000 times weaker than the $^1\mathrm{H}$ signal. Table 2.1 shows the NMR properties for some of the most used NMR nuclei.

The precession with Larmor frequency ω_0 is too fast for the common hardware to detect, since this would require several million data points per second in the Analog-to-Digital Converter (ADC) that transforms the acquired analog signal in the digital signal used in the post processing and data analysis. Instead, the signal $S(t)$ is interfered with a synthesized sinusoidal signal with frequency ω_{ref} from the RF-synthesizer. This can be interpreted as switching to a rotating frame with frequency ω_{ref}. In this thesis the assumption $\omega_{\mathrm{ref}} = \omega_0$ is used and therefore, the detection effectively takes place in the rotating frame with Lamor frequency that is also used in the description of the NMR dynamics.

A more detailed and also more technical description of the NMR detection and hardware can be found for example in Levitt [73].

2.1.5 Radiofrequency Pulses

The density operator can be manipulated using RF-pulses, whereby the effect of the RF-pulse on the probe depends on pulse strength, length of the pulse, pulse shape and also on relaxation effects during the application of the RF-pulse.

An RF-pulse is realized by applying an additional magnetic field $B_1(t)$ that is oscillating with a frequency ω_{RF} and transversal to the static magnetic field B_0. The Hamiltonian $\mathcal{H}_{\mathrm{RF}}$ of an arbitrary RF-pulse applied in the y-direction is given by

$$\hat{\mathcal{H}}_{\mathrm{RF}} = -\gamma B_1(t)\hat{I}_y \cos(\omega_{\mathrm{RF}} t) = -\omega_1(t)\hat{I}_y \cos(\omega_{\mathrm{RF}} t), \tag{2.48}$$

with $\omega_1(t) = \gamma B_1(t)$. Using $\hat{I}_y = i\sqrt{5/2}(\hat{T}_{11} + \hat{T}_{1-1})$ and transforming the Hamiltonian in the Lamor frequency rotating frame

$$\hat{\mathcal{H}}^*_{\mathrm{RF}} = -i\sqrt{5/2}\omega_1(t)\left(\hat{T}_{11}\mathrm{e}^{i(\omega_0-\omega_{\mathrm{RF}})t} + \hat{T}_{1-1}\mathrm{e}^{-i(\omega_0-\omega_{\mathrm{RF}})t}\right) \tag{2.49}$$

Here, terms oscillating with $\omega_0 + \omega_{\mathrm{RF}}$ were dropped since they average out. In the case of excitation on-resonance, i.e. $\omega_0 = \omega_{\mathrm{RF}}$, $\hat{\mathcal{H}}^*_{\mathrm{RF}}$ simplifies to

$$\hat{\mathcal{H}}^*_{\mathrm{RF}} = -i\sqrt{5/2}\omega_1(t)\left(\hat{T}_{11} + \hat{T}_{1-1}\right) = -\omega_1(t)\hat{I}_y. \tag{2.50}$$

Hard RF-Pulses

Throughout this thesis, the hard pulse approximation is used, which applies for short, strong RF-pulses, during which relaxation effects can be neglected and the effect of the pulse can be considered instant. In the experiments presented in this thesis, the pulse duration was in the range of 80-300 μs and therefore much shorter than the relaxation times which are in the range of several ms. The evolution of the density matrix σ^* under the influence of the hard pulse is only determined by $\mathcal{H}^*_{\mathrm{RF}}$ in the rotating frame. It is further assumed that the RF-pulse is a simple block pulse of length τ_p with constant frequency ω_{RF}. The effect of the RF-pulse is then given by the Liouville equation in the interaction picture

$$\frac{\mathrm{d}\hat{\sigma}^*}{\mathrm{d}t} = -i[\hat{\mathcal{H}}^*_{\mathrm{RF}}, \hat{\sigma}^*] = -i\omega_1(t)[\hat{I}_y, \hat{\sigma}^*] \tag{2.51}$$

with the formal solution

$$\hat{\sigma}^*(t) = \mathrm{e}^{-i\hat{\mathcal{H}}^*_{\mathrm{RF}}t}\hat{\sigma}^*(0)\mathrm{e}^{i\hat{\mathcal{H}}^*_{\mathrm{RF}}t}. \tag{2.52}$$

Analogously to a spin-½ system, this corresponds to a rotation of the spin-system around the y-axis by a flip angle θ of

$$\theta = \omega_1\tau_p. \tag{2.53}$$

The application of an RF-pulse in y-direction can be generalized to a pulse with arbitrary phase ϕ. This can be achieved by rotating the reference coordinate system

by ϕ around the z-axis on the y-axis, performing the RF-pulse in y-direction and rotating back by $-\phi$ around the z-axis. The RF-pulse superoperator $\hat{P}(\theta, \phi)$ for an RF-pulse with flip angle θ and phase ϕ can be expressed by the rotation superoperator [51]:

$$\hat{P}(\theta, \phi) = \hat{D}(-\phi, \theta, \phi). \tag{2.54}$$

The RF-pulse superoperator $P(\theta, \phi)$ acts on the ISTO basis elements like [51]

$$\hat{P}(\theta, \phi)\hat{T}_{lm} = \sum_{m'} \mathrm{e}^{-i(m'-m)\phi} d^l_{m'm}(\theta)\hat{T}_{lm'} \tag{2.55}$$

with the Wigner matrix elements $d^l_{m'm}(\theta)$ [81]. Hence, hard RF-pulses can only change the coherence order m of T_{lm} but leave the rank l unchanged. Moreover, a phase is accumulated that depends on the difference in coherence order and the phase of the pulse. This effect is exploited in Multiple Quantum (MQ) filtering sequences, which – with the right choice of pulse phases – makes the MQ signal distinguishable from the SQ signal or leads to suppression of all signal components but the desired MQ coherences.

2.1.6 Relaxation

After excitation, the spin system slowly returns back to thermal equilibrium magnetization by interaction of the spins with each other and the environment. This process is called relaxation and is driven by several different processes. For spin-1/2 nuclei, dipole-dipole interaction and the chemical shift usually dominate relaxation, but other processes like J-coupling also contribute. For quadrupole nuclei (spin $I > 1/2$), electric quadrupole interaction dominates relaxation in most situations and other interactions can be neglected. In this section, the electric quadrupole interaction and the NMR dynamics that follow from it are derived based on the work by Maarel [10, 11], Tanase and Boada [51], Jaccard et al. [53], Abragam [71], Slichter [72], and Levitt [73] and own calculations [63].

Quadrupole Interaction

Quadrupole nuclei are slightly deformed from perfect spherical shape. This leads to an electric quadrupole moment that interacts with surrounding electric fields. Thus, the required energy to reorient the nucleus does not only depend on the magnetic fields but also the electric environment. Figure 2.2 schematically shows a deformed nucleus in an electric field. The energy depends on the orientation of the nucleus.

These electric fields originate from electric charges distributed around the nucleus, with the electrons from the atomic shell being the primary source due to their closest distance to the nucleus. Classically, the potential electric energy of the electric charge

distribution $\rho(\boldsymbol{r})$ of the nucleus in the electric potential $V(\boldsymbol{r})$, created by the electric charges, is then given by

$$E_{\text{elec}} = \int \rho(\boldsymbol{r}) V(\boldsymbol{r}) \mathrm{d}\boldsymbol{r}. \tag{2.56}$$

With a Taylor expansion of the electric potential $V(\boldsymbol{r})$ around the origin $\boldsymbol{r} = 0$ the electric energy becomes

$$E_{\text{elec}} = \underbrace{V(0) \int \rho(\boldsymbol{r}) \mathrm{d}\boldsymbol{r}}_{E^{(0)}_{\text{elec}}} + \underbrace{\sum_i V_i \int x_i \rho(\boldsymbol{r}) \mathrm{d}\boldsymbol{r}}_{E^{(1)}_{\text{elec}}} + \underbrace{\frac{1}{2!} \sum_{i,j} V_{ij} \int x_i x_j \rho(\boldsymbol{r}) \mathrm{d}\boldsymbol{r}}_{E^{(2)}_{\text{elec}}} + \dots \tag{2.57}$$

where x_i with $i = 1, 2, 3$ are the three components x, y and z of $\boldsymbol{r}$ and the abbreviations

$$V_i := \left.\frac{\partial V}{\partial x_i}\right|_{\boldsymbol{r}=0} \quad \text{and} \quad V_{ij} := \left.\frac{\partial^2 V}{\partial x_i \partial x_j}\right|_{\boldsymbol{r}=0} \tag{2.58}$$

were used. $E^{(0)}_{\text{elec}}$ is the electrostatic energy or Coulomb energy of the nucleus and only leads to a constant shift of the energy, that does not contribute to the NMR dynamics and therefore can be ignored. $E^{(1)}_{\text{elec}}$ describes the interaction between the electric dipole moment $\int x_i \rho(\boldsymbol{r}) \mathrm{d}\boldsymbol{r}$ of the nucleus with the electric field $\boldsymbol{E} = -\boldsymbol{\nabla}\phi(\boldsymbol{r})$ of the environment. Since all experiments indicate that the nucleus has a defined parity, the electric dipole moment is an integral over an odd and and even function and therefore vanishes. A similar argumentation holds for all odd terms. For spin-½ nuclei this is the highest order term that is not vanishing and therefore there is no electric interaction of spin-½ in NMR.

$E^{(2)}_{\text{elec}}$ describes the interaction of the electric quadrupole moment of the nucleus with the EFG tensor V_{ij} created by the environment. In the principal axis system, the the off-diagonal elements of the EFG tensor vanish and since the electric potential V satisfies the Laplace equation $\nabla^2 V = 0$ in most cases[1], the trace of the EFG tensor vanishes, too. The electric quadrupole moment results from an asymmetric charge distribution of the nucleus that occurs for all nuclei with $I > 1/2$. The electric quadrupole tensor Q_{ij} is defined as

$$Q_{ij} = \int (3 x_i x_j - \delta_{ij} r^2) \rho(\boldsymbol{r}) \mathrm{d}\boldsymbol{r} \tag{2.59}$$

[1] In some cases the Poisson equation applies. In this case, there is an additional orientation independent electrostatic term which describes the interaction of the nucleus charge distribution with electrons at the same position. Similar as $E^{(0)}_{\text{elec}}$ does not matter for NMR.

with the Kronecker delta $\delta_{ij} = 1$ for $i = j$ and $\delta_{ij} = 0$ otherwise and $r^2 = x^2+y^2+z^2$. Using Q_{ij} and the Laplace equation $\nabla^2 V = 0$, the quadrupole energy $E^{(2)}_{\text{elec}}$ can be simplified to

$$E^{(2)}_{\text{elec}} = \frac{1}{6}\sum_{i,j}\left(V_{ij}Q_{ij} + V_{ij}\delta_{ij}\int r^2\rho(\boldsymbol{r})\mathrm{d}\boldsymbol{r}\right) = \frac{1}{6}\sum_{i,j}V_{ij}Q_{ij}. \tag{2.60}$$

For quantum mechanical treatment of the interaction, the classical charge distribution, $\rho(\boldsymbol{r})$, has to be translated into its quantum mechanical operator analogue, which is given by the sum over all nucleons. Since neutrons are neutral, only the sum over the protons is left

$$\hat{\rho}(\boldsymbol{r}) = \sum_{k=1}^{Z} q_k\delta(\hat{\boldsymbol{r}} - \hat{\boldsymbol{r}}_k), \tag{2.61}$$

where $q_k = e$ is the electric charge of the nucleon. The electric quadrupole tensor becomes

$$\hat{Q}_{ij} = e\sum_{k=1}^{Z}(3\hat{x}_{ik}\hat{x}_{jk} - \delta_{ij}\hat{r}_k^2) \tag{2.62}$$

where $\hat{x}_{ik}$ is the i position operator for proton k and $\hat{r}_k^2 = \sum_i \hat{x}_{ik}^2$. Instead of the energy, the Hamiltonian $\hat{H}_Q$ of the quadrupole interaction is used:

$$\hat{H}_Q = \frac{1}{6}\sum_{i,j}V_{ij}\hat{Q}_{ij}. \tag{2.63}$$

By using the angular momentum, momentum and position operator commutator relations it can be shown that

$$\hat{H}_Q = \frac{eQ}{6I(2I-1)}\sum_{i,j}V_{ij}\left(\frac{3}{2}\left(\hat{I}_i\hat{I}_j + \hat{I}_j\hat{I}_i\right) - \delta_{ij}\hat{I}^2\right), \tag{2.64}$$

where eQ is the quadrupole moment of the nucleus. Note, that only one nuclear constant is necessary to represent the electric quadrupole tensor $\hat{Q}_{ij}$ since the nucleus is in a state of definite angular momentum which is the quantum mechanical analogue of classical cylindrical symmetry of the charge distribution. The energy to change the orientation of the nucleus only depends on the difference between the charge distribution parallel and transverse to the symmetry axis (usually set to the z axis).

The EFG tensor can be fully described by two parameters, the electric field gradient eq and the asymmetry parameter η in the principal axis system. q and η are defined as

$$\begin{aligned} eq &= V_{zz} \\ \eta &= \frac{V_{xx} - V_{yy}}{V_{zz}}. \end{aligned} \tag{2.65}$$

The Hamiltonian then simplifies to

$$\hat{H}_Q = \frac{e^2qQ}{4I(2I-1)}\left(3\hat{I}_z^2 - I(I+1) + \frac{\eta}{2}\left(\hat{I}_+^2 + \hat{I}_-^2\right)\right), \tag{2.66}$$

The quadrupole interaction is determined by two parameters. The first is the nuclear quadrupole moment eQ, a nuclear specific constant. Example values are 10.4 fm^2 for ^{23}Na, 2.0 fm^2 for ^{14}N and 5.9 fm^2 for ^{39}K [73]. The second parameter is the electric field gradient eq which is determined by the molecular environment of the nucleus. Therefore, the NMR signal of quadrupole nuclei can be used to investigate interactions of the nucleus with ions and molecules, especially macromolecules like proteins.

Usually, the EFG has approximately axial symmetry, $\eta \approx 0$ or $V_{xx} \approx V_{yy}$. Moreover, it is sufficient to only consider the first order quadrupole interaction and the Hamiltonian simplifies to

$$\hat{H}_Q = \omega_Q^{(1)}\left(\frac{3\cos^2(\theta)-1}{2}\right)\frac{1}{6}\left(3\hat{I}_z^2 - I(I+1)\mathbb{1}\right) = \omega_Q\hat{T}_{20}, \tag{2.67}$$

with

$$\begin{aligned}\omega_Q^{(1)} &= \frac{3e^2qQ}{2I(2I-1)\hbar} \qquad \text{and}\\ \omega_Q &= \omega_Q^{(1)}\left(\frac{3\cos^2(\theta)-1}{2}\right)\end{aligned} \tag{2.68}$$

and θ is the angle to transform the principal axis system into the laboratory system. Thus, $\omega_Q^{(1)}$ is the first order quadrupole coupling in the principal axis system and ω_Q is the first order quadrupole coupling in the laboratory frame. A more detailed description of the quadrupole Hamiltonian, including higher order terms and without assuming axial symmetry can be found for example in Levitt [73] and Jerschow [82].

In the high field limit, the quadrupole interaction can be considered a small perturbation of the Hamiltonian, that is dominated by the Zeeman interaction:

$$\hat{\mathcal{H}} = \hat{\mathcal{H}}_Z + \hat{\mathcal{H}}_Q + \hat{\mathcal{H}}_{\text{others}} \tag{2.69}$$

and the energy eigenvalues are

$$E = -\gamma\hbar m B_0 + E_Q(m) \tag{2.70}$$

where $E_Q(m)$ is the correction of the Zeeman energy eigenvalues by the quadrupole interaction which can be calculated by perturbation theory. In most cases in biological tissue it is sufficient to truncate after the first order of $E_Q^{(1)}$ and E_Q is then given by

$$E_Q = \hbar\frac{\omega_Q}{2}\frac{[3m^2 - I(I+1)]}{3}. \tag{2.71}$$

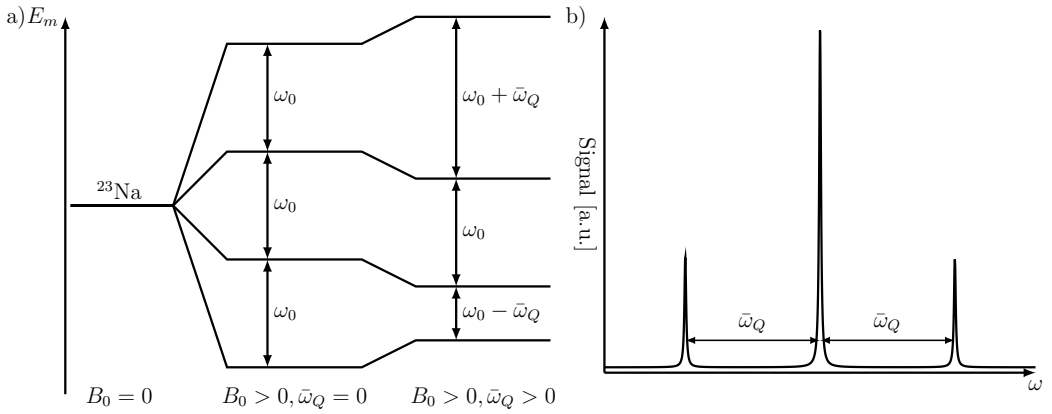

Fig. 2.4.: a) Exaggerated influence of the quadrupole interaction on the Zeeman energy levels. The energy levels are non-equidistantly shifted by the quadrupole interaction. b) The corresponding NMR spectrum has three resonances that are split by the residual quadrupole coupling $\hat{\omega}_Q$.

Thus, the energy levels are shifted depending on m^2 and therefore the energy levels are not equidistantly spaced anymore, as shown in Figure 2.4. The spacing depends on the angle θ between the principal axis system and the EFG parameter q. For the magic angle, $\theta \approx 54.7°$, it is $3\cos^2(\theta) - 1 = 0$ and therefore the quadrupole interaction vanishes, while it reaches its maximum for $\theta = 0$.

In soft matter, Brownian motion and rotation of molecules leads to a fluctuating electric fields in the environment of the nucleus and hence fluctuating EFG. Thus, both q and θ and consequently also the splitting of the energy levels are time dependent. The quadrupole interaction $\hat{\mathcal{H}}_Q$ can be separated into a static part $\hat{\mathcal{H}}_{QS}$ which is characterized by the time average of the quadrupole constant

$$\bar{\omega}_Q = \frac{3e^2Q}{4I(2I-1)\hbar}\overline{q\,(3\cos^2(\theta)-1)}. \tag{2.72}$$

and a fluctuating part $\hat{\mathcal{H}}_{QF}$ with vanishing time average, which leads to relaxation and is discussed in the following subsection. The fluctuating part is usually characterized by spectral densities $J_m(\omega)$ which depend on the quadratic mean of the the quadrupole coupling ω_Q^{RMS} and a single correlation time τ_c, which is the typical length of a half-period of the fluctuations.

Different types of environments of the nuclei result in different spectra. Most biological tissue are isotropic, i.e. $\bar{\omega}_Q = 0$, and the energy levels shift only temporarily and a single line appears in the spectrum. However, the time scale and strength of the fluctuations influence the NMR dynamics of the quadrupole interaction. For $\bar{\omega}_Q \neq 0$, or anisotropic environment, the spectral lines can split up (see Figure 2.4). The strength of the anisotropy $\bar{\omega}_Q$, the orientation of the principal axis system of the EFG relative to the quantization axis (axis of $\boldsymbol{B}_0$) and if there is one global (e.g. as in crystals) or multiple local (e.g. as in powders) EFG orientations decides how the spectral lines split. The occurring spectra are subdivided in type a, b (both in

anisotropic environment), c, and d (both in isotropic environment) spectra and are discussed in Subsection 2.1.7 in more detail.

Fluctuating Quadrupole Interaction

In the following, effect of the fluctuation quadrupole interaction on the density operator is derived. In a first step, the case of vanishing residual quadrupole interaction, i.e., $\hat{\mathcal{H}}^*_{\mathrm{QS}} = 0$, is discussed. The Liouville equation in the interaction picture is then given by

$$\frac{\mathrm{d}\hat{\sigma}^*(t)}{\mathrm{d}t} = -i\left[\hat{\mathcal{H}}^*_{\mathrm{QF}}(t), \hat{\sigma}^*(t)\right]. \tag{2.73}$$

We can solve this equation using second-order perturbation theory by iteratively inserting the formal solution $\hat{\sigma}^*(t) = \hat{\sigma}^*(0) - i\int_0^t \left[\hat{\mathcal{H}}^*_{\mathrm{QF}}, \hat{\sigma}^*(t)\right]$ into the Liouville equation leading to

$$\frac{\mathrm{d}\hat{\sigma}^*(t)}{\mathrm{d}t} = -i\left[\hat{\mathcal{H}}^*_{\mathrm{QF}}(t), \hat{\sigma}^*(0)\right] - \int_0^t \left[\hat{\mathcal{H}}^*_{\mathrm{QF}}(t), \left[\hat{\mathcal{H}}^*_{\mathrm{QF}}(t-\tau), \hat{\sigma}^*(t-\tau)\right]\right]\mathrm{d}\tau \tag{2.74}$$

Here, a coordinate transformation of the time from t' to $t+\tau$ was used. The next step is to take the ensemble average to account for the fact that different parts of the sample are affected differently by the stochastic processes. Since $\overline{\hat{\mathcal{H}}^*_{\mathrm{QF}}(t)} = 0$, the time average over the first part vanishes which leads to

$$\frac{\mathrm{d}\overline{\hat{\sigma}^*(t)}}{\mathrm{d}t} = -\int_0^t \overline{\left[\hat{\mathcal{H}}^*_{\mathrm{QF}}(t), \left[\hat{\mathcal{H}}^*_{\mathrm{QF}}(t-\tau), \hat{\sigma}^*(t-\tau)\right]\right]}\mathrm{d}\tau \tag{2.75}$$

For simplicity, the overbar of the ensemble average density operator is omitted in the following. In order to correctly obtain the thermal equilibrium density operator $\hat{\sigma}_{\mathrm{eq}}$ for $t \to \infty$, the thermal equilibrium is added to the equation:

$$\frac{\mathrm{d}\hat{\sigma}^*(t)}{\mathrm{d}t} = -\int_0^t \overline{\left[\hat{\mathcal{H}}^*_{\mathrm{QF}}(t), \left[\hat{\mathcal{H}}^*_{\mathrm{QF}}(t-\tau), \hat{\sigma}^*(t-\tau) - \hat{\sigma}_{\mathrm{eq}}\right]\right]}\mathrm{d}\tau. \tag{2.76}$$

An alternative way to introduce the return to the thermal equilibrium is a full quantum mechanical discussion of the problem where the environment of the nuclei are also treated quantum mechanically which is discussed for example in Abragam [71].

In NMR the typical time scale of the fluctuations is much faster than the change of the density operator, which is also called weak collision limit or Redfield limit. Then, the density operator is quasi static in the integral on the right hand side and the approximation $\hat{\sigma}^*(t-\tau) = \hat{\sigma}^*(t)$ is used. Moreover, the upper integral boundary can

be extended to ∞ since the time t is much longer than the typical time scale of the fluctuations:

$$\frac{\mathrm{d}\hat{\sigma}^*(t)}{\mathrm{d}t} = -\int_0^\infty \overline{\left[\hat{\mathcal{H}}^*_{\mathrm{QF}}(t), \left[\hat{\mathcal{H}}^*_{\mathrm{QF}}(t-\tau), \hat{\sigma}^*(t) - \hat{\sigma}_{\mathrm{eq}}\right]\right]}\mathrm{d}\tau. \tag{2.77}$$

Note, that since the fluctuations of the Hamlitonian are much faster, the same approximation cannot be made for $\hat{\mathcal{H}}^*_{\mathrm{QF}}(t-\tau)$. The Hamiltonian of the fluctuating part can be written out as [10]

$$\hat{\mathcal{H}}^*_{\mathrm{QF}}(t) = C_Q \sum_{m=-2}^{2} (-1)^m \hat{T}_{2m} \exp(im\omega_0 t) F_{2-m}(t) \tag{2.78}$$

where $C_Q = eQ/\hbar$ is a constant depending on quadrupole moment of the nucleus and $F_{2-m}(t)$ are functions of the EFG tensor elements. Inserting $\hat{\mathcal{H}}^*_{\mathrm{QF}}(t)$ from Equation (2.78) in Equation (2.77) and simplifying leads to

$$\begin{aligned}\frac{\mathrm{d}\hat{\sigma}^*(t)}{\mathrm{d}t} &= -C_Q^2 \int_0^\infty \sum_{m,m'} \mathrm{e}^{i((m+m')\omega_0 t} \overline{\left[\hat{T}_{2m}, \left[\hat{T}_{2m'}, \hat{\sigma}^*(t) - \hat{\sigma}_{\mathrm{eq}}\right]\right]} \\ &\qquad \overline{F_{2-m}(t) F_{2-m'}(t-\tau)} \mathrm{e}^{-im'\omega_0\tau} \mathrm{d}\tau \\ &= -\sum_{m=-2}^{2} \left[\hat{T}_{2m}, \left[\hat{T}_{2m}, \hat{\sigma}^* - \hat{\sigma}_{\mathrm{eq}}\right]\right] \left(J_m(m\omega_0) + iK_m(\omega_0)\right)\end{aligned} \tag{2.79}$$

The right hand side of Equation (2.79) is also called the Redfield relaxation superoperator acting on the density operator. In the last step, it was used that $\mathrm{e}^{-i(m+m')\omega_0 t}$ averages out for $m' \neq -m$ and the spectral densities $J_m(\omega)$ and $K_m(\omega)$ were introduced which are defined as the real and imaginary parts of the Fourier transform of the EFG's auto-correlation function

$$\begin{aligned} J_m(\omega) &= C_Q^2 \cdot \mathrm{Re}\left(\int_0^\infty \overline{F^*_{2-m}(t) F_{2-m}(t-\tau)} \mathrm{e}^{-i\omega\tau} \mathrm{d}\tau\right) \\ K_m(\omega) &= C_Q^2 \cdot \mathrm{Im}\left(\int_0^\infty \overline{F^*_{2-m}(t) F_{2-m}(t-\tau)} \mathrm{e}^{-i\omega\tau} \mathrm{d}\tau\right). \end{aligned} \tag{2.80}$$

A common assumption is, that the autocorrelation function of the EFG is exponentially decaying with a single time constant, the correlation time τ_c. The spectral densities J_m and K_m then are given by

$$\begin{aligned} J_m(m\omega_0) &= \frac{(\omega_Q^{\mathrm{RMS}})^2}{5} \frac{\tau_c}{1 + (m\omega_0\tau_c)^2} \\ K_m(m\omega) &= m\omega_0\tau_c J_m(m\omega) \end{aligned} \tag{2.81}$$

where ω_Q^{RMS} is the root mean square of the quadrupole coupling ω_Q. $K_m(\omega)$ leads to a small dynamic frequency shift and can usually be neglected [10]. In the following

the abbreviation $J_m \coloneqq J_m(m\omega_0)$ is used. This model is also known as the Debye model and is a simplification of the fluctuations of the EFG in biological tissue [8] which is more adequately characterized by a distribution $p(\tau_c)$ of correlation times and a correlation time dependent strength parameter $\omega_Q^{\mathrm{RMS}}(\tau_c)$. The spectral densities then are given by

$$J_m = \int_0^\infty p(\tau_c) J_m(\tau_c) \mathrm{d}\tau_c. \tag{2.82}$$

with $J_m(\tau_c) = \frac{1}{5}(\omega_Q^{\mathrm{RMS}}(\tau_c))^2 \tau_c / (1 + (m\omega_0\tau_c)^2)$. The fluctuating interactions of the nuclei with EFGs of the environment are then fully characterized by the three spectral densities J_0, J_1 and J_2.

The static Hamiltonian $\hat{\mathcal{H}}^*_{\mathrm{QS}} = \bar{\omega}_Q \hat{T}_{20}$ commutes with the Redfield relaxation superoperator in Equation (2.79) [10]. Hence, in the more general anisotropic case with non-vanishing static Hamiltonian, $\hat{\mathcal{H}}^*_{\mathrm{QS}} = \bar{\omega}_Q \hat{T}_{20}$ does not contribute to the Redfield relaxation superoperator and the Redfield equation becomes

$$\frac{\mathrm{d}\hat{\sigma}^*}{\mathrm{d}t} = -i\bar{\omega}_Q \left[\hat{T}_{20}, \hat{\sigma}^*\right] - \sum_{m=-2}^{2} \left[\hat{T}_{2m}, \left[\hat{T}_{2m}^\dagger, \hat{\sigma}^* - \hat{\sigma}^*_{\mathrm{eq}}\right]\right] \left(J_m(\omega_0) + iK_m(\omega_0)\right). \tag{2.83}$$

Explicitly writing out Equation (2.83) for all basis elements using the commutator relations in Bowden and Hutchison [79] and Bowden et al. [80] leads to a set of decoupled linear differential equations in a way that relaxation can only change the rank l of the tensor basis element $\hat{T}_{lm}$ and leaves the coherence order m unchanged. Therefore, relaxation affects the tensor basis complementary to RF-pulses, as shown in Subsection 2.1.5, which also demonstrates the advantage of using the ISTO basis. The allowed transitions by RF-pulses and relaxation are depicted in Figure 2.5. In the following, the resulting zero, single and multiple quantum relaxation equations are solved and discussed.

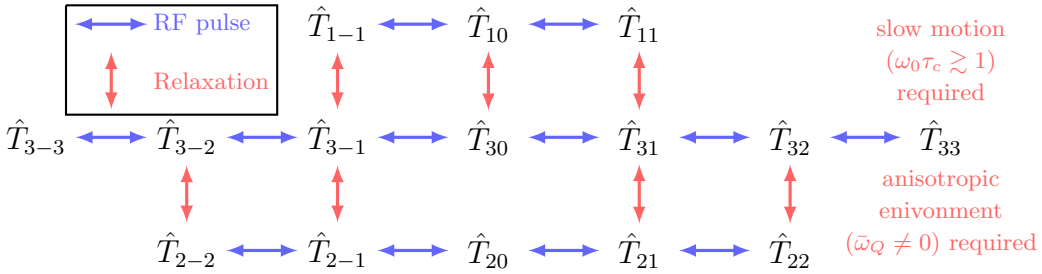

Fig. 2.5.: Visualization of allowed transitions under the effect of relaxation (red arrows) and hard RF pulses (blue arrows). The DQ branch (bottom) couples to the SQ (top) and TQ (center) branches only in an anisotropic environment. Relaxation effects only change the tensor rank, while hard RF pulses only affect the tensor order. This simple description demonstrates the power of the irreducible spherical tensor operator basis.

Zero Quantum Relaxation

Zero quantum relaxation ($m = 0$), or T_1 relaxation, differs from the higher order relaxation in two major ways. First, since $\hat{T}_{20}$ commutes with all other zero quantum coherences, the static quadrupole interaction part $-i\bar{\omega}_Q \left[\hat{T}_{20}, \sigma\right]$ does not have any effect. This also leads to a completely decoupled equation for $\hat{T}_{20}$. Secondly, the thermal equilibrium $\hat{\sigma}_{\text{eq}} \propto \hat{T}_{10}$ will be recovered for $t \to \infty$. In Equation (2.83) this is accounted for by the $-\hat{\sigma}_{\text{eq}}$ in the double commutator. The evolution equation for the amplitudes A_{l0} for zero quantum coherences is [62, 63]

$$\frac{\mathrm{d}}{\mathrm{d}t}\begin{pmatrix} A_{10} \\ A_{20} \\ A_{30} \end{pmatrix} = -\begin{pmatrix} \frac{2}{5}J_1 + \frac{8}{5}J_2 & 0 & \frac{4}{5}(J_1 - J_2) \\ 0 & 2(J_1 + J_2) & 0 \\ \frac{4}{5}(J_1 - J_2) & 0 & \frac{8}{5}J_1 + \frac{2}{5}J_2 \end{pmatrix} \cdot \begin{pmatrix} A_{10} \\ A_{20} \\ A_{30} \end{pmatrix} + \begin{pmatrix} \frac{2}{5}J_1 + \frac{8}{5}J_2 \\ 0 \\ \frac{4}{5}(J_1 - J_2) \end{pmatrix}. \tag{2.84}$$

The vector $\left(\frac{2}{5}J_1 + \frac{8}{5}J_2, 0, \frac{4}{5}(J_1 - J_2)\right)^T$ accounts for the recovery of thermal equilibrium. Solving the differential equation leads to a transition equation [63]

$$\begin{pmatrix} A_{10} \\ A_{20} \\ A_{30} \end{pmatrix} \to \begin{pmatrix} 1 - f_{11}^{(0)}(t) \\ 0 \\ -f_{31}^{(0)}(t) \end{pmatrix} + \begin{pmatrix} f_{11}^{(0)}(t) & 0 & f_{13}^{(0)}(t) \\ 0 & f_{22}^{(0)}(t) & 0 \\ f_{31}^{(0)}(t) & 0 & f_{33}^{(0)}(t) \end{pmatrix} \cdot \begin{pmatrix} A_{10} \\ A_{20} \\ A_{30} \end{pmatrix} \tag{2.85}$$

with the transfer functions

$$\begin{aligned} f_{11}^{(0)}(t) &= \frac{1}{5}\left(4\mathrm{e}^{-t/T_{1s}} + \mathrm{e}^{-t/T_{1f}}\right), \\ f_{13}^{(0)}(t) = f_{31}^{(0)}(t) &= \frac{2}{5}\left(\mathrm{e}^{-t/T_{1f}} - \mathrm{e}^{-t/T_{1s}}\right), \\ f_{33}^{(0)}(t) &= \frac{1}{5}\left(\mathrm{e}^{-t/T_{1s}} + 4\mathrm{e}^{-t/T_{1f}}\right), \\ f_{22}^{(0)}(t) &= \mathrm{e}^{-t/T_{1d}}. \end{aligned} \tag{2.86}$$

Here, $T_{1s} = (R_{1s})^{-1} \coloneqq 1/2J_2$ and $T_{1f} = (R_{1f})^{-1} \coloneqq 1/2J_1$ are the slow and fast relaxation times, respectively, and $T_{1d} = (R_{1d})^{-1} \coloneqq 1/(2J_1 + 2J_2)$ is the relaxation time of the rank 2 zero quantum coherences. The relaxation times are composed of the spectral densities J_1 and J_2, which encode information about the motion of the sodium nuclei in their molecular environment.

As can be seen in Equation (2.85), relaxation of the rank 1 and rank 3 coherences is bi-exponential with a slow component, that contributes to 80 % of the relaxation, and a fast component, that contributes 20 %. Furthermore, the rank 1 and rank 3 evolution equations are coupled, which allows the transitions $\hat{T}_{10} \to \hat{T}_{30}$ and $\hat{T}_{30} \to \hat{T}_{10}$ and the creation of zero order TQ coherences.

The model parameters τ_c and ω_Q of the Debye model can be calculated using the relaxation times T_{1s} and T_{1f}, by using the relation from Equation (2.81), $J_m =$

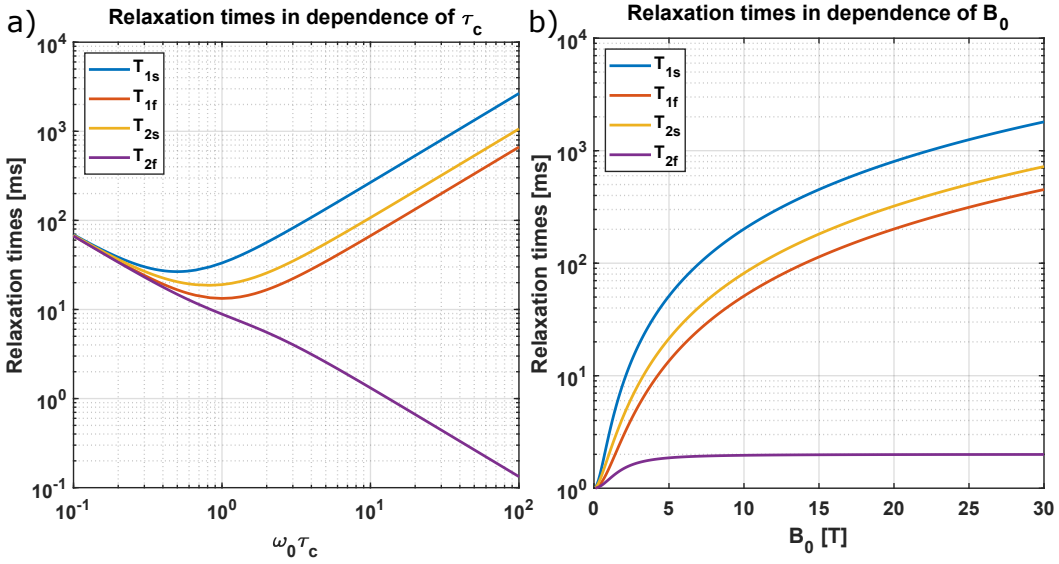

Fig. 2.6.: a) T_1 and T_2 relaxation times in dependence of the product $\omega_0\tau_c$. Other parameters: $B_0 = 9.4\,\mathrm{T}$ and $\omega_Q = 0.5\,\mathrm{MHz}$. b) T_1 and T_2 relaxation times in dependence of B_0. Other parameters: $\tau_c = 10\,\mathrm{ns}$ and $\omega_Q = 0.5\,\mathrm{MHz}$.

$\omega_Q^2\tau_c/(1+(m\omega_0\tau_c)^2)$ and solving for τ_c and ω_Q. First, the ratio and the difference of the relaxation rates $R_{2f/2s}$ is calculated

$$\begin{aligned} a_0 &:= \frac{R_{1f}}{R_{1s}} = \frac{J_1}{J_2} = \frac{1+4x}{1+x} \\ b_0 &:= R_{1f} - R_{1s} = 2(J_1 - J_2) = \frac{6\tau_c\omega_Q^2 x}{5(4x^2+5x+1)} \end{aligned} \tag{2.87}$$

with $x = (\omega_0\tau_c)^2$. Then, τ_c and ω_Q are given by

$$\begin{aligned} \tau_c &= \frac{1}{\omega_0}\sqrt{\frac{a_0-1}{4-a_0}} \\ \omega_Q &= \sqrt{\frac{5b_0}{6x\tau_c}(4x^2+5x+1)}. \end{aligned} \tag{2.88}$$

Figure 2.6 shows the relaxation times in dependence of the product of correlation time and Lamor frequency $\omega_0\tau_c$, which indicates the motional regime, and the magnetic field strength B_0. The T_1 relaxation times reach their minimum around $\omega_0\tau_c \sim 1$, where the quadrupole interaction is most efficient, and increase again afterwards. As $\lim_{x\to\infty} a_0 = 4$, the ratio of the relaxation times plateaus at 4, but the difference is increasing further with increasing τ_c. Moreover, the T_1 relaxation times increase with increasing magnetic field strength B_0.

In the presence of an anisotropy ($\bar{\omega}_Q \neq 0$), the rank 2 couple with the rank 1 and rank 3 coherences for single quantum relaxation ($m = \pm 1$), also called T_2 relaxation. The evolution equation for the amplitudes $A_{l\pm1}$ for zero quantum coherences is

$$\frac{\mathrm{d}}{\mathrm{d}t}\begin{pmatrix} A_{1\pm1} \\ A_{2\pm1} \\ A_{3\pm1} \end{pmatrix} = -\begin{pmatrix} \frac{3}{5}J_0 + J_1 + \frac{2}{5}J_2 & \mp i\sqrt{\frac{3}{5}}\bar{\omega}_Q & \frac{\sqrt{6}}{5}(J_1 - J_2) \\ \mp i\sqrt{\frac{3}{5}}\bar{\omega}_Q & J_0 + J_1 + 2J_2 & \mp i\sqrt{\frac{3}{5}}\bar{\omega}_Q \\ \frac{4}{5}(J_1 - J_2) & \mp i\sqrt{\frac{3}{5}}\bar{\omega}_Q & \frac{2}{5}J_0 + J_1 + \frac{3}{5}J_2 \end{pmatrix} \cdot \begin{pmatrix} A_{1\pm1} \\ A_{2\pm1} \\ A_{3\pm1} \end{pmatrix}. \tag{2.89}$$

The solution of the evolution Equation (2.89) leads to the following transition equation:

$$\begin{pmatrix} A_{1\pm1} \\ A_{2\pm1} \\ A_{3\pm1} \end{pmatrix} \rightarrow \begin{pmatrix} f_{11}^{(1a)}(t) & f_{12}^{(1a)}(t) & f_{13}^{(1a)}(t) \\ f_{21}^{(1a)}(t) & f_{22}^{(1a)}(t) & f_{23}^{(1a)}(t) \\ f_{31}^{(1a)}(t) & f_{32}^{(1a)}(t) & f_{33}^{(1a)}(t) \end{pmatrix} \cdot \begin{pmatrix} A_{1\pm1} \\ A_{2\pm1} \\ A_{3\pm1} \end{pmatrix} \tag{2.90}$$

with the anisotropic transition functions $f_{ij}^{(1a)}(t)$

$$\begin{aligned}
f_{11}^{(1a)}(t) &= \frac{1}{5}\left(\frac{3}{2}\left(1 + \frac{J_2}{\mu}\right)\mathrm{e}^{-R_1^{(1)}t} + 2\mathrm{e}^{-R_2^{(1)}t} + \frac{3}{2}\left(1 - \frac{J_2}{\mu}\right)\mathrm{e}^{-R_3^{(1)}t}\right), \\
f_{13}^{(1a)}(t) = f_{31}^{(1a)}(t) &= \frac{\sqrt{6}}{5}\left(\frac{1}{2}\left(1 + \frac{J_2}{\mu}\right)\mathrm{e}^{-R_1^{(1)}t} - \mathrm{e}^{-R_2^{(1)}t} + \frac{1}{2}\left(1 - \frac{J_2}{\mu}\right)\mathrm{e}^{-R_3^{(1)}t}\right), \\
f_{33}^{(1a)}(t) &= \frac{1}{5}\left(\left(1 + \frac{J_2}{\mu}\right)\mathrm{e}^{-R_1^{(1)}t} + 3\mathrm{e}^{-R_2^{(1)}t} + \left(1 - \frac{J_2}{\mu}\right)\mathrm{e}^{-R_3^{(1)}t}\right), \\
f_{22}^{(1a)}(t) &= \frac{1}{2}\left(\left(1 + \frac{J_2}{\mu}\right)\mathrm{e}^{-R_1^{(1)}t} + \left(1 - \frac{J_2}{\mu}\right)\mathrm{e}^{-R_3^{(1)}t}\right), \\
f_{12}^{(\pm1a)}(t) = f_{21}^{(\pm1a)}(t) &= \frac{\sqrt{3}i}{10}\frac{\bar{\omega}_Q}{\mu}\left(\pm\mathrm{e}^{-R_1^{(1)}t} \mp 2\mathrm{e}^{-R_3^{(1)}t}\right), \\
f_{23}^{(\pm1a)}(t) = f_{32}^{(\pm1a)}(t) &= \frac{i}{\sqrt{10}}\frac{\bar{\omega}_Q}{\mu}\left(\pm\mathrm{e}^{-R_1^{(1)}t} \mp 2\mathrm{e}^{-R_3^{(1)}t}\right).
\end{aligned} \tag{2.91}$$

where $R_1^{(1)} = J_0 + J_1 + J_2 - \mu$, $R_2^{(1)} = J_1 + J_2$ and $R_3^{(1)} = J_0 + J_1 + J_2 + \mu$ are the relaxation rates and $\mu = \sqrt{J_2^2 - \bar{\omega}_Q^2}$. For large $\bar{\omega}_Q > J_2$, μ is imaginary. This leads to a non-equidistant splitting of the energy levels as shown in Figure 2.4a) and consequently a splitting of the resonance in the spectrum as shown in Figure 2.4b).

Most biological tissues are isotropic ($\bar{\omega}_Q \rightarrow 0$) which decouples the rank 2 components from the rank 1 and rank 3 coherences. The simplified transition equation in arrow notation is

$$\begin{pmatrix} A_{1\pm1} \\ A_{2\pm1} \\ A_{3\pm1} \end{pmatrix} \rightarrow \begin{pmatrix} f_{11}^{(1)}(t) & 0 & f_{13}^{(1)}(t) \\ 0 & f_{22}^{(1)}(t) & 0 \\ f_{31}^{(1)}(t) & 0 & f_{33}^{(1)}(t) \end{pmatrix} \cdot \begin{pmatrix} A_{1\pm1} \\ A_{2\pm1} \\ A_{3\pm1} \end{pmatrix} \tag{2.92}$$

with simplified transition functions

$$\begin{aligned} f_{11}^{(1)}(t) &= \frac{1}{5}\left(2\mathrm{e}^{-t/T_{2s}} + 3\mathrm{e}^{-t/T_{2f}}\right), \\ f_{13}^{(1)}(t) &= f_{31}^{(1)}(t) = \frac{\sqrt{6}}{5}\left(\mathrm{e}^{-t/T_{2f}} - \mathrm{e}^{-t/T_{2s}}\right), \\ f_{33}^{(1)}(t) &= \frac{1}{5}\left(3\mathrm{e}^{-t/T_{2s}} + 2\mathrm{e}^{-t/T_{2f}}\right), \\ f_{22}^{(1)}(t) &= \mathrm{e}^{-t/T_{2d}}. \end{aligned} \tag{2.93}$$

and $T_{2s} = (R_{2s})^{-1} \coloneqq 1/(J_1 + J_2)$ and $T_{2f} = (R_{2f})^{-1} \coloneqq 1/(J_0 + J_1)$ are the slow and fast relaxation times, respectively, and $T_{2d} = (R_{2d})^{-1} \coloneqq 1/(J_0 + J_1 + 2J_2)$ is the relaxation time of the rank 2 single quantum coherences. The fast component contributes 60 % to the signal and the slow component 40 %. Again, rank 1 and rank 3 coherences couple, which allows the transitions $\hat{T}_{1\pm1} \rightarrow \hat{T}_{3\pm1}$ and $\hat{T}_{3\pm1} \rightarrow \hat{T}_{1\pm1}$ and the creation of order 1 TQ coherences. Note, that the transfer functions of the anisotropic case in Equation (2.91) approach the transfer functions of the isotropic case in Equation (2.93) for $\bar{\omega}_Q \rightarrow 0$.

Similar to the calculations for the T_1 relaxation times, the model parameters τ_c and ω_Q of the Debye model can be calculated using the T_2 relaxation times T_{2s} and T_{2f}. Again, the ratio and the difference of the relaxation rates is calculated

$$\begin{aligned} a_1 &\coloneqq \frac{R_{2f}}{R_{2s}} = \frac{J_0 + J_1}{J_1 + J_2} = \frac{4x^2 + 9x + 2}{2 + 5x} \\ b_1 &\coloneqq R_{2f} - R_{2s} = J_0 - J_2 = \omega_Q^2 \tau_c \frac{4x}{5(1 + 4x)} \end{aligned} \tag{2.94}$$

with $x = (\omega_0 \tau_c)^2$. Then, τ_c and ω_Q are given by

$$\begin{aligned} \tau_c &= \frac{1}{\omega_0}\sqrt{\frac{1}{8}(5a_1 - 9 + \sqrt{25a_1^2 - 58a_1 + 49})} \\ \omega_Q &= \sqrt{\frac{5b_1(4x+1)}{4x\tau_c}}. \end{aligned} \tag{2.95}$$

Figure 2.6 shows the relaxation times in dependence of the product of correlation time and Lamor frequency $\omega_0\tau_c$ and the magnetic field strength B_0. T_{2s} can be considered a mean value of the T_1 relaxation times and therefore behaves similar to them with increasing τ_c and B_0. T_{2f} on the other hand depends on J_0 and

therefore decreases with increasing τ_c even beyond $\omega_0\tau_c \sim 1$ and plateaus after an initial increase with increasing B_0. This also leads to increasing ratio a_1 of the T_2 relaxation times. The unique dependence on J_0 leads to a strong TQ signal in the slow motion regime $\omega_0\tau_c \gtrsim 1$, which is commonly found in biological tissue and especially in the extracellular space.

Multiple Quantum Relaxation

The double quantum evolution equation is given by

$$\frac{\mathrm{d}}{\mathrm{d}t}\begin{pmatrix} A_{2\pm2} \\ A_{2\pm3} \end{pmatrix} = -\begin{pmatrix} J_0 + 2J_1 + J_2 & \mp i\bar{\omega}_Q \\ \mp i\bar{\omega}_Q & J_0 + J_2 \end{pmatrix} \cdot \begin{pmatrix} A_{2\pm2} \\ A_{2\pm3} \end{pmatrix}. \tag{2.96}$$

Solving the evolution equation leads to the following transition equation:

$$\begin{pmatrix} A_{2\pm2} \\ A_{2\pm3} \end{pmatrix} \rightarrow \begin{pmatrix} f_{22}^{(2a)}(t) & f_{23}^{(2a)}(t) \\ f_{32}^{(2a)}(t) & f_{33}^{(2a)}(t) \end{pmatrix} \cdot \begin{pmatrix} A_{2\pm2} \\ A_{2\pm3} \end{pmatrix} \tag{2.97}$$

with the transfer functions

$$\begin{aligned} f_{22}^{(2a)}(t) &= \frac{1}{2}\left(\left(1 + \frac{J_2}{\mu}\right)\mathrm{e}^{-R_1^{(2)}t} + \left(1 - \frac{J_2}{\mu}\right)\mathrm{e}^{-R_2^{(2)}t}\right), \\ f_{23}^{(\pm2a)}(t) &= f_{32}^{(\pm2a)}(t) = -\frac{i}{2}\frac{\bar{\omega}_Q}{\mu}\left(\pm\mathrm{e}^{-R_1^{(2)}t} \mp 2\mathrm{e}^{-R_2^{(2)}t}\right), \\ f_{33}^{(2a)}(t) &= \frac{1}{2}\left(\left(1 + \frac{J_2}{\mu}\right)\mathrm{e}^{-R_1^{(2)}t} + \left(1 - \frac{J_2}{\mu}\right)\mathrm{e}^{-R_2^{(2)}t}\right). \end{aligned} \tag{2.98}$$

Here, $R_1^{(2)} = J_0 + J_1 + J_2 - \mu$ and $R_2^{(2)} = J_0 + J_1 + J_2 + \mu$ are the relaxation rates and $\mu = \sqrt{J_2^2 - \bar{\omega}_Q^2}$ is the same abbreviation as for the SQ relaxation. Again, the rank 2 coherences decouple from the rank 3 tensors in the isotropic case where $\bar{\omega}_Q \rightarrow 0$. In this case the transition equation becomes

$$\begin{pmatrix} A_{2\pm2} \\ A_{2\pm3} \end{pmatrix} \rightarrow \begin{pmatrix} f_{22}^{(2)}(t) & 0 \\ 0 & f_{33}^{(2)}(t) \end{pmatrix} \cdot \begin{pmatrix} A_{2\pm2} \\ A_{2\pm3} \end{pmatrix} \tag{2.99}$$

with the transition functions

$$\begin{aligned} f_{22}^{(2)}(t) &= \mathrm{e}^{-R_1^{(2)}t} \\ f_{33}^{(2)}(t) &= \mathrm{e}^{-R_1^{(2)}t}, \end{aligned} \tag{2.100}$$

where $R_1^{(2)} = J_0 + 2J_1 + J_2$ and $R_2^{(2)} = J_0 + J_2$.

Since $\hat{T}_{33}$ does not couple to any other tensors, triple quantum relaxation is simply given by

$$A_{33} \rightarrow f_{33}^{(3)} A_{33} = \mathrm{e}^{-R_1^{(3)}t} A_{33} \tag{2.101}$$

with $R_1^{(3)} = J_1 + J_2$. Therefore, the triple quantum relaxation time is equal to the slow single quantum relaxation time T_{2s}.

Influence of B_0 inhomogeneities and T_2^* relaxation

Local constant variations of the magnetic field are additional sources of relaxation due to local variations of the Lamor-frequency, that cause dephasing of the spins and consequently signal lost. The local variations of the magnetic field can be caused e.g. by heterogeneous susceptibility of the probe and inhomogeneities of the static magnetic field B_0.

A local shift in Lamor frequency $\omega_{\text{shift}} = \omega_0 - \omega_{0,\text{shift}}$ relative to the main Lamor frequency ω_0 leads to rotation of the spins in the rotating frame, that rotates with ω_0. This additional rotation depends on the coherence order l as it determines the rotation frequency and can be taken into account in the transfer functions $f_{ij,\omega_{\text{shift}}}^{(l)}$:

$$f_{ij,\text{shift}}^{(l)}(t) = f_{ij}^{(l)}(t) \cdot \exp(il\omega_{\text{shift}}t). \tag{2.102}$$

Generally, the frequency is not only shifted by a single offset but by whole set of shift following a statistical distribution $p(\omega_{\text{shift}})$. The resulting adapted transfer functions $f_{ij,B0}^{(l)}$ are

$$f_{ij,B0}^{(l)}(t) = f_{ij}^{(l)}(t) \cdot \int_{-\infty}^{\infty} p(\omega_{\text{shift}}) \exp(il\omega_{\text{shift}}t) \mathrm{d}\omega_{\text{shift}}. \tag{2.103}$$

This integral has the form of a Fourier Transform (FT) of the distribution $p(\omega_{\text{shift}})$ of B_0 inhomogeneities. Usually it is assumed [49, 83, 84] that the B_0 inhomogeneities are Lorentzian distributed,

$$p(\omega_{\text{shift}}) = \frac{1}{\pi} \frac{\Delta_{B0}}{\omega_{\text{shift}}^2 + \Delta_{B0}^2} \tag{2.104}$$

where Δ_{B0} is the width of the Lorentzian. The Fourier transform of a Lorentzian is a one-sided exponential. Therefore, the transfer function in Equation (2.103) can be written as

$$f_{ij,B0}^{(l)}(t) = f_{ij}^{(l)}(t) \cdot \int_{-\infty}^{\infty} p(\omega_{\text{shift}}) \exp(il\omega_{\text{shift}}t) \mathrm{d}\omega_{\text{shift}} = f_{ij}^{(l)}(t) \cdot \exp(-l\Delta_{B0}t). \tag{2.105}$$

Combining the exponential functions in $f_{ij}^{(l)}$ and the exponential of the B_0 inhomgeneities leads to new effective relaxation rates of the form

$$R_{i,B0}^{(l)} = R_i^{(l)} + l \cdot \Delta_{B0}. \tag{2.106}$$

While T_1 relaxation ($l = 0$) is unaffected by B_0 inhomogeneities, T_2 relaxation ($l = 1$) becomes T_2^* relaxation, and DQ ($l = 2$) and TQ ($l = 3$) relaxation is affected twice or trice, respectively, relative to T_2 relaxation. While T_2 relaxation is determined by the nucleus' environment and therefore a tissue specific material constant, T_2^* relaxation can vary between measurements due to varying shim quality and is generally hardware dependent. Since B_0 inhomogeneities are static, they be corrected by refocusing the spins creating an echo in spin echo sequences. This is not possible for relaxation caused by statistical fluctuations of the quadrupole interaction.

2.1.7 Biological Environment

Different types of environments of the nuclei result in different spectra that are characterized as one of four spectra, type a, b, c or d spectra as shown in Figure 2.7. In biological tissue, sodium is usually surrounded by a hydration shell with multiple layers and additionally interact with molecules of various sizes and forms. The EFGs at the position of the nucleus are primarily created by fluctuations of the inner hydration shell. But slower modulations can occur in the presence of macromolecules like proteins. Moreover, depending on cell form and the local environment, motion and electric fields can have a preferred direction or are isotropic.

Most biological tissues are approximately isotropic, i.e. $\bar{\omega}_Q \approx 0$, and the energy levels shift only temporarily and a single line appears in the spectrum. However, the time scale τ_c and strength ω_Q^{RMS} of the fluctuations influence the NMR dynamics of the quadrupole interaction:

- **Type d spectrum:** Fast fluctuations in the extreme narrowing regime, $\omega_0\tau_c \ll 1$, occur when sodium ions interact primarily with small molecules and ions. The EFGs average out and the spectral densities then equal each other, $J_0(\omega_0) \approx J_1(\omega_0) \approx J_2(\omega_0)$ and consequently the T_1 and T_2 relaxation times equal each other. Furthermore, the transitions $\hat{T}_{10} \leftrightarrow \hat{T}_{30}$ and $\hat{T}_{1\pm1} \leftrightarrow \hat{T}_{3\pm1}$ rely on a difference between the relaxation times and are therefore suppressed. The result is mono-exponential T_1 and T_2 relaxation and only a single resonance at frequency ω_0 occurs in the spectrum.
- **Type c spectrum:** Slow fluctuations in the slow motion regime, $\omega_0\tau_c \gtrsim 1$, occurs when the sodium ions interact with macromolecules like proteins such that the correlation time is in the range of the inverse Lamor frequency. For $B_0 = 9.4\,\mathrm{T}$ and $B_0 = 21.1\,\mathrm{T}$ this is the case for τ_c in the range of ns. Then, the spectral densities J_0, J_1 and J_2 differ from each other and relaxation is bi-exponential as shown in Subsection 2.1.6. Moreover, the transitions $\hat{T}_{10} \leftrightarrow \hat{T}_{30}$ and $\hat{T}_{1\pm1} \leftrightarrow \hat{T}_{3\pm1}$ are allowed and the TQ coherences can be created. Since $\bar{\omega}_Q \approx 0$, the rank 2 tensors are decoupled and the creation of $\hat{T}_{2\pm2}$ DQ coherences is impossible. The slow motion regime primarily occurs for interactions with negatively charged groups of proteins, carbohydrates, DNA and RNA [43, 46]. Up to 35 % of the cell volume are filled with proteins [44] leading to a strong intercellular TQ signal. The resulting spectrum is a

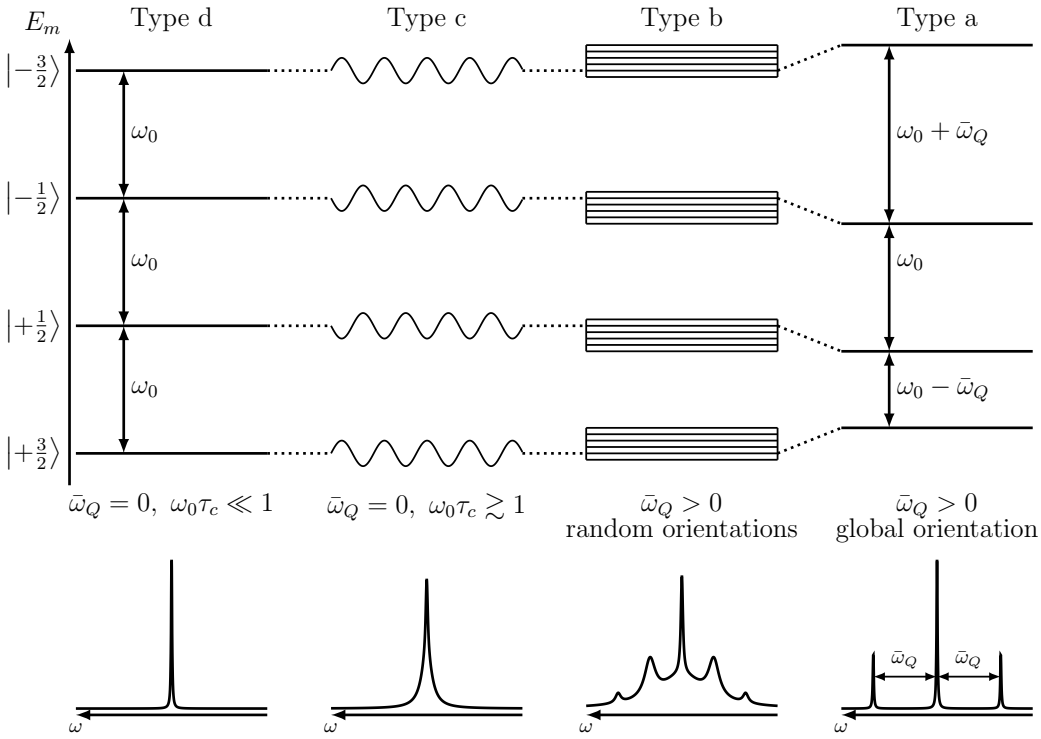

Fig. 2.7.: Effect of different molecular environments on the NMR spectra of spin-3/2 nuclei according to Rooney and Springer [8]. In an isotropic environment (type c and type d), i.e., $\hat{\omega}_Q = 0$, the static part of the quadrupole interaction vanishes. In the type c case (slow motion regime $\omega_0\tau_c \gtrsim 1$), as it occurs in most biological tissues where the nuclei interact with macromolecules like proteins, the energy levels split up only temporarily, too short to split up the resonances. The spectrum then only consists of a superposition of two Lorentzian shaped resonances with different widths both at the same Lamor frequency. In the type d case (extreme narrowing regime $\omega_0\tau_c \ll 1$), as it occurs in saline solution, there is only a single Lorentzian shaped resonance. For residual splittings $\hat{\omega}_Q > 0$ (type a and type b) there is a permanent shift of the energy levels leading to a splitting of the resonances in the NMR spectrum. In the case of a single global orientation, as it occurs in crystals, the spectrum consists of three resonances spaced by $\hat{\omega}_Q$. In the case of domains with different orientations, as it occurs in powders, the spectrum is more complicated. Adapted from Rooney and Springer [8].

superposition of two resonances at the same frequency, ω_0, a broader one for the satellite transitions with a relative amplitude of 60 % and a narrower one for the central transition with a relative amplitude of 40 %.

Most biological tissues yield type c and type d spectra and in the case of type c spectra MQ coherences. Since the intracellular protein concentration of macromolecules and especially proteins is large compared to that the extracellular space, it was shown that the TQ coherences are intracellular sensitive [15–22]. Therefore, the TQ signal provides a potentially valuable biomarker for cell viability.

For anisotropic environments with $\bar{\omega}_Q \neq 0$, the rank 2 tensors couple to the rank 1 and rank 3 tensors and DQ coherences $\hat{T}_{2\pm2}$ can be created via relaxation. Moreover, the coupling term is complex, which leads to a shift of the precession frequency of the outer energy levels. In the spectrum this causes a splitting of the resonance line, with a form depending on the strength of the anisotropy $\bar{\omega}_Q$, the orientation of the principal axis system of the EFG relative to the quantization axis (axis of $\boldsymbol{B}_0$). Again, there are two types of spectra:

- **Type a spectrum:** In the case of global anisotropy with one principal axis system across the whole sample, three distinct resonance lines at frequencies $\omega_0 - \bar{\omega}_Q$, ω_0 and $\omega_0 + \bar{\omega}_Q$ with a ratio of 3:4:3. This type of spectrum occurs for crystals and lyquid cystals with residual quadrupole couplings of up to several MHz. This can even lead to a splitting without a magnetic field that can sometimes be observed with nuclear quadrupole resonance (NQR) and also requires to consider higher order effects [73].
- **Type b spectrum:** For unordered samples with local non-vanishing residual quadrupole couplings with each little domain having their own principal axis system, the resulting spectrum is a superposition of many type a spetra with different orientations and splittings. The resulting global spectrum is called powder spectrum and consists of a dominating central peak and inhomogeneous satellite peaks. It appears, e.g. for powders and for large and very slow fluctuations with correlation times larger than $\bar{\omega}_Q^{-1}$ [8].

By suppressing the $\hat{T}_{3\pm2}$ DQ coherence, which can also be created in isotropic environments, by using the magic angle, the occurrence of a Magic Angle (MA)-DQ signal ($\hat{T}_{3\pm2}$) directly shows a non-vanishing $\bar{\omega}_Q$ and an anisotropy even if the splitting of the spectral lines is smaller than the width of the resonances. In some biological tissue, the existence of a small residual quadrupolar coupling, usually $< 200\,\mathrm{Hz}$ [7], was shown, e.g. in the brain [85, 86] and muscles [87]. For $^{23}\mathrm{Na}$ in cartilage [88] and for $^{39}\mathrm{K}$ in muscle [89] a triplet spectrum was observed.

2.2 NMR Spectroscopy and MRI

NMR experiments are based on the excitation and manipulation of the thermal equilibrium magnetization of nuclei in a magnetic field using RF-pulses and detecting the excited transversal magnetization. In between the initial excitation and the

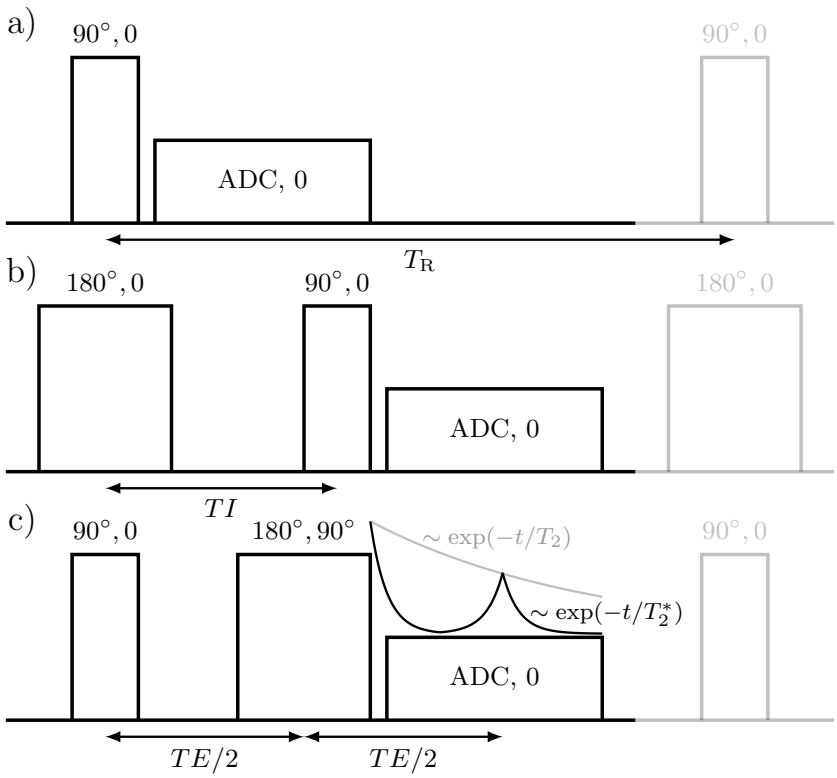

Fig. 2.8.: Schematic depiction of the basic NMR sequences, a) Single-Pulse (SP), b) the Inversion Recovery (IR) and c) Spin Echo (SE) sequences. a) SP sequence only has a single excitation pulse with subsequent acquisition window using an ADC. The decay is sensitive to T_2^* relaxation. b) The IR sequence starts with an inversion of the magnetization with a 180° inversion pulse, a evolution period called inversion time and a subsequent acquisition window to investigate T_1 relaxation. c) In the SE sequence, dephasing of the spins after the initial excitation pulse is refocused by a 180° refocusing pulse. The spins refocus and during the acquisition a so called spin echo proportional to T_2 decay is formed.

detection, a multitude of different manipulations of the nuclear spins is possible using multiple RF pulses and gradient fields, so-called pulse sequences. In this section, the basic building blocks of these pulse sequences, basic sequences, as well as more sophisticated sequences to detect MQ coherences are discussed. Moreover, a short introduction to spatial encoding and MRI will be given.

2.2.1 The Basics: Single Pulse, Inversion Recovery and Spin Echo Sequences

The most basic sequence, the SP sequence, consists of a single excitation pulse and an subsequent acquisition window as shown in Figure 2.8a). To maximize the signal, the RF pulse usually has a 90° flip angle, however, every flip angle is possible. Only

$\hat{T}_{1\pm1}$ tensors evolve and contribute to the signal which decay with the T_2^* relaxation times.

The T_1 relaxation times can be determined using an IR sequence and sampling multiple inversion times TI. The sequence consists of an 180° inversion pulse, an evolution period called inversion time, 90° pulse and a subsequent acquisition window as shown in Figure 2.8b). The inversion pulse flips the thermal equilibrium magnetization creating no transversal magnetization. Consequently, the signal relaxes only with T_1 relaxation. After the inversion time, the signal then is converted to transversal magnetization with the 90° pulse and the signal is detected. By measuring the signal for several inversion times, the T_1 relaxation curve can be sampled and the T_1 relaxation times can be determined. However, since the T_1 relaxation times are usually close together, it is very challenging to separate the short and long T_1 relaxation times and most studies use a mono-exponential approximation [6, 83, 90–98].

The SE sequence can be used to refocus B_0 inhomogeneities and determine the T_2 relaxation times. The sequence consists of an initial 90° excitation pulse, an evolution period called echo time TE with a 180° refocusing pulse with phase shift of 90° relative to the excitation pulse after $TE/2$ and a subsequent acquisition window as shown in Figure 2.8c). As described in Subsection 2.1.6, static B_0 inhomogeneities lead to additional dephasing of the spins. The refocusing pulse rotates the spin in the transversal plane and the spins keep their frequency and direction of precession, they now rephase leading to an echo after TE. The peak value of the echo is proportional to the T_2 decay. Stochastic loss of coherence, as it occurs for T_2 relaxation, cannot be refocused. Hence, the T_2 relaxation curve can be sampled by varying TE.

With these sequences as a basis, more complicated pulse sequences can be build that allow for example the detection of MQ coherences.

2.2.2 MQ Sequences

In order to create MQ coherences, a combination of evolution periods and RF pulses is necessary, since relaxation only changes the rank of the tensors and hard RF-pulses only change coherence order, as shown in Figure 2.5. Since only the $\hat{T}_{1-1}$ tensors are detectable, it is necessary to convert the MQ coherences back to SQ coherenece s. The typical MQ sequence is a three pulse sequence with evolution periods in between the pulses as depicted in Figure 2.9. In between the first and second pulse, an additional 180° refocusing pulse may be used to refocus signal loss due to B_0 inhomogeneities similar to a SE sequence.

The sequence can be divided into two parts. In the first part, the thermal equilibrium magnetization $\hat{\sigma}_{\text{eq}} = \hat{T}_{10}$ is excited and then the magnetization evolves to higher rank tensors. Three relaxation pathways can be utilized. The $\hat{T}_{10} \rightarrow \hat{T}_{30}$ pathway using T_1 relaxation can be investigated in inversion recovery MQ sequences [10, 53]. T_1 relaxation can only create rank 3 tensors. T_2 relaxation can lead to rank 2 and rank 3 tensors via the $\hat{T}_{1\pm1} \rightarrow \hat{T}_{2\pm1}$ and $\hat{T}_{1\pm1} \rightarrow \hat{T}_{3\pm1}$ pathways. All three

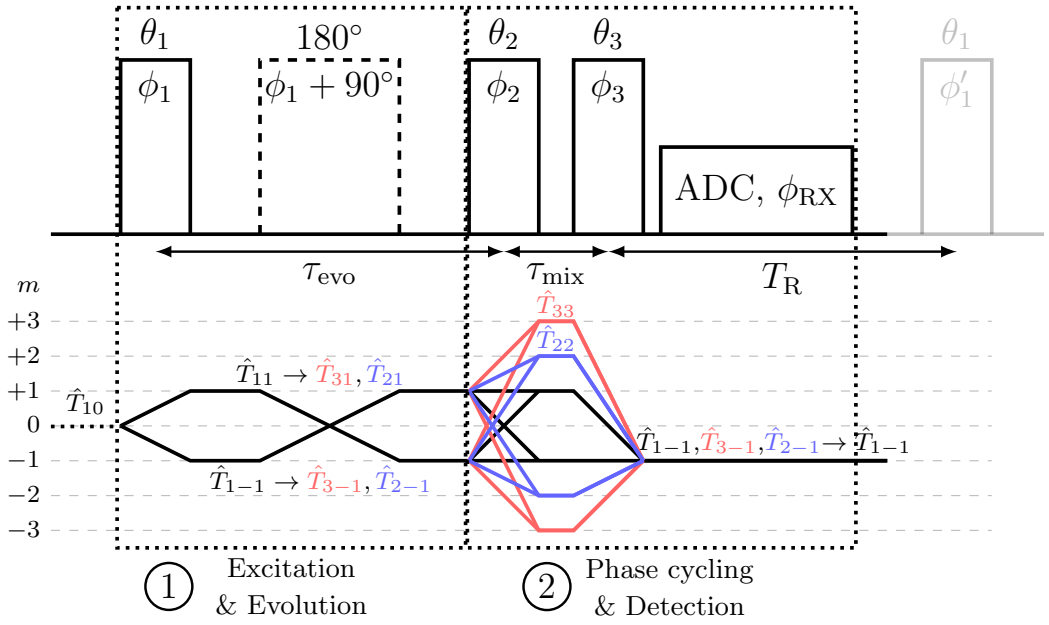

Fig. 2.9.: The general MQ sequence consists of three RF pulses with flip angles θ_i and phases ϕ_i and with evolution periods in between the RF pulses. An optional 180° refocusing pulse can be used during the first evolution period to refocus B_0 inhomogeneities. The ADC has the receiver phase ϕ_{RX}. The sequence can be divided into two parts. During the first part, the magnetization is excited and the higher rank signal evolves, which carries information about the molecular environment of the nuclei. Since the higher rank signal is not MR detectable, a sophisticated detection process using phase cycling is required.

pathways are sensitive to different molecular environments of the nuclei [10]. Rank 2 tensors are only created in the presence of a residual quadrupole interaction and thus a macroscopic anisotropy in the environment. The creation of Rank 3 tensors requires an intermediate motional regime ($\omega_0\tau_c \sim 1$) for the T_1 pathway and a slow motion regime ($\omega_0\tau_c \gtrsim 1$) for the T_2 pathway. The creation of the higher rank tensors encodes all the information about the molecular environment of the nuclei obtainable by an NMR experiment. However, since the higher rank tensors are not NMR detectable, the signal has to be transformed back to detectable $\hat{T}_{1-1}$ tensors in a way, that makes the higher rank signal distinguishable from the rank 1 SQ signal.

The second part of the sequence has the sole purpose of detecting the signal form the higher rank tensors and does not add any information about the nuclei – environment interactions. The higher rank tensors are converted to MQ coherences by the second pulse and back to higher rank SQ coherences by the third pulse. The second evolution period, also called mixing period, is kept as short as possible to avoid unnecessary signal loss due to relaxation. During the acquisition window, the higher rank coherences relax to detectable $\hat{T}_{1-1}$ that create a signal in the the RF receiver coil. The sequence is run multiple times with varying combinations of RF-pulse phases, which is called phase cycling. Here, the sequence makes use of the fact that during application of RF-pulses, the tensors accumulate a phase depending on the change in coherence order as described in Subsection 2.1.5. The creation of MQ coherences adds more phase to the signal than the creation of SQ coherences and with a clever choice of phases the SQ and MQ signals can be distinguished from each other.

The signal can be interpreted as two dimensional with the first dimension being the acquisition time dimension along the Free Induction Decay (FID) and the second dimension being the phase cycle dimension along the different phase combinations. Additional dimensions can be introduced by incrementing the evolution and/or mixing period. For ^{1}H, multidimensional NMR experiments are common [73, 99]. In NMR experiments with spin-3/2 nuclei the mixing time is usually held constant and as short as possible and usually the dimensions are reduced to one dimension, which is partially necessary to extract the MQ signal form the FID. There are two major methods to extract the MQ signal from the overall signal, Multiple Quantum Filtering (MQF) and for the TQ signal the Time Proportional Phase Increment (TPPI) approach.

The MQF method is based on the summation along the phase cycle dimension as shown in Figure 2.10. The evolution period is held constant at the maximum of the MQ evolution curve to maximize the MQ signal. The phases are chosen such that the MQ signal always accumulates the same phase, while the other coherences destructively interfere. This method allows versatile adaptations of the phase cycle to suppress unwanted signal pathways, stimulated echoes, and B_1 and B_0 inhomogeneities that all may affect the MQ signal.

In the TPPI method, the evolution time is incremented in every phase step defining the second dimension. The method is based on the integration of the FIDs along the acquisition time dimension. every integral defines a data point in an FID in the

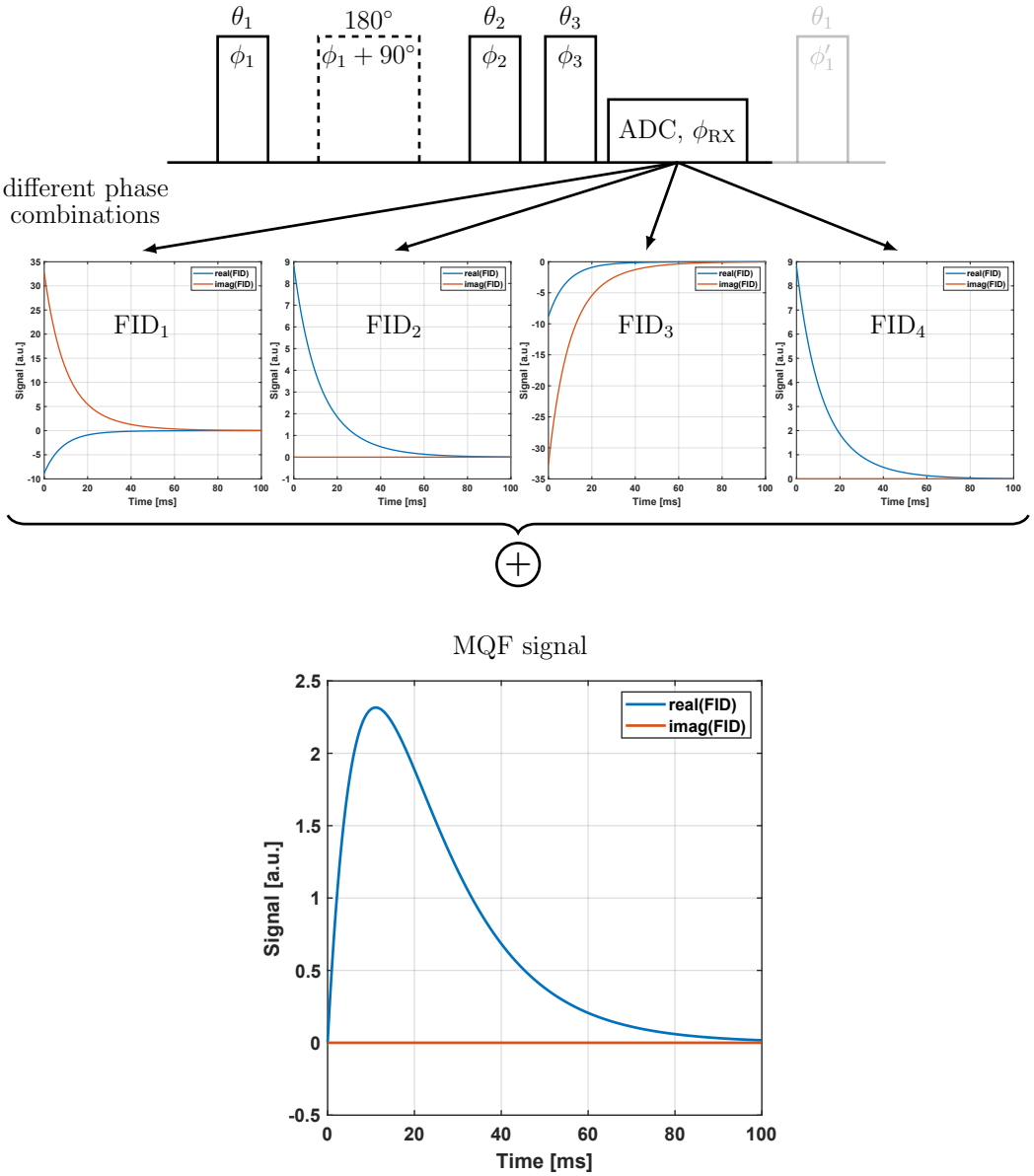

Fig. 2.10.: Schematic overview of the MQF evaluation method. Each phase combination yields a first dimension FID. The evolution time is kept constant. The FIDs are summed up leading a combined FID along the acquisition time dimension. The phases are chosen in a way that only the desired MQ signal passes the filter and all other coherences vanish.

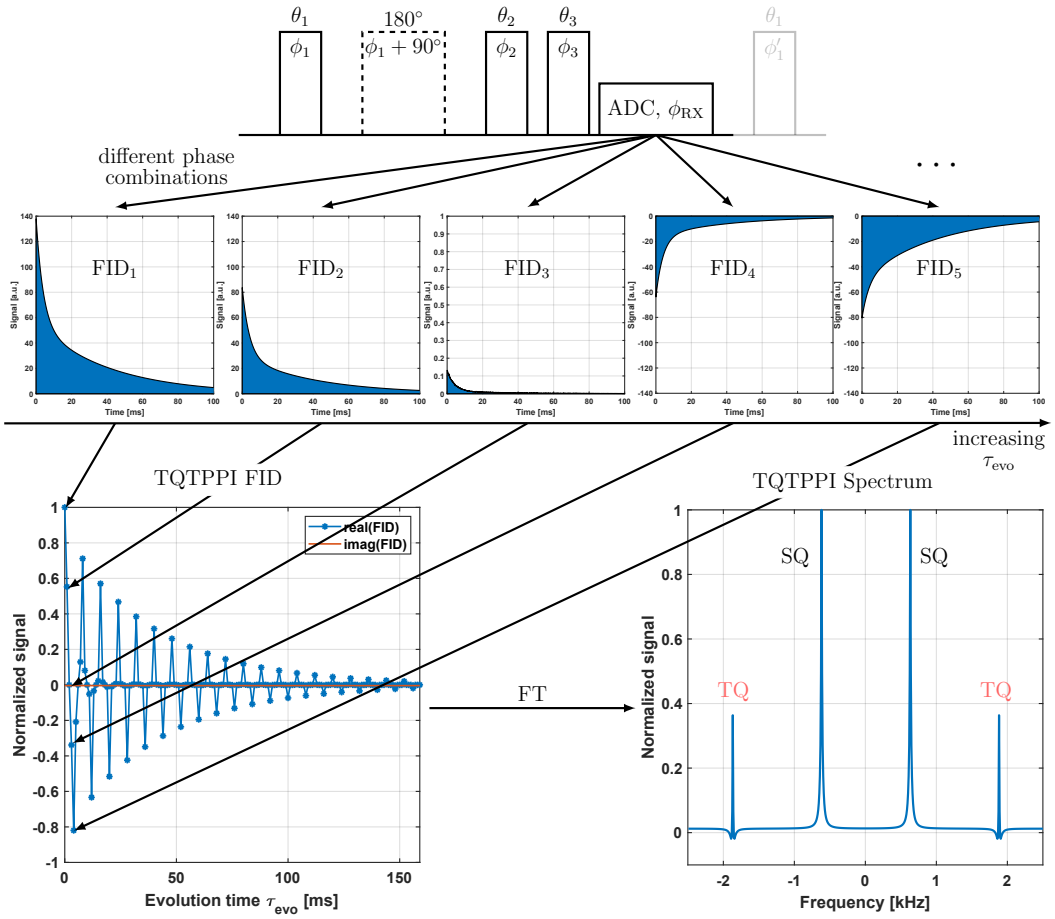

Fig. 2.11.: Schematic overview of the Triple Quantum Time Proportional Phase Increment (TQTPPI) evaluation method. For each phase combination the evolution time is increased and an FID along the acquisition time dimension is acquired. The integrals of the FIDs define a data point in the TQTPPI FID. After applying the Fourier transform, the spectrum of the TQTPPI FID contains the SQ, DQ and TQ signals at distinct frequencies.

evolution time dimension as shown in Figure 2.11. A FT of the TPPI FID reveals the signal of the ZQ, SQ, DQ and TQ coherences at distinct frequencies. Consequently, the TPPI sequence acquires multiple coherences simultaneously and the MQ signal can be normalized on the SQ signal. Currently, only a TQ variant of this sequence is available, the TQTPPI sequence [7]. There is also a variant of this method that uses a constant evolution time and the phase cycle as the second dimension leading to increased Signal to Noise Ratio (SNR), easier data evaluation and shorter measurement duration but without the relaxation time information of the TQTPPI sequence [39].

2.2.3 Imaging

Until now, only spectroscopic sequences were discussed. The NMR spectroscopy signal is the integrated signal over the whole probe in the sensitive region of the RF coils. For medical appications a spatially resolved signal is more interesting. In this subsection, the spectial encoding is briefly discussed, as the main part of this thesis is concerned with spectroscopic sequences. A more detailed discussion can be found e.g. in Haacke et al. [74].

In spectroscopic sequences, the goal is to keep the main magnetic field B_0 as homogeneous as possible to minimize T_2^* relaxation and get narrow peaks. The basic idea behind spatial encoding is to deliberately destroy this homogeneity by adding a spatially dependent magnetic field $\boldsymbol{r}\boldsymbol{G}(t)$. Consequently, the Lamor-frequency is spatially dependent,

$$\omega_0(\boldsymbol{r}, t) = \gamma(B_0 + \boldsymbol{r}\boldsymbol{G}(t)), \tag{2.107}$$

and thus, encodes the region of origin of the signal. The accumulated phase due to the gradient up to time t is

$$\phi_G(t) = -\gamma \int_0^t \mathrm{d}t' \boldsymbol{G}(t'). \tag{2.108}$$

The spatial frequency can be defined as

$$\boldsymbol{k}(t) = \frac{\gamma}{2\pi} \int_0^t \boldsymbol{G}(t')\mathrm{d}t', \tag{2.109}$$

which is also called k-space. The signal $S(\boldsymbol{k}(t), t)$ in k-space is then given by the integral of the spatial distribution of the transversal magnetization $\boldsymbol{M}_\perp(\boldsymbol{r})$ over the whole sample volume V:

$$S(\boldsymbol{k}(t), t) \propto \int_V \boldsymbol{M}_\perp(\boldsymbol{r}, t) \mathrm{e}^{-2\pi i \boldsymbol{k}(t)\cdot\boldsymbol{r}} \mathrm{d}^3 r. \tag{2.110}$$

The integral Equation (2.110) is the FT of the spatial distribution of the transversal magnetization $\boldsymbol{M}_\perp(\boldsymbol{r})$, which is then proportional to the inverse FT of the measured signal:

$$\boldsymbol{M}_\perp(\boldsymbol{r}) \propto \int_V S(\boldsymbol{k}(t), t) \mathrm{e}^{-2\pi i \boldsymbol{k}(t)\cdot\boldsymbol{r}} \mathrm{d}^3 k, \tag{2.111}$$

which defines the Magnetic Resonance (MR) image. This means, an MR image can be acquired by sampling the k-sapce and applying the FT. The time-dependence of the transversal magnetization, i.e. relaxation effects, was neglected. Relaxation effects introduce a signal bias, that leads to the well-known MR imaging contrasts T1 weighting (T1w) and T2 weighting (T2w) that will not be discussed here as they were not relevant for this thesis.

Typically, the Cartesian k-space trajectories are used. However, the short T_2^* relaxation times of $^{23}\mathrm{Na}$ necessitate non-Cartesian trajectories and special

sequences such as the Ultra-Short Echo Time (UTE) sequence with center-out radial readout [84, 100].

2.3 Sodium in Biology

As discussed in the previous sections, the sodium nuclei are interesting from the NMR perspective and yields the second strongest NMR signal in biological tissue. Moreover, sodium ions play an important role in the viability of cells and therefore investigating them is also interesting from a biological perspective. This section gives a brief overview of the involvement of sodium ions in cell processes. A detailed discussion can be found in standard references of physiology like Deetjen and Benndorf [101], Silbernagl and Despopoulos [102], and Brandes et al. [103].

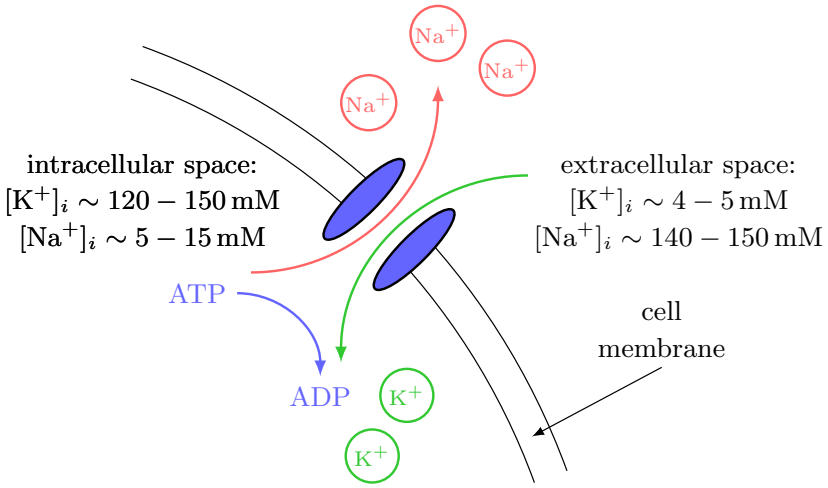

Fig. 2.12.: The Na/K pump constantly pumps three sodium ions out of the cell and two potassium ions into the cell to maintain the large concentration gradients of the ions between intra- and extracellular space.

For healthy cells, there is a large concentration gradient between the intra- and extracellular space. The intracellular sodium concentration is small ($[Na^+]_i \sim 5 - 15\,\mathrm{mmol/L}$) as compared to a large extracellular sodium concentration ($[Na^+]_e \sim 140 - 150\,\mathrm{mmol/L}$). In contrast, the intracellular potassium concentration is large ($[K^+]_i \sim 120 - 150\,\mathrm{mmol/L}$) in comparison to the extracellular potassium concentration ($[K^+]_e \sim 4 - 5\,\mathrm{mmol/L}$). Diffusion processes through the cell membrane constantly lead to an influx of sodium ions in the cell and potassium ions out of the cell. Without counter measures, this would equalize the concentration gradient. The cell uses up to 70 % of its energy for the Na/K pump to maintain this concentration gradient. The Na/K pump pumps three Na^+ ions out of the cell and two K^+ ions into the cell. The energy for this process that works against the potential of the concentration gradient comes from the conversion of adenosine triphosphate (ATP) to adenosine diphosphate (ADP). Moreover, the Na/K pump contributes to the negative electric membrane potential of the cells in the range of -20 to $-120\,\mathrm{mV}$.

The cell uses the electrochemical potentials created by the Na/K pump to transport other ions and nutrients accross the cell membrane against their electrochemical potential. Moreover, the large concentration gradient allows a fast influx of sodium ions into the cell through ion channels that are open for a few ms, which is crucial for excitation of muscle cells and the electric signaling between neurons.

In the case of insufficient energy supply to the cell, the function of the Na/K pump is impaired leading to an influx of sodium ion into the cell. As a result, the cell membrane potential becomes positive which leads to an influx of chloride ions. This again leads to an influx of water in the cell and irreversible cell swelling and necrosis. Several pathologies, such as strokes, ischemia and different types of tumors, can lead to an impairment of the Na/K pump. Thus, the sodium concentration gradient is closely connected with cell viability.

3 Methods

This chapter introduces the experimental setup and samples as well as the sequences, the simulation framework and models developed and used in this thesis. Section 3.1 describes the experimental setup, including the Magnetic Resonance (MR) scanners, radio-frequency (RF) coils and the samples used for the experiments. Section 3.2 describes the simulation framework including the 2xDebye motional. Section 3.3 describes the MR pulse sequences, including the Inversion Recovery Triple Quantum Time Proportional Phase Increment (IRTQTPPI) sequence to measure the T_1 Triple Quantum (TQ) signal and the Single-Pulse (SP) TQ method to approximate the TQ signal using only a single pulse sequence. Parts of this chapter have been submitted for publication in Reichert et al. [63, 64] or have been published as a conference paper in Reichert et al. [104–107].

3.1 Experimental Setup

3.1.1 MRI Scanner and RF Coils

The experiments were performed at 9.4 T and 21.1 T preclinical Magnetic Resonance Imaging (MRI) systems which are described in the following including the RF coils. Both scanners were equipped with a Bruker AVANCE NEO console and ParaVision 360.

9.4T

The majority of experiments were performed at a 9.4 T preclinical MRI system (Bruker BioSpec 94/20 USR, Ettlingen, Germany) with a Lamor frequency of 400.3 MHz for $^{1}\mathrm{H}$ and 105.9 MHz for $^{23}\mathrm{Na}$. A 2$^{\mathrm{nd}}$ order shim set up is integrated in the scanner. The gradient system has a maximum amplitude of 740 mT/m, maximum slew rate of 6900 T/ms and a bore size of 116 mm. The scanner and RF coils are depicted in Figure 3.1.

Two RF coil setups were used in the experiments. The first coil is a linear polarized double resonant Bruker $^{1}\mathrm{H}/^{23}\mathrm{Na}$ volume coil with a length of 315 mm and a diameter of 72 mm. The $^{23}\mathrm{Na}$ part of the coils had a length of 100 mm. Using a RF power of 690 W, the length of a 90° RF pulse was in the range 120-140 μs. The second coil setup was comprised of a quadrature double resonant $^{1}\mathrm{H}/^{23}\mathrm{Na}$ volume birdcage coil by the manufacturer Rapid Biomedical GmbH (Rapid Biomedical GmbH, Rimpar, Germany) and a $^{23}\mathrm{Na}$ Rapid receive-only surface coil. The volume coil has an inner

Fig. 3.1.: a) 9.4 T preclinical Bruker MRI scanner. b) Linear polarized double resonant Bruker $^{1}H/^{23}Na$ RF coil. c) Quadrature double resonant Rapid $^{1}H/^{23}Na$ RF coil.

diameter of 72 mm and the ^{23}Na part of the coil has a length of 103 mm. The surface receiver coils has a single loop with a diameter of 30 mm. Using a RF power of 690 W, the length of a 90° RF pulse was in the range 130-140 μs.

21.1T

Additionally, some of the experiments were performed at a 21.1 T preclinical MRI scanner located at the National High Magnetic Field Laboratory (NHMFL) in Tallahassee, Florida, USA [108]. This scanner has currently the world strongest magnetic field strength for an MRI scanner with a ^{1}H Lamor frequency of 900 MHz and a ^{23}Na Lamor frequency of 237.5 MHz and a bore size of 105 mm. For all experiments, the scanner was equipped with a custom-built linear polarized double resonant $^{1}H/^{23}Na$ birdcage volume coil as described in Qian et al. [109] with an inner diameter of 33 mm with a RF power of 300 W, the length of 90-100 μs. The scanner and coil are depicted in Figure 3.2.

3.1.2 In-vitro Samples: Model Systems for Biological Tissue

This section describes the different samples used in the experiments as model system. The purpose of the model systems was to validate the methods developed in this thesis in a controlled environment that resembles the in-vivo situation in biological

Fig. 3.2.: a) 21.1 T preclinical MRI scanner at the NHMFL. b) Linear polarized double resonant $^{1}H/^{23}Na$ RF coil with a sample.

tissue without the limitations that arise from using actual biological tissue or even small animals or healthy volunteers.

Agarose

The majority of the experiments was performed on agarose, a polysaccharide with similar Nuclear Magnetic Resonance (NMR) properties as ^{23}Na as biological tissue [7, 54, 84]. Even small agar concentrations are sufficient to yield bi-exponential relaxation and a sodium TQ signal. However, it is important to note, that the agar TQ signal is slightly larger than the in-vivo TQ signal [7].

The agarose samples used in this thesis contained 154 mM sodium chloride, and agarose concentrations of 0 % (just sodium chloride solution), 2 %, 4 % or 6 % w/w, respectively. Here, a concentration of 1 % w/w corresponds to 1 g of agarose per 100 g of solution. The phantoms contained 10 mL sample in 20 mL syringes with a diameter of 20 mm and a sample length of 35 mm. The small size of the samples ensured that the whole sample is located in the homogeneous region of the coils and hence, minimizes flip angle deviations.

The agarose phantoms were produced by heating a solution of distilled water, sodium chloride and agarose in the respective concentrations above 88 °C on a heating plate. To ensure even heating, the solution was constantly stirred. After heating the solution was weighted and water was added until the preheating weight was reached to

account for evaporated water during the heating process. The solution was filled in 20 mL syringes in a way that minimizes the amount of air bubbles in the phantom and direct contact of the solution to air. This was necessary to ensure a stable shim and thus minimize B_0 inhomogeneities in the sample. Also see Hu [110], where the production of the agarose samples was described in more detail.

Proteins

Slow interactions of sodium ions with proteins, and more specifically with negatively charged groups on the protein surface, are one of the major contributors to the TQ signal in biological tissues. This is due to the high abundance of proteins in cells [44] and the availability of negatively charged groups [6, 43].

Most studies of the sodium NMR signal in the presence of proteins examine the protein Bovine Serum Albumin (BSA) [9, 43, 45, 46]. BSA is a well-characterized serum albumin protein found in bovine blood that is often used in biology as a concentration standard or when an arbitrary pure protein is required. With 583 amino acids (66.5 kDa), BSA is a relatively large globular protein [111] with 100 negatively charged groups. However, sodium ions have a very low binding affinity for BSA [47]. As a result, solutions of BSA and sodium give a strong pH dependent TQ signal that is weaker than that of cells [9, 43, 45, 46]. The BSA samples had a NaCl concentration of 154 mM and a BSA concentration of 10 %, 15 %, 20 %, 25 % or 30 % w/w, respectively. Similar to the agarose samples, the BSA samples contained 10 mL of solution in a 20 mL syringe.

Since previous studies have limited the investigation of the sodium TQ signal to BSA solutions, several other proteins were investigated in this thesis. These studies had two main objectives. First, the TQ and relaxation behavior of BSA was compared to the TQ and relaxation behavior of a form of bovine hemoglobin, methemoglobin, a protein very similar to BSA in size and sodium binding affinity, but paramagnetic. Second, the TQ signal and relaxation behavior of several globular proteins of different sizes were studied to determine the dependence of the TQ signal on protein size. Since the rotational correlation time of globular proteins increases with protein size, a positive correlation of the TQ signal with protein size is expected.

Hemoglobin (Hem) is a globular protein whose main function is to transport oxygen from the respiratory organs to the rest of the cells and is present in almost all vertebrates [112]. Hemoglobin is a tetrameric protein complex consisting of four subunits. There is a heme group, each containing an iron atom in the center, bound to each of the subunits. Oxygen molecules can bind to the heme group, as can other molecules such as carbon monoxide and carbon dioxide, which can change the electron configuration of the iron atom between the ferrous state (Fe^{2+}) and the ferric state (Fe^{3+}). This also influences the magnetic properties of the heme group and consequently of hemoglobin. In this work, mainly methemoglobin was used, an oxidized form of hemoglobin in which the iron is in the ferric Fe^{3+} state, which makes the protein paramagnetic. With 574 amino acids (64.5 kDa), bovine hemoglobin is almost as large as BSA. In addition, Carr [47] showed that the binding

affinity of sodium to hemoglobin is as low as for BSA. Thus, hemoglobin is very similar in structure to BSA and has the same binding affinity, but is paramagnetic. Paramagnetic quenching [22, 38, 59] can reduce the TQ signal of hemoglobin compared to BSA. Since hemoglobin is less soluble than BSA, the hemoglobin samples contained 154 mM NaCl and a hemoglobin concentration of 2 %, 4 %, 6 %, 8 % and 10 % w/w, respectively. Similar to the agarose samples. Again, the samples contained 10 mL of the solution in a 20 mL syringe.

In addition, human stabilized ferrous hemoglobin solutions were used. Since ferrous hemoglobin naturally oxidizes, the ferrous hemoglobin form used was stabilized with Ficoll. This may have affected the structure and especially the hydration shell of the protein. The protein was solubilized in 154 mM NaCl solution with a 2 % w/w concentration and then saturated with 100 % O_2 gas. In one solution, the excess O_2 gas was removed by exposing the sample to air immediately prior to measurement (referred to as "air"), and one solution was just saturated (referred to as "O_2"). This was used to study the influence of the paramagnetic O_2 gas. In contrast to the other samples, the solutions were not filled into a syringe, but kept in the spherical container in which they were prepared.

For the measurement of the protein size dependence of the TQ signal, each sample contained 154 mM NaCl and a concentration of 2 % w/w of the respective protein and were prepared at a pH value of 7 by adding NaOH solution until pH 7 value was reached. The solution was filled in a 10 mL syringe with diameter of 16 mm and a length of up to 40 mL. Table 3.1 summarizes all proteins used in the comparison. For protein size measurement, the Rapid RF coil setup was used. With α-lactalbumin (αLA, 14.2 kDa) (in a Ca depleted and a Ca saturated variant), β-lactoglobulin (βLG, 18 kDa) and myoglobin (Myo, 17 kDa), three small proteins with comparable size but very different properties were investigated. Sodium has a strong binding affinity to β-lactoglobulin [47, 113] and therefore the influence of the binding affinity can be investigated. Myoglobin is a oxygen binding protein and is paramagnetic in the metmyoglobin form. α-lactalbumin is a calcium binding protein. Sodium ions can strongly bind to the calcium binding sites of the protein in the Ca-depleted version of the protein [114]. Additionally, a Ca-saturated variant was investigated where the binding sites are occupied by Ca ions and therefore, sodium binding is not possible. Therefore, the impact of sodium binding on the TQ signal and the NMR relaxation behavior can be directly be investigated.

Tab. 3.1.: Summary of all globular proteins used for the comparison of the TQ signal. All substances were purchased from Sigma-Aldrich Chemie GmbH (Taufkirchen, Germany) except for BSA, which was purchased from Carl Roth GmBH (Karlsruhe, Germany).

2 % w/v protein sample	Size [kDa]	Product number	Comment
α-Lactalbumin Ca saturated	14.2	L5385	weak sodium binding
α-Lactalbumin Ca depleted	14.2	L6010	strong sodium binding
Myoglobin	17	M0630	heme protein, paramagnetic
β-Lactoglobulin	18	L3908	strong sodium affinity
Ovalbumin	42	A5503	
Human stabilized ferrous hemoglobin, O_2	64.5	H0267	saturated with O_2 gas
Human stabilized ferrous hemoglobin, air	64.5	H0267	satruated with O_2 gas, exposed to air prior to scan
Bovine methemoglobin	64.5	08449	weak sodium binding
BSA	66.5	8076.2	weak sodium binding
Lactoferrin	87	L4040	
γ-Globulin	150	345876	weak sodium binding
Thyroglobulin	305	89385	

3.2 Simulation and 2xDebye Model

Sodium NMR dynamics is complicated and especially the signal of multi-pulse sequences is a combination of various coherences from multiple relaxation pathways, which complicates the signal interpretation. Hence, an advanced simulation framework of spin-3/2, sodium, NMR dynamics provides a unique tool to characterize/quantify the signal components. Simulation frameworks for sodium NMR pulse sequences have been already proposed [30, 53, 60–62]. However, these simulation frameworks are not optimized for fast computation of arbitrary phase cycles with multiple iterations and varying time delays.

This thesis presents a computationally efficient modular simulation framework for spin-3/2, sodium, NMR dynamics in biological environments and under hard RF pulses. The framework provides a complete description of all signal components for arbitrary pulse sequences. Hence, pulse sequences can be optimized and the influence of sequence and probe parameters on the signal can be quantitatively evaluated in a controlled environment. This is especially useful for quick evaluation of phase cycling schemes and to predict the outcome of experiments.

The simulation framework was implemented using Matlab R2021a (The MathWorks, Natick MA, USA) and consists of three classes.

The first class is a helper class for storing constants like the gyromagnetic ratio and calculating the Lamor frequency, spectral densities, correlation times, relaxation times and transfer functions and more. Additionally, the class provides helping functions for the data evaluation.

The second class simulates the NMR dynamics of every Irreducible Spherical Tensor Operator (ISTO) representing the spin-3/2 density operator using the hard pulse approximation and the equations in Subsection 2.1.5 and Subsection 2.1.6. Thus, the class provides relaxation and RF pulse modules that can be used to build pulse sequences. The computation is efficiently performed using the solved evolution equations and therefore equations solvers as used e.g., in Gilles et al. [60] and Wu et al. [62] are not necessary.

The third class allows to build arbitrary sequences and phase cycles using relaxation and RF pulse elements provided by the second class.

Input parameters for the simulation framework are the magnetic field strength, the model parameters of the 2xDebye model, as described in Subsection 3.2.1 and the residual quadrupole coupling strength $\bar{\omega}_Q$. Additionally, sequence and data acquisition parameters can be chosen freely.

3.2.1 2xDebye Model

It is necessary to use a motional model for the spectral densities in the simulation framework that is compatible with the experimental relaxation times. This section introduces an effective model for the spectral densities as an alternative to the

common Debye model that is intrinsically more compatible with the experimental relaxation times and also easy to compute. This allows the translation of the experimental parameters into parameters for the simulation to allow more quantitative simulations.

In an isotropic environment, the T_1 and T_2 relaxation times are given by

$$\begin{aligned} T_{1s} &= \frac{1}{2J_1} & T_{1f} &= \frac{1}{2J_2} \\ T_{2s} &= \frac{1}{J_1 + J_2} & T_{2f} &= \frac{1}{J_0 + J_1} \end{aligned} \tag{3.1}$$

or equivalently, the relaxation rates are given by

$$\begin{aligned} R_{1s} &= 2J_1 & R_{1f} &= 2J_2 \\ R_{2s} &= J_1 + J_2 & R_{2f} &= J_0 + J_1. \end{aligned} \tag{3.2}$$

where J_0, J_1 and J_2 are the spectral densities.

As discussed in Subsection 2.1.6, the Debye model is the most simple model for the for the spectral densities that uses only a single correlation time τ_c and quadrupole strength parameter ω_Q such that the spectral densities J_m are given by

$$J_m(\tau_c) = \frac{(\omega_Q^{\mathrm{RMS}})^2}{5} \frac{\tau_c}{1 + (m\omega_0\tau_c)^2} \tag{3.3}$$

It was previously shown that the Debye model does not adequately describe sodium interactions [6, 8, 9]. However, the model is still widely used [7–10, 43, 61].

It is more accurate to use a distribution of correlations times $p(\tau_c)$ and a correlation time dependent $\omega_Q(\tau_c)$ [8, 54, 115–118]. As a general model, the spectral densities then become

$$J_m = \int_0^\infty p(\tau_c) J_m(\tau_c) \mathrm{d}\tau_c. \tag{3.4}$$

Assumptions about $p(\tau_c)$ and $\omega_Q(\tau_c)$ have to be made in order to extract useful information from Equation (3.4). The Debye model for example uses a delta-distribution as $p(\tau_c)$ and a constant ω_Q. Rooney and Springer Jr [9] on the other hand use a asymmetric log-Gauß distribution as $p(\tau_c)$ and a constant ω_Q. However, the actual distribution of $p(\tau_c)$ and $\omega_Q(\tau_c)$ is most probably more complicated as multiple processes at different time scales overlap and only a limited discrete number of measurement parameters, the relaxation times, is available to describe continuous functions. Many models need many model parameters or are limited to limited to specific situations like an anisotropic environment [6, 8, 9, 119] which makes it difficult to determine the model parameters and use the model in simulations and the evaluation of experimental data.

It is important to note, that correlation times in the extreme narrowing regime ($\omega_0\tau_c \ll 1$) and the slow motion regime ($\omega_0\tau_c \gtrsim 1$) influence the spectral densities

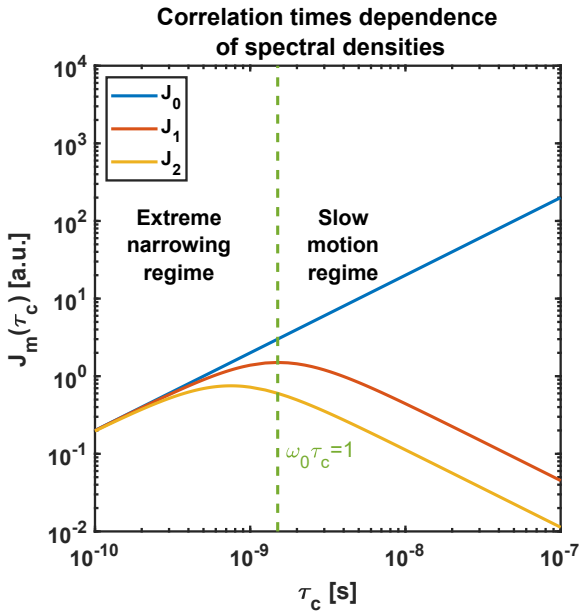

Fig. 3.3.: Spectral densities in dependence of correlation time τ_c for the Debye model. For $\omega_0\tau_c \ll 1$ the system is in the extreme narrowing regime and all spectral densities are approximately equal. For $\omega_0\tau_c \gtrsim 1$ the system is in the slow motion regime and the spectral densities split up.

differently. In the extreme narrowing regime, the spectral densities J_0, J_1 and J_2 are equal:

$$J_m = \frac{(\omega_Q^{\mathrm{RMS}})^2}{5} \frac{\tau_c}{1 + (m\omega_0\tau_c)^2} \rightarrow J_{\mathrm{en}} := \frac{(\omega_Q^{\mathrm{RMS}})^2}{5}\tau_c \tag{3.5}$$

while in the slow motion regime, they split up, which then also leads to the formation of Multiple Quantum (MQ) coherences. This is also shown in Figure 3.3. Most biological tissue may be described by Bull-exchange [120] with a fast exchange between a type c (slow motion regime) and a type d (extreme narrowing regime) site. Sodium usually does not directly bind to macromolecules but instead to the outer spheres of the hydration shell of the macromolecule, where the hydration shells of the macromolecule and the sodium ion mix and fast fluctuations of the hydration shell of the sodium ions are modulated by slower modulations of the macromolecule's hydration shell [8, 121–125]. Therefore, interactions in both motional regimes occur simultaneously and have to be taken into account in a motional model.

In this thesis, an effective motional model was used, that is simple and easy to compute, yet takes both motional regimes into account and is intrinsically more compatible with the experimental relaxation times. The model is an extension of the Debye model by comprising $p(\tau_c)$ with two δ-distributions with two correlation times and accompanying ω_Q, one for the extreme narrowing regime, τ_c^{en} and ω_Q^{en} and one for the slow motion regime, τ_c and ω_Q. With Equation (3.5), the two parameters τ_c^{en}

and ω_Q^{en} of the extreme narrowing regime can be summarized in a single parameter J_{en}. Then the model has only three parameters.

However, B_0 inhomogeneities also have to be taken into account which also decouples the T_1 and T_2 relaxation times. An effective description of the relaxation times in the presence of Lorentzian distributed B_0 inhomogeneities was given in Subsection 2.1.6. The result was that the relaxation rates are modified by an additional coherence order l dependent contribution

$$R_{i,B0}^{(l)} = R_i^{(l)} + l \cdot R_{B0} \tag{3.6}$$

with a single parameter R_{B0} describing the B_0 inhomogeneities. T_1 relaxation ($l = 0$) is unaffected by B_0 inhomogeneities, and thus, the T_2 relaxation times ($l = 1$) decouple from the T_1 relaxation times. This parameter can also be interpreted as an parameter, that takes other influences of the relaxation times into account, such as susceptibility effects or other NMR interactions.

In total the model has four parameters J_{en}, τ_c, ω_Q and R_{B0} that are determined using the four experimental relaxation times T_{1s}, T_{1f}, T_{2s} and T_{2f}. The model parameters are determined by an optimization algorithm that calculates the model relaxation times of the current parameter guess and minimizes the quadratic deviation of the model relaxation times form the experimental relaxation times.

In order to validate and investigate the model, experimental data was acquired at the 9.4 T scanner with the Bruker RF coil setup and the 21.1 T scanner. The T_1 and T_2 relaxation times were determined for the agar, hemoglobin and BSA samples using the IRTQTPPI and Triple Quantum Time Proportional Phase Increment (TQTPPI) sequences with a non-linear fit as described in Subsection 3.3.2 and Subsection 3.3.1, respectively.

The model parameters of the 2xDebye model was determined. Additionally, the model parameters of the Debye model were determined using both the T_1 and T_2 relaxation times and Equation (2.88) and Equation (2.95).

The performance of the simulation framework using the T1 and T2 Debye models and the 2xDebye model was compared with measurement data using the TQTPPI and IRTQTPPI pulse sequences. Measurements were performed at the 9.4 T scanner with the Bruker coil setup for the 2 %, 4 % and 6 % agar samples. The sequences as well as the data evaluation are described in Subsection 3.3.1 and Subsection 3.3.2. The sequence parameters for the TQTPPI sequence (with 180° refocusing pulse) were $T_{\text{R}} = 400\,\text{ms}$, $N_{\text{PC}} = 80$, $\Delta\tau_{\text{evo}} = 200\,\mu\text{s}$, $N_{\text{A}} = 16$ and a total scan time of $t_{\text{scan}} = 18\,\text{min}$ per sample. The sequence parameters for the IRTQTPPI sequence were $T_R = 400\,\text{ms}$, $N_{\text{PC}} = 80$ (40 with increased $\Delta\tau_{\text{evo}}$), $\Delta\tau_{\text{evo}} = 100\,\mu\text{s}$, $N_A = 16$ and a total scan time of $t_{\text{scan}} = 25\,\text{min}$ per sample. The improved data evaluation described in 3.3.2 was used.

Furthermore, the sequence parameters of the TQ and T2 Debye models and the 2xDebye model were compared and discussed for 9.4 T and 21.1 T. The T_1 and T_2 relaxation times were determined using the TQTPPI and IRTQTPPI sequences with the same imaging parameters as above for the 2 %, 4 % and 6 % agar samples.

3.3 Sequences

This section introduces the different sequences and data analysis methods used in this thesis. Several established calibration sequences were used to setup the scanner and the actual experiments. The T_2 TQ signal was investigated using the state-of-the-art TQTPPI sequence in multiple different variations as described in Subsection 3.3.1. The TQ signal can also be created using the T_1 relaxation pathway. For this, the IRTQTPPI sequence with multiple alterations of the phase cycle was developed and investigated in this thesis. The sequence and the different phase cycles are introduced in Subsection 3.3.2. As an alternative to the TQTPPI sequence, a novel method for TQ estimation was developed using only a SP sequence. Moreover the method can be generalized to a Spin Echo (SE) sequence to sample the T_2 Free Induction Decay (FID) and to imaging by using a multi-echo imaging sequence. The method as well as the spectroscopic and imaging sequences used in this thesis are introduced in Subsection 3.3.3. Data processing and evaluation was performed using Matlab (The MathWorks, Natick MA, USA). Parts of this chapter have been submitted for publication in Reichert et al. [63] and Reichert et al. [64].

Prior to the actual measurements, a series of calibration measurements and settings are necessary. First and most importantly, the magnetic field B_0 must be homogenized by the B_0 shim and the length of the 90° RF pulse has to calibrated. Finally, the repetition time has to be set depending on the T_1 relaxation time of the sample as a compromise of scan time and (almost) complete return to thermal equilibrium.

B_0 Shim

B_0 inhomogeneities cause faster signal decay, broad and non-Lorentzian spectra and signal reductions. The MQ signal is in particular prone B_0 inhomogeneities as MQ coherences oscillate faster than Single Quantum (SQ) coherences and accumulate a larger phase shift that leads to faster decoherence. Hence, a good homogenization of the magnetic field is crucial for MQ measurements. For ^{1}H experiments, a localized shim based on a B_0 map corrects B_0 inhomogeneities well. On Bruker scanners, such a map shim is not available for ^{23}Na measurements. Instead, a ^{23}Na global first and second order shim was performed at both the 9.4 T and 21.1 T scanner setups.

Flip Angle Calibration

An accurate calibration of the 90° flip angle is necessary to maximize the signal output since especially MQ sequences are very sensitive to the flip angle. The length of the longest RF pulses, the 180° RF pulses, for all scanner and RF coil setups in this thesis was below 300 μs while the relaxation times were in the range of several ms. Therefore, the hard pulse approximation is well justified. Then, the flip angle depends on the amplitude of the B_1^+-field and the the pulse length τ_p according

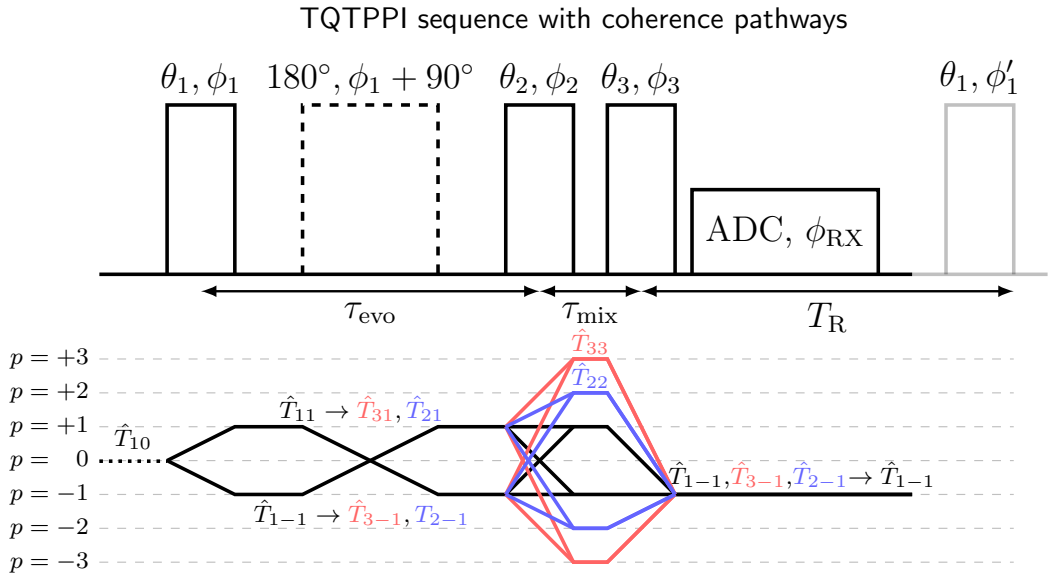

Fig. 3.4.: TQTPPI sequence with coherence pathways. After the 90° first excitation pulse an optional 180° pulse can be used to refocus signal loss due to B_0 inhomogeneities similar to a SE sequence.

to Equation (2.53). Since the effective B_1^+ amplitude is influenced by the sample conductivity and other factors, it is necessary to calibrate the flip angle for each sample. There are automated flip angle calibration methods available provided by Bruker. However, in order to use as short RF pulses as possible, the RF pulse power was set to the maximum value of the coil and RF pulse length was varied. For this, the RF flip angle calibration sequence by Neubauer [126] was used. The adapted single pulse sequence varies the RF pulse length at maximum RF pulse power. The length of the 90° RF pulse corresponds to the first maximum. Under ideal conditions, the 180° RF pulse length is twice the 90° RF pulse length. However, for a more accurate calibration, the 180° RF pulse length was set to the RF pulse length of the first minimum.

3.3.1 TQTPPI Sequence

This subsection describes the TQTPPI sequence [7, 53] and its different variants used in this thesis. The sequence is a three pulse pseudo 2D sequence with an additional optional 180° refocusing pulse as shown in Figure 3.4 and described in Subsection 2.2.2.

The three primary pulses were 90° pulses where the phase of the pulses were incremented in every phase step. The phase of the first pulse was $\phi_1 = \phi_{1,0} + i \cdot \Delta\phi$ and a phase increment of $\Delta\phi = 45°$, $i = 1, \ldots, n_{\mathrm{ps}}$, where $n_{\mathrm{ps}} = 8$ is the number of phase steps, and a start phase of $\phi_{1,0} = 90°$. In every phase step, the evolution time $\tau_{\mathrm{evo}} = \tau_{\mathrm{evo},0} + j \cdot \Delta\tau_{\mathrm{evo}}$ was incremented by $\Delta\tau_{\mathrm{evo}}$ with an initial evolution time $\tau_{\mathrm{evo},0}$ and $j = 1, \ldots, m$, where $m = n_{\mathrm{ps}} \cdot n_{\mathrm{pc}}$ is the number of phase steps n_{ps}

times the number of phase cycles n_{pc}. The phase of the optional 180° refocusing pulse was $\phi_{180} = \phi_1 + 90°$. The phase of the second 90° pulse, $\phi_2 = \phi_1 \pm 90°$, was altered by $\pm 90°$ to suppress Zero Quantum (ZQ) and Double Quantum (DQ) signals. The two signals with $+90°$ and $-90°$ were added such that the ZQ and DQ signals have a phase shift of 180° and therefore cancel out each other while the SQ and TQ signals constructively interfere. The reconstruction of the TQTPPI FID used the Time Proportional Phase Increment (TPPI) approach as described in Subsection 2.2.2.

The signal equation was given by [7]

$$\begin{aligned} S(\tau_{\text{evo}}) = &\sin(\omega\tau_{\text{evo}} + \theta_{sq}) \left(A_{\text{SQf}} \mathrm{e}^{-\tau_{\text{evo}}/T_{2f}} + A_{\text{SQs}} \mathrm{e}^{-\tau_{\text{evo}}/T_{2s}} \right) \\ &+ A_{\text{TQ}} \sin(3\omega\tau_{\text{evo}} + \theta_{tq}) \left(\mathrm{e}^{-\tau_{\text{evo}}/T_{2f}} - \mathrm{e}^{-\tau_{\text{evo}}/T_{2s}} \right) + DC, \end{aligned} \tag{3.7}$$

where T_{2f} and T_{2s} are the fast and the slow relaxation times, A_{SQf} and A_{SQs} are the amplitudes of the fast and slow components of the SQ signal, respectively, with theoretical values of $A_{\text{SQf}} = 0.6$ and $A_{\text{SQs}} = 0.4$ and A_{TQ} is the amplitude of the TQ signal. θ_{sq} and θ_{tq} are the relative phases of the SQ and TQ signals, respectively, and DC is a baseline offset. The SQ signal oscillates with a frequency of $\omega = 2\pi\Delta\phi/(360°\Delta\tau_{\text{evo}})$ and the TQ signal with three times the SQ frequency. To avoid additional signal contributions, the repetition time T_R of the sequence was set to values of at least $T_R > T_1$. The signal equation Equation (3.7) was non-linearly fitted to the experimental TQTPPI FID to extract the amplitudes and the relaxation times. The TQ/SQ ratio was defined by normalizing the TQ amplitude on the SQ amplitudes:

$$TQ/SQ = \frac{A_{\text{TQ}}}{A_{\text{SQf}} + A_{\text{SQs}}}. \tag{3.8}$$

As discussed in Subsection 2.2.2, in contrast to Triple Quantum Filtering (TQF) sequences, the TQTPPI sequence allows the simultaneous detection of the SQ and TQ signals and therefore the normalization of the TQ signal on the SQ signal. This makes the TQ signal a quantitative parameter.

The evolution time τ_{evo} can also be set constant instead of being incremented in every phase step. This fixed TQTPPI sequence [39] leads to an increased Signal to Noise Ratio (SNR) of the TQ signal if the evolution time is set to the optimal value

$$\tau_{evo,opt} = \frac{\ln(T_{2s}/T_{2f})}{1/T_{2f} - 1/T_{2s}}, \tag{3.9}$$

i.e., the evolution that yields the largest TQ signal. The peaks of the TQTPPI spectrum then are delta-peaks which removes the relaxation time dependence of the TQ and SQ peaks and leads to an easy extraction of the SQ and TQ signals. In this thesis, the SQ and TQ evolution curves were sampled along τ_{evo}, by measuring the sequence multiple times with varying τ_{evo} instead of setting τ_{evo} to the optimum

value $\tau_{evo,opt}$. The SQ and TQ signals then are separated instead of overlapping at distinct frequencies:

$$\begin{aligned} S_{\text{SQ}} &= A_{\text{SQf}} \mathrm{e}^{-\tau_{\text{evo}}/T_{2f}} + A_{\text{SQs}} \mathrm{e}^{-\tau_{\text{evo}}/T_{2s}} \\ S_{\text{TQ}} &= A_{\text{TQ}} \left(\mathrm{e}^{-\tau_{\text{evo}}/T_{2f}} - \mathrm{e}^{-\tau_{\text{evo}}/T_{2s}} \right) \end{aligned} \tag{3.10}$$

Disadvantage of this sequence is the much longer scan time as compared to the TQTPPI sequence, as the sequences has to be repeated multiple times.

Investigation of the TQ Signal of Globular Proteins

The measurements regarding the investigation of the TQ signal of globular proteins were performed at the 9.4 T scanner with either the Bruker volume coil or the Rapid volume and surface coil setup.

The TQ signals were determined using the TQTPPI sequence with 180° refocusing pulse. The FID was non-linearly fitted by the signal equation Equation (3.7) to determine the T_2 relaxation times and the TQ/SQ ratio. The sequence parameters were: number of averages $N_A = 20 - 60$ (note that the number of averages only affects the SNR, not the signal amplitude since the normalized signal is used), number of phase cycles $n_{\text{pc}} = 75 - 80$, $\Delta\tau_{\text{evo}} = 100 - 200\,\mu\text{s}$, $T_R = 5 \cdot T_1$. The mono-exponential approximation of T_1 was determined with an Inversion Recovery (IR) sequence and a non-linear fit as described in Neubauer [126].

To investigate the hemoglobin sample in more detail, additionally, the DQ signal was measured using the Double Quantum Filtering (DQF) sequence described in Gast et al. [87]. The sequence does not allow the simultaneous quatification of the SQ signal to normalize the DQ signal. Therefore, the DQ signal of a sample of 2 % w/w agar with 154 mM NaCl and 10 mM TmDOTP was measured. TmDOTP is paramagnetic and it was shown that this sample yields a DQ signal which is created by the Curie-spin interaction [127, 128]. In the methemoglibin sample, the sodium nuclei might also interact with the paramagnetic centers via the Curie-spin interaction. This was investigated by comparing the TQ and DQ signals and the relaxation behavior of both samples.

3.3.2 IRTQTPPI Sequence

As shown in Subsection 2.1.6 and Subsection 2.1.6, the T_1 pathway to TQ coherences might provide additional information about the molecular environment of the sodium ions comparison to the more commonly studied T_2 pathway. However, the short component of the T_1 pathway contributes only 20 % to the total signal, complicating quantification of the T_1-TQ signal and the T_1 relaxation times. In this section, the IRTQTPPI sequence is introduced as a reliable and robust method to simultaneously quantify the T_1-TQ signal and the T_1 relaxation times. Using the optimized IRTQTPPI sequence, T_1- and T_2 TQ- signals were compared between 9.4 T

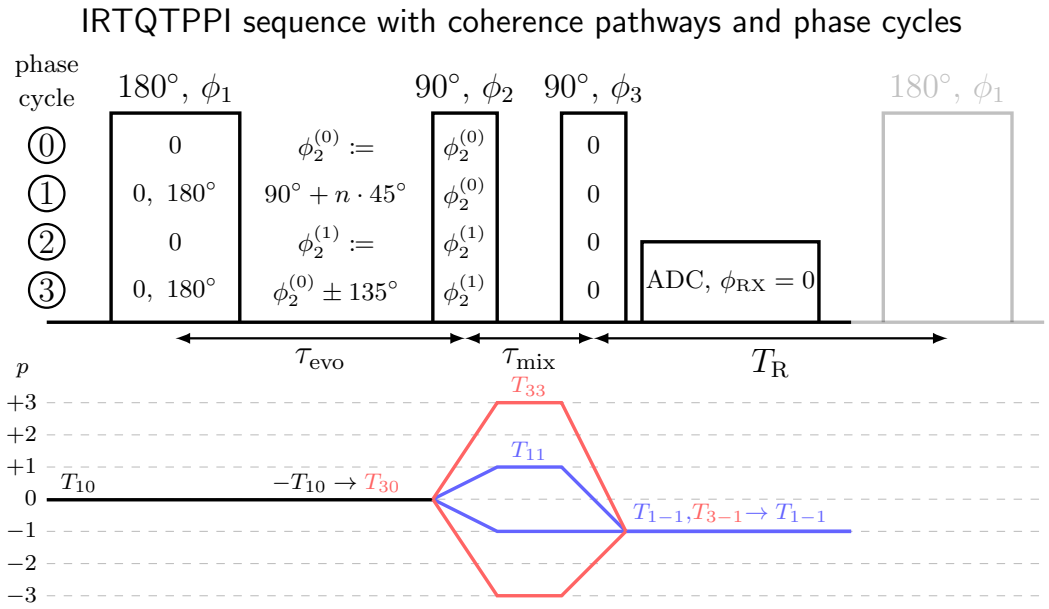

Fig. 3.5.: The IRTQTPPI pulse sequence and corresponding coherence pathways. The first 180° RF pulse inverts the longitudinal magnetization, which relaxes to $\hat{T}_{30}$ during the evolution period. The following 180° RF pulse creates $\hat{T}_{1\pm1}$ SQ and $\hat{T}_{3\pm3}$ TQ coherences. The second 90° RF pulse transfers these states of magnetization to $\hat{T}_{1-1}$ and $\hat{T}_{3-1}$, respectively. The following evolution converts $\hat{T}_{3-1}$ coherence to detectable $\hat{T}_{1-1}$ coherence. For each phase step, both the evolution time τ_{evo} and the RF phases are simultaneously incremented. The initial evolution time increment $\Delta\tau_{evo}$ was non-equidistant with $8\Delta\tau_{evo}$ at a later time point to shorten acquisition time

and 21.1 T for agar samples. The local motional environment was characterized by evaluating the correlation time and the nuclear quadrupole interaction strength.

IRTQTPPI Pulse Sequence and Optimized Phase Cycles

The IRTQTPPI is a three-pulse sequence as shown in Figure 3.5. The 180° inversion pulse flips the equilibrium magnetization to the state described by $-\hat{T}_{10}$, which evolves to the $\hat{T}_{30}$ state in the subsequent evolution period τ_{evo}. The second RF pulse with flip angle 90° transforms the $\hat{T}_{30}$ state to the triple quantum coherences $\hat{T}_{33}$. Immediately afterwards, the third RF pulse, also with flip angle of 90°, transforms the $\hat{T}_{33}$ coherence into $\hat{T}_{31}$ coherence. This state evolves later to the MR detectable $\hat{T}_{11}$ coherence during the acquisition window. The phases of the standard sequence PC0 are $\phi_1 = 0$ for the first RF pulse, $\phi_1 = 90° + 45° \cdot n$ with $n = 1, \ldots, 8$ and $\phi_3 = \phi_{RX} = 0$ for the last RF pulse and the receiver, respectively. In every phase step the evolution time τ_{evo} between the first and second RF pulse is incremented.

Imperfect RF pulses may lead to the creation of unwanted MR signal contributions, e.g., DQ signal [6]. For improved quantification of T_1 relaxation times and T_1-

TQ signal, three different phase cycles were evaluated for optimum reduction of unwanted signal contributions.

Phase cycle PC1 counteracts an imperfect inversion pulse by altering the phase of the inversion pulse by 180°. The $\hat{T}_{10}$ tensor remains unaffected, while accidentally created $\hat{T}_{11}$ coherences accumulate a 180° phase difference and thus are canceled.

Phase cycle PC2 alters the phase of the second pulse by $\pm 135°$, which results in a canceling of signal components with even coherence order differences $\Delta m = m - m' = 2n$ (n being an integer, here $n = 1$), like the transition $\hat{T}_{30} \rightarrow \hat{T}_{3\mp 2}$ or $\hat{T}_{1\pm 1} \rightarrow \hat{T}_{1\mp 1}$. Here, the $\pm 135°$ phase shifts add $\pm 2 \cdot 135° \cdot n = \pm 270° \cdot n$ phase adding up to in total $(540° \cdot n) \mod 360° = 180°$ phase difference. Since transitions with odd coherence order difference $\Delta m = m - m'$ accumulate a phase difference of $\Delta m \cdot 270°$, signal is lost due to inefficient interference. In comparison to PC0 and PC1, the SNR is reduced by a factor of $1/\sqrt{2}$. Additionally, this method leads to a 90° phase shift between the SQ and TQ peaks which may impact fit accuracy.

Phase cycle PC3 is a combination of PC1 and PC2. The phase of the first pulse is altered by 180°. Additionally, PC3 alters the phase of the second pulse by $\pm 135°$. This cycle therefore counteracts imperfections of both the 180° inversion pulse and the 90° pulses. However, this combination doubles the scan time compared to PC1 and PC2.

Signal Output and Non-Linear Fit

Like the TQTPPI sequence, the signal of the IRTQTPPI sequence, consists of a stack of spectra of the Fourier Transform (FT) transforms of every 1st dimension FIDs along the acquisition time axis. The second dimension yields another FID, which is a function of the evolution time and corresponding phase step increment. Thus, the final signal contains both the SQ and TQ signal at distinct frequencies. The FID signal in the second dimension can be described by

$$\begin{aligned} Y_1(t) = &\sin(\omega t + \phi_1) \cdot \left(1 - 2A_{1SQ}(A_{1s}e^{-t/T_{1s}} - A_{2f}e^{-t/T_{1f}})\right) \\ &+ A_{1TQ}\sin(3\omega t + \phi_2)\left(e^{-t/T_{1f}} - e^{-t/T_{1s}}\right) + DC, \end{aligned} \tag{3.11}$$

where $Y_1(t)$ is the IRTQTPPI FID amplitude. A_{1s}, A_{1f}, and A_{1TQ} are the amplitudes of the slow and fast SQ signal as well as the TQ signal, respectively.

$\omega = 2\pi\Delta\phi/(360°\Delta\tau_{\text{evo}})$ is the frequency of the SQ signal determined by the phase cycle step. The values of ϕ_1 and ϕ_2 represent the phases of the SQ and TQ signals, respectively. The output FID in the second dimension was non-linearly fitted by the above signal equation Equation (3.11). The total amplitude A_{1SQ} was used as a scaling factor accounting for imperfect inversion of magnetization. The amplitudes A_{1s} and A_{1f} of the slow and fast component were set to their theoretical values 0.8 and 0.2, respectively [10]. Multiple studies [7, 129] showed that the SQ amplitudes were close to their theoretical values for T_2 relaxation in agar samples and in-vivo. Hence, it is reasonable to assume the same for T_1 relaxation. Moreover, fixed values

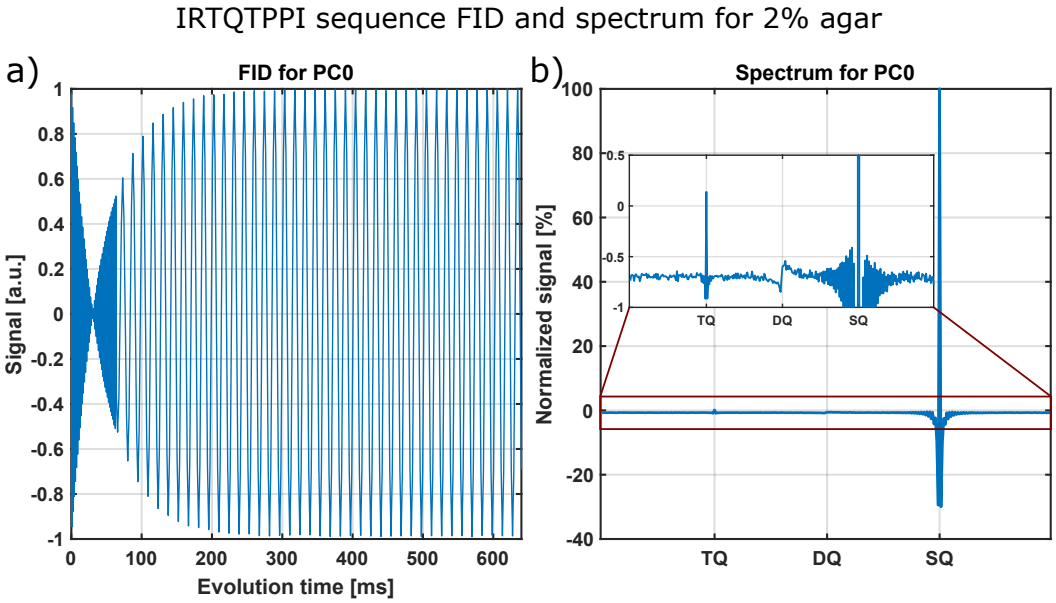

Fig. 3.6.: Sodium FID and spectrum of the 2 % agar sample for the phase cycle PC0 without DQ suppression at 9.4 T. a) The FID was sampled with two evolution time increments, $\Delta\tau_{\text{evo}}$ and $8\Delta\tau_{\text{evo}}$. b) The spectrum shows a TQ peak, which proofed that T_1 relaxation was bi-exponential. A DQ peak could potentially affect the reliability of the fitting and hence DQ suppression methods were necessary.

were necessary to stabilize the fit results since the fast component contributes only 20 % to the signal. We nevertheless evaluated the fit stability with bound and unbound amplitudes A_{1f} and A_{1s}.

A further improvement of fit accuracy and a reduction in measurement time were achieved in the IRTQTPPI sequence when two different evolution time increments were used. For small evolution times up to 65 ms, data was sampled more densely using a step of $\Delta\tau_{\text{evo}}$. For longer evolution times, data was sampled with a time step of $8\Delta\tau_{\text{evo}}$. Figure 3.6 shows an exemplary FID in second dimension with two evolution times. The FID in the second, evolution time, dimension is from now on referred to as FID.

Experimental

Measurements were performed at the 9.4 T scanner with the Bruker volume coil setup and the 21.1 T scanner setup and using the [0, 2, 4, 6]% w/w agarose samples.

The parameters of the IRTQTPPI sequence were: $T_{\text{R}} = 400\,\text{ms}$ at 9.4 T ($TR = 1\,\text{s}$ at 21.1 T), 4 averages at 9.4 T (1 average at 21.1 T), $\Delta\tau_{\text{evo}} = 100\,\mu\text{s}$, the number of phase cycles with step of $\Delta\tau_{\text{evo}}$ was $N_{\text{PC}} = 40$. The number of steps with $8\Delta\tau_{\text{evo}}$ was 300. To optimize the number of coarsely sampled data points, we varied the number of steps in the range of 0 to 320.

The SNR of the TQ peak was determined by dividing the TQ peak height by the noise level. The noise level was determined by the standard deviation of the part of the spectrum that did not contain any signals.

We performed two stability tests of the IRTQTPPI method by determining the T_1 relaxation times and the T_1-TQ signal. For the first stability test, we compared the fit results of all phase cycles. For the second test, we compared the fit results for varying numbers of points for the large evolution time increment $8\Delta\tau_{\text{evo}}$. For the T_2 TQTPPI measurements, we used the TQTPPI sequence with a 180° refocusing pulse to compensate for B_0 inhomogeneities [7, 43]. The FID was fitted using the signal equation

$$\begin{aligned} Y_2(t) = &\sin(\omega t + \phi_1) \cdot \left(A_{2s} e^{-t/T_{2s}} - A_{2f} e^{-t/T_{2f}}\right) \\ &+ A_{2TQ} \sin(3\omega t + \phi_2) \left(\mathrm{e}^{-t/T_{2f}} - \mathrm{e}^{-t/T_{2s}}\right) + DC \end{aligned} \tag{3.12}$$

where T_{2s} and T_{2f} are the slow and fast relaxation times, respectively. A_{2s} and A_{2f} are the amplitudes of the slow and fast component, respectively. A_{2TQ} is the amplitude of the TQ signal. Other definitions are analogous to the definition for $Y_1(t)$. The T_2-TQ/SQ ratio is defined as

$$\frac{TQ}{SQ} = \frac{A_{2TQ}}{A_{2s} + A_{2f}} \tag{3.13}$$

The standard deviation of the parameters was given by the fit uncertainties. The sequence parameters were $T_{\text{R}} = 400\,\text{ms}$ at 9.4 T ($TR = 1\,\text{s}$ at 21.1 T), 4 averages at 9.4 T (1 average at 21.1 T), $\Delta\tau_{\text{evo}} = 100\,\mu\text{s}$, the number of phase cycles was in the rage of 60 to 100, $\Delta\tau_{\text{evo}} = 200\,\mu\text{s}$.

The T_1-TQ/SQ ratio was determined in the same way as the T_2-TQ/SQ ratio as

$$\frac{TQ}{SQ} = \frac{A_{1TQ}}{A_{1s} + A_{1f}} \tag{3.14}$$

The $1 - 2f_{11}^{(0)}(t)$ behavior of the fit function in comparison to the TQTPPI pulse sequence makes the definition of the TQ/SQ ratio more complicated.

Many studies used a mono-exponential approximation for T_1 relaxation [90, 92–98]. Therefore, we also calculated a mono-exponential approximation T_{1m} of the T_1 relaxation times by [83]

$$T_{1m} = \frac{1}{0.8/T_{1s} + 0.2/T_{1f}} \tag{3.15}$$

The sensitivity to the motional environment is characterized by the typical time scale of motional averaging, the correlation time τ_c and the quadrupole interaction strength ω_Q. To investigate the motional regimes for both sequences, τ_c and ω_Q were calculated using equations Equation (2.88) and Equation (2.95) for all pairs of T_1 and T_2 relaxation times, respectively.

Improved Data Evaluation

During the work of this thesis, the data evaluation process of the IRTQTPPI sequence was substantially improved. As described before, the fit accuracy depends on the number of fit parameters. Hence, prior knowledge of the TQ signal evolution can be leveraged. Therefore, the number of fit parameters was reduced further by fixing the amplitude of the TQ signal to its theoretical value.

According to Equation (2.86), the theoretical amplitude of the $\hat{T}_{10} \rightarrow \hat{T}_{30}$ transition is 2/5. Additionally, the transition efficiencies of the RF pulses and the transition $\hat{T}_{3-1} \rightarrow \hat{T}_{1-1}$ during the acquisition window have to be taken into account. Moreover, $\hat{T}_{33}$ coherences are impacted three times stronger by B_0 inhomogeneities than $\hat{T}_{11}$ coherences. However, since the mixing time is in the range of only 100 μs leading to an effect of only a few percent and the exact influence is hard to estimate, this factor was neglected. In total the TQ amplitude is given by

$$A_{\mathrm{TQ}} = \sqrt{2} \cdot \frac{2}{5} \cdot \left| \frac{d^{(3)}_{3,0}(90°) \cdot d^{(3)}_{-1,3}(90°)}{d^{(1)}_{1,0}(90°) \cdot d^{(1)}_{-1,1}(90°)} \right| \cdot \frac{\sqrt{6}}{5} \frac{T^*_{2s} - T^*_{2f}}{A^*_{2s} T^*_{2s} + A^*_{2f} T^*_{2f}}, \tag{3.16}$$

where the factor of $\sqrt{2}$ accounts for the larger TQ signal of phase cycles PC2 and PC3 as described in 3.3.2 and [63] which is removed after the fit and for phase cycles PC0 and PC1. The second term accounts for the relative efficiency of the transitions of the TQ pathways to the SQ pathways. The last term accounts for the relative efficiency of the $\hat{T}_{3-1} \rightarrow \hat{T}_{1-1}$ transition to the efficiency of the $\hat{T}_{1-1} \rightarrow \hat{T}_{1-1}$ relaxation which is given by $\int f^{(1)}_{13}(t)\mathrm{d}t / \int f^{(1)}_{11}(t)\mathrm{d}t$. A^*_{2f}, T^*_{2f}, A^*_{2s} and T^*_{2s} are the amplitudes and relaxation times of the fast and slow components, respectively. The T^*_2 relaxation times are determined by a fit of the FID of a singlepulse sequence or the first 1$^{\mathrm{st}}$ dimenstion FID of the IRTQTPPI sequence with the fit function

$$Y(t) = \left(0.4 \cdot \exp\left(\frac{-t}{T^*_{2s}}\right) + 0.6 \cdot \exp\left(\frac{-t}{T^*_{2f}}\right) \right) \cos(\Delta\omega \cdot t) + D.C., \tag{3.17}$$

where the cos term accounts for a possible shift $\Delta\omega$ of the reference frequency of the receiver relative to the Lamor frequency.

The signal function of the IRTQTPPI sequence is the same as before in equation Equation (3.11) except that the TQ amplitude A_{TQ} is fixed to the value from Equation (3.16).

To evaluate the accuracy of this data evaluation approach, again the fit results of the four different phase cycles PC0, PC1, PC2, PC3 were compared using the same experimental data as before.

Similar to the fixed TQTPPI sequence by Kleimaier et al. [39], a fixed version of the IRTQTPPI sequence was implemented, that uses a fixed evolution time instead of incrementing it in every phase step. By using multiple evolution times, and separating the SQ and TQ signals by a Fourier transform, the SQ and TQ curves can be investigated separated from each other. Measurements were performed at the

9.4 T scanner with the Bruker coil setup and the 2 %, 4 % and 6 % agar samples. 37 evolution times in a range of $0.201 - 280\,\mathrm{ms}$ were sampled with a repetition time of $T_\mathrm{R} = 600\,\mathrm{ms}$, 4 averages and $N_\mathrm{PC} = 16$ and phase cycle PC2. The SQ and TQ signal in dependence of the evolution time were extracted using a FT and simultaneously fitted using the equations

$$\begin{aligned} S_\mathrm{SQ} &= 1 - A_\mathrm{SQ}\left(0.8\exp\left(-\frac{t}{T_{1s}}\right) + 0.2\exp\left(-\frac{t}{T_{1f}}\right)\right) + c_1 \\ S_\mathrm{TQ} &= A_\mathrm{TQ}\left(\exp\left(-\frac{t}{T_{1f}}\right) - \exp\left(-\frac{t}{T_{1s}}\right)\right) + c_2. \end{aligned} \tag{3.18}$$

where A_SQ is the amplitude of the SQ signal that accounts for imperfect inversion, A_TQ is the TQ amplitude and c_1 and c_2 are offsets. Total scan time for each sample was 5 h 50 min. For the standard IRTQTPPI sequence, the same parameters as before and phase cycle PC2 were used.

Again, the fit results were compared between the IRTQTPPI sequence and TQTPPI sequence at 9.4 T and 21.1 T.

3.3.3 Single-Pulse TQ Method

Complicated multi-pulse phase cycling sequences lead to long scan times and high Specific Absorption Rate (SAR) values, which currently hinder the clinical application of the sodium TQ signal. In the following, a completely new alternative approach to estimate the sodium TQ signal is presented, which only requires the FID as input. This method oly requires a SP sequence instead of sophisticated multi-pulse phase cycling sequences as the TQTPPI.

The SP Method

As described in Subsection 2.1.2, the density operator $\hat{\sigma}$ describing the sodium nuclei spin system can be expressed in the ISTO [130, 131] basis

$$\hat{\sigma} = \sum_{lm} A_{lm}\hat{T}_{lm}, \tag{3.19}$$

where A_{lm} are the amplitudes of the ISTO basis elements $\hat{T}_{lm}$. We further use the substitutions $A_{SQ} = A_{11}$ and $A_{TQ} = A_{31}$ to clarify the meaning of the respective amplitudes.

Immediately after the 90° excitation RF pulse, the MR signal completely consists of $\hat{T}_{11}$ coherences. The coherences evolve according to the evolution equation [10, 11]

$$\begin{pmatrix} A_{SQ} \\ A_{TQ} \end{pmatrix} \rightarrow \begin{pmatrix} f_{11}^{(1)}(t) & f_{13}^{(1)}(t) \\ f_{31}^{(1)}(t) & f_{33}^{(1)}(t) \end{pmatrix} \cdot \begin{pmatrix} A_{SQ} \\ A_{TQ} \end{pmatrix} \tag{3.20}$$

where

$$
\begin{aligned}
f_{11}^{(1)}(t) &= 0.4\exp\left(-\frac{t}{T_{2s}}\right) + 0.6\exp\left(-\frac{t}{T_{2f}}\right) \\
f_{13}^{(1)}(t) = f_{31}^{(1)}(t) &= \frac{\sqrt{6}}{5}\left(\exp\left(-\frac{t}{T_{2f}}\right) - \exp\left(-\frac{t}{T_{2s}}\right)\right) \\
f_{33}^{(1)}(t) &= 0.6\exp\left(-\frac{t}{T_{2s}}\right) + 0.4\exp\left(-\frac{t}{T_{2f}}\right)
\end{aligned}
\tag{3.21}
$$

are the evolution functions for the transitions $\hat{T}_{11} \rightarrow \hat{T}_{11}$ and $\hat{T}_{31} \rightarrow \hat{T}_{11}$. After the evolution period τ_{evo}, the amplitude of the T_{11} coherence is $A_{SQ} = f_{11}^{(1)}(\tau_{\text{evo}})$ and the T_{31} amplitude is $A_{TQ} = f_{31}^{(1)}(\tau_{\text{evo}})$. The amplitude A_{TQ} and its shape encode information about the molecular environment of the sodium nucleus.

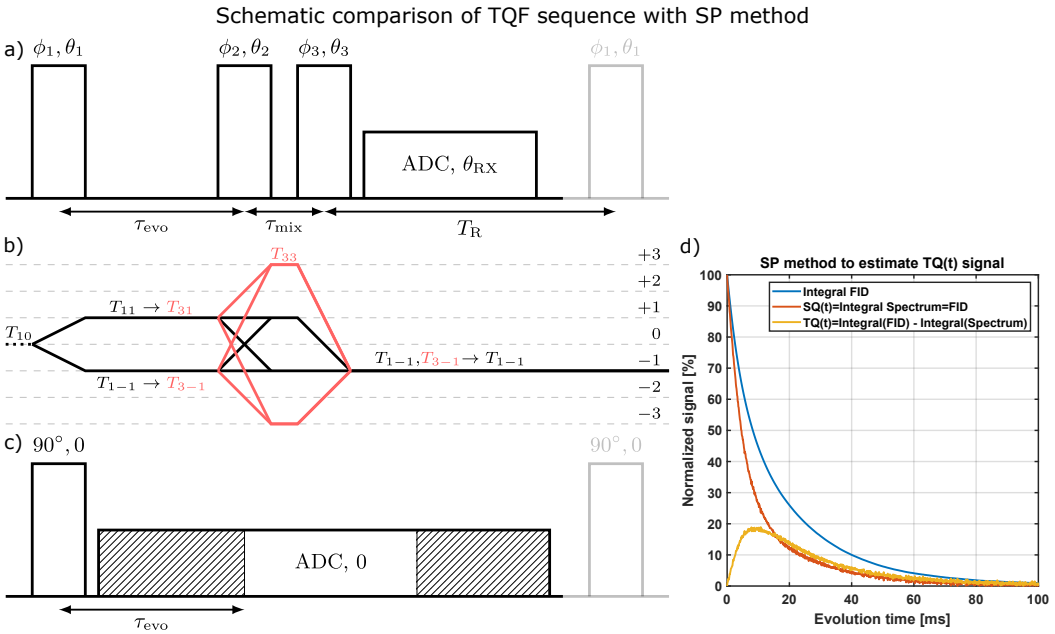

Fig. 3.7.: a) Exemplary conventional TQ pulse sequence. The $\hat{T}_{31}$ coherences are created after the first 90° pulse during τ_{evo}. The rest of the pulse sequence is only necessary to extract TQ signal from the $\hat{T}_{31}$ state by observing oscillations of the final $\hat{T}_{11}$ signal. b) Coherence pathways for the TQTPPI pulse sequence. c) In this study, the three-pulse TQ sequence was replaced by a SP sequence with a prolonged acquisition window. Shifting the processing window across the total acquisition data yields the signal for a set of different τ_{evo}. The shaded area indicates the points removed from the FID for the specific evolution time τ_{evo}. d) The difference of the integration of the whole FID and the SQ spectrum for each τ_{evo} represents the TQ signal.

However, the $\hat{T}_{31}$ coherences are invisible to the receiver coil and therefore it is impossible to directly detect them [61]. Thus, the $\hat{T}_{31}$ coherences must be converted back to the detectable $\hat{T}_{11}$ coherences. The conventional TQF sequence applies a

second and third 90° RF pulse to transfer the $\hat{T}_{31}$ coherences to $\hat{T}_{33}$ coherences and back combined with phase cycling as shown in Figure 3.7a).

Our aim was to reduce the complexity of the TQ pulse sequence, while still being able to extract the TQ signal. In contrast to the TQF approach, which measures the transition $\hat{T}_{11} \rightarrow \hat{T}_{31} \rightarrow \hat{T}_{33} \rightarrow \hat{T}_{31} \rightarrow \hat{T}_{11}$, our method measures only the transition $\hat{T}_{11} \rightarrow \hat{T}_{31} \rightarrow \hat{T}_{11}$. The following introduces our method step-by-step.

First, the FID after a SP and evolution period of τ_{evo} is described by:

$$FID(t, \tau_{\text{evo}}) = A_{SQ}(\tau_{\text{evo}}) f_{11}^{(1)}(t) + A_{TQ}(\tau_{\text{evo}}) f_{13}^{(1)}(t). \tag{3.22}$$

The second term on the right side represents the evolution of the $\hat{T}_{31}$ coherences that evolved during the first evolution period (amplitude $A_{TQ}(\tau_{\text{evo}})$ from the detectable $\hat{T}_{11}$ coherences.

Secondly, for extraction of A_{SQ} and A_{TQ}, we exploit the fact that the integral of a Lorentzian function, i.e., the real part of the FT of a one-sided decaying exponential function, is independent of the width, i.e. relaxation time $T_2^{(*)}$:

$$\int_{\infty}^{+\infty} \frac{T_2}{1 + T_2^2 \omega^2} \mathrm{d}\omega = \pi. \tag{3.23}$$

The TQ signal, i.e.,$A_{TQ} = f_{31}^{(1)}(\tau_{\text{evo}})$, consists of a difference between two exponential functions and therefore the integral over its FT vanishes. On the other hand, the integral over the FT of the SQ signal part is proportional to its amplitude A_{SQ}. In contrast, the integral over the FID contains both signals. The TQ signal then can be extracted by subtraction of both normalized integrals for every τ_{evo}-step

$$\begin{aligned} A_{TQ}(\tau_{\text{evo}}) =& \frac{1}{Norm} \left(\frac{\int_0^{+\infty} FID(t, \tau_{\text{evo}}) \mathrm{d}t}{\int_0^{+\infty} FID(t, 0) \mathrm{d}t} - \frac{\int_{-\infty}^{+\infty} FT(FID(t, \tau_{\text{evo}}))(\omega, \tau_{\text{evo}}) \mathrm{d}\omega}{\int_{-\infty}^{+\infty} FT(FID(t, 0))(\omega, 0) \mathrm{d}\omega} \right) \\ =& \frac{1}{Norm} \left(\frac{\int_0^{+\infty} FID(t, \tau_{\text{evo}}) \mathrm{d}t}{\int_0^{+\infty} FID(t, 0) \mathrm{d}t} - \frac{FID(t, \tau_{\text{evo}})}{FID(t, 0)} \right) \end{aligned} \tag{3.24}$$

The full calculation can be found in Appendix A.2.1, which also demonstrates the necessity of a normalization factor with respect to $f_{31}^{(1)}(t)$ from equation Equation (3.21):

$$Norm = \frac{\int f_{11}^{(1)}(t) \mathrm{d}t}{\int f_{13}^{(1)}(t) \mathrm{d}t} = \frac{A_s T_{2s} + A_f T_{2f}}{\frac{\sqrt{6}}{5}(T_{2s} - T_{2f})}. \tag{3.25}$$

Lastly, in contrast to the conventional TQF/TQTPPI pulse sequence, an extended acquisition window can be used to retrieve results of many evolution times from

the same measurement. As illustrated in Figure 3.7c), the acquisition window starts directly after the excitation pulse instead of waiting for a certain evolution duration τ_{evo}. If τ_{acq} is the desired acquisition time, then for a specific evolution time τ_{evo}, only the FID points between $[\tau_{\text{evo}}, \tau_{\text{evo}} + \tau_{\text{acq}}]$ are used. Thus, the desired acquisition time is shifted across the extended acquisition window to extract the effect of the evolution time on the TQ signal.

Note, that the method can be applied to any equidistantly sampled FID, independent of the sampling method of the FID. Hence, this method is also applicable to imaging using for example a multi-echo sequence. However, if the FID is not equidistantly sampled, either the integral must be adapted by considering the τ_{evo} step-width or the missing points need to be interpolated.

Simulations

For Multi Compartment System (MCS), which yield a more accurate description for biological tissue, the integrals in Equation (3.24) become more complicated. To investigate the validity of the proposed method in such environments, we consider the case of a two-compartment system with two bi-exponential compartments. The corresponding FID and theoretical TQ signal are

$$FID_{\text{MCS}}(t) = (1 - c_{\text{ex}})FID_{\text{in}}(t) + c_{\text{ex}}FID_{ex}(t), \tag{3.26}$$

$$TQ_{\text{exp}}(t) = (1 - c_{\text{ex}})TQ_{\text{in}}(t) + c_{\text{ex}}TQ_{ex}(t), \tag{3.27}$$

where $FID_{\text{in}}(t)$, $FID_{\text{ex}}(t)$, $TQ_{\text{in}}(t)$ and $TQ_{\text{ex}}(t)$ are the FID and TQ signals which correspond to the intra- and extracellular compartment, respectively. It has been previously shown that both the extra- and intracellular compartments yield a TQ signal [22, 60, 132–135] and bi-exponential relaxation [15–22]. For quantitative evaluation of such case, the T_2 relaxation times of 2 % agar ("extracellular", $T_{2s} = 44\,\text{ms}$, $T_{2f} = 9\,\text{ms}$) and 6 % agar ("intracellular", $T_{2s} = 32\,\text{ms}$, $T_{2f} = 3.7\,\text{ms}$) were used to model the two-compartment system with two bi-exponential compartments [15–22].

The value of c_{ex} was varied in the range from 0 to 1 and FIDs were generated according to Equation (3.26). The SP TQ method was applied to the FID to extract the TQ signal. The results were compared to the expected TQ signal calculated by Equation (3.27).

To investigate the impact of noise on the TQ quantification using the SP method, we simulated FIDs in a single compartment system according to Equation (3.22) and added Gaussian white noise to the signal. The output of the SP method was evaluated for different noise levels corresponding to a SNR of the SQ signal of 50, 20, 10 and 5. Additionally, the same noise was subtracted from the TQ signal subsequently to applying the SP method. This allowed us to investigate the systematic error on the TQ signal.

Experimental

Measurements were performed at a 9.4 T preclinical MRI scanner (Biospec 94/20, Bruker, Ettlingen, Germany) using a linear polarized $^{1}H/^{23}Na$ Bruker volume coil. Inner diameter was 72 mm with a length of 100 mm for the ^{1}Na channel. The [0, 2, 4, 6]% w/w agarose samples were used. For MR imaging, all agar samples were combined in a single phantom as depicted in Figure 4.21.

The standard Bruker SP sequence was used to measure FIDs with the following sequence parameters: flip angle 90°, repetition time $T_R = 500\,\mathrm{ms}$, number of averages $N_A = 64$, number of FID points $N_{fid} = 4096$, length of acquisition window $t_{acq} = 410\,\mathrm{ms}$ and a dwelltime of 100 μs. The pre-acquisition delay was 50 μs. The number of τ_{evo} points was set to 2048 with $\tau_{evo,max} = 205\,\mathrm{ms}$. Total acquisition time of the SP sequence was 32 s per sample. The FID was preprocessed as described in Appendix A.2.2.

To determine the validity and accuracy of our method, the results were compared with theoretical predictions of the TQ signal and the results from TQTPPI sequence. The shapes of the TQ, SQ evolution curves and the quantitative values of the TQ signal maxima were used for analysis. The TQ signal maxima represents the mean over 10 points around maximum value to minimize the impact of single outliers. For the TQTPPI sequence, we fitted the TQ signal with the function $TQ(t) = A_{TQ}(\exp(-t/T_{2s}) - \exp(-t/T_{2f}))$ and subtracted it from the signal to obtain an approximation of the noise level. The standard deviation of this noise level defines the uncertainty of the TQTPPI TQ signal maximum.

Theoretical behavior of the TQ signal is determined by the transfer functions $f_{31}^{(1)}(\tau_{evo})$. The necessary $T_2^{(*)}$ relaxation times for the sample were determined by a bi-exponential fit of the FID:

$$Y(t) = A_{SQ,1} \cdot \exp\left(-\frac{t}{t_{2s}}\right) + A_{SQ,2} \cdot \exp\left(-\frac{t}{t_{2f}}\right) + c, \tag{3.28}$$

Where $Y(t)$ is the SP FID and c is an offset. The 0 % agar sample FID was fitted with a mono-exponential function

$$Y(t) = A_{SQ} \cdot \exp\left(-\frac{t}{T_2}\right) + c. \tag{3.29}$$

The TQTPPI relaxation times were determined in the same way.

For the TQTPPI measurements we used a set of fixed-τ_{evo} TQTPPI sequence [7, 39] measurements with a 180° refocusing pulse at 26 different τ_{evo} times in the range of 0.4-200 ms. The repetition time T_R was 400 ms, the number of phase cycles was 16 with 8 phase steps and the number of averages N_A was 4. Total acquisition time for each sample was in the range of 3 h. We used the sequence with the 180° refocusing pulse since the sequence without the 180° pulse resulted in additional stimulated echoes in the signal, see Appendix A.2.3 for further information and Fiege et al. [29], Hoesl et al. [30], and Tanase and Boada [51]. The resulting FID decayed neither

with the T_2 nor the T_2^* relaxation times which complicates the comparison between both sequences.

For a better comparison of our method with the TQTPPI sequence signal, which decays with the T_2 instead of the T_2^* relaxation times, we sampled the T_2 FID with a SE sequence followed by application of our method. For the SE sequence, 256 echoes were equidistantly sampled with a minimum TE of 0.137 ms and an echo spacing of 0.78 ms. The maximum echo time was 300 ms, $T_\mathrm{R} = 500\,\mathrm{ms}$, number of averages $N_\mathrm{A} = 16$. Total scan time for each sample was 45 min. The SE FID was created by the maximum values of the echoes for each echo time. The FIDs were normalized using the inverse of the normalization factor in Equation (3.25) with the T_2 relaxation times. The normalization factor of the TQTPPI sequence uses the T_2^* relaxation times since the first dimension FIDs decay with the T_2^* relaxation times as determined with Equation (3.28) and Equation (3.29). To ensure a fair comparison, we also calculated the theoretical prediction using Equation (3.21) and the T_2 relaxation times obtained from a fit of the SE FID with Equation (3.29) for the 0 % agar sample and Equation (3.28) for the 2 %, 4 % and 6 % agar samples.

For MR imaging, a multi-echo version of the Ultra-Short Echo Time (UTE) sequence [136] was used with 64 echoes, a minimum TE of 0.09 ms and an echo spacing of 3.78 ms. Other imaging parameters were $T_\mathrm{R} = 30\,\mathrm{ms}$, number of averages $N_\mathrm{A} = 4$, $FoV = 68 \times 68 \times 68\mathrm{mm}^3$, imaging matrix = $32 \times 32 \times 32$, spatial resolution of $2.125 \times 2.125 \times 2.125\mathrm{mm}^3$, 3176 projections, a receiver bandwidth of 5 kHz and a total acquisition duration of 1 h 3 min. To suppress noise from voxels outside the samples, we set voxels with less than 50 % of the overall maximum value in the SQ image to 0. This method works well for simple phantoms, but for in vivo measurements more sophisticated methods like region growing, more sophisticated magnitude thresholding or manual segmentation are used as a standard process [137–139]. The SQ and TQ image were acquired simultaneously with the SQ scan time. From every echo, we created an SQ image and the stack of SQ images yielded an FID in a second dimension for every voxel. For the reconstruction of the TQ image, we applied the SP TQ method described in this study voxelwise. The result was a TQ(t) evolution for every voxel. From this a max(TQ) image was created that showed the maximum TQ values for each voxel. The sum(TQ) image was calculated by summing over the TQ(t) signal and normalizing it over the sum of the SQ(t) signal. We also calculated the mean TQ signal for each sample over an exemplary slice. The uncertainty of the values was determined by the standard deviation of all voxels.

4 Results

This chapter presents the results of the different experiments of this thesis. Section 4.1 compares simulated spectra with experimental data for different motional models of the simulation framework. Section 4.2 compares the Triple Quantum (TQ) signals and relaxation times of different globular proteins of various sizes. Section 4.3 presents the results of the Inversion Recovery Triple Quantum Time Proportional Phase Increment (IRTQTPPI) sequence including a comparison of the different phase cycles as well as a comparison of the T_1- and T_2-TQ signals and T_1 and T_2 relaxation times at 9.4 T and 21.1 T. The last section compares the Single-Pulse (SP) TQ method with theory and experimental data. Parts of this chapter have been submitted for publication in Reichert et al. [63, 64] or have been published as a conference paper in Reichert et al. [104–107].

4.1 Simulation and 2xDebye Model

The accuracy of the simulation framework was quantitatively analyzed by comparing simulated spectra for the T1 Debye, T2 Debye and 2xDebye models with experimental spectra for the IRTQTPPI and Triple Quantum Time Proportional Phase Increment (TQTPPI) sequences.

Figure 4.1 and Figure 4.2 compare spectra for the 6 % agar sample of the three motional models and experimental data for the TQTPPI and IRTQTPPI sequences, respectively. The T1 Debye model resulted in a TQ signal, which was by a factor of 0.1 and 0.01 smaller than the experiment for the IRTQTPPI and TQTPPI sequences, respectively. Hence, this model was not adequately describing the motional environment. The T_1-TQ peak in the IRTQTPPI spectrum for the T2 Debye model was much larger by a factor of 16 than for the experiment. In contrast, the 2xDebye model only slightly overestimated the T_1 TQ signal in the IRTQTPPI spectrum by a factor of 1.78. For the TQTPPI sequence, the experimental and simulated spectra almost matched for the T2 Debye and 2xDebye models. Both models only slightly overestimated the T_2-TQ signal by a factor of only 1.15.

A more detailed analysis of the simulated and experimental data for the 2 %, 4 % and 6 % agar samples, as presented in Table 4.1, Table A.1 and Table A.2, revealed that the T_1 relaxation times of the T1 Debye model and the experimental relaxation times were in close agreement. But the T_{2f} relaxation time of the T1 Debye model was much larger than the experimental T_{2f} relaxation time. For both sequences, the simulated TQ signals were much smaller than the experimental TQ signals. For the T2 Debye model on the other hand, the T_2 relaxation times closely matched the experimental T_2 relaxation times, while the separation of T_1 relaxation times

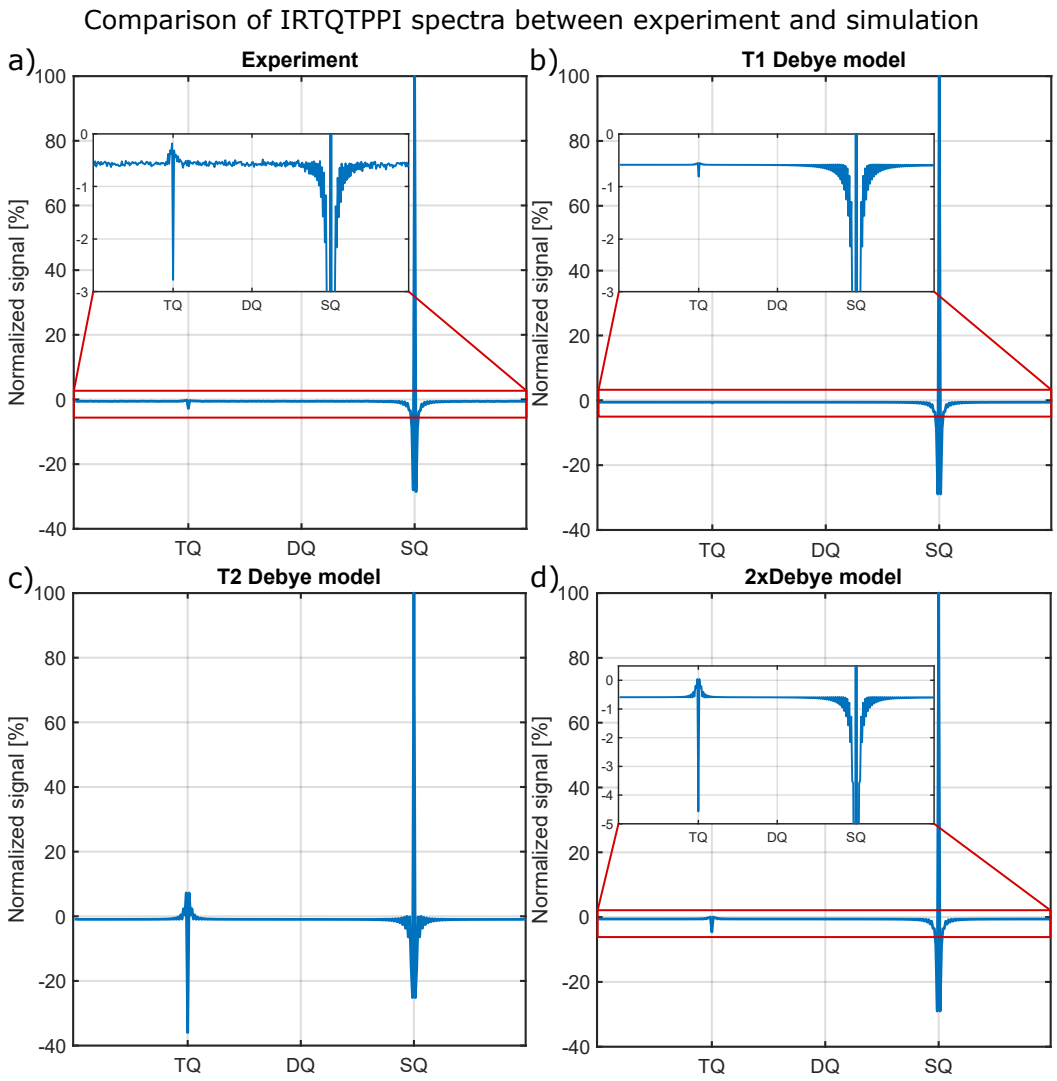

Fig. 4.1.: Comparison of simulated and measured spectra of the IRTQTPPI sequence for the 6 % agar sample. The simulations using the T1 and T2 Debye models yielded a much too weak or too strong TQ peak, respectively. The simulation using the 2xDebye model only slightly overestimated the TQ signal relative to the experiment.

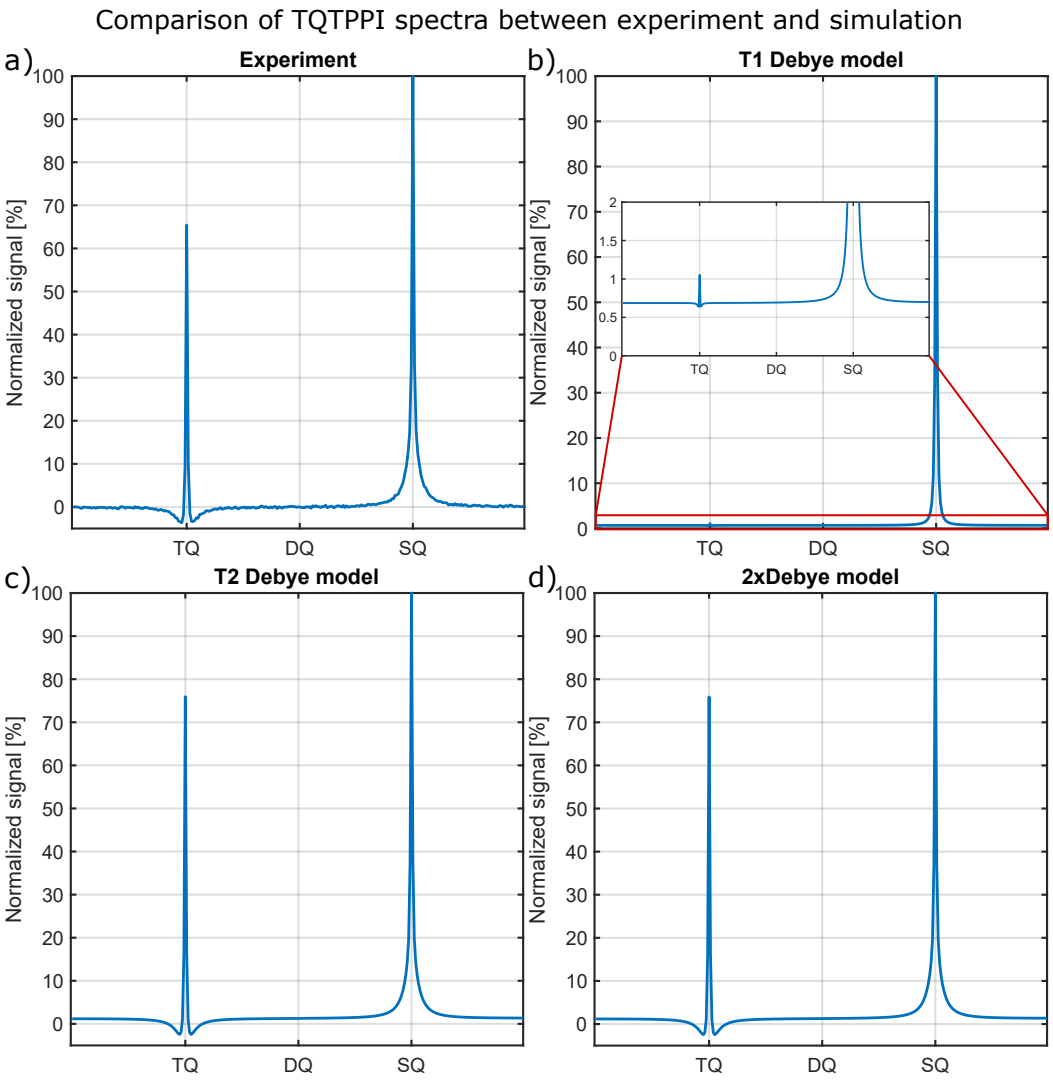

Fig. 4.2.: Comparison of simulated and measured spectra of the TQTPPI sequence for the 6 % agar sample. The simulation using the T1 Debye model yielded a very weak TQ peak, much smaller than the experiment. The simulations using the T2 Debye and 2xDebye models yielded a slightly larger TQ peak than the experiment.

Tab. 4.1.: Comparison of the fit results of the IRTQTPPI and TQTPPI sequences between experimental data, the T1 Debye model, the T2 Debye model and the 2xDebye model for the 2 % agar sample. T_{is} and T_{if} are the long and short component of the T_1 (IRTQTPPI sequence) or T_2 (TQTPPI sequence) relaxation times, respectively. The 2xDebye model used the experimental T_1 and T_2 relaxation times and came closest to the experimental TQ signal for both sequences. The other two models showed substantial deviations in the relaxation times and the TQ signals compared to experiment.

2 % **agar**		T_{is} [ms]	T_{if} [ms]	**TQ/SQ** [%]	**TQ peak** [%]
IRTQTPPI sequence (T_1)	**experiment**	46.65 ± 0.54	41.92 ± 0.19	16.15 ± 0.44	1.01 ± 0.05
	T1 Debye	46.66 ± 0.02	41.91 ± 0.01	1.03 ± 0.01	0.05 ± 0.00
	T2 Debye	97.70 ± 0.29	30.80 ± 0.17	38.19 ± 0.36	37.72 ± 0.07
	2xDebye	46.88 ± 0.04	41.85 ± 0.01	34.00 ± 0.25	1.89 ± 0.00
TQTPPI sequence (T_2)	**experiment**	43.35 ± 0.10	9.13 ± 0.33	21.78 ± 0.24	34.25 ± 0.46
	T1 Debye	43.85 ± 0.11	40.87 ± 0.12	0.79 ± 0.4	0.06 ± 0.00
	T2 Debye	43.32 ± 0.01	9.10 ± 0.03	27.24 ± 0.03	42.47 ± 0.53
	2xDebye	43.35 ± 0.00	9.13 ± 0.00	27.19 ± 0.00	42.37 ± 0.54

Tab. 4.2.: Comparison of the model parameters of the T1 Debye, T2 Debye and 2xDebye models at 9.4 T. The 2xDebye model uses both the T_1 and T_2 relaxation times as input parameters, while the T1 Debye and T2 Debye models use only either the T_1 or T_2 relaxation times.

9.4 T		2 % **agar**	4 % **agar**	6 % **agar**
input parameters	T_{1s} [ms]	46.65 ± 0.54	41.38 ± 0.42	36.33 ± 0.24
	T_{1f} [ms]	41.92 ± 0.19	33.62 ± 0.17	28.50 ± 0.11
	T_{2s} [ms]	43.35 ± 0.10	37.22 ± 0.06	32.57 ± 0.04
	T_{2f} [ms]	9.13 ± 0.33	5.12 ± 0.22	3.66 ± 0.16
T1 Debye	τ_c [ns]	0.30	0.43	0.47
	ω_Q [MHz]	0.46	0.43	0.45
T2 Debye	τ_c [ns]	3.06	4.05	4.59
	ω_Q [MHz]	0.38	0.46	0.52
2xDebye	J_{en} [Hz]	10.31	11.13	12.48
	τ_c [ns]	10.91	10.00	10.32
	ω_Q [MHz]	0.20	0.29	0.34
	R_{B0} [Hz]	0.42	-0.09	-0.60

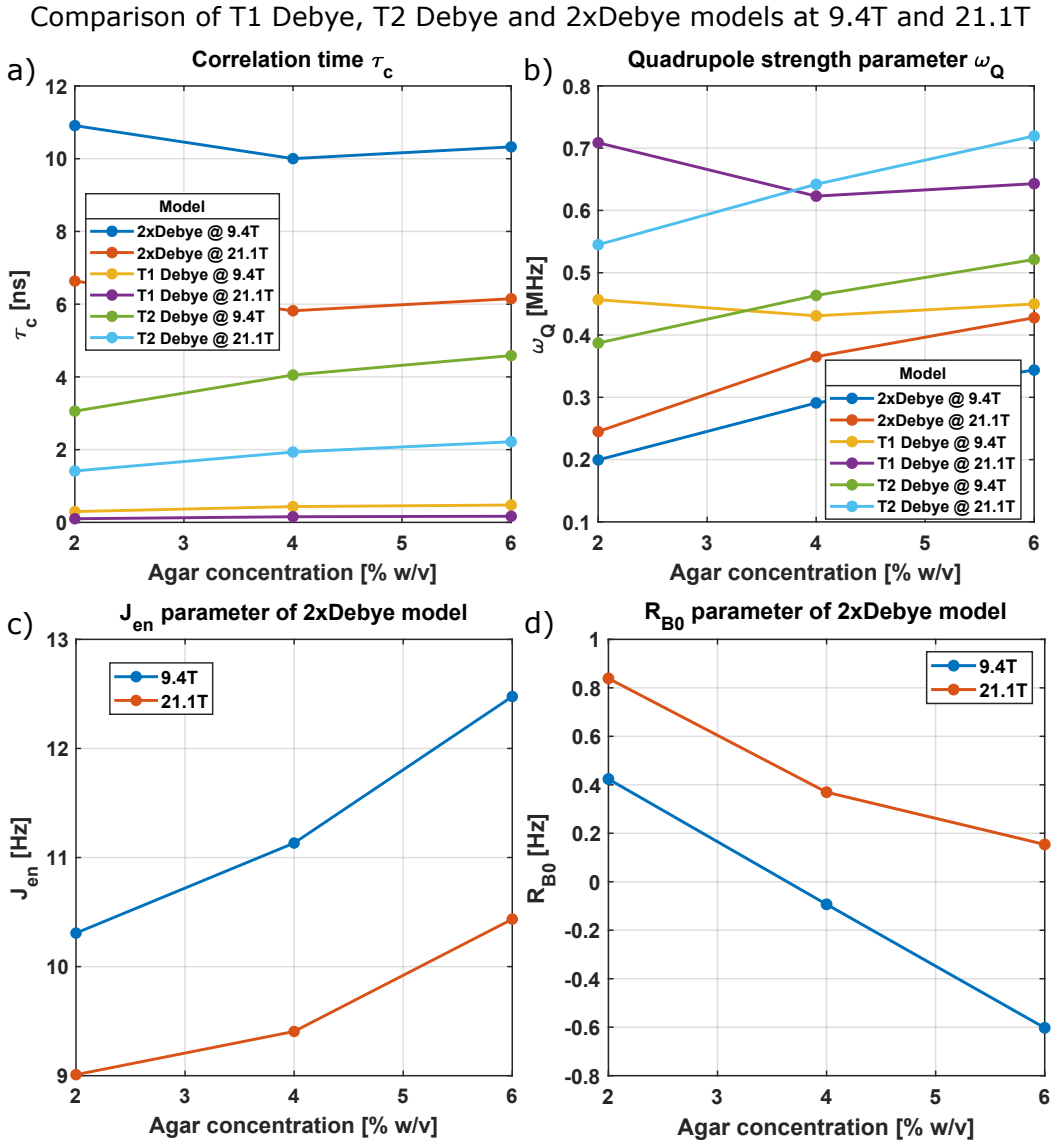

Fig. 4.3.: Comparison of model parameters of the T1 Debye, T2 Debye and 2xDebye models at 9.4 T and 21.1 T. The T1 Debye and T2 Debye models only have two parameters, the correlation time τ_c and ω_Q which were calculated using the T_1 and T_2 relaxation times, respectively. The 2xDebye model has two additional parameters, the extreme narrowing regime parameter, J_{en} and the B_0 inhomogeneity parameters R_{B0}. The parameters of the 2xDebye model were calculated using both the T_1 and T_2 relaxation times.

Tab. 4.3.: Comparison of the model parameters of the T1 Debye, T2 Debye and 2xDebye models at 21.1 T. The 2xDebye model uses both the T_1 and T_2 relaxation times as input parameters, while the T1 Debye and T2 Debye models use only either the T_1 or T_2 relaxation times.

21.1 T		2 % **agar**	4 % **agar**	6 % **agar**
input parameters	T_{1s} [ms]	54.28 ± 0.67	50.41 ± 0.49	45.04 ± 0.37
	T_{1f} [ms]	50.95 ± 0.22	43.73 ± 0.18	38.25 ± 0.15
	T_{2s} [ms]	50.34 ± 0.06	46.04 ± 0.03	41.11 ± 0.03
	T_{2f} [ms]	10.07 ± 0.23	5.67 ± 0.15	4.02 ± 0.18
T1 Debye	τ_c [ns]	0.10	0.16	0.17
	ω_Q [MHz]	0.71	0.62	0.64
T2 Debye	τ_c [ns]	1.41	1.93	2.22
	ω_Q [MHz]	0.54	0.64	0.72
2xDebye	J_{en} [Hz]	9.00	9.41	10.43
	τ_c [ns]	6.64	5.82	6.15
	ω_Q [MHz]	0.25	0.37	0.43
	R_{B0} [Hz]	0.84	0.37	0.15

was substantially overestimated by the model. Furthermore, the T_1-TQ signal was overestimated while the T_2-TQ signal was only slightly overestimated. Both the T_1 and T_2 relaxation times of the 2xDebye model closely matched the experimental values. Additionally, the TQ signals of the TQTPPI and IRTQTPPI sequence were only slightly overestimated.

Table 4.2, Table 4.3 and Figure 4.3 show a comparison of the model parameters of the T1 and T2 Debye models and the 2xDebye model at 9.4 T and 21.1 T. For the T1 Debye model, ω_Q and τ_c were approximately constant. For the T2 Debye model, ω_Q and τ_c were increasing with agar concentration and the correlation times were substantially larger than for the T1 Debye model. ω_Q was similar for both models but probably subject to noise for the T1 Debye model. The transition in the magnetic field strength from 9.4 T to 21.1 T increased ω_Q and decreased τ_c.

For the 2xDebye model, τ_c was approximately constant but noisy and ω_Q was increasing with agar concentration. The extreme narrowing parameter J_{en} was slightly increasing with agar concentration and the B_0 inhomogeneneity parameter R_{B0} was slightly decreasing with agar concentration and close to 0. At 9.4 T, R_{B0} was negative for the 4 % and 6 % agar samples. The transition in magnetic field strength from 9.4 T to 21.1 T increased ω_Q and J_{en} and decreased τ_c.

Tab. 4.4.: Summary of the fit results for all globular proteins. * TQ SNR < 3.

2 % w/v protein sample	Size [kDa]	T_1 [ms]	T_{2s} [ms]	T_{2f} [ms]	A_{TQ}/A_{SQ} [%]
α-Lactalbumin Ca saturated *	14.2	50.49 ± 0.15	52.24 ± 0.67	45.77 ± 0.86	0.12 ± 0.02
α-Lactalbumin Ca depleted	14.2	27.00 ± 0.10	22.67 ± 0.00	8.10 ± 0.00	15.24 ± 0.00
Myoglobin *	17	53.54 ± 0.05	53.80 ± 0.48	49.25 ± 0.77	0.08 ± 0.02
β-Lactoglobulin	18	46.06 ± 0.12	43.89 ± 0.25	40.82 ± 0.30	6.36 ± 0.18
Ovalbumin	42	48.82 ± 0.04	48.25 ± 0.82	40.34 ± 0.91	1.90 ± 0.07
Human stabilized ferrous hemoglobin, O_2	64.5	45.17 ± 0.26	47.23 ± 0.76	37.75 ± 0.69	0.97 ± 0.01
Human stabilized ferrous hemoglobin, air	64.5	45.45 ± 0.29	44.00 ± 0.35	39.54 ± 0.31	1.70 ± 0.03
Bovine methemoglobin	64.5	46.61 ± 0.20	40.45 ± 0.15	20.17 ± 0.08	8.66 ± 0.14
BSA	66.5	50.26 ± 0.06	50.84 ± 0.82	43.02 ± 1.14	0.32 ± 0.02
Lactoferrin	87	49.75 ± 0.05	49.42 ± 1.37	35.62 ± 1.28	2.96 ± 0.08
γ-Globulin	150	51.19 ± 0.04	50.00 ± 0.94	34.12 ± 0.60	4.52 ± 0.05
Thyroglobulin	305	50.38 ± 0.06	48.94 ± 0.04	26.57 ± 0.02	7.66 ± 0.01

4.2 Investigation of the TQ Signal of Globular Proteins

This section presents the results of the measurements regarding the TQ signal and relaxation times of multiple globular proteins of various sizes in the range of 14.2-305 kDa and different sodium binding affinities.

Figure 4.4 shows the TQ signals in dependence of the protein size. With the exception of the proteins, α-Lactalbumin (Ca depleted) (14.2 kDa), β-Lactoglobulin (18 kDa), Bovine Serum Albumin (BSA) (66.5 kDa) and all hemoglobin forms (64.5 kDa), the TQ signal increased with protein size. A linear and square root fit revealed that the size dependence of the TQ signal was less than linear. The datapoints of α-Lactalbumin (Ca depleted) and β-Lactoglobulin were excluded from the fit, as sodium binds strongly to these two proteins as described in Subsection 3.1.2.

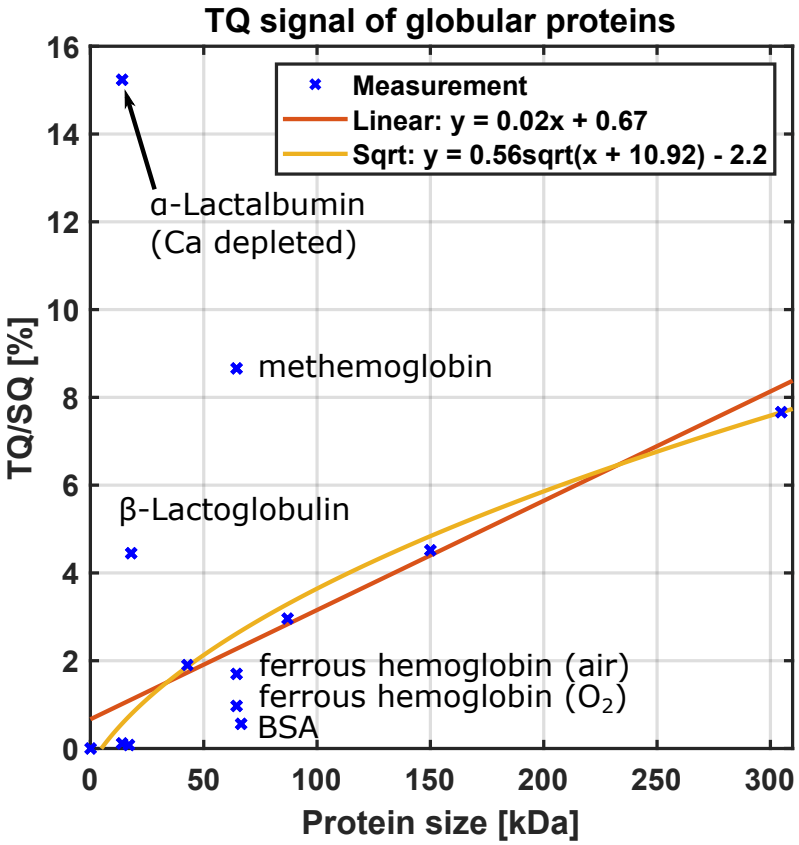

Fig. 4.4.: TQ/SQ ratio was plotted for globular proteins of various sizes. All samples contained 2 % w/v of the respective protein. The data was fitted with a linear and a square root function. The datapoints of the proteins β-Lactoglobulin and α-Lactalbumin (Ca depleted) were excluded from the fit since sodium has unusual large binding affinity to these proteins.

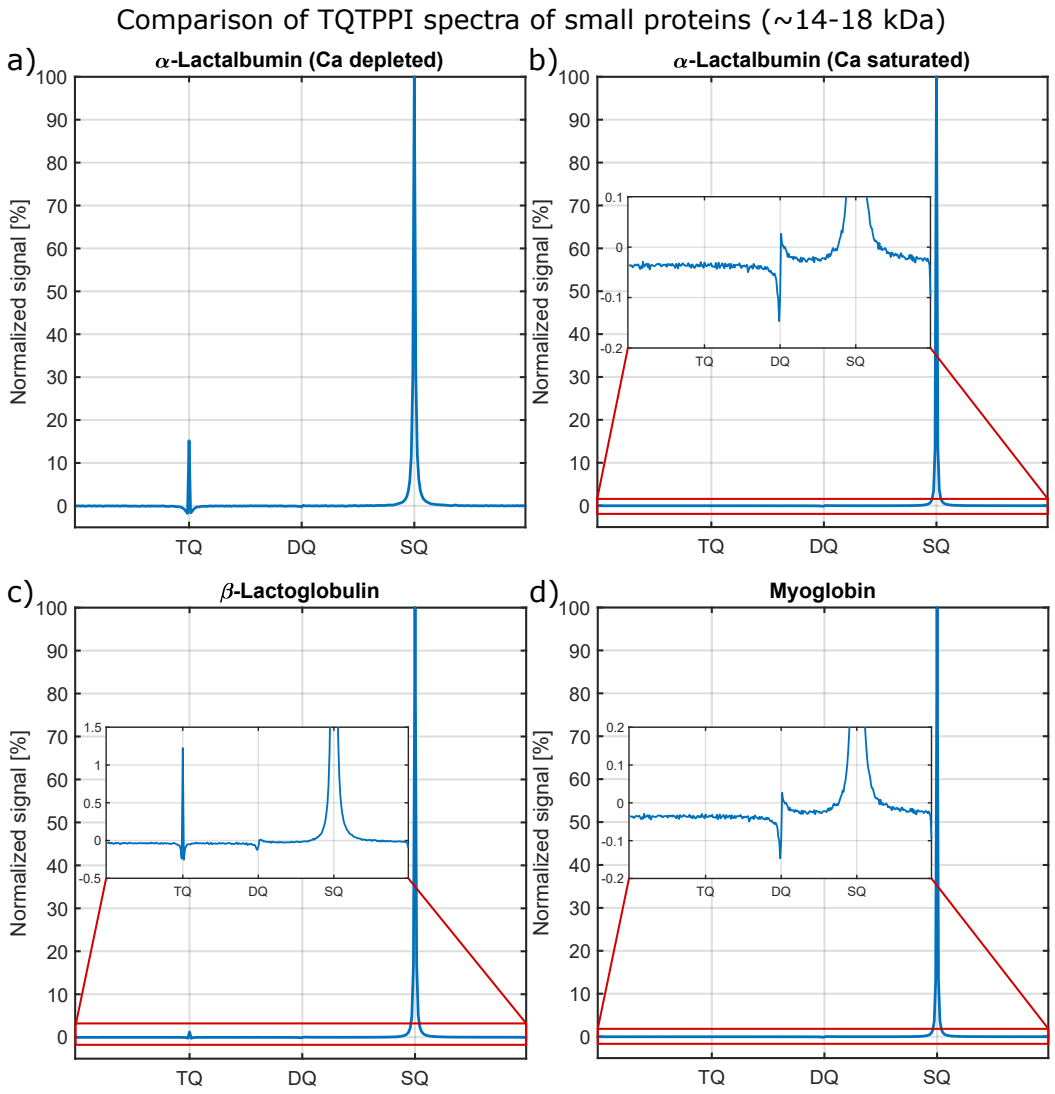

Fig. 4.5.: Comparison of TQTPPI spectra of the small globular proteins α-lactalbumin (in both the Ca depleted and Ca saturated forms), β-lactoglobulin and myoglobin. The sodium binding affinity to both Myoglobin and Ca saturated α-lactalbumin is weak and both samples so not yield a TQ signal. The sodium binding affinity to Ca depleted α-lactalbumin and β-lactoglobulin on the other hand is strong and the proteins yield strong TQ signals.

Table 4.4 shows the relaxation times and TQ/SQ ratios for all proteins. Despite a similar size, the proteins α-Lactalbumin (Ca depleted) and β-Lactoglobulin yielded a much larger TQ signal than the myoglobin and α-Lactalbumin (Ca saturated) samples which yielded an almost vanishing TQ signal with Signal to Noise Ratio (SNR) < 3. Figure 4.5 compares the spectra of α-Lactalbumin (Ca depleted), β-Lactoglobulin, myoglobin and α-Lactalbumin (Ca saturated) samples. Similarly, the methemoglobin sample yielded a substantially larger TQ signal than the ferrous hemoglobin and the BSA samples. The BSA sample yielded a substantially weaker TQ signal than expected for a protein of this size. Figure 4.6 compares the spectra of the BSA, ferrous hemoglobin and methemoglobin samples.

For all samples the T_1 relaxation times were in the range of 45-55 ms independent of protein size, except for the α-Lactalbumin (Ca depleted) sample, with $T_1 = 27.00 \pm 0.10\,\mathrm{ms}$. For most samples, the slow relaxation time T_{2s} was close to T_1. Notable exceptions were the proteins methemoglobin, β-Lactoglobulin and again the α-Lactalbumin (Ca depleted), where T_{2s} was substantially smaller than T_1. In general, T_{2f} was smaller and the difference between T_{2s} and T_{2f} was larger, the stronger the TQ signal.

To investigate the intense TQ signal of the methemoglobin sample in more detail, the TQ signal was measured in dependence of the protein concentration for hemoglobin and BSA. As shown in Figure 4.7, the TQ signal increased approximately linearly with BSA concentration from $0.32 \pm 0.02\,\%$ to $6.61 \pm 0.68\,\%$. Despite lower concentration, the TQ signal of the hemoglobin samples was much stronger than for the BSA samples. However, the TQ signal only increased up to a concentration of 6 % from $6.92 \pm 0.26\,\%$ to $21.13 \pm 0.21\,\%$, and decreased even for the 10 % sample to $19.46 \pm 0.27\,\%$. Moreover, the DQ signal was measured using a MA-Double Quantum Filtering (DQF) sequence. As Figure 4.8 shows, the methemoglobin sample resulted in no a DQ signal in contrast to the TmDOTP sample which yielded a strong DQ signal.

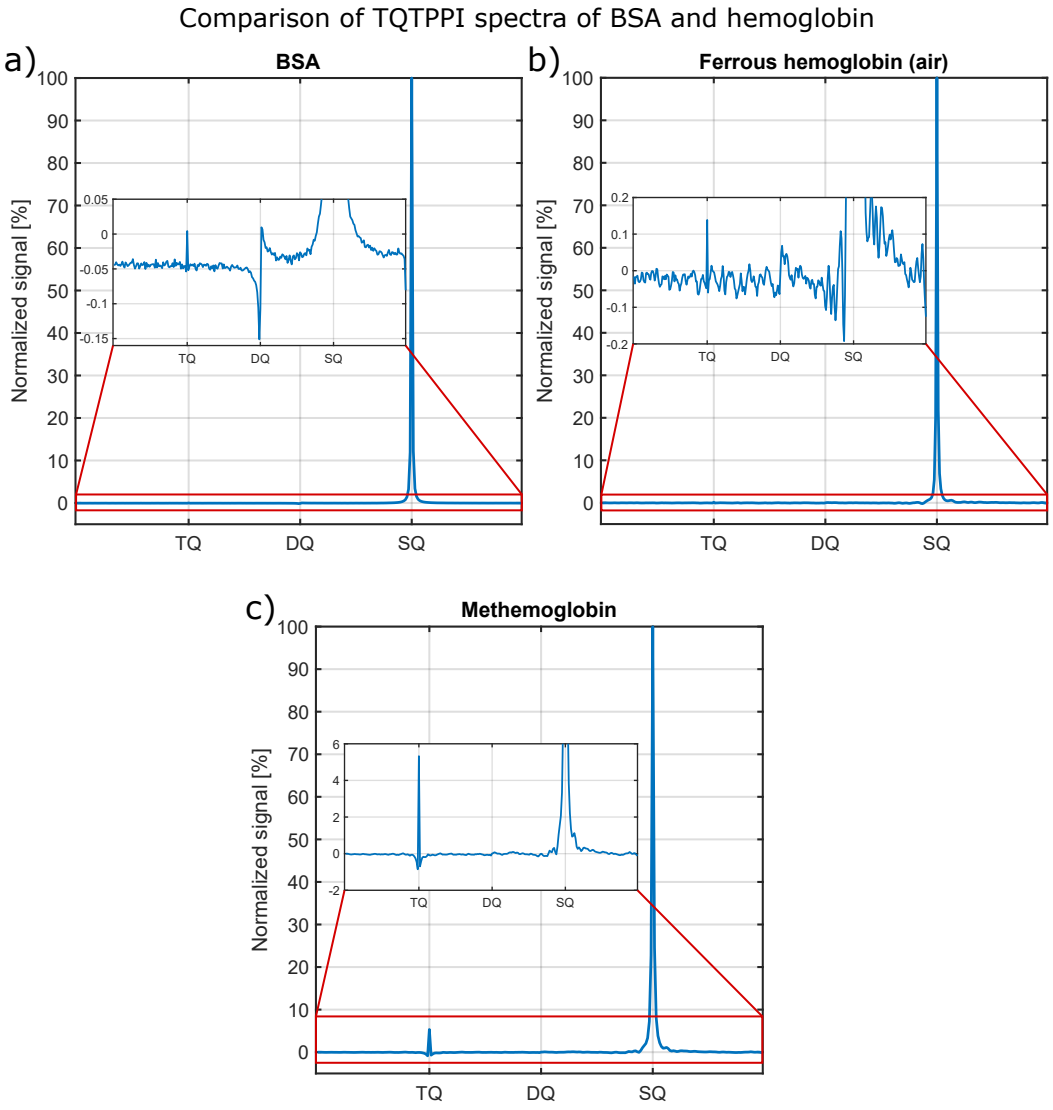

Fig. 4.6.: Comparison of TQTPPI spectra of BSA, ferrous hemoglobin and methemoglobin. Despite the paramagnetism of methemoglobin and a similar sodium binding affinity as BSA and ferrous hemoglobin, methemoglobin yielded a much larger TQ signal.

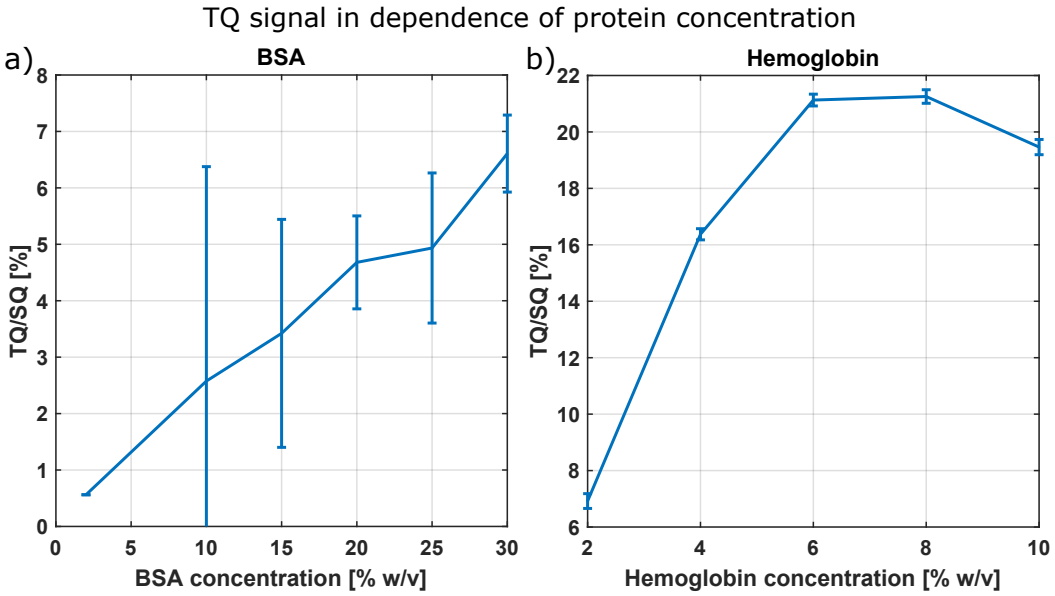

Fig. 4.7.: Comparison of dependence of the TQ signal on a) BSA and b) methemoglobin concentration. TQ signal increased approximately linearly with BSA concentration while it reached a saturation above a hemoglobin concentration of 6 % w/v. For all concentrations, TQ signal was much stronger for hemoglobin than BSA.

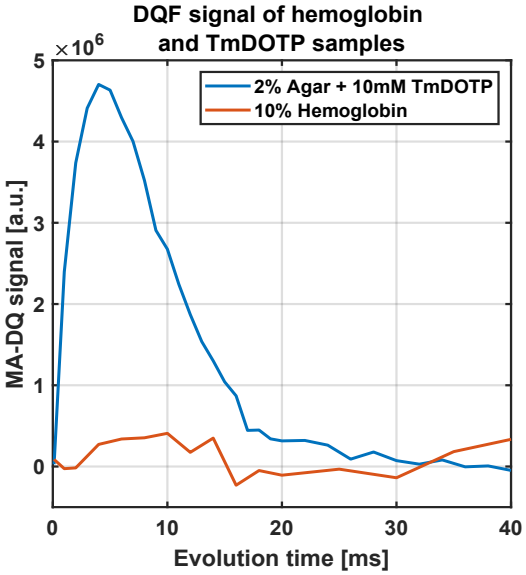

Fig. 4.8.: Comparison of Magic Angle (MA)-Double Quantum (DQ) signal of hemoglobin sample with an agar sample with TmDOTP. The measurement with the hemoglobin sample resulted in no a MA-DQ signal, while the TmDOTP sample yielded a strong DQ signal.

4.3 IRTQTPPI

Figure 4.9 shows spectra of all phase cycles at 9.4 T for the 2 % agar sample. While phase cycle PC0 showed a DQ peak, the phase cycles PC1, PC2 and PC3 successfully suppressed it. PC2 and PC3 shifted the phase of the TQ peak relative to the Single Quantum (SQ) peak by 90°. This resulted in the TQ peak pointing in the opposite direction compared to the corresponding SQ peak.

4.3.1 Stability of IRTQTPPI Fit Results

The stability of the IRTQTPPI fitting results was evaluated using three different methods. The fitting results are shown in Table 4.5 and Table 4.6. First, we compared the fitting results with bound and unbound amplitudes A_{1f} and A_{1s}. The fit results with unbound amplitudes yielded large uncertainties and unrealistic amplitudes that strongly deviated from the theoretical values $A_{1f} = 0.2$ and $A_{1s} = 0.8$. For the 2 % and 4 % agar samples, the fast amplitude contributed $> 90\,\%$ instead of $20\,\%$ to the overall SQ signal. Therefore, we only used the fit using bound A_{1f} and A_{1s} values.

Second, we compared the fit results for the different phase cycles. Figure 4.10 and Table 4.6 show that for all samples and phase cycles, the fit results for the relaxation times were consistent with each other. T_{1m} and T_{1s} almost perfectly matched for the different phase cycles with deviations of less than 0.5 ms. The maximum deviation between T_{1f} of the different phase cycles was less than 1 ms. However, there was a substantial deviation of the T_1-TQ/SQ ratios. Phase cycles PC0 and PC1 yielded approximately the same T_1-TQ/SQ ratio, which was substantially lower than the T_1-TQ/SQ ratios of PC2 and PC3.

As the fit results for the relaxation times of all phase cycles were very similar, we chose phase cycle PC2 for all further measurements.

In the third stability test, we varied the number of data points with larger evolution time increment of $8\Delta\tau_{\text{evo}}$. Figure 4.11 shows the relaxation times and the TQ signal in dependence of the number of points with large evolution time increment for the 4 % agar sample. For all samples, both the T_1-TQ/SQ ratio and the T_1 relaxation times showed a large variation for a low number of additional points. However, between 100 to 200 additional points, the fit converged to a stable set of parameters. For all further measurements, we set the number of additional points to 300.

4.3.2 Comparison of T_1 and T_2 Relaxation Times and T_1- and T_2-TQ Signals at 9.4 T and 21.1 T

For all samples, both T_1 and T_2 relaxation were bi-exponential at 9.4 T and 21.1 T, as shown in Figure 4.12. At 9.4 T, the separation in relaxation times was in the range of 15-18 ms for T_1 and 28-35 ms for T_2. At 21.1 T it was in the range of 15-21 ms

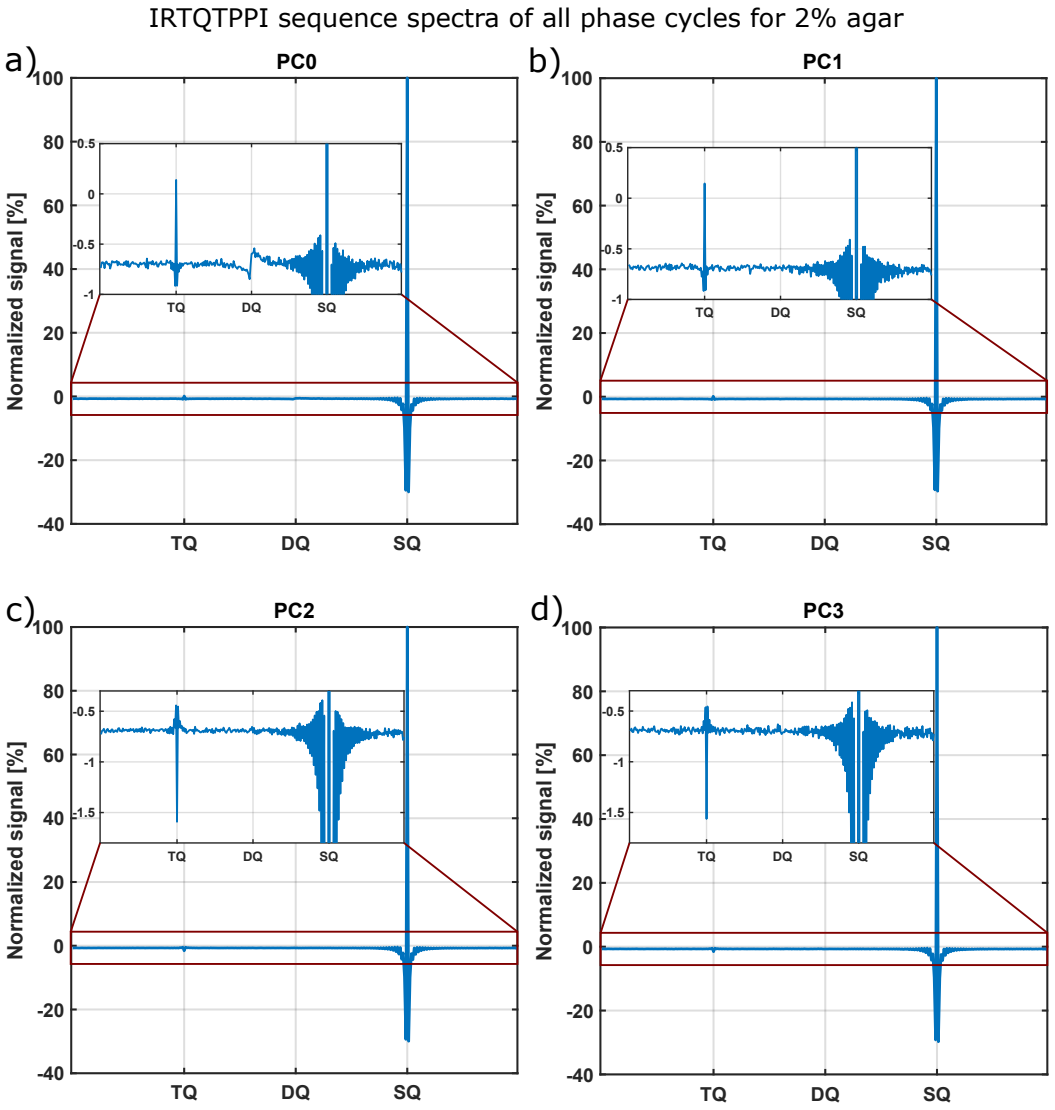

Fig. 4.9.: Comparison of all three DQ suppression methods for the IRTQTPPI sequence, a) phase cycle PC0, b) phase cycle PC1, c) phase cycle PC2 and d) phase cycle PC3 for the 2 % agar sample at 9.4 T. Phase cycles PC1, PC2 and PC3 effectively suppressed the DQ peak that was visible in the spectrum during phase cycle PC0. The TQ signal during PC2 and PC3 phase cycling accumulated an additional 90° phase shift relative to the SQ signal.

Tab. 4.5.: Fit values for unbound SQ amplitudes A_{1s} and A_{1f} for phase cycle PC2 at 9.4 T. Both amplitudes strongly deviated from the theoretical values of $A_{1s} = 80\,\%$ and $A_{1f} = 20\,\%$ for the 2 % and 4 % agar samples. Furthermore, the T_{1s} relaxation time was close to the unrealistic upper bound of 100 ms and T_{1f} showed a large uncertainty.

Agar	2%	4%	6%
T_{1s} [ms]	99.98 ± 0.40	99.99 ± 0.37	45.18 ± 1.57
T_{1f} [ms]	43.06 ± 12.28	41.27 ± 10.24	28.77 ± 3.51
T_{1m} [ms]	44.61 ± 12.45	43.04 ± 10.42	33.89 ± 6.92
A_{1s} [%]	5.45 ± 1.66	6.19 ± 1.50	38.64 ± 13.20
A_{1f} [%]	94.17 ± 1.69	93.33 ± 1.53	60.29 ± 13.24
TQ/SQ [%]	2.93 ± 0.42	3.42 ± 0.39	17.05 ± 3.62

Tab. 4.6.: Comparison of the fit parameters using the IRTQTPPI sequence using the different phase cycles PC0, PC1, PC2 and PC3 at 9.4 T. The SQ amplitudes A_{1s} and A_{1f} were bound to their theoretical values of 0.8 and 0.2, respectively.

Agar		2%	4%	6%
PC0	T_{1s} [ms]	49.44 ± 0.96	43.79 ± 1.18	37.50 ± 1.70
	T_{1f} [ms]	29.92 ± 0.31	25.67 ± 0.37	23.94 ± 0.50
	T_{1m} [ms]	43.78 ± 0.62	38.65 ± 0.75	34.00 ± 1.13
	TQ/SQ [%]	3.14 ± 0.53	5.77 ± 0.87	11.78 ± 2.37
PC1	T_{1s} [ms]	49.55 ± 0.90	43.62 ± 1.22	37.51 ± 1.66
	T_{1f} [ms]	30.19 ± 0.29	26.32 ± 0.38	23.75 ± 0.49
	T_{1m} [ms]	44.18 ± 0.59	38.92 ± 0.79	34.02 ± 1.10
	TQ/SQ [%]	3.09 ± 0.50	6.00 ± 0.93	11.47 ± 2.25
PC2	T_{1s} [ms]	49.22 ± 0.73	43.92 ± 0.98	37.92 ± 0.90
	T_{1f} [ms]	30.87 ± 0.23	25.65 ± 0.31	22.90 ± 0.27
	T_{1m} [ms]	44.10 ± 0.48	38.73 ± 0.62	33.91 ± 0.58
	TQ/SQ [%]	5.32 ± 0.48	8.67 ± 0.89	15.87 ± 1.50
PC3	T_{1s} [ms]	49.21 ± 0.81	43.78 ± 0.98	37.78 ± 0.86
	T_{1f} [ms]	30.87 ± 0.26	25.83 ± 0.31	23.09 ± 0.26
	T_{1m} [ms]	$44.12 \pm .53$	38.76 ± 0.63	33.89 ± 0.56
	TQ/SQ [%]	5.34 ± 0.53	8.84 ± 0.91	15.86 ± 1.45

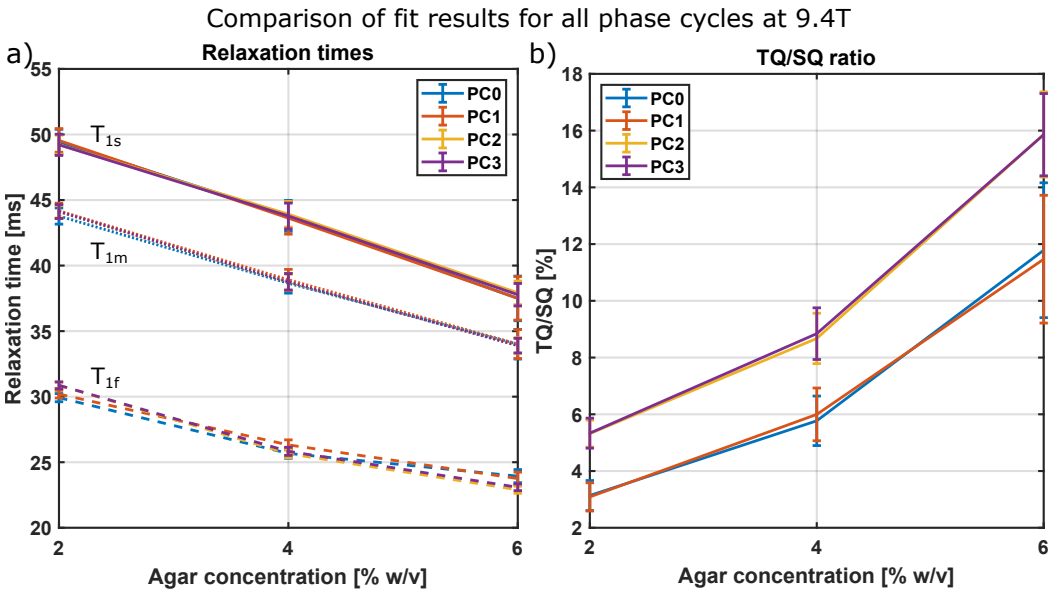

Fig. 4.10.: Comparison of fit parameters a) the T_1 relaxation times and b) the T_1-TQ/SQ ratios for all phase cycles using IRTQTPPI pulse sequence at 9.4 T. The relaxation times T_{1s}, T_{1f} and T_{1m} were in close agreement for all phase cycles. The T_1-TQ/SQ ratios of phase cycle PC0 and PC1 were in close agreement as well as the ratios between PC2 and PC3. However, there was a substantial difference between these two pairs.

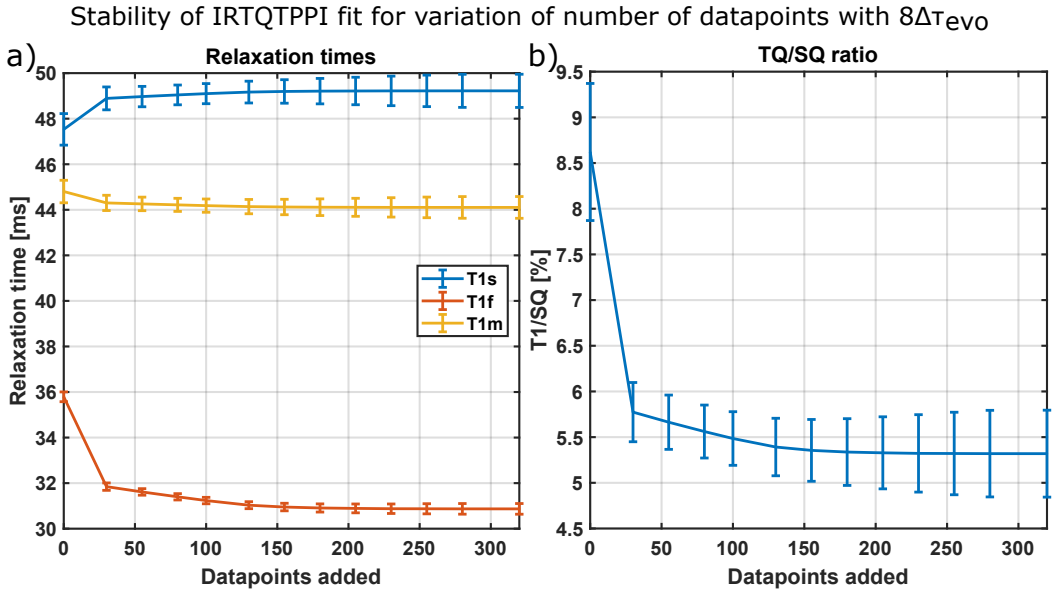

Fig. 4.11.: Dependence of a) the relaxation times and b) the T_1-TQ/SQ ratio on the datapoints with an evolution time step of $8\Delta\tau_{evo}$ for the 2 % agar sample using IRTQTPPI with phase cycle PC2 at 9.4 T. All fit parameters converged to stable values after approximately 100-200 data points. Comparable results were observed for the other agarose samples.

for T_1 and 37-40 ms for T_2. In general, the uncertainties for the T_1 relaxation times were larger.

The T_1-TQ/SQ ratio was smaller than the T_2-TQ/SQ ratio. Both the T_1- and T_2-TQ/SQ ratio increased almost linearly with concentration with almost the same slope.

Increasing the magnetic field strength from 9.4 T to 21.1 T led to increasing T_1 and T_2 relaxation times for all samples. Yet, both the T_1-TQ and T_2-TQ signals decreased despite larger T_1 and T_2 splitting.

Figure 4.13 shows the correlation times τ_c and quadrupole strength parameters ω_Q calculated using the T_1 and T_2 relaxation times of 9.4 T and 21.1 T. ω_Q was larger at 21.1 T and slightly increasing for increasing agar concentration. The slope was steeper for the quadrupole strength parameters calculated with the T_2 relaxation times. The correlation time was almost constant with increasing agar concentration for the T_1 parameters. In contrast, the correlation time was increasing with agar concentration for the T_2 parameters. The τ_c was larger at 9.4 T than 21.1 T, while ω_Q was larger at 21.1 T compared to 9.4 T.

4.3.3 Improved Data Evaluation

This section presents the results of the IRTQTPPI sequence using an improved data evaluation. The number of fit parameters was minimized by setting the TQ amplitude A_{TQ} to its theoretical value.

First, similar to the results presented in the previous section, the four phase cycles were compared. Figure 4.14 shows that the fit results of all phase cycles were in good agreement between each other. Only the TQ/SQ ratios of the different phase cycles were slightly deviating from each other for the 2 % agar sample. In general, the TQ/SQ ratio was larger and the difference in T_1 relaxation times was smaller compared to the previous data evaluation method. Especially T_{1f} was substantially larger.

Furthermore, the results were compared to fit results for the IRTQTPPI sequence with a fixed τ_{evo} to evaluate which evaluation method produces more accurate results. Table 4.7 shows a good agreement within the uncertainties between the standard and the fixed sequence. The fit uncertainties were much larger for the fixed sequence as compared to the standard sequence, especially for the TQ/SQ ratio.

Figure 4.15 shows the T_1 and T_2 relaxation times and TQ/SQ ratios at 9.4 T and 21.1 T. As compared to the previous data evaluation method, the T_{1s}, T_{1m}, T_{1m} and T_{2s} relaxation times were much closer. The difference between T_{1s} and T_{1f} was only in the range of 5-8 ms at 9.4 T and 3-7 ms at 21.1 T as compared to 15-21 ms for the previous data evaluation. In contrast, the TQ/SQ ratio substantially increased and was only slightly smaller than the T_2 TQ signal.

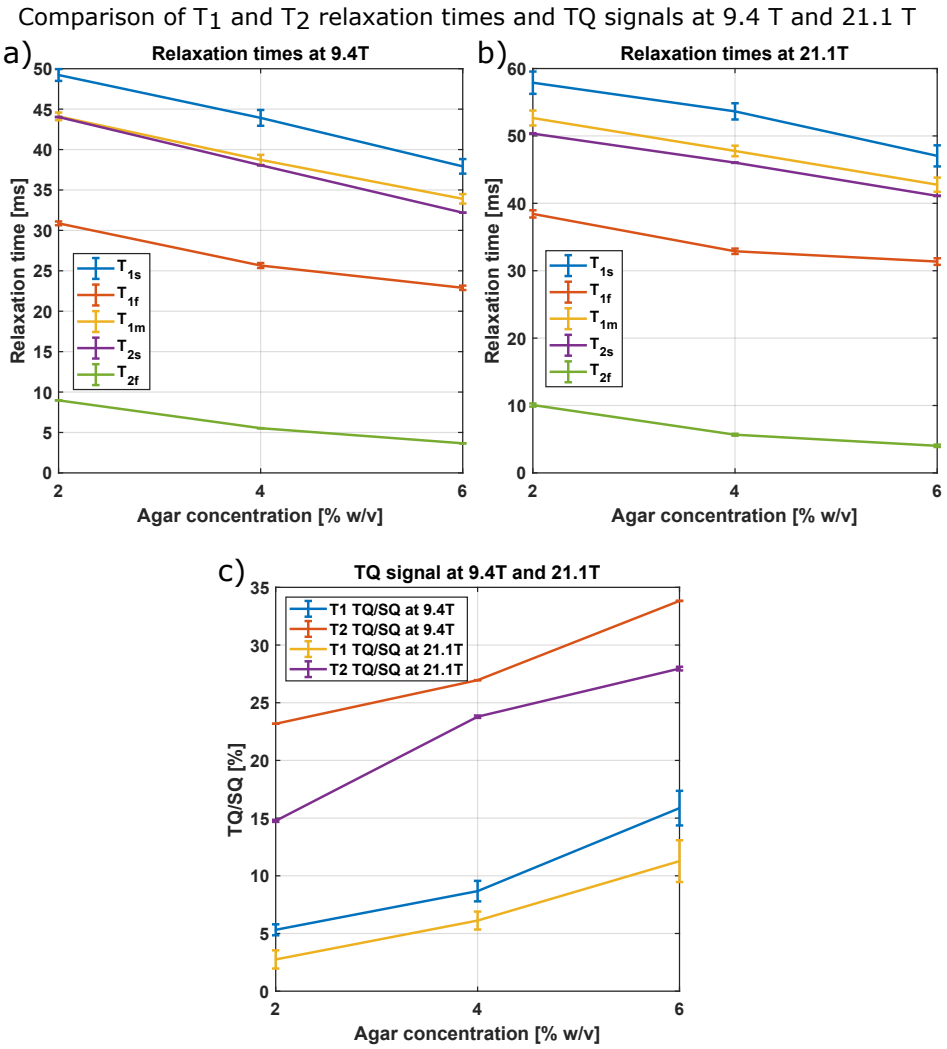

Fig. 4.12.: Comparison of sodium TQ/SQ and T_1, T_2 relaxation times for the IRTQTPPI and TQTPPI pulse sequences at 9.4 T and 21.1 T. At both magnetic field strengths, all agarose samples yielded a T_1-TQ signal and bi-exponential T_1 relaxation times. As expected form theory, the T_2 pathway yielded a larger TQ signal and faster bi-exponential relaxation than T_1 pathway. The TQ signals of both pathways were smaller at higher magnetic field strength.

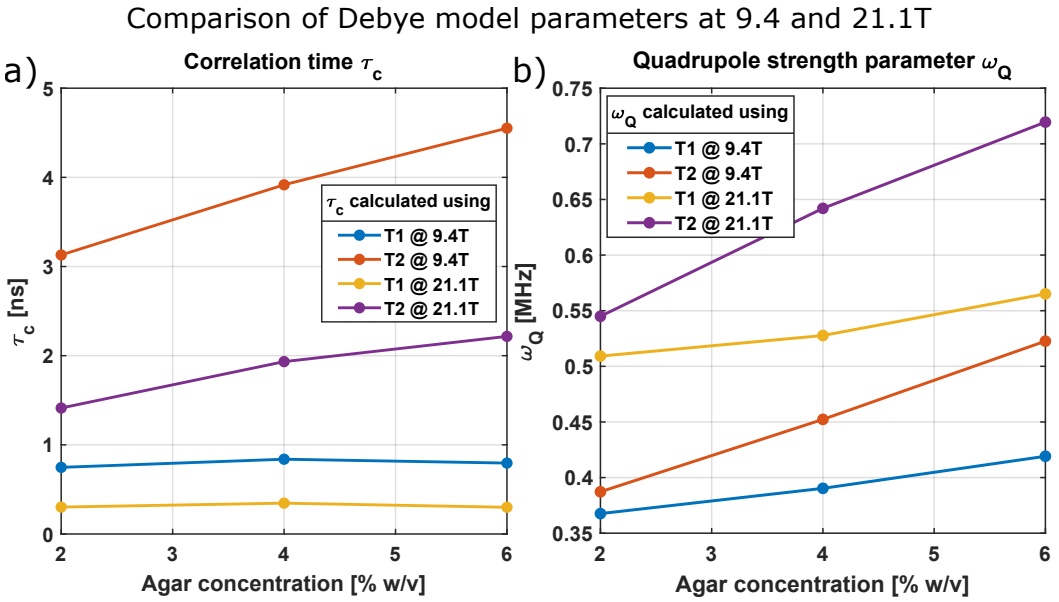

Fig. 4.13.: Comparison of the correlation time τ_c and the quadrupole interaction strength ω_Q calculated from T_1 and T_2 relaxation times measured at 9.4 T and 21.1 T according to Equation (2.88) and Equation (2.95).

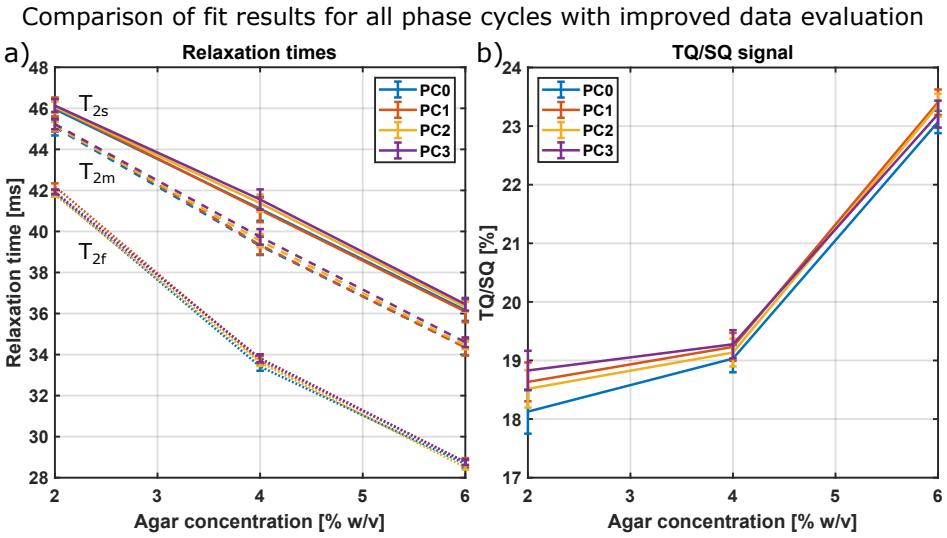

Fig. 4.14.: Comparison of fit results of all IRTQTPPI phase cycles using an improved data evaluation.

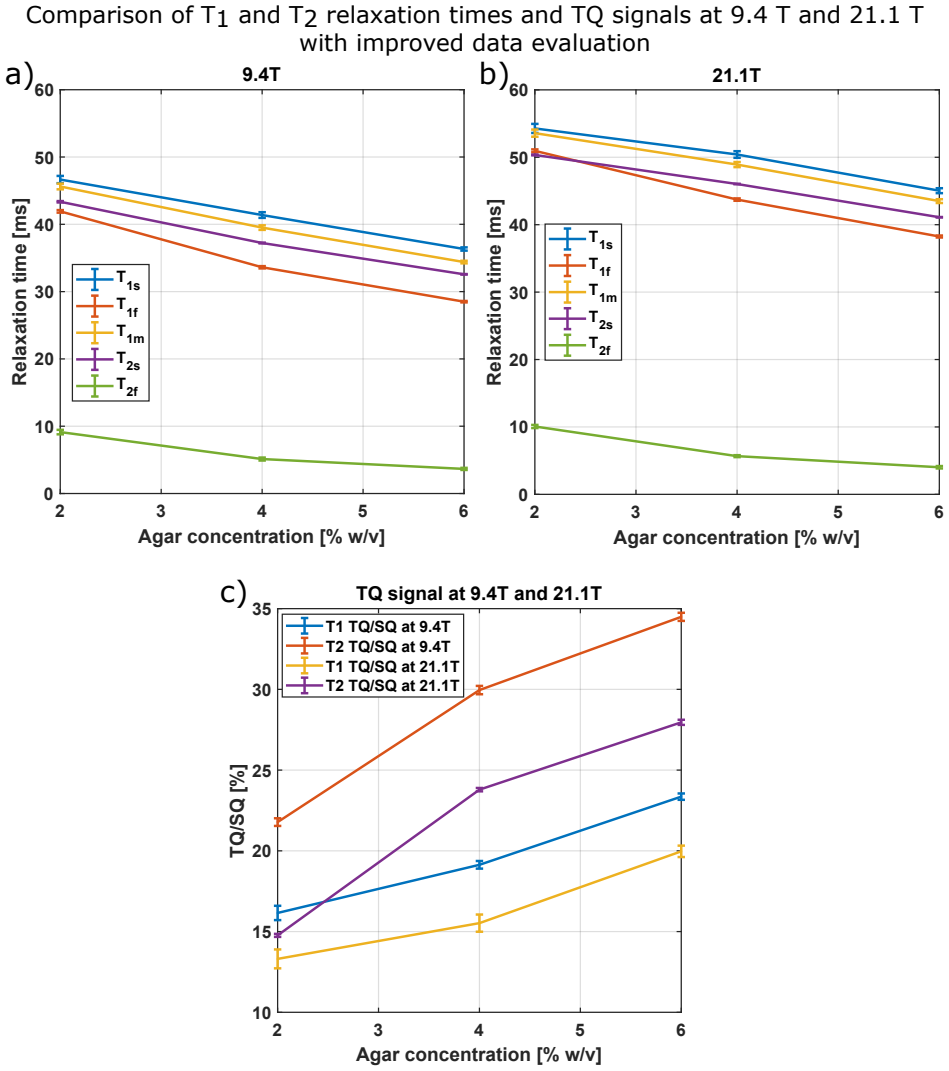

Fig. 4.15.: Comparison of T_1 and T_2 relaxation times and TQ signal at 9.4 T and 21.1 T for the data evaluation with A_{TQ} fixed to its expected value. The T_1 relaxation times were closer and the T_1-TQ signals were larger than for the previous data evaluation where A_{TQ} was a fit parameter.

Tab. 4.7.: Comparison of the fit results of the standard and the fixed IRTQTPPI sequences. All parameters were in agreement within the uncertainties. The uncertainties of the fixed sequence were large in comparison to the standard sequence.

	Sequence	2 % agar	4 % agar	6 % agar
T_{1s} [ms]	**standard**	46.05 ± 0.26	41.38 ± 0.42	36.33 ± 0.24
	fixed	46.68 ± 0.89	40.28 ± 0.67	36.04 ± 0.38
T_{1f} [ms]	**standard**	41.79 ± 0.10	33.62 ± 0.17	28.50 ± 0.11
	fixed	42.75 ± 3.22	35.60 ± 2.34	29.73 ± 1.27
T_{1m} [ms]	**standard**	45.13 ± 0.21	39.55 ± 0.32	34.44 ± 0.18
	fixed	45.84 ± 0.07	39.25 ± 0.06	34.57 ± 0.04
TQ/SQ [%]	**standard**	18.52 ± 0.32	19.13 ± 0.24	23.36 ± 0.20
	fixed	19.90 ± 21.61	31.52 ± 21.17	29.29 ± 8.18

4.4 Single-Pulse TQ method

4.4.1 Comparison of the SP TQ Signal with Theory and TQTPPI Sequence

A comparison of the TQ signal determined by the SP method and the theoretical transfer functions $f_{13}^{(1)}(\tau_{\text{evo}})$ for all samples is presented in Figure 4.16. Relaxation times for $f_{13}^{(1)}(\tau_{\text{evo}})$ were determined by a bi-exponential fit of the single-pulse FID as summarized in Table 4.8. For the 2 %, 4 % and 6 % agar samples, the maximum TQ signals and the shape of the TQ signal relaxation of the SP method were in close agreement with the theoretical curve. The maximum TQ signals are summarized in Table 4.9. The single-pulse and theoretical FIDs, i.e. the normalized $f_{13}^{(1)}(\tau_{\text{evo}})$ curves using Equation (3.25), had the same relaxation times by design. However, the amplitudes of the experimental FIDs deviated from the theoretical values of 0.6 for the fast and 0.4 for the slow component especially for the 4 % agar sample. The extracted TQ signal for the 0 % agar sample was non-zero for the SP method despite the theoretically expected zero TQ signal and a mono-exponential T_2 relaxation. In this case, also the shape of the TQ evolution strongly deviated from the expected build-up behavior.

Figure 4.17 compares the SP method with the TQTPPI pulse sequence. For both methods, the maxima of the TQ evolution curves approximately coincided for the 2 %, 4 % and 6 % agar samples. For the 0 % agar sample, the TQTPPI TQ signal was approximately zero while in the SP method the TQ signal was non-vanishing. The relaxation times of both the SQ and TQ signals deviated substantially as the SP FID decayed with the T_2^* relaxation times while the TQTPPI FID decayed with the T_2

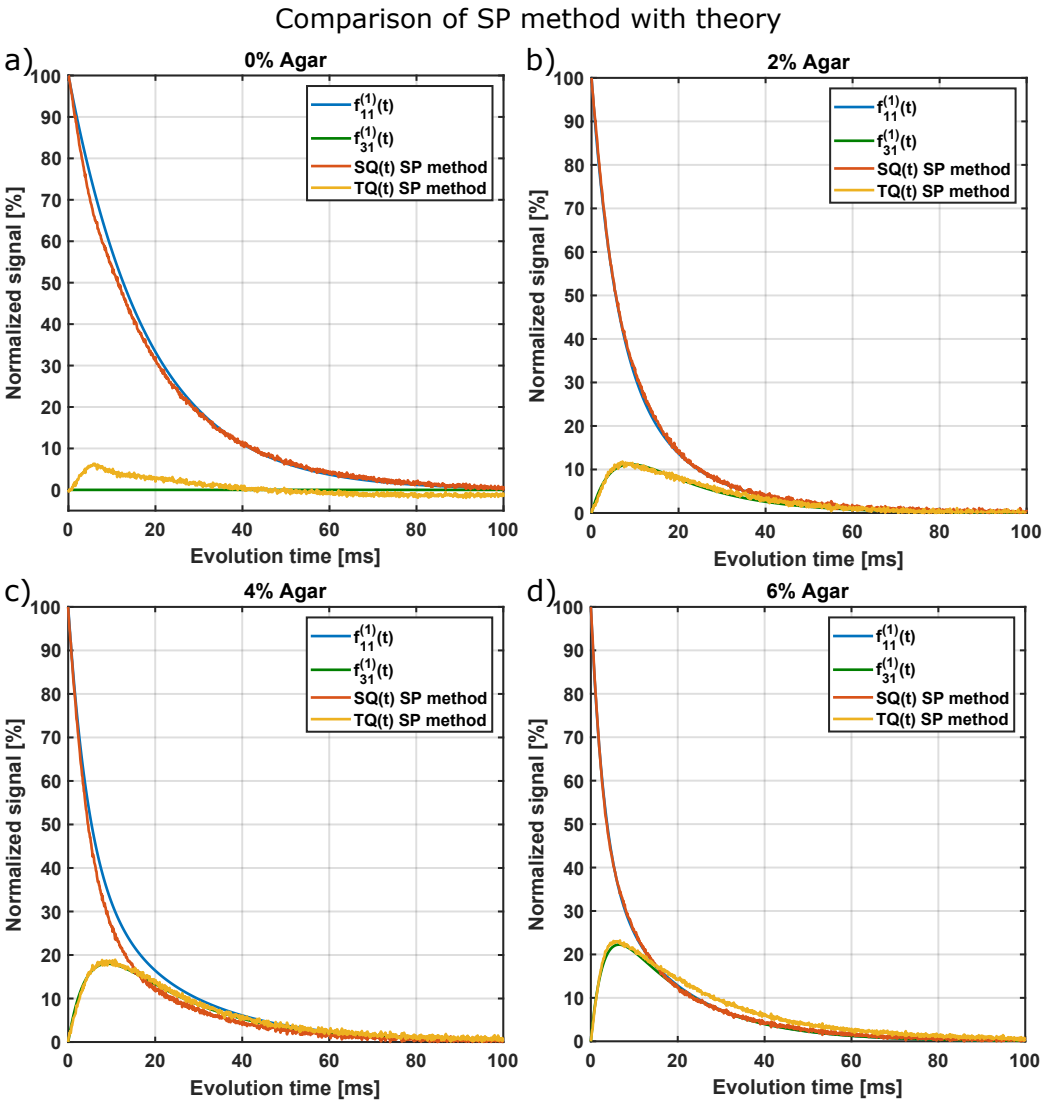

Fig. 4.16.: Comparison of the TQ signal from SP method and the normalized theoretical transfer function $f_{31}^{(1)}(\tau_{\mathrm{evo}})$ for (a) 0 %, (b) 2 %, (c) 4 %, and (d) 6 % agar samples. The relaxation times for the theoretical curve were determined by a bi-exponential fit of the single-pulse Free Induction Decay (FID). The TQ signals were in close agreement with theory for all samples except for the 0 % agar sample, where a non-zero TQ signal was extracted.

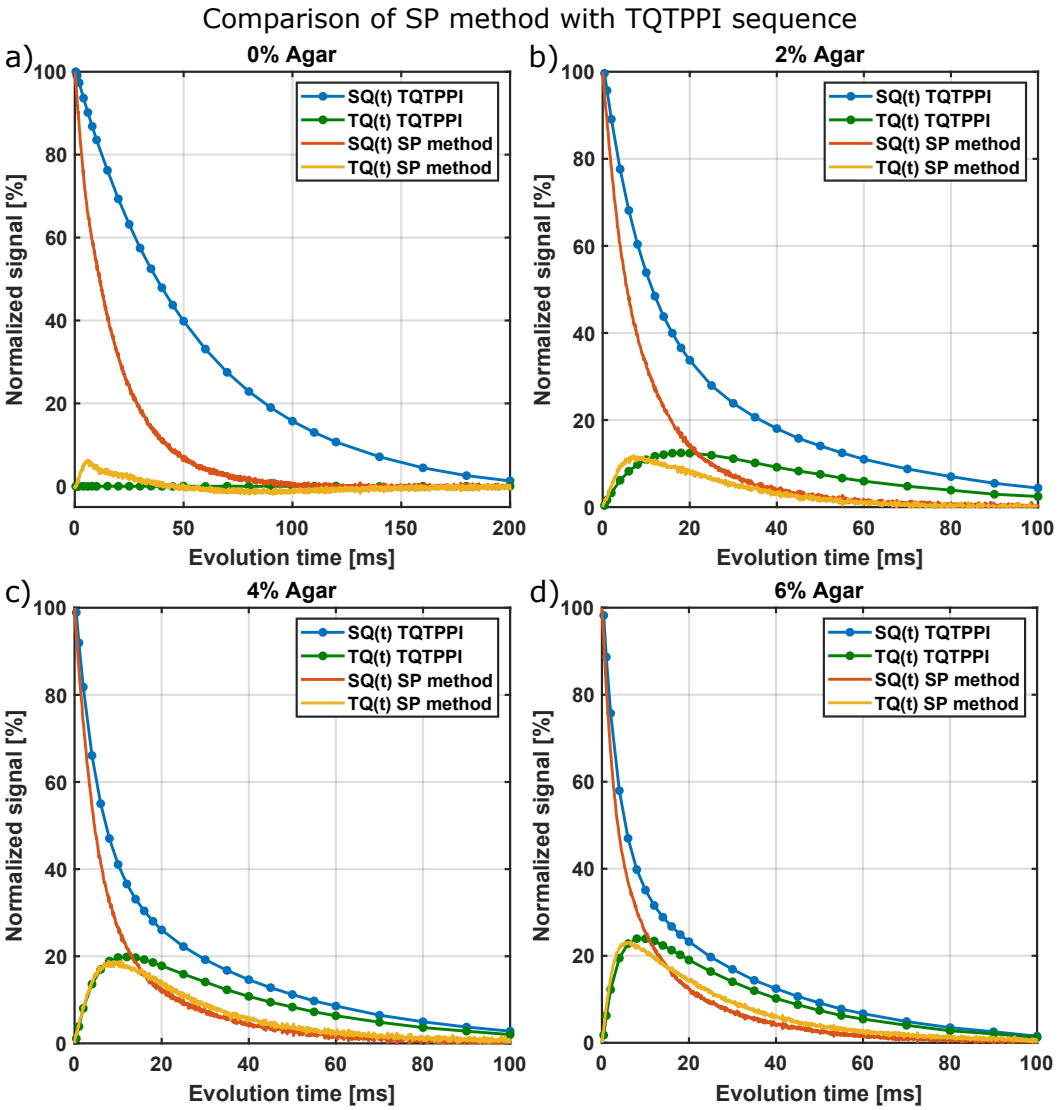

Fig. 4.17.: Comparison of the SP TQ signal and the TQTPPI sequence with 180° pulse for agar samples with (a) 0 %, (b) 2 %, (c) 4 % and (d) 6 % agar. Since the single-pulse FID decays with T_2^* and the TQTPPI FID with T_2, the SP extracted TQ signal decayed much faster.

Tab. 4.8.: Summary of the fit results for T_2^* and T_2 relaxation times and the amplitudes of the slow and fast component for all agar samples. The 2 %, 4 % and 6 % agar sample FIDs were fitted using a bi-exponential fit function and the 0 % agar sample using a mono-exponential fit function.

Fit results: Relaxation times and amplitudes				
Agar concentration	**0%**	**2%**	**4%**	**6%**
T_{2s}^* **[ms]**	19.00 ± 0.09	16.89 ± 0.24	21.26 ± 0.28	17.48 ± 0.13
T_{2f}^* **[ms]**	-	5.35 ± 0.09	4.65 ± 0.45	3.07 ± 0.32
A_s^*	-	0.42 ± 0.01	0.29 ± 0.01	0.40 ± 0.01
A_f^*	-	0.58 ± 0.01	0.72 ± 0.01	0.60 ± 0.01
T_{2s} **[ms]**	54.19 ± 0.95	45.03 ± 1.46	39.17 ± 0.73	33.05 ± 0.47
T_{2f} **[ms]**	-	9.04 ± 0.13	5.12 ± 0.06	3.54 ± 0.04
A_s	-	0.43 ± 0.01	0.42 ± 0.01	0.43 ± 0.01
A_f	-	0.61 ± 0.01	0.62 ± 0.01	0.63 ± 0.01

relaxation times. The maximum TQ values and relaxation times for all samples and methods are summarized in Table 4.8 and Table 4.9.

Figure 4.18 compares the TQ signal determined with the SE FID, the TQTPPI sequence and the theoretical prediction. For all samples, including the 0 % agar sample, the SE and TQTPPI TQ signals were in close agreement with each other and the theoretical prediction. Furthermore, as shown in Table 4.9, the maximum TQ values were in close agreement except for the 4 % agar sample, where the SE maximum TQ signal was larger than for the other two methods. This was caused by a peak close to the maximum of the TQ curve resulting from noise or a small artifact.

4.4.2 Simulations

For estimation of the accuracy of the proposed SP method, a two-compartment model was investigated using relaxation times from our results of the 2 % and the 6 % agar samples. We varied the size of the compartments, c_{ex}, in the range of 0 to 1. Figure 4.19 shows a comparison of the theoretically expected TQ signal with the TQ signal determined by the SP method for both models with varying values of c_{ex}. Furthermore, the FID and TQ signal are shown for the c_{ex} parameter with the strongest deviation between the SP TQ signal and the expected TQ signal. The theoretically expected TQ signal was determined by the weighted sum of the TQ signals of both compartments. The SP TQ signal and expected TQ signal were in close agreement with a maximum deviation of 2.5 %.

Tab. 4.9.: Summary of the sodium TQ/SQ signals for all methods and samples. Additionally, the maximum TQ signal from the TQTPPI sequence without the 180° refocusing pulse and the mean over the maximum TQ signals over a single slice for each sample of the imaging phantom are listed. For the comparison with the Spin Echo (SE) sequence, the SE TQ and the TQTPPI TQ signals were normalized using the T_2 and T_2^* relaxation times, respectively. The theoretical TQ signal was unnormalized.

	Maximum TQ signal [%]			
Agar concentration	**0%**	**2%**	**4%**	**6%**
SP method	6.04 ± 0.09	11.31 ± 0.34	18.25 ± 0.30	22.67 ± 0.30
Theory	0.00 ± 0.00*	11.16 ± 0.00	18.00 ± 0.00	22.25 ± 0.00
TQTPPI	0.04 ± 0.02*	12.46 ± 0.07*	19.84 ± 0.14*	23.93 ± 0.26*
TQTPPI wo/180	0.12 ± 0.04*	12.53 ± 0.18*	19.71 ± 0.24*	23.88 ± 0.16*
Imaging	7.31 ± 3.48	13.40 ± 3.65	17.55 ± 3.77	19.77 ± 4.97
Spin echo (normalized)	0.45 ± 0.60	24.51 ± 0.65	31.05 ± 1.52	32.14 ± 0.73
Theory (unnormalized)	0.00 ± 0.00	25.68 ± 0.00	30.98 ± 0.00	32.89 ± 0.00
TQTPPI (normalized)	0.08 ± 0.04	23.15 ± 0.23	29.94 ± 0.32	34.48 ± 0.46*

* statistically significant deviation from SP method/Spin echo (normalized)

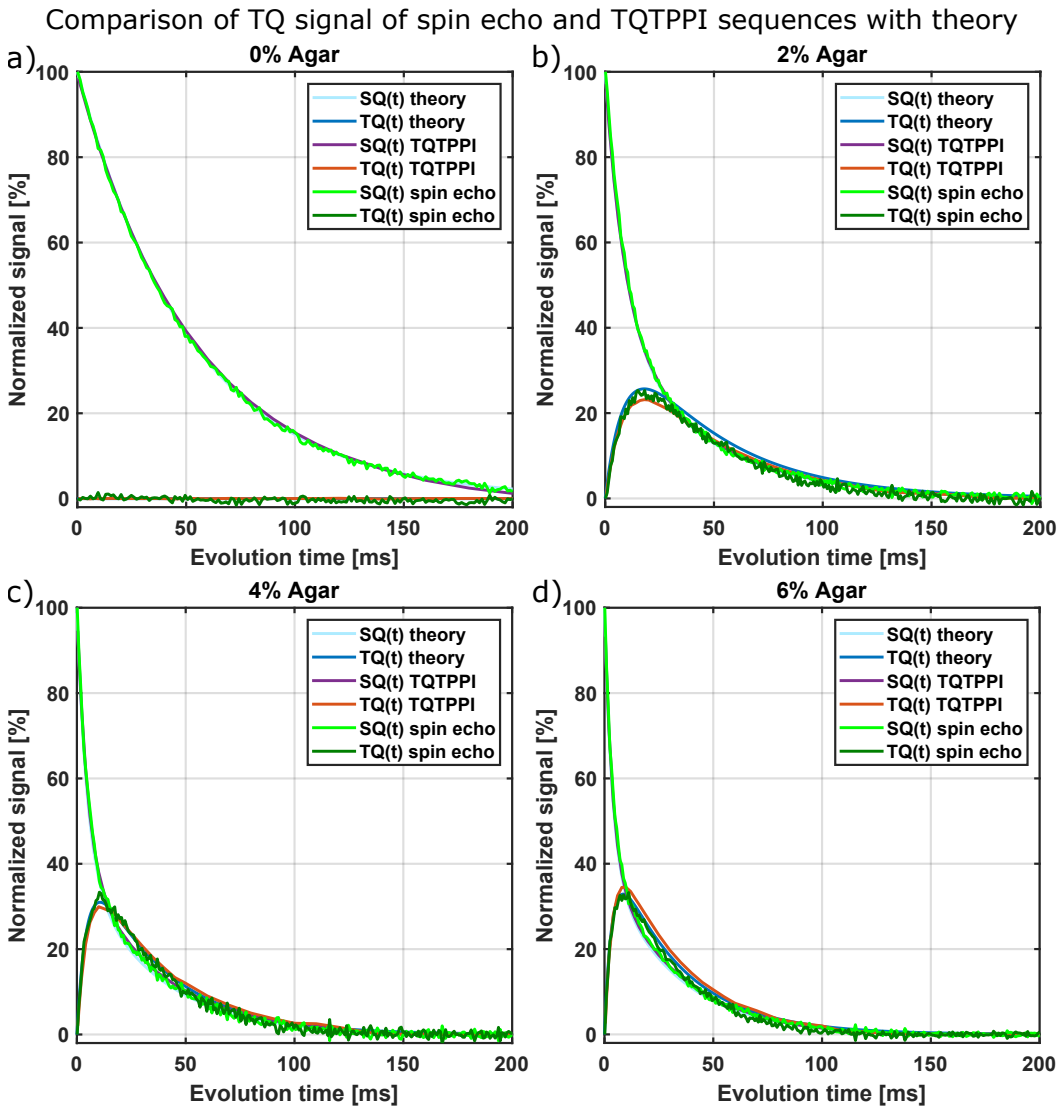

Fig. 4.18.: Comparison of the TQ signal of the SE sequence, TQTPPI sequence with 180° pulse and the unnormalized theoretical transfer function $f_{31}^{(1)}(\tau_{\mathrm{evo}})$ for (a) 0 %, (b) 2 %, (c) 4 %, and (d) 6 % agar samples. The TQ signals of all methods were in very close agreement. The SE TQ signal of the 4 % agar sample showed an additional increase in the TQ signal around the maximum, which might be an artifact or noise.

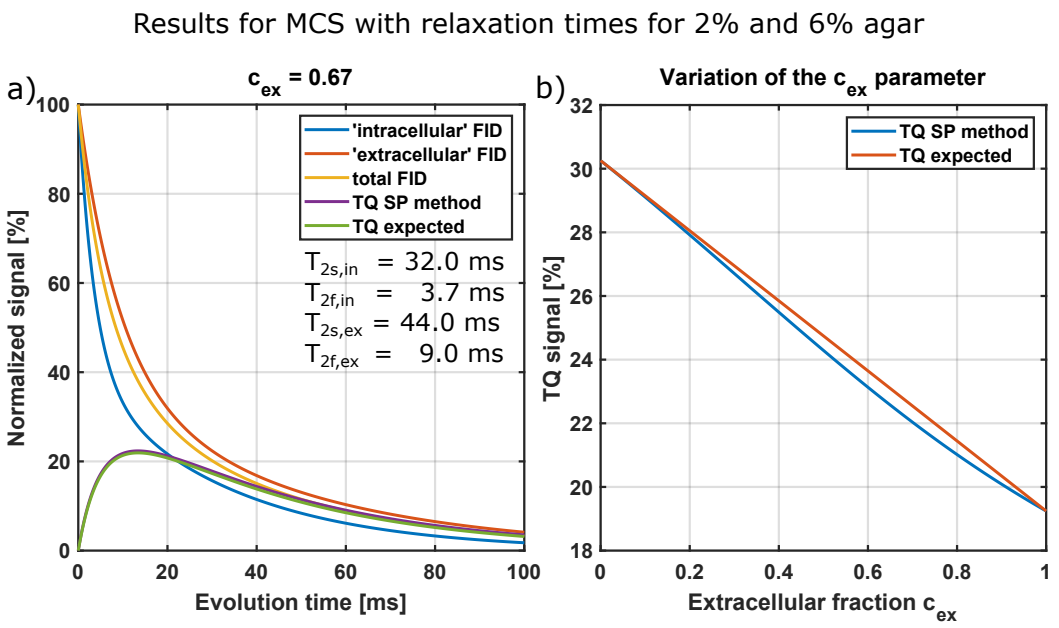

Fig. 4.19.: Comparison of the TQ signals extracted from the SP method with the expected TQ signal for simulated FIDs of a multi-compartment system with two bi-exponential compartments. The fraction of the "extracellular" compartment c_{ex} with smaller difference between T_{2f} and T_{2s} was varied. a) shows the SQ and TQ signals for the c_{ex} value with the maximum deviation of the TQ maximum between the SP method TQ signal and the expected TQ signal. b) shows the maximum SP method and expected TQ signals in dependence of c_{ex}. The SP method was in close agreement with the expected TQ signal for all c_{ex} values with a maximum deviation of 2.5 %.

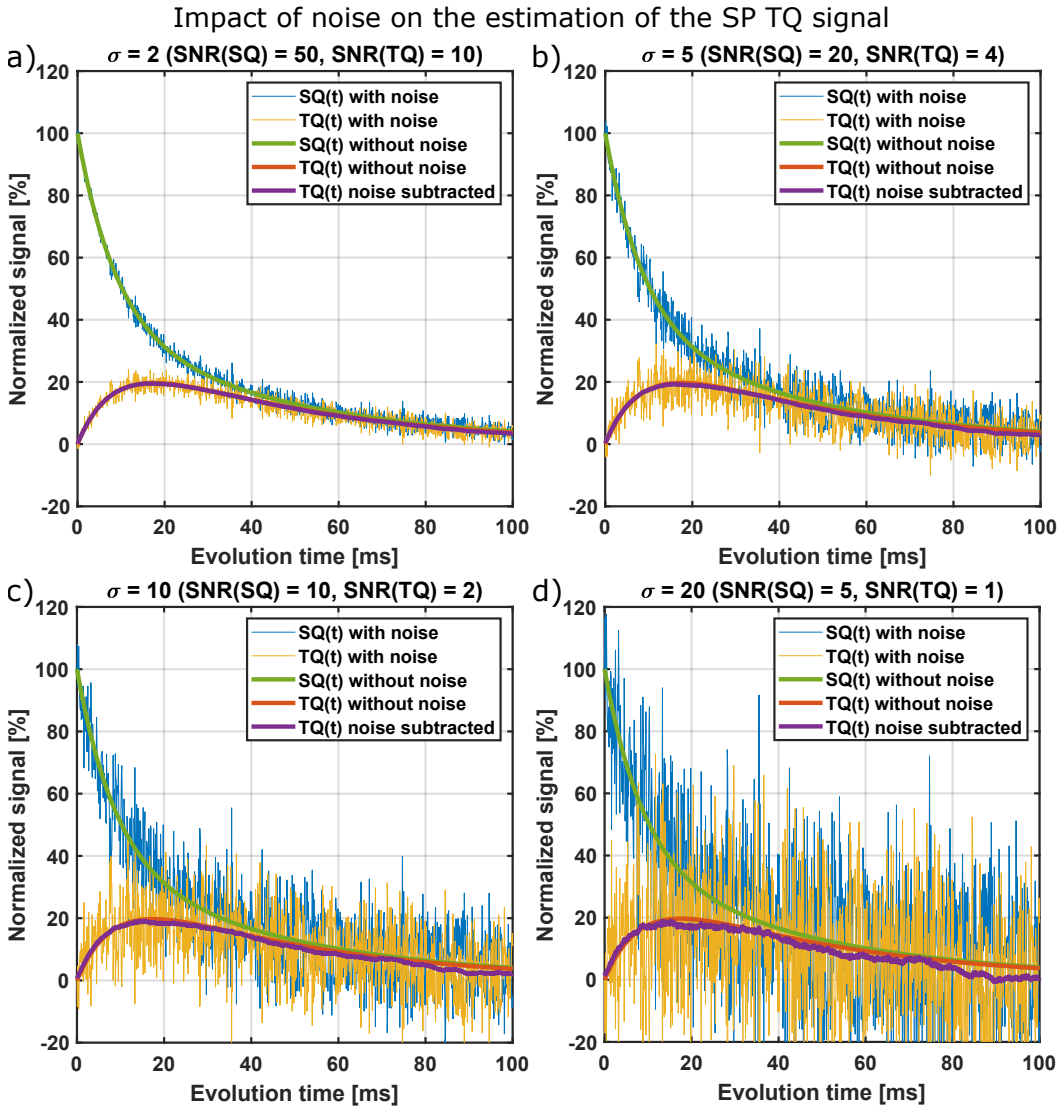

Fig. 4.20.: Comparison of the impact of different noise levels on the accuracy of the extracted TQ signal determined with the SP method. The TQ signal without noise is shown in red. The purple curve shows the SP TQ signal of the noisy FID with the same noise subtracted subsequently. This curve shows the systematic error of the SP method. Even for high noise levels, i.e. SQ SNR=5, the systematic error on the TQ signal was small for evolution times in the range of the maximum TQ signal. The typical SNR level in in-vivo Magnetic Resonance Imaging (MRI) scans is larger or equal to Nagel et al. [84] and Blunck et al. [136].

Figure 4.20 compares the FIDs and TQ curves with and without noise for different noise levels. Additionally, the noise was subtracted from the TQ signal subsequently to applying the SP method. Up to a SQ SNR of 10 corresponding to a TQ SNR of 2, the noise subtracted TQ signal was in close agreement to the TQ signal without noise. The latter can be considered as the ground truth. Even for a SQ SNR of 5 (TQ SNR of 1), the TQ signal only deviated substantially for larger τ_{evo}.

4.4.3 MR Imaging

Combination of a multi-echo version of the Ultra-Short Echo Time (UTE) sequence and the SP method provided a voxelwise extraction of SQ(t) and TQ(t) relaxation curves for different τ_{evo}. From this data, a SQ image ($\tau_{evo} = 0$), maximum TQ and sum TQ images were created. Figure 4.21 shows the SQ, maximum and sum TQ signal images for a sample consisting of agar concentrations of 0 %, 2 %, 4 % and 6 % with 154 mM NaCl. For voxels outside the samples, the noise led to random TQ/SQ values and consequently values outside the sample were set to 0.

The TQ signal was increasing with agar concentration as demonstrated in Table 4.9 for the average maximum TQ signal over one slice for each sample. All voxels, including the edge voxels, were weighted equally. The average value of the maximum TQ signal for the 4 % and 6 % agar samples were smaller than the values of the other methods. Contrary, the 0 % and 2 % agar values were slightly larger compared to the values of the other methods. The uncertainties of the TQ signals were much larger as compared to the single-pulse sequence and the relative deviations were in the range of 20 % to 30 % except for the 0 % agar sample where it was around 50 %. The relative standard deviation of the SQ image voxels was in the range of 9 % to 17 %. Similar to the previous spectroscopic Nuclear Magnetic Resonance (NMR) measurements, the maximum TQ signal in the Magnetic Resonance (MR) image was also non-zero for the 0 % agar sample. However, in the sum TQ image, the signal of the 0 % agar sample was mostly negative or close to 0.

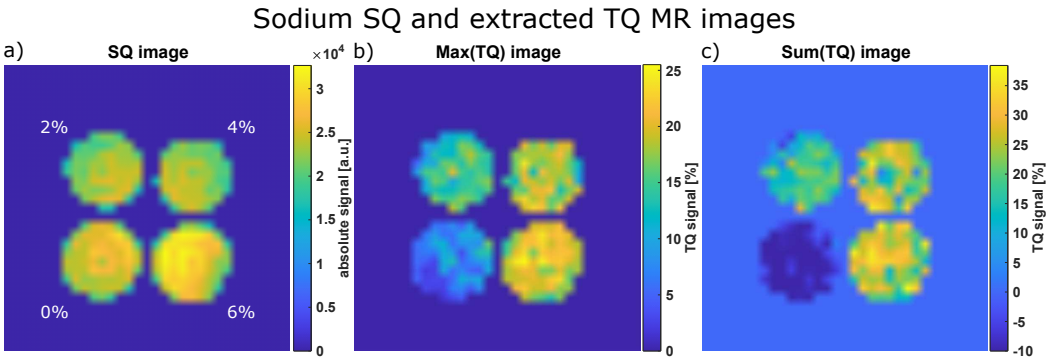

Fig. 4.21.: Sodium SQ and extracted TQ MR images from the agarose samples. (a) SQ signal using minimum τ_{evo}. (b) Maximum of the extracted TQ signal. The extracted TQ signal was increasing with agar concentration. The 0 % agar sample yielded a non-zero TQ signal as demonstrated on Figure 4.16 and Figure 4.17. (c) Sum of the extracted TQ signal normalized by the sum of the SQ signal. For the 0 % agar sample, the sum of the extracted TQ signals was negative, which resulted from the untypical extracted TQ evolution curve. The color bar range was limited to −10 % to increase visibility.

5 Discussion

The main aims of this thesis were to investigate the molecular origin of the sodium Triple Quantum (TQ) signal using suitable model systems and advanced acquisition methods and to accelerate the acquisition of the sodium TQ signal for clinical applications.

Slow modulations of the electric field gradient of sodium nuclei caused by interactions with surrounding environment yield a sodium TQ signal. These interactions occur during interactions of sodium ions with macromolecules like proteins. Since proteins are much more abundant inside cells than outside [44], the sodium TQ signal is intrinsically selective towards the intracellular space with a contribution of approximately 30-70 % to the overall TQ signal [15–21, 140]. Increases of the TQ signal are closely connected to a reduced cell viability, as demonstrated in experiments with perfused rat heart systems [15, 19, 20, 33–35], brain ischemia in non-human primates [36], tumors [37, 140] and a MR compatible bioreactor system [39, 41, 42]. However, to understand the influence of cellular processes on the TQ signal a deeper understanding of the TQ signal on a molecular and cellular level is necessary.

Therefore, one aim of this thesis is to deepen the understanding of the molecular origin of the TQ signal combined with advanced acquisition methods in a preclinical setting. This aim was achieved in three steps.

Sodium Nuclear Magnetic Resonance (NMR) dynamics are complicated especially during sophisticated phase cycles of multi-quantum sequences, e.g., the Triple Quantum Time Proportional Phase Increment (TQTPPI) and Inversion Recovery Triple Quantum Time Proportional Phase Increment (IRTQTPPI) sequences. Therefore, as a first step of this thesis a simulation framework of spin-3/2 NMR dynamics was implemented. Section 5.1 discusses the results of the comparison of this simulation framework with experimental data. The framework is particularly useful to investigate the contribution of each coherence pathway to the overall signal of the sequence. Furthermore, it allows the optimization of sequence parameters and predict the influence of different NMR parameters on the TQ signal.

Previous studies of the TQ signal of proteins investigated only the protein Bovine Serum Albumin (BSA). To advance our understanding of the TQ signal of proteins, this study investigated the TQ signals of various globular proteins as a second step. Section 5.2 discusses the the results and the validity of the TQ results of BSA for various globular proteins. Especially the size and sodium binding affinity were expected to influence the TQ signal.

For an improved characterization of the sodium molecular environment, not only the mainly investigated T_2 pathway of the TQ signal is of interest but also the T_1 pathway. This T_1 pathway has an unique sensitivity to intermediate interactions. Therefore, in a third step, this thesis introduced the IRTQTPPI sequence to investigate the T_1 pathway to create TQ coherences with a unique sensitivity to an intermediate motional regime. Section 5.3 discusses the results regarding the IRTQTPPI sequence with different phase cycles and compares the T_1- and T_2-TQ signals and relaxation times at 9.4 T and 21.1 T.

Moreover, phase cycling sequences combined with multiple radio-frequency (RF) pulses result in a long scan time and a large Specific Absorption Rate (SAR). This hinders a potential translation of preclinical sodium TQ signal research to clinical applications. Therefore, the second aim of this thesis was to reduce the scan time and SAR of TQ acquisition. A novel way to acquire the TQ signal using only a single excitation pulse sequence was proposed. This method substantially reduces scan time to a similar level as standard sodium Single Quantum (SQ) Magnetic Resonance Imaging (MRI) scans. Section 5.4 discusses the results of the comparison of this method with theoretical predictions and experimental data using the TQTPPI sequence.

Parts of this discussion have been submitted for publication in Reichert et al. [63, 64] or have been published as a conference paper in Reichert et al. [104–107].

5.1 Simulation and 2xDebye Model

The simulation framework allows to qualitatively investigate different phase cycle schemes and thus, enables to optimize the suppression of unwanted signal contributions. In the context of the IRTQTPPI sequence, it played a crucial role in fine-tuning Double Quantum (DQ) suppression. Unfortunately, due to the inability to isolate different pathways in the experiment, a direct comparison between experimental and simulation results was unattainable. Moreover, the simulation framework facilitates quantitative investigations into the impact of diverse sample and sequence parameters on the spin-3/2 NMR signal. The simulation output was compared to experimental data using the TQTPPI and IRTQTPPI sequences. Different motional models, the T1 Debye, T2 Debye and 2xDebye models were compared with each other and experimental data.

It was shown that the Debye model did not adequately describe sodium interactions in tissue and tissue model system. This was independent of the use of the T_1 or T_2 relaxation times. This is in accordance with the findings of others [6, 8, 9]. By design, the T_1 relaxation times of the T1 Debye model matched with the experimental T_1 relaxation times. However, the T_2 relaxation separation was much smaller than in the experiment. This resulted in a too small T_2-TQ signal and an almost vanishing T_1-TQ signal. Since the Zero Quantum (ZQ) signals were not detected by the coil, the signal of the sequences has to be transformed to detectable $\hat{T}_{1-1}$ and $\hat{T}_{3-1}$ coherences. Therefore, the IRTQTPPI signal also depends on the T_2 relaxation

times. The TQTPPI sequence signal on the other hand was almost independent of T_1 relaxation for sufficiently long repetition time ($T_R \sim 5T_1$). Consequently, the T2 Debye model simulation only slightly overestimated the TQ signal of the TQTPPI sequence.

Alternatives [6, 9, 78, 121] to the simple Debye model are often complicated and have many model parameters while there exist only four experimental parameters (T_{1s}, T_{1f}, T_{2s} and T_{2f}). Therefore, an extension of the Debye model was proposed, the 2xDebye model, which also takes interactions in the extreme narrowing regime into account. This is crucial since the majority of sodium interactions are in the extreme narrowing regime [9]. The 2xDebye model is designed to be in line with the experimental T_1 and T_2 relaxation times simultaneously. The simulated data using the 2xDebye model was in agreement with experimental data for both sequences. The TQ signal was only slightly overestimated by the simulation.

As Kleimaier [141] showed, the TQ signal in the TQTPPI sequence is negatively impacted by B_0 inhomogeneities despite the 180° refocusing pulse. Moreover, the TQ signal of the TQTPPI and IRTQTPPI sequences is sensitive to small changes in the flip angle θ with a dependence of $\sin^5(\theta)$ for TQ signal. The use of a refocusing pulse yields a more complicated flip angle dependence [130]. The simulation framework did not take B_0 and B_1 inhomogeneities into account, which might explain the small deviation between simulated and experimental TQ signals.

A full simulation of B_0 inhomogeneities requires a separate simulation of multiple spins or spin domains with individual B_0. This comes at a cost of a massive increase in computational cost. This functionality was added in an accompanying master thesis [142]. This work was especially important to fully simulate the signal of the TQTPPI sequence with and without a 180° refocusing pulse. The TQTPPI sequence without the 180° refocusing pulse is impacted by stimulated echos in experiments. Similarly, the simulation of B_1 inhomogeneities requires a separate simulation of multiple spins with individual flip angles according to a flip angle distribution. For both B_0 and B_1 inhomogeneities, diffusion of spins into another domain with different B_0 offsets and flip angles makes the problem even more complicated. Since the simulated and measured TQ signals were very similar for both sequences, B_0 inhomogeneities were only considered as described in Subsection 3.2.1. B_1 inhomogeneities were only considered with a constant flip angle offset where necessary. An example application case was the investigation of the different phase cycles of the IRTQTPPI sequence.

Licht et al. [139] extended the simulation framework for imaging. TThis enhancement opens possibilities for generating test data, thereby facilitating the refinement of TQ imaging sequences and reconstruction techniques. Notably, the extended framework also lends itself to straightforward adaptation for multi-compartment systems, offering a versatile tool for a broader range of applications.

5.2 Investigation of the TQ Signal of Globular Proteins

Previous studies of the TQ signal of proteins only investigated the large extracellular protein BSA [9, 43, 45, 46]. Since the size of the protein influences the correlation time, it is expected that the TQ signal depends on the protein size. Moreover, sodium affinity of the protein should influence the TQ signal. Therefore. the TQ signal of multiple different globular proteins was investigated to deepen the understanding of the origin of the TQ signal.

The TQ signal increased with the size of the protein excluding some exceptions. The increase was less than linear. The correlation time of the quadrupolar interaction is expected to be a combination of rotational (and diffusional) motion of macromolecules on the environment of the sodium ions, binding affinity of sodium to the macromolecules, diffusional motion of the sodium ions and others. The total correlation time $\tau_{c,\mathrm{tot}}$ is then given by [143]

$$\frac{1}{\tau_{c,\mathrm{tot}}} = \sum_i \frac{1}{\tau_{c,i}}, \tag{5.1}$$

where $\tau_{c,i}$ are the correlation times of the different influences. Thus, shorter correlation times dominate the total correlation time. Larger proteins rotate slower [143–145] and hence the TQ signal increases with protein size. The impact of the protein size becomes smaller with increasing size and the correlation time is dominated by binding affinity and diffusional motion of the sodium ions. The consequence is a dependence that is less than linear on the protein size. Note, that the sodium ion interactions with their environment are described by a distribution of correlation times [6, 8, 9] rather than a single correlation time. The sodium ions encounter fast fluctuations of the sodium hydration shell which are modulated by slower fluctuations occurring during interactions of the sodium ions with either negatively charged groups of the proteins or the hydration shell of the protein [6, 8, 43]. The correlation time in the discussion above can be considered as an effective correlation time. More accurately, the τ_c distribution shifts towards longer τ_c for larger proteins.

On the lower end of protein size, samples of proteins with sizes $\lesssim 18\,\mathrm{kDa}$ did not yield a TQ signal except for two proteins with strong sodium binding affinity. Most proteins are small which might indicate that only a few larger proteins and proteins with a high protein binding affinity contribute substantially to the overall in-vivo TQ signal. However, the intracellular protein concentration is in the range 20-30 % w/v [6, 44] and thus much larger than the protein concentration of 2 % w/w used in the experiments of this thesis. The larger protein concentration might increase viscosity and shift the rotational correlation time of the smaller proteins in the slow motion regime. Further investigations are necessary using higher concentrated protein mixtures or cell lysates. However, this also complicates the isolation of the influence of each protein to the total TQ signal.

More work is required with more realistic protein concentrations and mixtures, which makes it also more difficult to isolate the influence of different parameters

on the TQ signal. Also the contribution of the proteins of the mixture cannot be differentiated.

The samples of two of the smallest proteins, Ca depleted α-lactalbumin and β-lactoglobulin, yielded the strongest TQ signal of all proteins. While most proteins have a low sodium binding affinity, these two proteins showed strong sodium binding [8, 9, 47]. This indicates that sodium binding had a stronger effect on the TQ signal than protein size. Sodium binding also restricts the diffusional motion of the sodium ions and increases the corresponding correlation time in Equation (5.1). The rotational correlation time of the protein still needs to be long enough to be in the slow motion regime since shorter correlation times have a disproportional effect on Equation (5.1). This can be observed for the small molecule TmDOTP, which strongly binds five sodium ions [146] but does not yield a TQ signal [127, 128]. Since TmDOTP is also strongly paramagnetic [6, 127, 128], paramagnetic quenching might also reduce the TQ signal, nevertheless, mixtures of TmDOTP and agar yielded a strong TQ signal [127, 128].

Interestingly, the protein BSA has a weaker TQ signal than expected using the TQ protein size dependence. One might need to be careful with generalizations of results regarding the TQ signal using BSA as a model system. Advantages of using BSA are, that it is a well-characterized protein that is soluble at large concentrations and also easily available [43]. Therefore, it was used in many previous studies regarding the TQ signal of protein samples [9, 43, 45, 46].

For a direct comparison of BSA with a protein of similar size and sodium binding affinity [47], the protein methemoglobin was investigated. The main difference between the two proteins is, that methemoglobin is paramagnetic. Paramagentic substances usually decrease the TQ signal by paramagnetic quenching [22, 46, 140]. Yet, methemoglobin yielded the second strongest TQ signal. Samples of a diamagnetic ferrous hemoglobin form on the other hand yielded a much weaker TQ signal similar to the expected TQ signal for a protein of this size.

This raises the question if the paramagnetic nature of methemoglobin might had a positive influence on the TQ signal. Eliav et al. [127] and Ling and Jerschow [128] showed that the Curie spin interaction can yield a magic angle DQ signal for paramagnetic LnDOTP compounds. The influence of the Curie spin interaction on the TQ signal was not investigated. Paramagnetic forms of hemoglobin might also fulfill the conditions for the Curie spin interaction to apply [147, 148]. The electron longitudinal relaxation time T_{1e} of the paramagnetic centers was estimated to be around 1×10^{-11} s [147, 149]. This is much shorter than the sodium correlation time which is the range of ns as methemoglobin yields bi-exponential relaxation and thus the fluctuations are in the slow motion regime. The sodium nuclei then interact with the average magnetic moment of the electrons, i.e., the Curie spin [128]. In Eliav et al. [127] and Ling and Jerschow [128], the Magic Angle (MA)-DQ signal was created by a cross-correlation between the Curie-spin mechanism and the quadrupole interaction. This requires that the fluctuations of the Electric Field Gradient (EFG) are correlated with the fluctuations of the orientation of the axis between the sodium nucleus and the paramagetic center relative to the magnetic field B_0. This is the case for LnDOTP compounds since sodium ions are strongly

binding to LnDOTP [146]. However, sodium has a low binding affinity to hemoglobin and therefore the cross-correlated terms are expected to vanish and thus also the MA-DQ signal. This was also the result of the DQ measurement of the hemoglobin samples.

For the creation of a TQ signal, cross relaxation from $\hat{T}_{1\pm1}$ towards $\hat{T}_{3\pm1}$ is required. A similar equation as Equation (2.83) can be obtained for other Hamilton operators, e.g., for the Curie spin interaction. The allowed transitions are then given by the double-commutator relations of the Hamiltonian with the Irreducible Spherical Tensor Operator (ISTO) basis elements. As it turns out, cross relaxation $\hat{T}_{1\pm1} \rightarrow \hat{T}_{3\pm1}$ only occurs if the Hamiltonian has terms that are quadratic in the nuclear spin operators. The Curie spin interaction, and also other paramagnetic interactions, are only linear in the nuclear spin operators [71, 127, 128, 148]. Thus, cross relaxation towards $\hat{T}_{3\pm1}$ is not allowed and the interaction does not create a TQ signal. In contrast, paramagnetic interactions cause local susceptibility differences. The interactions can be treated similar to B_0 inhomogeneities and lead to paramagnetic quenching of the TQ signal [22, 46]. Only the quadrupole interaction consists of terms that are quadratic in the nuclear spin operators. Thus, the unusually large TQ signal of hemoglobin has to originate from an influence on the quadrupole interaction.

Sodium binding affinity to hemoglobin is low [47]. However, sodium might interact differently with the hydration shell of the protein. Latypova et al. [150] have shown that water mobility in the hemoglobin hydration shell depends strongly on the oxygenation state of the protein. This might explain the difference in TQ signal between the different hemoglobin forms in the experiment. Moreover, the ferrous hemoglobin forms were stabilized by ficoll, which also might influence the hydration shell of the protein. There is some evidence, that the first hydration shell of hemoglobin contains with ~ 1400 water molecules [151] substantially more water molecules than the BSA first hydration shell (~ 1100 water molecules) [152, 153]. Furthermore, at pH 7, i.e., a pH in the physiological relevant scale, ion mobility was lower for hemoglobin in comparison to hemoglobin [154], which indicates slower movement and thus longer correlation times for sodium ions in the vicinity of hemoglobin. Latypova et al. [151] showed that the hydration shells of hemoglobin molecules interact and neutralize surface charges of the protein. In combination with local susceptibility distortions that increase B_0 inhomogeneities, this might explain the saturation effect of the sodium TQ signal with increasing hemoglobin concentration in contrast to the almost linear increase in TQ signal with increasing BSA concentration observed in this thesis. In summary, multiple studies suggested special characteristics of the (met)hemoglobin hydration shell in comparison to the BSA hydration shell. This might explain the comparatively large TQ signal of methhemoglobin in comparison to other proteins, despite low sodium affinity to the protein and its paramagnetic nature.

In conclusion, it has been shown that the sodium TQ signal scales with the protein size. Nevertheless, sodium binding and special characteristics of the sodium hydration shell might have a stronger influence on the TQ signal than the protein size. More investigations of the interaction of sodium ions with different proteins

are necessary. It might not be sufficient to base TQ investigations solely on the commonly investigated protein BSA, which yields a weak TQ signal in comparison to most other proteins investigated in this thesis.

5.3 IRTQTPPI sequence

So far, knowledge about bi-exponential $^{23}\mathrm{Na}$ T_1 relaxation times of biological tissue is limited. Reasons for this are a contribution of the fast component of only 20 % to the total SQ signal and a small difference in T_1 relaxation times. Therefore, previous studies mainly approximated T_1 relaxation by a mono-exponential function [90, 92–98]. However, a reliable determination of both T_1 values is of importance for methods like magnetic resonance fingerprinting [83, 91, 155]. Furthermore, the unique sensitivity of the T_1-TQ signal to the intermediate motional regime provides additional insights about the sodium molecular environment. In this study, we proposed a reliable method for simultaneous quantification of the T_1 relaxation times and the T_1-TQ signal.

For a reliable quantification of T_1 and T_1-TQ values, we optimized the IRTQTPPI sequence in three steps: 1) Fixation of the relative contribution of the fast and slow signal component. 2) Non-linear sampling of the evolution time. 3) Suppression of unwanted signals.

The stability test showed that it was more crucial for the fit stability to sample the Free Induction Decay (FID) for sufficiently large τ_{evo}, to reduce the number of fit parameters and set the SQ amplitudes to their fixed theoretical values A_{1s} and A_{1f}. If the actual amplitudes deviated from the theoretical amplitudes, this could introduce errors in the determination of the relaxation times and other fit parameters. Multiple studies [7, 129] demonstrated for T_2 relaxation that the theoretical amplitudes were close to their theoretical amplitudes in agar samples and even in-vivo. Other studies also stabilized the T_2 fit by using fixed amplitudes [91, 136, 156, 157]. Both T_1 relaxation times are close in value and way larger than their T_2 counterpart. Therefore, signal is less affected by relaxation decay before the first echo/inversion, which potentially influences the amplitudes. Therefore, it is less affected by signal decay before the first echo/inversion. Hence, it is reasonable to assume, that fixed T_1 amplitudes introduce less errors than for T_2.

Non-linear sampling of the evolution time allowed us to avoid unreasonable long measurement times by using a second larger τ_{evo} increment. The number of data points with the increased τ_{evo} increment was varied to test the stability of the fit. For all samples and fit parameters, the fit stabilized and converged to a fixed set of parameters for a minimum of 100-200 additional data points.

For suppression of unwanted signals, we evaluated four different phase cycles for the IRTQTPPI sequence. In general, all phase cycles yielded similar T_1 relaxation times, while only the T_1-TQ/SQ ratio was altered. A large unsuppressed DQ peak may affect fit accuracy. Only PC0 did not suppress the DQ peak, however in these cases it did not influence the fit result substantially. The other phase cycles showed

a similar effectiveness in suppression of the DQ signal. PC1 suppresses signal contributions from an imperfect 180° inversion RF-pulse, while PC2 focuses on suppression of contributions with an even change in coherence order. PC3 combines both phase cycles, while doubling the scan time. The SQ signal of PC2 and PC3 did not perfectly constructively interfere leading to a lower SQ signal and consequently a larger normalized TQ signal. The relatively larger normalized TQ signal may make the extraction of small TQ signals easier, since its relative contribution to the FID increases. Other transitions than the wanted T_1 pathway cannot only create a DQ signal but also additional contributions to the SQ and TQ signals. For the SQ peak, these contributions should be much smaller than the signal from the $\hat{T}_{10} \rightarrow \hat{T}_{11}$ transition and therefore should not substantially influence the SQ peak. Alternative pathways that create a TQ peak however could in principle alter the TQ peak. As for example Madelin et al. [6] pointed out, the T_1- and T_2-TQ signals were not distinguishable in the case of imperfect flip angles. For our sequence, the only transitions that could create a TQ signal, i.e. change in the coherence order by 3, were the $\hat{T}_{30} \rightarrow \hat{T}_{33}$ transition (T_1-TQ signal) and the $\hat{T}_{3\pm1} \rightarrow \hat{T}_{3\mp2}$ transitions. In theory, both PC1 and PC3 corrected these contributions to the TQ signal by filtering out all contributions originating from $\hat{T}_{11}$ coherences created after an imperfect inversion pulse. In PC2, this pathway contributed to the signal. Nevertheless, the fit results almost perfectly matched between PC2 and PC3. Thus, the influence of this pathway should be negligible. Since PC2 and PC3 yielded a larger T_1-TQ/SQ signal compared to PC1 and a shorter scan time compared to PC3, we used PC2 in all further measurements.

The T_1 pathway is sensitive to the difference in J_1 and J_2 and thus an intermediate motional regime. In the T_2 pathway, T_{2s} is sensitive to J_1 and J_2, while the J_0 dependence in T_{2f} leads to a strong sensitivity to the slow-motion regime. Therefore, it is expected that the T_2-TQ signal and the separation of the T_2 relaxation times is stronger than for the T_1 pathway, which was confirmed by our measurements. Both measurements enabled the characterization of the motional environment of the sodium nuclei by calculating the correlation times τ_c and quadrupole strength parameters ω_Q. In our measurements, both values did not match between the two pathways, which is in agreement with literature [6, 8, 9]. Only in the case of a motional regime with a single τ_c and ω_Q, the τ_c and ω_Q values of both pathways match independent of the calculation method and B_0. In general, the motional regime is more accurately described by a distribution of correlation times and quadrupole strength parameters [8, 9]. Nevertheless, the simplified model still allows extracting qualitative and effective information about the motional environment of the nuclei. The T_1 correlation time was almost constant with increasing agar concentration in agreement with the sensitivity to interactions in the intermediate motional regime. On the other hand, the T_2 correlation time was increasing linearly with the agar concentration as expected from theory. The T_1-ω_Q was increasing slower with agar concentration than the T_2-ω_Q. This might indicate that with increasing agar concentration, slow interactions become stronger and more frequent, while intermediate interactions are not affected as much. Moreover, all samples yielded a strong T_1-TQ signal that increased with agar concentration with almost the same slope as the T_2-TQ signal. The similar increase

in T_1- and T_2-TQ signal combined with the dependence of the T_1 and T_2 correlation times, indicated that both the fraction of interactions in the intermediate and slow-motion regimes increased similarly.

In theory, the TQ/SQ ratio is expected to increase with B_0 since the intermediate ($\tau_c \cdot \omega_Q \sim 1$) and slow motion ($\tau_c \cdot \omega_Q \gtrsim 1$) regimes are shifted towards smaller correlation times [10]. This is in agreement with the lower correlation time at 21.1 T. Nonetheless, in our measurements, the TQ/SQ ratios decreased at 21.1 T compared to 9.4 T. This suggested a strong influence of B_0 and B_1 inhomogeneities on the TQ signal [49, 59]. In general, B_0 and B_1 inhomogeneities increase with field strength. Both T_1-TQ and T_2-TQ signals strongly depend on the flip angle accuracy and B_1 homogeneity. The T_2-TQ signal has a flip angle dependency of $\sin^5(\theta)$ [49]. Similarly, the T_1-TQ flip angle dependency can be calculated by the Wigner matrix elements: The flip angle dependency is $\cos(\theta_1)\sin^5(\theta_2)$, where θ_1 is the flip angle of the inversion pulse and θ_2 is the flip angle of the second and third pulse. Since RF absorption increases with B_0, B_1 inhomogeneity is expected to increase and therefore increasing field strength does not necessarily improve the TQ signal as theoretically expected. Moreover, the increased RF absorption increases SAR and necessitates longer repetition time, which increases scan time.

The IRTQTPPI sequence is also applicable with an imaging sequence. One drawback of the T_1-TQ signal was the smaller signal compared to the T_2-TQ signal, which is already only a tenth of the SQ signal. Furthermore, the 180° pulse doubles the SAR compared to the 90° pulse. Consequently, the T_2-TQ measurement will be a better choice for clinical applications due to the higher Signal to Noise Ratio (SNR) and lower SAR. Nevertheless, the IRTQTPPI sequence still improves the characterization of the motional environment and T_1 relaxation behavior of the sodium nuclei.

5.3.1 Improved Data Evaluation

As shown before, a reduction of fit parameters potentially stabilizes fit accuracy and increases the confidence in the fit results. Therefore, the amplitude of the TQ signal was fixed to its theoretical value and the impact on the fit results was investigated.

The separation of the T_1 relaxation times was substantially smaller than for the previous data evaluation, mainly because of larger T_{1f} values. This raises the question about what set of fit parameters was more accurate. Due to the lack of literature values regarding T_1 relaxation times, a fixed version of the IRTQTPPI similar to the fixed TQTPPI sequence [39] was investigated and used as a comparison method. The data evaluation method with a fixed TQ amplitude was in close agreement with the fit parameters of the fixed IRTQTPPI sequence, while the other method showed substantial deviations, especially for T_{1f}. However, despite much longer scan time of the fixed sequence to sample the different evolution times (5 h 50 min as compared to 25 min for the standard sequence), the fit uncertainties were much larger, especially for the TQ/SQ ratio. Fixing A_{TQ} to its expected value might be a way to improve the accuracy and reliability of the determination of the T_1 relaxation times even for a small separation in T_1 relaxation times.

In contrast to fixing the SQ amplitudes, it is much more complicated to calculated the TQ amplitudes, which might have introduced a possible error source. The impact of the transition efficiencies of the pulses is given by the Wigner matrix elements. The Wigner matrix elements are sensitive to the flip angles ($\propto \sin^2(\theta/2)\sin^2(\theta)$) and B_1 inhomogeneities. The influence of the RF pulse on A_{TQ} might be calculated using a B_1^+ map for higher accuracy. Moreover, A_{TQ} depends on the T_2^* relaxation times. For the simple samples, the fitted T_2^* relaxation times were most likely close to the real values. In multi-compartment systems, e.g., in tissue, the determination might be more difficult. In those cases, it might be necessary to use a more complicated fit function than a bi-exponential fit and this method should not be more inaccurate than the previous data evaluation. The T_1 relaxation pathway is not influenced by B_0 inhomogeneities and the B_0 inhomogeneities are already accounted for by fitting the T_2^* relaxation times. Therefore, it is not expected that there is an additional B_0 influence. The fit parameters were in close agreement with the fit parameters of the fixed IRTQTPPI sequence, which did not use the fixed A_{TQ}. Therefore, it can be concluded that the influence of these error sources was small.

A_{TQ} does not depend on the T_1 relaxation times but on the T_2^* relaxation times. This indicates, that the T_1-TQ/SQ ratio is not a useful parameter to characterize the TQ signal of the IRTQTPPI sequence. Instead, the maximum TQ signal might be used, which can be calculated from the T_1 relaxation times by inserting τ_{opt} into $f_{13}^{(0)}(t)$. The same applies for the previous data evaluation, where ideally the fitted A_{TQ} should be close to the expected A_{TQ} calculated in Equation (3.16).

5.4 Singlepulse TQ method

The sodium TQ signal promises to be a valuable biomarker for cell viability. Its clinical application has the potential to substantially increase increase the value of sodium MRI. However, common TQ techniques require at least three RF pulses and a sophisticated RF pulse phase cycling. Such pulse sequences inherently have a long scan time, increased SAR and increased sensitivity to B_0 and B_1 inhomogeneity. Altogether, these major obstacles currently hinder a clinical application of the TQ signal. In this study, a novel way to detect the TQ signal was investigated using only a single excitation pulse. Such method allows simultaneous SQ and TQ Magnetic Resonance (MR) imaging with the same scan time as for the SQ MR image. This approach could be a major step ahead towards the clinical TQ imaging.

Comparison of the Single-Pulse (SP) method with theory and the TQTPPI pulse sequence demonstrated the possibility to extract the TQ signal using only a single-pulse sequence. The extracted TQ signal maxima of the 2 %, 4 % and 6 % agar samples were in close agreement with theory and TQTPPI experiments. However, the SP FID decays with T_2^* and the TQTPPI FID with the T_2 relaxation times, respectively. Therefore, for a better comparison of the method with the TQTPPI TQ signal, the T_2 FID was additionally sampled using a spin echo sequence followed by application of the SP method. This comparison also showed a very close

agreement between the SP method of the Spin Echo (SE) FID, the TQTPPI sequence and the theoretical prediction for these samples. Consequently, the application of SP method is not limited to SP sequences. Nevertheless, the 0 % agar sample yielded a non-zero TQ signal using the SP method of the SP FID, while it vanished for the SE FID. The non-zero TQ signal of the SP FID did not result in the typical "buildup" behavior of the TQ signal. This cannot be explained by a multi-compartment model and a non-exponential shape of the FID. This might be caused by non-Lorentzian distributed B_0 inhomogeneities. For example Steidle and Schick [158] reported a Gaussian component in the intravoxel distribution of B_0 inhomogeneities for ^{1}H scans. Another possible explanation for the non-exponential decay might be a hardware artifact. The Gibbs-like artifact described in Appendix A.2.2 was caused by the impulse response of digital filters [159], which might also introduce additional imperfections. Measurements on other MRI systems are necessary to further investigate the origin of the non-exponential behavior in the SP FID.

The non-zero TQ signal of 0 % agar sample may be an indication of the influence of B_0 inhomogeneity on the TQ signal. For example, non-Lorentzian distributed B_0 inhomogeneities with a non-exponential T_2^* decay can lead to a contribution to the TQ signal that does not originate from $\hat{T}_{31}$ coherences. The influence on the TQ signal of the 2 %, 4 % and 6 % agar samples may be reduced due to a short T_{2f} component. The impact of B_0 inhomogeneity on the conventional TQ multi-pulse sequences is more complicated as different coherence orders are influenced differently. There exist different approaches to minimize the effect of B_0 inhomogeneity on the signal, e.g., by adapting the phase cycle [29, 30, 48, 49, 51]. Another approach is to use a 180° refocusing pulse, which refocuses the signal such that T_2 instead of T_2^* relaxation times determine the signal [7]. However, this approach requires an accurate calibration of the 180° pulse. In summary, both methods to measure the TQ signal are affected by B_0 inhomogeneity in a different way.

In contrast to B_0 inhomogeneity, the flip angle, i.e. B_1 inhomogeneity, only determines the overall SQ signal using the SP method. Thus, it changes the absolute signal value, but not the relative TQ/SQ signal. Contrary, the conventional TQ pulse sequences are very sensitive to imperfect pulses, e.g. the TQ signal depends with $\sin^5(\theta)$ on the flip angle θ [49]. Thus, small imperfections in the calibration or an inhomogeneous RF excitation have severe effects on the TQ signal [7]. In summary, the SP method is less prone to B_1 inhomogeneities compared to conventional TQ pulse sequences.

The in vivo situation is more complex and closer to a multi-compartment system. In this case, the integrals in equation Equation (3.24) become more complicated and the difference between both terms does not exactly equal the TQ signal anymore. We used a two-compartment system with two bi-exponential compartments to simulate the in-vivo situation. The TQ signal was systematically slightly overestimated by the SP method. However, the deviation to the expected TQ signal was less than 2.5 % for the case of bi-exponential relaxation in both compartments. Hence, the SP method is also applicable to more complicated in-vivo situations.

One drawback of this method arises in the case of two mono-exponential compartments. This case cannot be distinguished mathematically from the case of

one bi-exponential compartment and the SP "TQ" signal is the same in both cases. In contrast, the TQTPPI TQ signal is vanishing for a two mono-exponential case. In our experiment, a similar situation occurred for the 0 % agar sample. Here, the FID did not decay mono-exponentially and consequently the SP "TQ" signal was not zero compared to the TQTPPI sequence. Therefore, we may call the SP extracted "TQ" signal a measure of the "deviation from mono-exponential decay". However, the main source for bi-exponential decay is the quadrupole interaction. Furthermore, the signal in the multi-compartment case was in close agreement to the TQ signal and showed the expected behavior for the increase of the TQ signal. Therefore, the extracted TQ signal of this method approximates the usually observed TQ signal.

The SP method is attractive not only for spectroscopy but in particular for the fast estimation of the TQ signal in MR imaging. The method approximates the TQ signal in a single shot with the high time efficiency of the SQ signal. This means that, without increasing scan time, both SQ and TQ images can be acquired instead of only an SQ image. As a proof-of-concept, we used a 3D Ultra-Short Echo Time (UTE) sequence with multiple echoes to sample the complete FID in one shot. Since T_{R} is usually set to $3 \cdot T_1$ to $5 \cdot T_1$, there is plenty of time to sample the entire FID with only one excitation. Furthermore, the SP method samples the entire TQ evolution curve instead of the TQ signal at a specific evolution time τ_{evo}. Hence, the maximum TQ signal of different tissues with different optimum evolution times can be obtained within a single measurement.

The TQ signals of a single slice were smaller with larger uncertainties than the spectroscopic sequences. Partial volume effects and a large noise level influence the TQ signals. Our current pulse sequence was not optimized for sodium MR imaging and was only used as a proof of concept. Both sequence parameters as well as image reconstruction method can be further improved, e.g., by optimizing the bandwidth, correcting for imperfections in the k-space trajectories etc. [136, 139, 160, 161]. Alternatively, the SP method can also simply be added to the processing pipeline of existing sodium multi-echo imaging protocols [129, 136, 162] to acquire the TQ signal additionally without increasing overall scan time.

In preparation for the imaging sequence, the impact of noise on the accuracy of the SP method was investigated with simulated data. Even for low SNRs, i.e. SQ SNR $<$ 10, the systematic error of the method was small for the relevant evolution times around the TQ maximum. Typical $^{23}\mathrm{Na}$ MRI SNR values are equal or larger than 10 [84, 136]. However, since the TQ signal in tissue is around 10 % of the SQ signal, longer scan times to increase SNR might still be necessary. In conclusion, the SP method performed well in low SNR scenarios and was only limited by the fact that the TQ signal is smaller than the SQ signal.

6 Conclusion and Outlook

The two main aims of this thesis were (i) to investigate the molecular origin of the sodium Triple Quantum (TQ) signal in a preclinical setting using model systems and advanced TQ techniques, and (ii) to accelerate the acquisition of the sodium TQ signal. These two objectives were achieved in four parts.

In the first part, a simulation framework for the Nuclear Magnetic Resonance (NMR) dynamics of spin $^3/_2$ nuclei was implemented and investigated. The commonly used Debye model was not simultaneously compatible with the experimental relaxation times T_1 and T_2. Therefore, an alternative model for motional averaging of interactions of the sodium nuclei with their environment, the 2xDebye model, was introduced. This model takes into account the interactions in the extreme narrowing regime. With this model the simulated spectra of the Inversion Recovery Triple Quantum Time Proportional Phase Increment (IRTQTPPI) and Triple Quantum Time Proportional Phase Increment (TQTPPI) sequences were in agreement with the experiment. Small deviations between simulation and experiment could be attributed to B_0 and B_1 inhomogeneities, which were neglected in favour of computational time. The simulation framework allows not only qualitative simulations to optimize phase cycling sequences, but also quantitative predictions of experimental results from sodium NMR studies. Using the simulation framework as a foundation, it can be easily extended to multi-compartment systems and adapted for imaging, generating test data to improve image reconstruction and imaging sequences.

In the second part, the TQ signal of various proteins was examined. With few exceptions, the TQ signal correlated positively with protein size. In addition, sodium binding and specific features of the protein hydration shell have a strong influence on the sodium TQ signal. Samples of two of the smallest proteins with a strong sodium binding, yielded the largest TQ signals in this study. The physiologically relevant protein hemoglobin resulted in a large TQ signal despite its very low sodium binding affinity and its paramagnetic nature. This was attributed to abnormalities in the hydration shell of the protein. Samples of the commonly studied protein Bovine Serum Albumin (BSA) showed an unusually weak TQ signal compared to the other proteins. Therefore, this part emphasized the need for a diverse range of proteins to obtain a deeper understanding of the sodium molecular environment. Building on these findings, future investigations could explore the pH dependence of the TQ signal, particularly in sodium-binding proteins like α-lactalbumin.

In the third part, the T_1 and T_2 relaxation times and T_1- and T_2-TQ signals using the TQTPPI and IRTQTPPI sequences were compared. The IRTQTPPI sequence was demonstrated as a reliable method for simultaneous quantification of sodium T_1-TQ signal, Single Quantum (SQ) signal and bi-exponential T_1 relaxation times.

Combination of optimized fit parameters, non-uniform sampling of the evolution time and suppression of unwanted signals resulted in reliable and stable IRTQTPPI measurements. At 9.4 T and 21.1 T, all samples of the agar model system yielded a T_1-TQ signal and bi-exponential sodium relaxation times. In contrast to theoretical expectations, the T_1- and T_2-TQ signals decreased with increasing field strength mostly due to B_0 and B_1 inhomogeneity. The T_2-TQ signal and the T_1-TQ signal are sensitive to different sodium nuclei motion as demonstrated for the agar tissue model system. Consequently, the IRTQTPPI sequence allows for reliable and simultaneuos measurements of SQ and TQ signals. Hence, the combination of T_1-TQ and T_2-TQ signals yields an improved characterization of the molecular environment due to their different sensitivities of molecular motion. Next steps include the implementation of an imaging sequence for the IRTQTPPI sequence and the translation to clinical scanners. Such an imaging IRTQTPPI sequence allows investigate the potential of the T_1-TQ signal and characterize the T_1 relaxation times in vivo.

In the last part a novel method for acquiring the TQ signal using only a single pulse sequence was demonstrated. This method allows a simultaneous acquisition of SQ and TQ signals without extra radio-frequency (RF) pulses and extensive phase cycling. The extracted TQ signal was in close agreement with theory and the results of TQTPPI sequence. In multi-compartment systems and for noisy data, the extracted TQ signal reproduced the expected TQ signal behavior. This approach combined with multi-echo Ultra-Short Echo Time (UTE) imaging represents an efficient method to extract the sodium TQ signal in vivo in SQ scan time. In future research, the method might be implemented for clinical scanners or applied to existing sodium protocols that sample Free Induction Decay (FID) and compared with conventional phase cycling sequences in vivo for healthy volunteers. The method can be easily incorporated into existing SQ imaging protocols and sodium Magnetic Resonance Imaging (MRI) studies without increasing scan time or Specific Absorption Rate (SAR). This approach may expand TQ imaging applications and thus may leverage the full potential of sodium TQ signal in clinical applications.

In conclusion, novel detection methods for the sodium TQ signal were established and the molecular origin of the TQ signal was investigated in a preclinical setting. The first method, the IRTQTPPI sequence, used the alternative T_1 coherence pathway to create the TQ signal with a unique sensitivity to the motional environment of the sodium ions. Similar to T_2 TQ phase cycling sequences, this sequence can be translated to a clinical imaging sequence and may yield deeper insights into the sodium Magnetic Resonance (MR) environment. However, clinical applications require short scan times and low SAR, which is difficult to achieve with the conventional multi-pulse phase cycling approach. Consequently, a completely novel approach for fast TQ detection was introduced that uses only single excitation pulse. By comparison to theoretical predictions and experimental data the novel method yielded similar information to the state-of-the-art TQTPPI sequence in drastically reduced scan time. This method may leverage the full potential of the sodium TQ signal in clinical applications. For the first time, the value of the sodium TQ signal as a biomarker for cell viability can be investigated in a clinical setting in reasonable scan time similar to that of a conventional sodium SQ scan.

Appendix

A

A.1 Simulation and 2xDebye Model

Tab. A.1.: Comparison of the fit results of the IRTQTPPI and TQTPPI sequences between experimental data, the T1 Debye model, the T2 Debye model and the 2xDebye model for the 4 % agar sample. T_{is} and T_{if} are the long and short component of the T_1 (IRTQTPPI sequence) or T_2 (TQTPPI sequence) relaxation times, respectively.

4 % agar		T_{is} [ms]	T_{if} [ms]	TQ/SQ [%]	TQ peak [%]
IRTQTPPI sequence (T_1)	**experiment**	41.38 ± 0.42	33.62 ± 0.17	19.13 ± 0.24	2.05 ± 0.04
	T1 Debye	41.39 ± 0.00	33.65 ± 0.00	1.68 ± 0.00	0.20 ± 0.00
	T2 Debye	89.69 ± 0.28	25.71 ± 0.19	35.16 ± 0.33	45.33 ± 0.10
	2x Debye	41.77 ± 0.09	33.86 ± 0.03	34.06 ± 0.29	4.18 ± 0.01
TQTPPI sequence (T_2)	**experiment**	37.22 ± 0.06	5.12 ± 0.22	29.96 ± 0.26	55.86 ± 1.06
	T1 Debye	36.75 ± 0.02	32.03 ± 0.03	1.81 ± 0.01	0.27 ± 0.00
	T2 Debye	37.22 ± 0.00	5.12 ± 0.00	36.58 ± 0.00	66.75 ± 1.19
	2x Debye	37.22 ± 0.00	5.12 ± 0.00	36.58 ± 0.00	66.67 ± 1.19

Tab. A.2.: Comparison of the fit results of the IRTQTPPI and TQTPPI sequences between experimental data, the T1 Debye model, the T2 Debye model and the 2xDebye model for the 6 % agar sample.

6 % agar		T_{is} [ms]	T_{if} [ms]	TQ/SQ [%]	TQ peak [%]
IRTQTPPI sequence (T_1)	**experiment**	36.33 ± 0.24	28.50 ± 0.11	23.36 ± 0.20	2.60 ± 0.03
	T1 Debye	36.35 ± 0.00	28.56 ± 0.00	2.21 ± 0.00	0.26 ± 0.00
	T2 Debye	81.12 ± 0.13	19.80 ± 0.21	34.94 ± 0.00	43.19 ± 0.11
	2x Debye	36.89 ± 0.11	28.33 ± 0.04	35.33 ± 0.38	4.61 ± 0.02
TQTPPI sequence (T_2)	**experiment**	32.57 ± 0.04	3.66 ± 0.16	34.49 ± 0.25	68.20 ± 1.44
	T1 Debye	31.71 ± 0.01	26.98 ± 0.02	2.36 ± 0.01	0.42 ± 0.01
	T2 Debye	32.57 ± 0.00	3.65 ± 0.00	40.82 ± 0.01	78.37 ± 1.93
	2x Debye	32.57 ± 0.00	3.66 ± 0.00	40.83 ± 0.00	78.34 ± 1.93

A.2 Supplementary Information Single Pulse TQ Signal

A.2.1 Theory: Calculation of the SP TQ Signal

In the following, equation Equation (3.24) for the TQ signal is derived. The Fourier Transform (FT) of a one-sided decaying exponential is a Lorentzian:

$$FT(\mathrm{e}^{-t/T_2})(\omega) = \frac{T_2}{1+T_2^2\omega^2} \tag{A.1}$$

The integral over this function yields

$$\int_{-\infty}^{+\infty} \frac{T_2}{1+T_2^2\omega^2}\mathrm{d}\omega = \pi \tag{A.2}$$

The result of Equation (A.2) is a constant and thus independent of the relaxation time T_2. Combination of Equation (A.2) and equation Equation (3.24) with the use of Equation (2.93) and the linearity of the FT, we obtain

$$\begin{aligned}
&\int_{-\infty}^{+\infty} FT(FID(t,\tau_{\mathrm{evo}}))(\omega,\tau_{\mathrm{evo}})\mathrm{d}\omega = \\
&= A_{SQ}(\tau_{\mathrm{evo}}) \int_{-\infty}^{+\infty} \left(A_s \frac{T_{2s}}{1+T_{2s}^2\omega^2} + A_f \frac{T_{2f}}{1+T_{2f}^2\omega^2} \right) \mathrm{d}\omega \\
&\quad + \frac{\sqrt{6}}{5} A_{TQ}(\tau_{\mathrm{evo}}) \int_{-\infty}^{+\infty} \left(\frac{T_{2s}}{1+T_{2s}^2\omega^2} - \frac{T_{2f}}{1+T_{2f}^2\omega^2} \right) \mathrm{d}\omega \\
&= A_{SQ}(\tau_{\mathrm{evo}})(A_s\pi + A_f\pi) + \frac{\sqrt{6}}{5} A_{TQ}(\tau_{\mathrm{evo}})(\pi - \pi) \\
&= A_{SQ}(\tau_{\mathrm{evo}})(A_s + A_f)\pi
\end{aligned} \tag{A.3}$$

Consequently, the TQ part of the signal vanishes. On the other hand, integration of the FID from equation Equation (3.22) yields

$$\begin{aligned}
&\int_0^{+\infty} FID(t,\tau_{\text{evo}})\mathrm{d}t = \\
&= A_{SQ}(\tau_{\text{evo}}) \int_0^{+\infty} A_s \exp(-t/T_{2s}) + A_s \exp(-t/T_{2s}) + A_f \exp(-t/T_{2f})\mathrm{d}t \\
&\quad + \frac{\sqrt{6}}{5} A_{TQ}(\tau_{\text{evo}}) \int_0^{+\infty} \exp(-t/T_{2s}) + A_s \exp(-t/T_{2s}) - \exp(-t/T_{2f})\mathrm{d}t \\
&= A_{SQ}(\tau_{\text{evo}}) \left(\frac{A_s}{T_{2s}} + \frac{A_f}{T_{2f}}\right) + \frac{\sqrt{6}}{5} A_{TQ}(\tau_{\text{evo}}) \left(\frac{1}{T_{2s}} - \frac{1}{T_{2f}}\right)
\end{aligned} \tag{A.4}$$

This equation contains both the SQ and TQ parts of the signal with some additional constant factors. Normalization of integrals in Equation (A.3) and Equation (A.4) with the use of the $\tau_{\text{evo}} = 0$ terms and subtraction of both equations removes the SQ signal:

$$\begin{aligned}
S_{TQ}(\tau_{\text{evo}}) =& \frac{\int_0^{+\infty} FID(t,\tau_{\text{evo}})\mathrm{d}t}{\int_0^{+\infty} FID(t,0)\mathrm{d}t} - \frac{\int_{-\infty}^{+\infty} FT(FID(t,\tau_{\text{evo}}))(\omega,\tau_{\text{evo}})\mathrm{d}\omega}{\int_{-\infty}^{+\infty} FT(FID(t,0))(\omega,0)\mathrm{d}\omega} \\
=& \frac{A_{SQ}(\tau_{\text{evo}}) \left(\frac{A_s}{T_{2s}} + \frac{A_f}{T_{2f}}\right) + \frac{\sqrt{6}}{5} A_{TQ}(\tau_{\text{evo}}) \left(\frac{1}{T_{2s}} - \frac{1}{T_{2f}}\right)}{A_{SQ}(0) \left(\frac{A_s}{T_{2s}} + \frac{A_f}{T_{2f}}\right) + \frac{\sqrt{6}}{5} A_{TQ}(0) \left(\frac{1}{T_{2s}} - \frac{1}{T_{2f}}\right)} \\
& - \frac{A_{SQ}(\tau_{\text{evo}})(A_s + A_f)\pi}{A_{SQ}(0)(A_s + A_f)\pi} \\
=& \frac{\frac{\sqrt{6}}{5} A_{TQ}(\tau_{\text{evo}}) \left(\frac{1}{T_{2s}} - \frac{1}{T_{2f}}\right)}{A_{SQ}(0) \left(\frac{A_s}{T_{2s}} + \frac{A_f}{T_{2f}}\right)} = \frac{\frac{\sqrt{6}}{5}(T_{2s} - T_{2f})}{A_s T_{2s} + A_f T_{2f}} A_{TQ}(\tau_{\text{evo}})
\end{aligned} \tag{A.5}$$

Here, it was used that $A_{TQ}(0) = 0$ and $A_{SQ}(0) = 1$. The normalization removes the factor $(A_s\pi + A_f\pi)$ in the second term. Thus, instead of integrating the spectrum, it is sufficient to use the first data point from the FID of each τ_{evo}. The prefactor of $A_{TQ}(\tau_{\text{evo}})$ in Equation (A.5) is the inverse of the normalization factor from Equation (3.25). This normalization factor can also be interpreted as the transition efficiency of the $\hat{T}_{31}$ signal to the detectable $\hat{T}_{11}$ signal. The transition efficiency is given by the integral over the $\hat{T}_{11}$ signal divided by the integral over the $\hat{T}_{31}$ signal:

$$Norm = \frac{\int f_{11}^{(1)}(t)\mathrm{d}t}{\int f_{13}^{(1)}(t)\mathrm{d}t} = \frac{A_s T_{2s} + A_f T_{2f}}{\frac{\sqrt{6}}{5}(T_{2s} - T_{2f})} \tag{A.6}$$

Consequently, the TQTPPI sequence requires a similar normalization factor. In the TQTPPI sequence, the $\hat{T}_{31}$ signal also has to be transferred to the detectable $\hat{T}_{11}$

signal. Furthermore, the TQTPPI normalization factor has additional contributions from the transition efficiencies of the RF pulses, given by the Wigner matrix elements and $\hat{T}_{33}$ tensor relaxation. The Wigner matrix correction is given by

$$N_{\text{Wigner}} = \frac{d^{(1)}_{11}(90°) \cdot d^{(1)}_{1-1}(90°)}{d^{(3)}_{13}(90°) \cdot d^{(3)}_{3-1}(90°)} \approx 1.0667, \tag{A.7}$$

Where $d^{(l)}_{mm'}(\theta))$ are the Wigner matrix elements for the transition $\hat{T}_{lm} \rightarrow \hat{T}_{lm'}$ and the flip angle θ. The $\hat{T}_{33}$ coherences are influenced three times more by B_0 inhomogeneities compared to the tensors of coherence order 1 ($\hat{T}_{11}$ and $\hat{T}_{31}$). To avoid $\hat{T}_{33}$ relaxation, τ_{mix} is set as short as possible depending on the pulse length, in our case $\tau_{\text{mix}} = 137\,\text{ms}$. The exact value of the correction factor of B_0 inhomogeneities is hard to estimate, however, it should be small and was therefore neglected.

A.2.2 Preprocessing of the SP FID

A Gibbs-like artifact was observed in the raw FID data. A standard preprocessing step [7, 159, 163] was applied to reduce this artifact by adding the left part of the red dotted line in Figure A.1 to the right part. Additionally, the first 10 points, up to approximately 1 ms, were removed. This should minimize the FID part that contains non-(bi-)exponential relaxation behavior and imperfect correction of the Analog-to-Digital Converter (ADC) artifact.

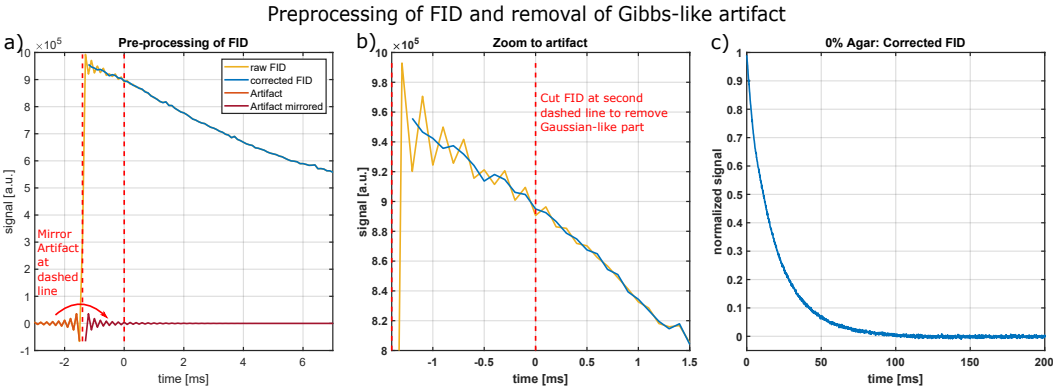

Fig. A.1.: Schematic overview of the single-pulse FID pre-processing. (a) The Gibbs-like artifact was removed by inverting the left part of the first dashed red line to the FID. (b) Zoomed area of the corrected Gibbs artifact. To remove the non-exponential part of the FID, the FID was cut at the second dashed red line which is defined as $t = 0\,\text{ms}$. This removed 1 ms of the FID. (c) Final post-processed FID for 0 % agar.

A.2.3 Comparison of SP Method with TQTPPI Sequence wo/180° Refocusing Pulse

We used the TQTPPI sequence with a 180° refocusing pulse for the comparison with the Single-Pulse (SP) method. This comparison is not optimal as the refocused TQTPPI FID decays with the T_2 relaxation times, while the SP FID decays with the T_2^* relaxation times. Therefore, the TQTPPI sequence without the 180° refocusing pulse would be the sequence of choice for the comparison. However, as Figure A.2 shows, the first dimension FIDs, acquired FIDs, yielded stimulated echo that resulted from the second and third pulse. Both 90° pulses act like a refocusing pulse. As the TQTPPI FID was created from the integrals over these first dimension FIDs, this led to a bias in the relaxation times corresponding neither to T_2 nor T_2^*. To simplify the interpretation of the data, we used instead the refocused TQTPPI sequence for comparison. Figure A.3 shows a comparison of the SP method and the TQTPPI sequence without the 180° refocusing pulse. Especially the 0 % agar sample results in a non-exponential relaxation behavior of the TQTPPI FID. With increasing agar concentration the FID came closer to the T_2^* decay of the SP sequence. Similar to the refocused TQTPPI sequence, the TQ maxima of the SP method were in close agreement with the unrefocused TQTPPI sequence for all samples except the 0 % agar sample.

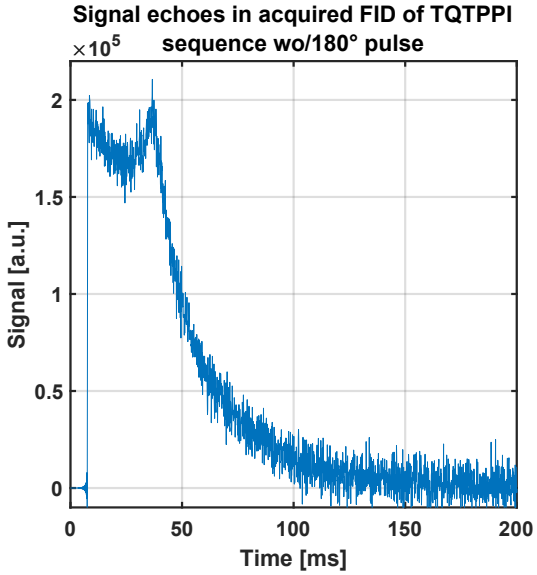

Fig. A.2.: First dimension FID of the TQTPPI sequence without the 180° refocusing pulse using the 0 % agar sample and an evolution time of 30 ms. The second and third 90° pulses effectively acted like an 180° pulse, leading to a signal echo. Since the TQTPPI FID was created using the integral over the first dimension FIDs, this led to relaxation times not equal to T_2 or T_2^*.

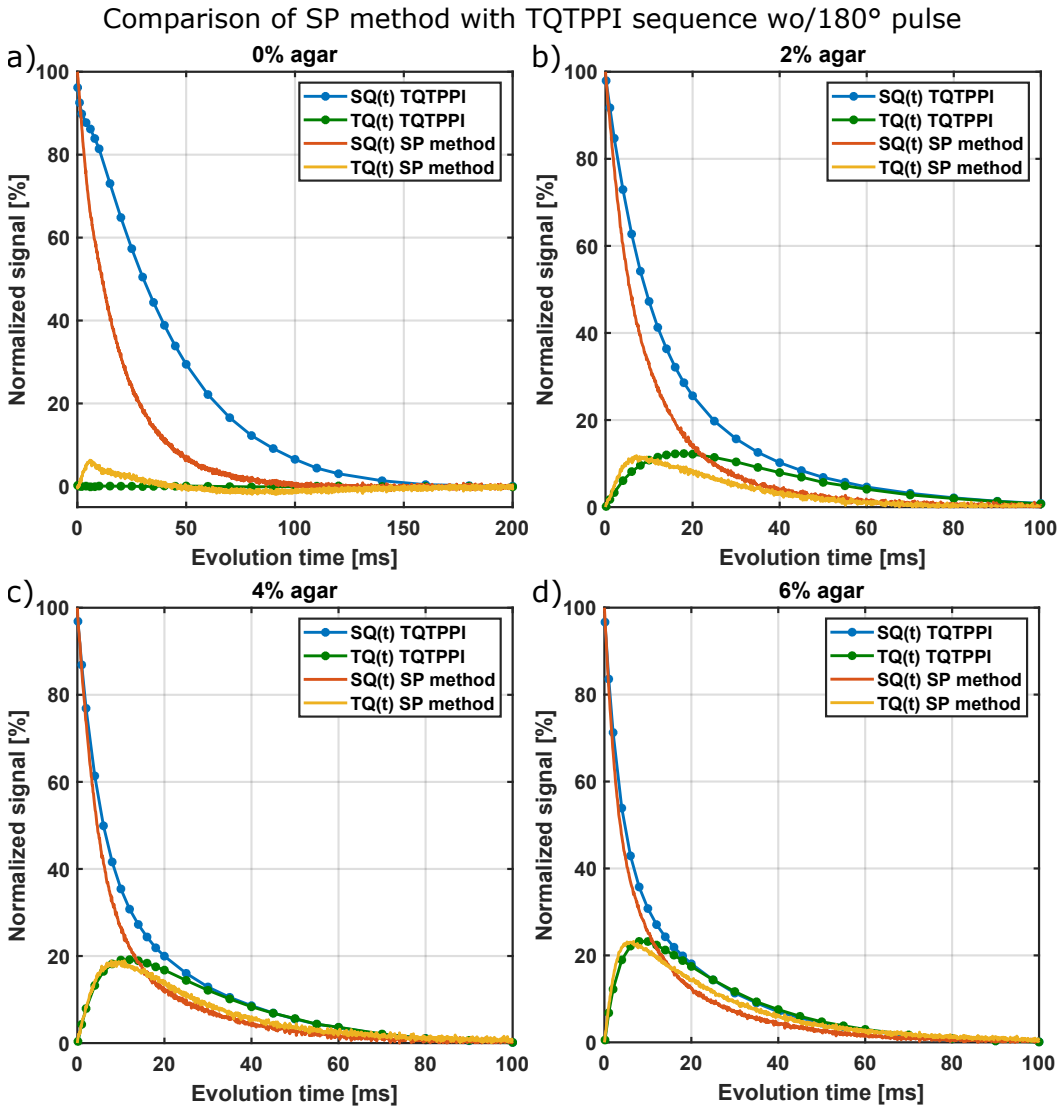

Fig. A.3.: Comparison of the SP TQ signal and the TQTPPI sequence (without 180° refocusing pulse) for agar samples with (a) 0 %, (b) 2 %, (c) 4 % and (d) 6 % agar. The TQTPPI FID was biased by echoes in the first dimension FIDs Figure A.2. The resulting TQTPPI FID did neither decay with T_2 nor T_2^* relaxation times.

List of Publications

Peer-Reviewed Journal Articles

- Simon Reichert, Victor D. Schepkin, Dennis Kleimaier, Frank G Zöllner, and Lothar R. Schad. "Comparison of triple quantum (TQ) TPPI and inversion recovery TQ TPPI pulse sequences at 9.4 and 21.1T". in: *NMR in Biomedicine* (Submitted on October 24, 2023) (2023)
- Simon Reichert, Victor D. Schepkin, Dennis Kleimaier, Frank G Zöllner, and Lothar R. Schad. "23Na Triple Quantum MR Signal Extraction Using a Single-pulse Sequence with Single Quantum Time Efficiency". In: *Magnetic Resonance in Medicine* (Submitted on November 7, 2023) (2023)
- Christian Licht, Simon Reichert, Maxime Guye, Lothar R. Schad, and Stanislas Rapacchi. "Multidimensional compressed sensing to advance 23Na multi-quantum coherences MRI". in: *Magnetic Resonance in Medicine* n/a.n/a (2023). ISSN: 0740-3194. DOI: https://doi.org/10.1002/mrm.29902
- Anne Adlung, Christian Licht, Simon Reichert, Safa Özdemir, Sherif A. Mohamed, Melina Samartzi, Marc Fatar, Achim Gass, Eva Neumaier Prost, and Lothar R. Schad. "Quantification of tissue sodium concentration in the ischemic stroke: A comparison between external and internal references for 23Na MRI". in: *Journal of Neuroscience Methods* 382 (2022), p. 109721. ISSN: 0165-0270. DOI: https://doi.org/10.1016/j.jneumeth.2022.109721
- Christian Licht, Simon Reichert, Mark Bydder, Jascha Zapp, Shirley Corella, Maxime Guye, Frank G. Zöllner, Lothar R. Schad, and Stanislas Rapacchi. "Low-rank reconstruction for simultaneous Double-Half-Echo 23Na and undersampled 23Na Multi-Quantum Coherences MRI". in: *Magnetic Resonance in Medicine* (Submitted on November 20, 2023) (2023)

Conference Contributions

- Simon Reichert, Dennis Kleimaier, and Lothar Schad. "Comparison of low rank compressed sensing with non-uniform undersampled non-linear FID fitting for time efficient 23Na TQTPPI measurements". In: *Proc. Intl. Soc. Mag. Reson. Med.* 29 (2021)
- Simon Reichert, Dennis Kleimaier, and Lothar Schad. "Comparison of Double Quantum (DQ) Suppression Methods for Inversion Recovery TQTPPI (IRTQTPPI) Sequence". In: *Proc. Intl. Soc. Mag. Reson. Med.* 30 (2022)

- Simon Reichert, Dennis Kleimaier, and Lothar Schad. “Simulation of Spin 3/2 Quadrupole Nuclei Dynamics in Biological Environments for Arbitrary Pulse Sequences”. In: *Proc. Intl. Soc. Mag. Reson. Med.* 30 (2022)
- Simon Reichert, Dennis Kleimaier, and Lothar Schad. “Dependence of 23Na Triple Quantum (TQ) Signal on Protein Size”. In: *Proc. Intl. Soc. Mag. Reson. Med.* 30 (2022)
- Simon Reichert, Dennis Kleimaier, Vichtor D. Schepkin, and Lothar Schad. “23Na Triple Quantum (TQ) Signal Estimation from Single-Pulse Sequence with Single Quantum (SQ) Time Efficiency”. In: *Proc. Intl. Soc. Mag. Reson. Med.* 31 (2023)
- Simon Reichert, Denis Kleimaier, Victor D. Schepkin, and Lothar Schad. “Combining Extreme Narrowing and Slow Motion Regime in a Simple Motional Model for Sodium NMR Environment”. In: *Proc. Intl. Soc. Mag. Reson. Med.* 31 (2023)
- Simon Reichert, Dennis Kleimaier, Dominik Zehender, Frank G. Zöllner, and Lothar Schad. “A Novel Method to Estimate 23Na Triple Quantum (TQ) Signal: Spin Echo Sequence, Impact of Noise and Proof-of-Concept Imaging”. In: *Proc. Intl. Soc. Mag. Reson. Med.* (Submitted) (2023)
- D. Kleimaier, S. Reichert, V. D. Schepkin, and L. Schad. “Sodium TQ signal of amino acids and alpha-lactalbumin in comparison to bovine serum albumin”. In: *Proc. Intl. Soc. Mag. Reson. Med.* 29 (2021)
- C. Licht, E. Ilicak, S. Reichert, D. Zehender, Frank G. Zöllner, L. Schad, and S. Rapacchi. “Dynamic Mode Decomposition reveals 23Na Multi-Quantum Coherences and allows incomplete RF Phase-Cycling”. In: *Proc. Intl. Soc. Mag. Reson. Med.* (Submitted) (2023)
- C. Licht, S. Reichert, G. M. Bydder, M. Guye, S. Corella, L. Schad, and S. Rapacchi. “Low-rank reconstructions for simultaneous Double-Half Echo 23Na and prospectively undersampled 23Na Multi-Quantum Coherences MRI”. in: *Proc. Intl. Soc. Mag. Reson. Med.* (Submitted) (2023)
- Dominik Zehender, Simon Reichert, Frank G. Zöllner, and Lothar Schad. “Feasibility of undersampled fixed evolution time 23Na TQTPPI FID reconstruction for optimal 23Na TQ/SQ-signal estimation”. In: *Proc. Intl. Soc. Mag. Reson. Med.* (Submitted) (2023)
- Simon Reichert, Victor D. Schepkin, Denis Kleimaier, and Lothar Schad. “Simultaneous 23Na Triple Quantum (TQ) Signal Estimation from Single-Pulse Sequence with Single Quantum (SQ) Time Efficiency”. In: *ISMRM 2023 Workshop on MR Imaging of X-Nuclei 23Na & Friends: From Controversies to Potential Clinical Applications Part II* (2023)
- Christian Licht, Simon Reichert, Jascha Zapp, Mark Bydder, Maxime Guye, Lothar R. Schad, and Stanislas Rapacchi. “Low-Rank Reconstruction for Double-Half-Echo 23Na and undersampled 23Na Multi-Quantum Coherences

MRI". in: *ISMRM 2023 Workshop on MR Imaging of X-Nuclei 23Na & Friends: From Controversies to Potential Clinical Applications Part II* (2023)

- Christian Licht, Simon Reichert, Jascha Zapp, Mark Bydder, Maxime Guye, Lothar R. Schad, and Stanislas Rapacchi. "Prospectively undersampled higher resolution 23Na Multi-Quantum Coherences MRI". in: *ESMRMB 2023 Annual Meeting* (2023)

Awards and Talks

- Invited Talk: "Overview of Multiquantum Imaging" at "ISMRM 2023 Workshop on MR Imaging of X-Nuclei 23Na & Friends): From Controversies to Potential Clinical Applications Part II"
- Best Poster Award at "ISMRM 2023 Workshop on MR Imaging of X-Nuclei 23Na & Friends): From Controversies to Potential Clinical Applications Part II"

Supervised Theses

- Valentin Jost. "NMR simulation of 23Na in a biomedical environment". Thesis. 2023

List of Figures

List of Tables

Bibliography

[1] Ruomin Hu, Dennis Kleimaier, Matthias Malzacher, et al. “X-nuclei imaging: Current state, technical challenges, and future directions”. In: *Journal of Magnetic Resonance Imaging* 51.2 (2020), pp. 355–376. ISSN: 1053-1807. DOI: https://doi.org/10.1002/jmri.26780 (cit. on p. 1).

[2] Keith R. Thulborn. “Quantitative sodium MR imaging: A review of its evolving role in medicine”. In: *NeuroImage* 168 (2018), pp. 250–268. ISSN: 1053-8119. DOI: https://doi.org/10.1016/j.neuroimage.2016.11.056 (cit. on p. 1).

[3] Guillaume Madelin and Ravinder R. Regatte. “Biomedical applications of sodium MRI in vivo”. In: *Journal of Magnetic Resonance Imaging* 38.3 (2013), pp. 511–529. ISSN: 1053-1807. DOI: https://doi.org/10.1002/jmri.24168 (cit. on p. 1).

[4] B. Alberts, A. Johnson, J.H. Wilson, et al. *Molecular Biology of the Cell*. Garland Science, 2008. ISBN: 9780815341116 (cit. on p. 1).

[5] Michael V. Clausen, Florian Hilbers, and Hanne Poulsen. “The Structure and Function of the Na,K-ATPase Isoforms in Health and Disease”. In: *Frontiers in Physiology* 8.371 (2017). ISSN: 1664-042X. DOI: 10.3389/fphys.2017.00371 (cit. on p. 1).

[6] Guillaume Madelin, Jae-Seung Lee, Ravinder R. Regatte, and Alexej Jerschow. “Sodium MRI: Methods and applications”. In: *Progress in Nuclear Magnetic Resonance Spectroscopy* 79 (2014), pp. 14–47. ISSN: 0079-6565. DOI: https://doi.org/10.1016/j.pnmrs.2014.02.001 (cit. on pp. 1–5, 40, 52, 56, 63, 106–109, 112).

[7] Victor D. Schepkin, Andreas Neubauer, Armin M. Nagel, and Thomas F. Budinger. “Comparison of potassium and sodium binding in vivo and in agarose samples using TQTPPI pulse sequence”. In: *Journal of Magnetic Resonance* 277 (2017), pp. 162–168. ISSN: 1090-7807. DOI: https://doi.org/10.1016/j.jmr.2017.03.003 (cit. on pp. 1–3, 38, 44, 51, 56, 60, 61, 64, 66, 72, 111, 115, 122).

[8] William D. Rooney and Charles S. Springer. “A comprehensive approach to the analysis and interpretation of the resonances of spins 3/2 from living systems”. In: *NMR Biomed* 4.5 (1991), pp. 209–226. ISSN: 09523480 10991492. DOI: 10.1002/nbm.1940040502 (cit. on pp. 1, 29, 37, 38, 56, 57, 106, 108, 109, 112).

[9] William D Rooney and Charles S Springer Jr. “The molecular environment of intracellular sodium: 23Na NMR relaxation”. In: *NMR in Biomedicine* 4.5 (1991), pp. 227–245. ISSN: 0952-3480 (cit. on pp. 1, 2, 52, 56, 106–109, 112).

[10] Johan R. C. van der Maarel. “Thermal relaxation and coherence dynamics of spin 3/2. I. Static and fluctuating quadrupolar interactions in the multipole basis”. In: *Concepts in Magnetic Resonance* 19A.2 (2003), pp. 97–116. ISSN: 1043-7347 1099-0534. DOI: 10.1002/cmr.a.10087 (cit. on pp. 1, 2, 5, 11, 22, 28, 29, 40, 42, 56, 64, 68, 113).

[11] Johan R.C. van der Maarel. “Thermal relaxation and coherence dynamics of spin 3/2. II. Strong radio-frequency field”. In: *Concepts in Magnetic Resonance Part A* 19A.2 (2003), pp. 117–133. ISSN: 1546-6086. DOI: 10.1002/cmr.a.10088 (cit. on pp. 1, 5, 11, 22, 68).

[12] Sebastian Lachner, Laurent Ruck, Sebastian C. Niesporek, et al. “Comparison of optimized intensity correction methods for 23Na MRI of the human brain using a 32-channel phased array coil at 7 Tesla”. In: *Zeitschrift für Medizinische Physik* 30.2 (2020), pp. 104–115. ISSN: 0939-3889. DOI: https://doi.org/10.1016/j.zemedi.2019.10.004 (cit. on p. 1).

[13] Matthias Malzacher, Jorge Chacon-Caldera, Nadia Paschke, and Lothar R. Schad. “Feasibility study of a double resonant (1H/23Na) abdominal RF setup at 3T”. In: *Zeitschrift für Medizinische Physik* 29.4 (2019), pp. 359–367. ISSN: 0939-3889. DOI: https://doi.org/10.1016/j.zemedi.2018.12.004 (cit. on p. 1).

[14] William D. Rooney, Xin Li, Manoj K. Sammi, et al. “Mapping human brain capillary water lifetime: high-resolution metabolic neuroimaging”. In: *NMR in Biomedicine* 28.6 (2015). https://doi.org/10.1002/nbm.3294, pp. 607–623. ISSN: 0952-3480. DOI: https://doi.org/10.1002/nbm.3294 (cit. on p. 1).

[15] José M. Dizon, Joseph S. Tauskela, David Wise, et al. “Evaluation of triple-quantum-filtered 23Na NMR in monitoring of intracellular na content in the perfused rat heart: Comparison of intra- and extracellular transverse relaxation and spectral amplitudes”. In: *Magnetic Resonance in Medicine* 35.3 (1996), pp. 336–345. ISSN: 0740-3194. DOI: https://doi.org/10.1002/mrm.1910350311 (cit. on pp. 2, 38, 71, 105).

[16] Thomas R. Eykyn, Dunja Aksentijević, Karen L. Aughton, et al. “Multiple quantum filtered 23Na NMR in the Langendorff perfused mouse heart: Ratio of triple/double quantum filtered signals correlates with [Na]i”. In: *Journal of Molecular and Cellular Cardiology* 86 (2015), pp. 95–101. ISSN: 0022-2828. DOI: https://doi.org/10.1016/j.yjmcc.2015.07.009 (cit. on pp. 2, 38, 71, 105).

[17] Linda A. Jelicks and Raj K. Gupta. “On the extracellular contribution to multiple quantum filtered 23Na NMR of perfused rat heart”. In: *Magnetic Resonance in Medicine* 29.1 (1993), pp. 130–133. ISSN: 0740-3194. DOI: https://doi.org/10.1002/mrm.1910290124 (cit. on pp. 2, 38, 71, 105).

[18] Tatyana Knubovets, Hadassah Shinar, and Gil Navon. “Quantification of the Contribution of Extracellular Sodium to23Na Multiple-Quantum-Filtered NMR Spectra of Suspensions of Human Red Blood Cells”. In: *Journal of Magnetic Resonance* 131.1 (1998), pp. 92–96. ISSN: 1090-7807. DOI: https://doi.org/10.1006/jmre.1997.1337 (cit. on pp. 2, 38, 71, 105).

[19] V. D. Schepkin, I. O. Choy, and T. F. Budinger. “Sodium alterations in isolated rat heart during cardioplegic arrest”. In: *Journal of Applied Physiology* 81.6 (1996), pp. 2696–2702. DOI: 10.1152/jappl.1996.81.6.2696 (cit. on pp. 2, 38, 71, 105).

[20] Victor D. Schepkin, I. Oojin Choy, Thomas F. Budinger, et al. “Sodium TQF NMR and intracellular sodium in isolated crystalloid perfused rat heart”. In: *Magnetic Resonance in Medicine* 39.4 (1998), pp. 557–563. ISSN: 0740-3194. DOI: https://doi.org/10.1002/mrm.1910390408 (cit. on pp. 2, 38, 71, 105).

[21] Viswanathan Seshan, A. Dean Sherry, and Navin Bansal. “Evaluation of triple quantum-filtered 23Na NMR spectroscopy in the in situ rat liver”. In: *Magnetic Resonance in Medicine* 38.5 (1997), pp. 821–827. ISSN: 0740-3194. DOI: https://doi.org/10.1002/mrm.1910380519 (cit. on pp. 2, 38, 71, 105).

[22] Patrick M. Winter and Navin Bansal. “Triple-Quantum-Filtered 23Na NMR Spectroscopy of Subcutaneously Implanted 9L Gliosarcoma in the Rat in the Presence of TmDOTP5-”. In: *Journal of Magnetic Resonance* 152.1 (2001), pp. 70–78. ISSN: 1090-7807. DOI: https://doi.org/10.1006/jmre.2001.2390 (cit. on pp. 2, 38, 53, 71, 109, 110).

[23] Eva Neumaier-Probst, Simon Konstandin, Judith Ssozi, et al. “A double-tuned 1H/23Na resonator allows 1H-guided 23Na-MRI in ischemic stroke patients in one session”. In: *International Journal of Stroke* 10.SA100 (2015), pp. 56–61. DOI: 10.1111/ijs.12547 (cit. on p. 2).

[24] Ronald Ouwerkerk, Karen B. Bleich, Joseph S. Gillen, Martin G. Pomper, and Paul A. Bottomley. “Tissue Sodium Concentration in Human Brain Tumors as Measured with 23Na MR Imaging”. In: *Radiology* 227.2 (2003), pp. 529–537. DOI: 10.1148/radiol.2272020483 (cit. on p. 2).

[25] Victor D. Schepkin, Brian D. Ross, Thomas L. Chenevert, et al. “Sodium magnetic resonance imaging of chemotherapeutic response in a rat glioma”. In: *Magnetic Resonance in Medicine* 53.1 (2005), pp. 85–92. ISSN: 0740-3194. DOI: https://doi.org/10.1002/mrm.20332 (cit. on p. 2).

[26] Victor D. Schepkin, Thomas L. Chenevert, Kyle Kuszpit, et al. “Sodium and proton diffusion MRI as biomarkers for early therapeutic response in subcutaneous tumors”. In: *Magnetic Resonance Imaging* 24.3 (2006), pp. 273–278. ISSN: 0730-725X. DOI: https://doi.org/10.1016/j.mri.2005.12.004 (cit. on p. 2).

[27] Victor D. Schepkin, Kuei C. Lee, Kyle Kuszpit, et al. “Proton and sodium MRI assessment of emerging tumor chemotherapeutic resistance”. In: *NMR in Biomedicine* 19.8 (2006), pp. 1035–1042. ISSN: 0952-3480. DOI: https://doi.org/10.1002/nbm.1074 (cit. on p. 2).

[28] Olgica Zaric, Katja Pinker, Stefan Zbyn, et al. “Quantitative Sodium MR Imaging at 7 T: Initial Results and Comparison with Diffusion-weighted Imaging in Patients with Breast Tumors”. In: *Radiology* 280.1 (2016), pp. 39–48. DOI: 10.1148/radiol.2016151304 (cit. on p. 2).

[29] Daniel P. Fiege, Sandro Romanzetti, Christian C. Mirkes, Daniel Brenner, and N. Jon Shah. “Simultaneous single-quantum and triple-quantum-filtered MRI of 23Na (SISTINA)”. In: *Magnetic Resonance in Medicine* 69.6 (2013), pp. 1691–1696. ISSN: 0740-3194. DOI: https://doi.org/10.1002/mrm.24417 (cit. on pp. 2, 3, 72, 115).

[30] Michaela A. U. Hoesl, Lothar R. Schad, and Stanislas Rapacchi. “Efficient 23Na triple-quantum signal imaging on clinical scanners: Cartesian imaging of single and triple-quantum 23Na (CRISTINA)”. In: *Magnetic Resonance in Medicine* 84.5 (2020), pp. 2412–2428. ISSN: 0740-3194. DOI: https://doi.org/10.1002/mrm.28284 (cit. on pp. 2–4, 55, 72, 115).

[31] Wieland A. Worthoff, Aliaksandra Shymanskaya, and N. Jon Shah. “Relaxometry and quantification in simultaneously acquired single and triple quantum filtered sodium MRI”. In: *Magnetic Resonance in Medicine* 81.1 (2019), pp. 303–315. ISSN: 0740-3194. DOI: https://doi.org/10.1002/mrm.27387 (cit. on p. 2).

[32] John F. Schenck. “The role of magnetic susceptibility in magnetic resonance imaging: MRI magnetic compatibility of the first and second kinds”. In: *Medical Physics* 23.6 (1996), pp. 815–850. ISSN: 0094-2405. DOI: https://doi.org/10.1118/1.597854 (cit. on p. 2).

[33] Isaac O. Choy, Victor D. Schepkin, Thomas F. Budinger, et al. “Effects of Specific Sodium/Hydrogen Exchange Inhibitor During Cardioplegic Arrest”. In: *The Annals of Thoracic Surgery* 64.1 (1997), pp. 94–99. ISSN: 0003-4975. DOI: https://doi.org/10.1016/S0003-4975(97)00245-2 (cit. on pp. 2, 105).

[34] Victor D. Schepkin, Isaac O. Choy, Thomas F. Budinger, J. Nilas Young, and William M. DeCampli. “Multi-dose Crystalloid Cardioplegia Preserves Intracellular Sodium Homeostasis in Myocardium”. In: *Journal of Molecular and Cellular Cardiology* 31.9 (1999), pp. 1643–1651. ISSN: 0022-2828. DOI: https://doi.org/10.1006/jmcc.1999.1002 (cit. on pp. 2, 105).

[35] Joseph S. Tauskela, José M. Dizon, John Whang, and José Katz. “Evaluation of Multiple-Quantum-Filtered23Na NMR in Monitoring Intracellular Na Content in the Isolated Perfused Rat Heart in the Absence of a Chemical-Shift Reagent”. In: *Journal of Magnetic Resonance* 127.1 (1997), pp. 115–127. ISSN: 1090-7807. DOI: https://doi.org/10.1006/jmre.1997.1181 (cit. on pp. 2, 105).

[36] G. LaVerde, E. Nemoto, C.A. Jungreis, C. Tanase, and F.E. Boada. “Serial triple quantum sodium MRI during non-human primate focal brain ischemia”. In: *Magnetic Resonance in Medicine* 57.1 (2007), pp. 201–205. ISSN: 0740-3194. DOI: https://doi.org/10.1002/mrm.21087 (cit. on pp. 2, 105).

[37] Andriy M. Babsky, Hong Zhang, Shahryar K. Hekmatyar, Gary D. Hutchins, and Navin Bansal. “Monitoring chemotherapeutic response in RIF-1 tumors by single-quantum and triple-quantum-filtered 23Na MRI, 1H diffusion-weighted MRI and PET imaging”. In: *Magnetic Resonance Imaging* 25.7 (2007), pp. 1015–1023. ISSN: 0730-725X. DOI: https://doi.org/10.1016/j.mri.2006.11.004 (cit. on pp. 2, 105).

[38] Patrick M. Winter, Harish Poptani, and Navin Bansal. “Effects of Chemotherapy by 1,3-Bis(2-chloroethyl)-1-nitrosourea on Single-Quantum- and Triple-Quantum-filtered 23Na and 31P Nuclear Magnetic Resonance of the Subcutaneously Implanted 9L Glioma”. In: *Cancer Research* 61.5 (2001), pp. 2002–2007 (cit. on pp. 2, 53).

[39] Dennis Kleimaier, Victor Schepkin, Cordula Nies, Eric Gottwald, and Lothar R. Schad. "Intracellular Sodium Changes in Cancer Cells Using a Microcavity Array-Based Bioreactor System and Sodium Triple-Quantum MR Signal". In: *Processes* 8.10 (2020), p. 1267. ISSN: 2227-9717 (cit. on pp. 2, 3, 44, 61, 67, 72, 105, 113).

[40] Eric Gottwald, Tanja Kleintschek, Stefan Giselbrecht, et al. "Characterization of a chip-based bioreactor for three-dimensional cell cultivation via Magnetic Resonance Imaging". In: *Zeitschrift für Medizinische Physik* 23.2 (2013), pp. 102–110. ISSN: 0939-3889. DOI: https://doi.org/10.1016/j.zemedi.2013.01.003 (cit. on p. 2).

[41] Michaela A.U. Hoesl, Dennis Kleimaier, Ruomin Hu, et al. "23Na Triple-quantum signal of in vitro human liver cells, liposomes, and nanoparticles: Cell viability assessment vs. separation of intra- and extracellular signal". In: *Journal of Magnetic Resonance Imaging* 50.2 (2019), pp. 435–444. ISSN: 1053-1807. DOI: https://doi.org/10.1002/jmri.26666 (cit. on pp. 2, 3, 105).

[42] Andreas Neubauer, Cordula Nies, Victor D. Schepkin, et al. "Tracking protein function with sodium multi quantum spectroscopy in a 3D-tissue culture based on microcavity arrays". In: *Scientific Reports* 7.1 (2017), p. 3943. ISSN: 2045-2322. DOI: 10.1038/s41598-017-04226-2 (cit. on pp. 2, 3, 105).

[43] Dennis Kleimaier, Victor Schepkin, Ruomin Hu, and Lothar R. Schad. "Protein conformational changes affect the sodium triple-quantum MR signal". In: *NMR in Biomedicine* 33.10 (2020), e4367. ISSN: 0952-3480. DOI: https://doi.org/10.1002/nbm.4367 (cit. on pp. 2, 3, 36, 52, 56, 66, 108, 109).

[44] Guy C. Brown. "Total cell protein concentration as an evolutionary constraint on the metabolic control distribution in cells". In: *Journal of Theoretical Biology* 153.2 (1991), pp. 195–203. ISSN: 0022-5193. DOI: https://doi.org/10.1016/S0022-5193(05)80422-9 (cit. on pp. 2, 36, 52, 105, 108).

[45] Chun-Wa Chung and Stephen Wimperis. "Optimum detection of spin-32 biexponential relaxation using multiple-quantum filtration techniques". In: *Journal of Magnetic Resonance (1969)* 88.2 (1990), pp. 440–447. ISSN: 0022-2364. DOI: https://doi.org/10.1016/0022-2364(90)90204-M (cit. on pp. 2, 3, 52, 108, 109).

[46] Allan M Torres, David J Philp, Richard Kemp-Harper, Chris Garvey, and Philip W Kuchel. "Determination of Na+ binding parameters by relaxation analysis of selected 23Na NMR coherences: RNA, BSA and SDS". In: *Magnetic Resonance in Chemistry* 43.3 (2005), pp. 217–224. ISSN: 0749-1581 (cit. on pp. 2, 36, 52, 108–110).

[47] Charles W. Carr. "Studies on the binding of small ions in protein solutions with the use of membrane electrodes. VI. The binding of sodium and potassium ions in solutions of various proteins". In: *Archives of Biochemistry and Biophysics* 62.2 (1956), pp. 476–484. ISSN: 0003-9861. DOI: https://doi.org/10.1016/0003-9861(56)90146-1 (cit. on pp. 2, 52, 53, 109, 110).

[48] Lazar Fleysher, Niels Oesingmann, and Matilde Inglese. "B0 inhomogeneity-insensitive triple-quantum-filtered sodium imaging using a 12-step phase-cycling scheme". In: *NMR in Biomedicine* 23.10 (2010), pp. 1191–1198. ISSN: 0952-3480. DOI: https://doi.org/10.1002/nbm.1548 (cit. on pp. 2, 3, 115).

[49] Ileana Hancu, Fernando E Boada, and Gary X Shen. “Three-dimensional triple-quantum-filtered 23Na imaging of in vivo human brain”. In: *Magnetic Resonance in Medicine: An Official Journal of the International Society for Magnetic Resonance in Medicine* 42.6 (1999), pp. 1146–1154. ISSN: 0740-3194 (cit. on pp. 2, 3, 35, 113, 115).

[50] Gil Navon, Hadassah Shinar, Uzi Eliav, and Yoshiteru Seo. “Multiquantum filters and order in tissues”. In: *NMR in Biomedicine* 14.2 (2001), pp. 112–132. ISSN: 0952-3480. DOI: https://doi.org/10.1002/nbm.687 (cit. on pp. 2, 3).

[51] Costin Tanase and Fernando E. Boada. “Algebraic description of spin 3/2 dynamics in NMR experiments”. In: *Journal of Magnetic Resonance* 173.2 (2005), pp. 236–253. ISSN: 1090-7807. DOI: https://doi.org/10.1016/j.jmr.2004.12.009 (cit. on pp. 2, 3, 11, 22, 72, 115).

[52] Geoffrey Bodenhausen. “Multiple-quantum NMR”. In: *Progress in Nuclear Magnetic Resonance Spectroscopy* 14.3 (1980), pp. 137–173. ISSN: 0079-6565. DOI: https://doi.org/10.1016/0079-6565(80)80007-0 (cit. on pp. 2, 3).

[53] Guy Jaccard, Stephen Wimperis, and Geoffrey Bodenhausen. “Multiple-quantum NMR spectroscopy of S=3/2 spins in isotropic phase: A new probe for multiexponential relaxation”. In: *The Journal of Chemical Physics* 85.11 (1986), pp. 6282–6293. ISSN: 0021-9606 1089-7690. DOI: 10.1063/1.451458 (cit. on pp. 2–4, 22, 40, 55, 60).

[54] Jan Andrasko. “Nonexponential relaxation of 23Na+ in agarose gels”. In: *Journal of Magnetic Resonance (1969)* 16.3 (1974), pp. 502–504. ISSN: 0022-2364. DOI: https://doi.org/10.1016/0022-2364(74)90233-9 (cit. on pp. 2, 51, 56).

[55] C. A. Boicelli and A. M. Giuliani. “Sodium ion distribution in the vitreous body”. In: *Magnetic Resonance Materials in Physics, Biology and Medicine* 4.3 (1996), pp. 241–245. ISSN: 1352-8661. DOI: 10.1007/BF01772012 (cit. on p. 2).

[56] H. Monoi. “Nuclear magnetic resonance of 23Na ions interacting with the gramicidin channel”. In: *Biophys J* 48.4 (1985), pp. 643–62. DOI: 10.1016/s0006-3495(85)83820-0 (cit. on p. 2).

[57] R. Reddy, M. Shinnar, Z. Wang, and J. S. Leigh. “Multiple-Quantum Filters of Spin-32 with Pulses of Arbitrary Flip Angle”. In: *Journal of Magnetic Resonance, Series B* 104.2 (1994), pp. 148–152. ISSN: 1064-1866. DOI: https://doi.org/10.1006/jmrb.1994.1068 (cit. on p. 3).

[58] M. Rance, O. W. Sørensen, G. Bodenhausen, et al. “Improved spectral resolution in COSY 1H NMR spectra of proteins via double quantum filtering”. In: *Biochemical and Biophysical Research Communications* 117.2 (1983), pp. 479–485. ISSN: 0006-291X. DOI: https://doi.org/10.1016/0006-291X(83)91225-1 (cit. on p. 3).

[59] Costin Tanase and Fernando E. Boada. “Triple-quantum-filtered imaging of sodium in presence of B0 inhomogeneities”. In: *Journal of Magnetic Resonance* 174.2 (2005), pp. 270–278. ISSN: 1090-7807. DOI: https://doi.org/10.1016/j.jmr.2005.02.012 (cit. on pp. 3, 53, 113).

[60] Alina Gilles, Armin M. Nagel, and Guillaume Madelin. “Multipulse sodium magnetic resonance imaging for multicompartment quantification: Proof-of-concept”. In: *Scientific Reports* 7.1 (2017), p. 17435. ISSN: 2045-2322. DOI: 10.1038/s41598-017-17582-w (cit. on pp. 4, 55, 71).

[61] Victor D. Schepkin. “Statistical tensor analysis of the MQ MR signals generated by weak quadrupole interactions”. In: *Zeitschrift für Medizinische Physik* (2019). ISSN: 0939-3889. DOI: https://doi.org/10.1016/j.zemedi.2019.03.002 (cit. on pp. 4, 55, 56, 69).

[62] Chengchuan Wu, Yasmin Blunck, and Leigh A. Johnston. “The “Spin-3/2 Bloch Equation”: System matrix formalism of excitation, relaxation, and off-resonance effects in biological tissue”. In: *Magnetic Resonance in Medicine* 88.3 (2022), pp. 1370–1379. ISSN: 0740-3194. DOI: https://doi.org/10.1002/mrm.29276 (cit. on pp. 4, 30, 55).

[63] Simon Reichert, Victor D. Schepkin, Dennis Kleimaier, Frank G Zöllner, and Lothar R. Schad. “Comparison of triple quantum (TQ) TPPI and inversion recovery TQ TPPI pulse sequences at 9.4 and 21.1T”. In: *NMR in Biomedicine* (Submitted on October 24, 2023) (2023) (cit. on pp. 5, 11, 22, 30, 49, 59, 67, 75, 106, 125).

[64] Simon Reichert, Victor D. Schepkin, Dennis Kleimaier, Frank G Zöllner, and Lothar R. Schad. “23Na Triple Quantum MR Signal Extraction Using a Single-pulse Sequence with Single Quantum Time Efficiency”. In: *Magnetic Resonance in Medicine* (Submitted on November 7, 2023) (2023) (cit. on pp. 5, 49, 59, 75, 106, 125).

[65] I. I. Rabi, J. R. Zacharias, S. Millman, and P. Kusch. “A New Method of Measuring Nuclear Magnetic Moment”. In: *Physical Review* 53.4 (1938). PR, pp. 318–318. DOI: 10.1103/PhysRev.53.318 (cit. on p. 7).

[66] Walther Gerlach and Otto Stern. “Über die Richtungsquantelung im Magnetfeld”. In: *Annalen der Physik* 379.16 (1924), pp. 673–699. ISSN: 0003-3804. DOI: https://doi.org/10.1002/andp.19243791602 (cit. on p. 7).

[67] F. Bloch. “Nuclear Induction”. In: *Physical Review* 70.7-8 (1946). PR, pp. 460–474. DOI: 10.1103/PhysRev.70.460 (cit. on pp. 7, 19).

[68] E. M. Purcell, H. C. Torrey, and R. V. Pound. “Resonance Absorption by Nuclear Magnetic Moments in a Solid”. In: *Physical Review* 69.1-2 (1946). PR, pp. 37–38. DOI: 10.1103/PhysRev.69.37 (cit. on p. 7).

[69] P. Mansfield and P. K. Grannell. “NMR diffraction in solids?” In: *Journal of Physics C: Solid State Physics* 6.22 (1973), p. L422. ISSN: 0022-3719. DOI: 10.1088/0022-3719/6/22/007 (cit. on p. 7).

[70] P. C. Lauterbur. “Image Formation by Induced Local Interactions: Examples Employing Nuclear Magnetic Resonance”. In: *Nature* 242.5394 (1973), pp. 190–191. ISSN: 1476-4687. DOI: 10.1038/242190a0 (cit. on p. 7).

[71] A. Abragam. *The Principles of Nuclear Magnetism*. Clarendon Press, 1983. ISBN: 9780198512363 (cit. on pp. 7, 11, 22, 27, 110).

[72] C.P. Slichter. *Principles of Magnetic Resonance*. Springer Berlin Heidelberg, 2013. ISBN: 9783662094426 (cit. on pp. 7, 22).

[73] M. H. Levitt. *Spin Dynamics: Basics of Nuclear Magnetic Resonance*. 2nd ed. John Wiley & Sons, 2008, p. 740. ISBN: 9780470511176 (cit. on pp. 7, 11, 12, 19, 20, 22, 25, 38, 42).

[74] E. M. Haacke, R. W. Brown, M. R. Thompson, and R. Venkatesan. *Magnetic Resonance Imaging: Physical Principles and Sequence Design*. John Wiley & Sons, 1999, p. 944. ISBN: 9780471351283 (cit. on pp. 7, 20, 45).

[75] R.A. de Graaf. *In Vivo NMR Spectroscopy: Principles and Techniques*. Wiley, 2013. ISBN: 9781118681305 (cit. on p. 7).

[76] Robin K. Harris, Edwin D. Becker, Sonia M. Cabral De Menezes, Robin Goodfellow, and Pierre Granger. "NMR nomenclature: Nuclear spin properties and conventions for chemical shifts (IUPAC recommendations 2001)". In: *Concepts in Magnetic Resonance* 14.5 (2002), pp. 326–346. ISSN: 1043-7347. DOI: https://doi.org/10.1002/cmr.10035 (cit. on p. 11).

[77] Paul S. Hubbard. "Nonexponential Nuclear Magnetic Relaxation by Quadrupole Interactions". In: *The Journal of Chemical Physics* 53.3 (2003), pp. 985–987. ISSN: 0021-9606. DOI: 10.1063/1.1674167 (cit. on p. 11).

[78] Herman J. C. Berendsen and Hommo T. Edzes. "THE OBSERVATION AND GENERAL INTERPRETATION OF SODIUM MAGNETIC RESONANCE IN BIOLOGICAL MATERIAL". In: *Annals of the New York Academy of Sciences* 204.1 (1973), pp. 459–485. ISSN: 0077-8923. DOI: https://doi.org/10.1111/j.1749-6632.1973.tb30799.x (cit. on pp. 11, 107).

[79] G. J. Bowden and W. D. Hutchison. "Tensor operator formalism for multiple-quantum NMR. 1. Spin-1 nuclei". In: *Journal of Magnetic Resonance (1969)* 67.3 (1986), pp. 403–414. ISSN: 0022-2364. DOI: https://doi.org/10.1016/0022-2364(86)90378-1 (cit. on pp. 14, 29).

[80] G. J. Bowden, W. D. Hutchison, and J. Khachan. "Tensor operator formalism for multiple-quantum NMR. 2. Spins 32, 2, and 52 and general I". In: *Journal of Magnetic Resonance (1969)* 67.3 (1986), pp. 415–437. ISSN: 0022-2364. DOI: https://doi.org/10.1016/0022-2364(86)90379-3 (cit. on pp. 14, 29).

[81] Norbert Mueller, Geoffrey Bodenhausen, and Richard R. Ernst. "Relaxation-induced violations of coherence transfer selection rules in nuclear magnetic resonance". In: *Journal of Magnetic Resonance (1969)* 75.2 (1987), pp. 297–334. ISSN: 0022-2364. DOI: https://doi.org/10.1016/0022-2364(87)90038-2 (cit. on p. 22).

[82] Alexej Jerschow. "From nuclear structure to the quadrupolar NMR interaction and high-resolution spectroscopy". In: *Progress in Nuclear Magnetic Resonance Spectroscopy* 46.1 (2005), pp. 63–78. ISSN: 0079-6565. DOI: https://doi.org/10.1016/j.pnmrs.2004.12.001 (cit. on p. 25).

[83] Fabian J. Kratzer, Sebastian Flassbeck, Sebastian Schmitter, et al. “3D sodium (23Na) magnetic resonance fingerprinting for time-efficient relaxometric mapping”. In: *Magnetic Resonance in Medicine* 86.5 (2021), pp. 2412–2425. ISSN: 0740-3194. DOI: https://doi.org/10.1002/mrm.28873 (cit. on pp. 35, 40, 66, 111).

[84] Armin M. Nagel, Frederik B. Laun, Marc-André Weber, et al. “Sodium MRI using a density-adapted 3D radial acquisition technique”. In: *Magnetic Resonance in Medicine* 62.6 (2009), pp. 1565–1573. ISSN: 0740-3194. DOI: https://doi.org/10.1002/mrm.22157 (cit. on pp. 35, 46, 51, 102, 116).

[85] Adrian Tsang, Robert W. Stobbe, and Christian Beaulieu. “In vivo double quantum filtered sodium magnetic resonance imaging of human brain”. In: *Magnetic Resonance in Medicine* 73.2 (2015), pp. 497–504. ISSN: 0740-3194. DOI: https://doi.org/10.1002/mrm.25131 (cit. on p. 38).

[86] Robert W. Stobbe and Christian Beaulieu. “Residual quadrupole interaction in brain and its effect on quantitative sodium imaging”. In: *NMR in Biomedicine* 29.2 (2016), pp. 119–128. ISSN: 0952-3480. DOI: https://doi.org/10.1002/nbm.3376 (cit. on p. 38).

[87] Lena V. Gast, Teresa Gerhalter, Bernhard Hensel, Michael Uder, and Armin M. Nagel. “Double quantum filtered 23Na MRI with magic angle excitation of human skeletal muscle in the presence of B0 and B1 inhomogeneities”. In: *NMR in Biomedicine* 31.12 (2018), e4010. ISSN: 0952-3480. DOI: https://doi.org/10.1002/nbm.4010 (cit. on pp. 38, 62).

[88] Uzi Eliav, Keren Keinan-Adamsky, and Gil Navon. “A new method for suppressing the central transition in I=3/2 NMR spectra with a demonstration for 23Na in bovine articular cartilage”. In: *Journal of Magnetic Resonance* 165.2 (2003), pp. 276–281. ISSN: 1090-7807. DOI: https://doi.org/10.1016/j.jmr.2003.09.002 (cit. on p. 38).

[89] M. B. Rösler, A. M. Nagel, R. Umathum, P. Bachert, and N. Benkhedah. “In vivo observation of quadrupolar splitting in 39K magnetic resonance spectroscopy of human muscle tissue”. In: *NMR in Biomedicine* 29.4 (2016), pp. 451–457. ISSN: 0952-3480. DOI: https://doi.org/10.1002/nbm.3476 (cit. on p. 38).

[90] Gregory Chang, Guillaume Madelin, Orrin H. Sherman, et al. “Improved assessment of cartilage repair tissue using fluid-suppressed 23Na inversion recovery MRI at 7 Tesla: preliminary results”. In: *European Radiology* 22.6 (2012), pp. 1341–1349. ISSN: 1432-1084. DOI: 10.1007/s00330-012-2383-8 (cit. on pp. 40, 66, 111).

[91] Fabian J. Kratzer, Sebastian Flassbeck, Armin M. Nagel, et al. “Sodium relaxometry using 23Na MR fingerprinting: A proof of concept”. In: *Magnetic Resonance in Medicine* 84.5 (2020), pp. 2577–2591. ISSN: 0740-3194. DOI: https://doi.org/10.1002/mrm.28316 (cit. on pp. 40, 111).

[92] R. P. Kline, E. X. Wu, D. P. Petrylak, et al. “Rapid in vivo monitoring of chemotherapeutic response using weighted sodium magnetic resonance imaging”. In: *Clin Cancer Res* 6.6 (2000), pp. 2146–56. ISSN: 1078-0432 (Print) 1078-0432 (cit. on pp. 40, 66, 111).

[93] Guillaume Madelin, Jae-Seung Lee, Souheil Inati, Alexej Jerschow, and Ravinder R. Regatte. "Sodium inversion recovery MRI of the knee joint in vivo at 7T". In: *Journal of Magnetic Resonance* 207.1 (2010), pp. 42–52. ISSN: 1090-7807. DOI: https://doi.org/10.1016/j.jmr.2010.08.003 (cit. on pp. 40, 66, 111).

[94] Guillaume Madelin, Alexej Jerschow, and Ravinder R Regatte. "Sodium MRI with fluid suppression: will it improve early detection of osteoarthritis?" In: *Imaging in Medicine* 3.1 (2011), p. 01. ISSN: 1755-5191 (cit. on pp. 40, 66, 111).

[95] Guillaume Madelin, James S. Babb, Ding Xia, et al. "Reproducibility and repeatability of quantitative sodium magnetic resonance imaging in vivo in articular cartilage at 3 T and 7 T". In: *Magnetic Resonance in Medicine* 68.3 (2012), pp. 841–849. ISSN: 0740-3194. DOI: https://doi.org/10.1002/mrm.23307 (cit. on pp. 40, 66, 111).

[96] Guillaume Madelin, James Babb, Ding Xia, et al. "Articular Cartilage: Evaluation with Fluid-suppressed 7.0-T Sodium MR Imaging in Subjects with and Subjects without Osteoarthritis". In: *Radiology* 268.2 (2013), pp. 481–491. DOI: 10.1148/radiol.13121511 (cit. on pp. 40, 66, 111).

[97] Peng Rong, Ravinder R. Regatte, and Alexej Jerschow. "Clean demarcation of cartilage tissue 23Na by inversion recovery". In: *Journal of Magnetic Resonance* 193.2 (2008), pp. 207–209. ISSN: 1090-7807. DOI: https://doi.org/10.1016/j.jmr.2008.04.036 (cit. on pp. 40, 66, 111).

[98] Robert Stobbe and Christian Beaulieu. "In vivo sodium magnetic resonance imaging of the human brain using soft inversion recovery fluid attenuation". In: *Magnetic Resonance in Medicine* 54.5 (2005), pp. 1305–1310. ISSN: 0740-3194. DOI: https://doi.org/10.1002/mrm.20696 (cit. on pp. 40, 66, 111).

[99] M. Hayashi, Y. M. Chang, T. K. Wang, S. H. Lin, and Joseph L. Knee. "Ultrafast Spectroscopy and its Applications". In: *Encyclopedia of Physical Science and Technology (Third Edition)*. Ed. by Robert A. Meyers. New York: Academic Press, 2003, pp. 217–226. ISBN: 978-0-12-227410-7. DOI: https://doi.org/10.1016/B0-12-227410-5/00797-3 (cit. on p. 42).

[100] Simon Konstandin, Philipp Krämer, Matthias Günther, and Lothar R. Schad. "Sodium magnetic resonance imaging using ultra-short echo time sequences with anisotropic resolution and uniform k-space sampling". In: *Magnetic Resonance Imaging* 33.3 (2015), pp. 319–327. ISSN: 0730-725X. DOI: https://doi.org/10.1016/j.mri.2014.12.007 (cit. on p. 46).

[101] P. Deetjen and K. Benndorf. *Physiologie*. Urban und Fischer, 1999. ISBN: 9783437413162 (cit. on p. 46).

[102] Stefan Silbernagl and Agamemnon Despopoulos. *Taschenatlas physiologie*. Georg Thieme Verlag, 2007. ISBN: 3135677079 (cit. on p. 46).

[103] R. Brandes, F. Lang, and R.F. Schmidt. *Physiologie des Menschen: mit Pathophysiologie*. Springer Berlin Heidelberg, 2019. ISBN: 9783662564684 (cit. on p. 46).

[104] Simon Reichert, Dennis Kleimaier, and Lothar Schad. “Simulation of Spin 3/2 Quadrupole Nuclei Dynamics in Biological Environments for Arbitrary Pulse Sequences”. In: *Proc. Intl. Soc. Mag. Reson. Med.* 30 (2022) (cit. on pp. 49, 75, 106, 126).

[105] Simon Reichert, Denis Kleimaier, Victor D. Schepkin, and Lothar Schad. “Combining Extreme Narrowing and Slow Motion Regime in a Simple Motional Model for Sodium NMR Environment”. In: *Proc. Intl. Soc. Mag. Reson. Med.* 31 (2023) (cit. on pp. 49, 75, 106, 126).

[106] Simon Reichert, Dennis Kleimaier, and Lothar Schad. “Dependence of 23Na Triple Quantum (TQ) Signal on Protein Size”. In: *Proc. Intl. Soc. Mag. Reson. Med.* 30 (2022) (cit. on pp. 49, 75, 106, 126).

[107] Simon Reichert, Victor D. Schepkin, Denis Kleimaier, and Lothar Schad. “Simultaneous 23Na Triple Quantum (TQ) Signal Estimation from Single-Pulse Sequence with Single Quantum (SQ) Time Efficiency”. In: *ISMRM 2023 Workshop on MR Imaging of X-Nuclei 23Na & Friends: From Controversies to Potential Clinical Applications Part II* (2023) (cit. on pp. 49, 75, 106, 126).

[108] R. Fu, W. W. Brey, K. Shetty, et al. “Ultra-wide bore 900MHz high-resolution NMR at the National High Magnetic Field Laboratory”. In: *Journal of Magnetic Resonance* 177.1 (2005), pp. 1–8. ISSN: 1090-7807. DOI: https://doi.org/10.1016/j.jmr.2005.07.013 (cit. on p. 50).

[109] Chunqi Qian, Ihssan S. Masad, Jens T. Rosenberg, et al. “A volume birdcage coil with an adjustable sliding tuner ring for neuroimaging in high field vertical magnets: Ex and in vivo applications at 21.1T”. In: *Journal of Magnetic Resonance* 221 (2012), pp. 110–116. ISSN: 1090-7807. DOI: https://doi.org/10.1016/j.jmr.2012.05.016 (cit. on p. 50).

[110] R. Hu. “Exploring Quadrupolar Interactions of 23Na and 35Cl with Triple-Quantum MRS/MRI”. Thesis. 2020 (cit. on p. 52).

[111] Luciano Brocchieri and Samuel Karlin. “Protein length in eukaryotic and prokaryotic proteomes”. In: *Nucleic acids research* 33.10 (2005), pp. 3390–3400. ISSN: 1362-4962 0305-1048. DOI: 10.1093/nar/gki615 (cit. on p. 52).

[112] Anthea Maton. *Human biology and health*. 1st. Prentice Hall science. Englewood Cliffs, N.J.: Prentice Hall Englewood Cliffs, N.J., 1993. ISBN: 0139811761; 9780139811760; 0139867872; 9780139867873 (cit. on p. 52).

[113] H. Powell Baker and H. A. Saroff. “Binding of Sodium Ions to beta-Lactoglobulin”. In: *Biochemistry* 4.8 (1965), pp. 1670–1677. ISSN: 0006-2960. DOI: 10.1021/bi00884a033 (cit. on p. 53).

[114] Johan Desmet, Ignace Hanssens, and Frans van Cauwelaert. “Comparison of the binding of Na+ and Ca2+ to bovine alpha-lactalbumin”. In: *Biochimica et Biophysica Acta (BBA) - Protein Structure and Molecular Enzymology* 912.2 (1987). Na binding to alpha Lactalbumin, pp. 211–219. ISSN: 0167-4838. DOI: https://doi.org/10.1016/0167-4838(87)90091-4 (cit. on p. 53).

[115] Mordechai Shporer and Mortimer M. Civan. “Effects of temperature and field strength on the NMR relaxation times of 23Na in frog striated muscle”. In: *Biochimica et Biophysica Acta (BBA) - General Subjects* 354.2 (1974), pp. 291–304. ISSN: 0304-4165. DOI: https://doi.org/10.1016/0304-4165(74)90014-2 (cit. on p. 56).

[116] Alfred Delville, Christian Detellier, and Pierre Laszlo. “Determination of the correlation time for a slowly reorienting spin-32 nucleus: Binding of Na+ with the 5-GMP supramolecular assembly”. In: *Journal of Magnetic Resonance (1969)* 34.2 (1979), pp. 301–315. ISSN: 0022-2364 (cit. on p. 56).

[117] William H. BRAUNLIN, Hans J. VOGEL, and Sture FORSÉN. “Potassium-39 and sodium-23 NMR studies of cation binding to phosvitin”. In: *European Journal of Biochemistry* 142.1 (1984), pp. 139–144. ISSN: 0014-2956. DOI: https://doi.org/10.1111/j.1432-1033.1984.tb08261.x (cit. on p. 56).

[118] Laura Lerner and Dennis A. Torchia. “An analysis of non-Lorentzian sodium-23 line shapes in two model systems”. In: *Journal of the American Chemical Society* 108.15 (1986). doi: 10.1021/ja00275a004, pp. 4264–4268. ISSN: 0002-7863. DOI: 10.1021/ja00275a004 (cit. on p. 56).

[119] Geoffrey S. Payne, Anne-Marie L. Seymour, Peter Styles, and George K. Radda. “Multiple quantum filtered 23Na NMR spectroscopy in the perfused heart”. In: *NMR in Biomedicine* 3.3 (1990), pp. 139–146. ISSN: 0952-3480. DOI: https://doi.org/10.1002/nbm.1940030307 (cit. on p. 56).

[120] T. E. Bull. “Nuclear magnetic relaxation of spin-32 nuclei involved in chemical exchange”. In: *Journal of Magnetic Resonance (1969)* 8.4 (1972), pp. 344–353. ISSN: 0022-2364. DOI: https://doi.org/10.1016/0022-2364(72)90052-2 (cit. on p. 57).

[121] H T Edzes and H J C Berendsen. “The Physical State of Diffusible Ions in Cells”. In: *Annual Review of Biophysics and Bioengineering* 4.1 (1975), pp. 265–285. DOI: 10.1146/annurev.bb.04.060175.001405 (cit. on pp. 57, 107).

[122] Robert Kurland, Carolyn Newton, Shlomo Nir, and Demetrios Papahadjopoulos. “Specificity of Na+ binding to phosphatidylserine vesicles from A 23Na NMR relaxation rate study”. In: *Biochimica et Biophysica Acta (BBA) - Biomembranes* 551.1 (1979), pp. 137–147. ISSN: 0005-2736. DOI: https://doi.org/10.1016/0005-2736(79)90360-2 (cit. on p. 57).

[123] Hans Gustavsson and Bjorn Lindman. “Alkali ion binding to aggregates of amphiphilic compounds studied by nuclear magnetic resonance chemical shifts”. In: *Journal of the American Chemical Society* 100.15 (1978). doi: 10.1021/ja00483a002, pp. 4647–4654. ISSN: 0002-7863. DOI: 10.1021/ja00483a002 (cit. on p. 57).

[124] J. W. Pettegrew, J. F. M. Post, K. Panchalingam, G. Withers, and D. E. Woessner. “7Li NMR study of normal human erythrocytes”. In: *Journal of Magnetic Resonance (1969)* 71.3 (1987), pp. 504–519. ISSN: 0022-2364. DOI: https://doi.org/10.1016/0022-2364(87)90250-2 (cit. on p. 57).

[125] Robert Kurland, Shinpei Ohki, and Shlomo Nir. “A Phosphorus-31 NMR Study of Monovalent Cation Interactions with the Negatively Charged Surface of Phosphatidylserine Vesicles”. In: *Solution Behavior of Surfactants: Theoretical and Applied Aspects Volume 2*. Ed. by K. L. Mittal and E. J. Fendler. Boston, MA: Springer US, 1982, pp. 1443–1453. ISBN: 978-1-4613-3494-1. DOI: 10.1007/978-1-4613-3494-1_46 (cit. on p. 57).

[126] A. Neubauer. “Modellierung und Validierung ionischer Regulationsprozesse in Nervenzellen mittels X-Kern-Magnetresonanztomographie”. Thesis. 2017 (cit. on pp. 60, 62).

[127] Uzi Eliav, S. Chandra shekar, Wen Ling, Gil Navon, and Alexej Jerschow. “Magnetic alignment and quadrupolar/paramagnetic cross-correlation in complexes of Na with LnDOTP5-”. In: *Journal of Magnetic Resonance* 216 (2012), pp. 114–120. ISSN: 1090-7807. DOI: https://doi.org/10.1016/j.jmr.2012.01.012 (cit. on pp. 62, 109, 110).

[128] Wen Ling and Alexej Jerschow. “Relaxation-allowed nuclear magnetic resonance transitions by interference between the quadrupolar coupling and the paramagnetic interaction”. In: *The Journal of Chemical Physics* 126.6 (2007), p. 064502. DOI: 10.1063/1.2435343 (cit. on pp. 62, 109, 110).

[129] Ahmad A. Alhulail, Pingyu Xia, Xin Shen, et al. “Fast in vivo 23Na imaging and mapping using accelerated 2D-FID UTE magnetic resonance spectroscopic imaging at 3 T: Proof of concept and reliability study”. In: *Magnetic Resonance in Medicine* 85.4 (2021), pp. 1783–1794. ISSN: 0740-3194. DOI: https://doi.org/10.1002/mrm.28576 (cit. on pp. 64, 111, 116).

[130] Ileana Hancu, Johan R. C. van der Maarel, and Fernando E. Boada. “A Model for the Dynamics of Spins 3/2 in Biological Media: Signal Loss during Radiofrequency Excitation in Triple-Quantum-Filtered Sodium MRI”. In: *Journal of Magnetic Resonance* 147.2 (2000), pp. 179–191. ISSN: 1090-7807. DOI: https://doi.org/10.1006/jmre.2000.2177 (cit. on pp. 68, 107).

[131] Ugo Fano and G. Racah. *Irreducible tensorial sets [by] U. Fano [and] G. Racah*. Pure and applied physics, v. 4. (Giulio). New York: Academic Press, 1959 (cit. on p. 68).

[132] B. D. Foy and D. Burstein. “Interstitial sodium nuclear magnetic resonance relaxation times in perfused hearts”. In: *Biophysical Journal* 58.1 (1990), pp. 127–134. ISSN: 0006-3495. DOI: https://doi.org/10.1016/S0006-3495(90)82358-4 (cit. on p. 71).

[133] Jay W. Pettegrew, Donald E. Woessner, Nancy J. Minshew, and Thomas Glonek. “Sodium-23 NMR analysis of human whole blood, erythrocytes, and plasma. Chemical shift, spin relaxation, and intracellular sodium concentration studies”. In: *Journal of Magnetic Resonance (1969)* 57.2 (1984), pp. 185–196. ISSN: 0022-2364. DOI: https://doi.org/10.1016/0022-2364(84)90118-5 (cit. on p. 71).

[134] Eilat Shinar, Eliezer A. Rachmilewitz, Alisa Shifter, Ezra Rahamin, and Paul Saltman. "Oxidative damage to human red cells induced by copper and iron complexes in the presence of ascorbate". In: *Biochimica et Biophysica Acta (BBA) - Molecular Cell Research* 1014.1 (1989), pp. 66–72. ISSN: 0167-4889. DOI: https://doi.org/10.1016/0167-4889(89)90241-3 (cit. on p. 71).

[135] H. Shinar and G. Navon. "Sodium-23 NMR relaxation times in nucleated red blood cells and suspensions of nuclei". In: *Biophysical Journal* 59.1 (1991), pp. 203–208. ISSN: 0006-3495. DOI: https://doi.org/10.1016/S0006-3495(91)82211-1 (cit. on p. 71).

[136] Yasmin Blunck, Sonal Josan, Syeda Warda Taqdees, et al. "3D-multi-echo radial imaging of 23Na (3D-MERINA) for time-efficient multi-parameter tissue compartment mapping". In: *Magnetic Resonance in Medicine* 79.4 (2018), pp. 1950–1961. ISSN: 0740-3194. DOI: https://doi.org/10.1002/mrm.26848 (cit. on pp. 73, 102, 111, 116).

[137] J. Kullberg, H. Ahlström, L. Johansson, and H. Frimmel. "Automated and reproducible segmentation of visceral and subcutaneous adipose tissue from abdominal MRI". In: *International Journal of Obesity* 31.12 (2007), pp. 1806–1817. ISSN: 1476-5497. DOI: 10.1038/sj.ijo.0803671 (cit. on p. 73).

[138] Safa Özdemir and Yusuf Ziya Ider. "bSSFP phase correction and its use in magnetic resonance electrical properties tomography". In: *Magnetic Resonance in Medicine* 81.2 (2019), pp. 934–946. ISSN: 0740-3194. DOI: https://doi.org/10.1002/mrm.27446 (cit. on p. 73).

[139] Christian Licht, Simon Reichert, Maxime Guye, Lothar R. Schad, and Stanislas Rapacchi. "Multidimensional compressed sensing to advance 23Na multi-quantum coherences MRI". In: *Magnetic Resonance in Medicine* n/a.n/a (2023). ISSN: 0740-3194. DOI: https://doi.org/10.1002/mrm.29902 (cit. on pp. 73, 107, 116, 125).

[140] Patrick M. Winter and Navin Bansal. "TmDOTP5- as a 23Na shift reagent for the subcutaneously implanted 9L gliosarcoma in rats". In: *Magnetic Resonance in Medicine* 45.3 (2001), pp. 436–442. ISSN: 0740-3194. DOI: https://doi.org/10.1002/1522-2594(200103)45:3<436::AID-MRM1057>3.0.CO;2-6 (cit. on pp. 105, 109).

[141] D. Kleimaier. "Exploring Protein Interactions with 23Na Triple-Quantum MRS and 1H Chemical Exchange Saturation Transfer MRI". Thesis. 2021 (cit. on p. 107).

[142] Valentin Jost. "NMR simulation of 23Na in a biomedical environment". Thesis. 2023 (cit. on pp. 107, 127).

[143] Zoltán Gáspári and András Perczel. "Chapter 2 - Protein Dynamics as Reported by NMR". In: *Annual Reports on NMR Spectroscopy*. Ed. by Graham A. Webb. Vol. 71. Academic Press, 2010, pp. 35–75. ISBN: 0066-4103. DOI: https://doi.org/10.1016/B978-0-08-089054-8.00002-2 (cit. on p. 108).

[144] Zahedeh Bashardanesh, Johan Elf, Haiyang Zhang, and David van der Spoel. "Rotational and Translational Diffusion of Proteins as a Function of Concentration". In: *ACS Omega* 4.24 (2019). Correlation time, pp. 20654–20664. DOI: 10.1021/acsomega.9b02835 (cit. on p. 108).

[145] J. Cavanagh, N.J. Skelton, W.J. Fairbrother, M. Rance, and A.G. Palmer. *Protein NMR Spectroscopy: Principles and Practice*. Elsevier Science, 2010. ISBN: 9780080471037 (cit. on p. 108).

[146] A. D. Sherry, J. Ren, J. Huskens, et al. "Characterization of Lanthanide(III) DOTP Complexes: Thermodynamics, Protonation, and Coordination to Alkali Metal Ions". In: *Inorganic Chemistry* 35.16 (1996), pp. 4604–4612. ISSN: 0020-1669. DOI: 10.1021/ic9600590 (cit. on pp. 109, 110).

[147] M. Gueron. "Nuclear relaxation in macromolecules by paramagnetic ions: a novel mechanism". In: *Journal of Magnetic Resonance (1969)* 19.1 (1975), pp. 58–66. ISSN: 0022-2364. DOI: https://doi.org/10.1016/0022-2364(75)90029-3 (cit. on p. 109).

[148] Alexander J. Vega and Daniel Fiat. "Nuclear relaxation processes of paramagnetic complexes The slow-motion case". In: *Molecular Physics* 31.2 (1976), pp. 347–355. ISSN: 0026-8976. DOI: 10.1080/00268977600100261 (cit. on pp. 109, 110).

[149] William E. Blumberg. "[19] The study of hemoglobin by electron paramagnetic resonance spectroscopy". In: *Methods in Enzymology*. Vol. 76. Academic Press, 1981, pp. 312–329. ISBN: 0076-6879. DOI: https://doi.org/10.1016/0076-6879(81)76129-9 (cit. on p. 109).

[150] Larisa Latypova, Gregory Barshtein, Alexander Puzenko, et al. "Oxygenation state of hemoglobin defines dynamics of water molecules in its vicinity". In: *The Journal of Chemical Physics* 153.13 (2020), p. 135101. DOI: 10.1063/5.0023945 (cit. on p. 110).

[151] Larisa Latypova, Alexander Puzenko, Yuri Poluektov, et al. "Hydration of methemoglobin studied by in silico modeling and dielectric spectroscopy". In: *The Journal of Chemical Physics* 155.1 (2021), p. 015101. DOI: 10.1063/5.0054697 (cit. on p. 110).

[152] Ali Charkhesht, Chola K. Regmi, Katie R. Mitchell-Koch, Shengfeng Cheng, and Nguyen Q. Vinh. "High-Precision Megahertz-to-Terahertz Dielectric Spectroscopy of Protein Collective Motions and Hydration Dynamics". In: *The Journal of Physical Chemistry B* 122.24 (2018). doi: 10.1021/acs.jpcb.8b02872, pp. 6341–6350. ISSN: 1520-6106. DOI: 10.1021/acs.jpcb.8b02872 (cit. on p. 110).

[153] K. Shiraga, Y. Ogawa, and N. Kondo. "Hydrogen Bond Network of Water around Protein Investigated with Terahertz and Infrared Spectroscopy". In: *Biophys J* 111.12 (2016). 1542-0086 Shiraga, Keiichiro Ogawa, Yuichi Kondo, Naoshi Journal Article United States 2016/12/22 Biophys J. 2016 Dec 20;111(12):2629-2641. doi: 10.1016/j.bpj.2016.11.011., pp. 2629–2641. ISSN: 0006-3495 (Print) 0006-3495. DOI: 10.1016/j.bpj.2016.11.011 (cit. on p. 110).

[154] Danu Ariono, Putu Teta P. Aryanti, Anita Kusuma Wardani, and I Gede Wenten. "Analysis of Protein Separation Mechanism in Charged Ultrafiltration Membrane". In: *Journal of Engineering and Technological Sciences* Vol. 50 No. 2 (2018) (2018). DOI: https://doi.org/10.5614/j.eng.technol.sci.2018.50.2.4 (cit. on p. 110).

[155] Gonzalo G. Rodriguez, Zidan Yu, Lauren F. O Donnell, et al. "Repeatability of simultaneous 3D 1H MRF/23Na MRI in brain at 7T". In: *Scientific Reports* 12.1 (2022), p. 14156. ISSN: 2045-2322. DOI: 10.1038/s41598-022-18388-1 (cit. on p. 111).

[156] Nadia Karina Paschke, Wiebke Neumann, Tanja Uhrig, et al. "Influence of Gadolinium-Based Contrast Agents on Tissue Sodium Quantification in Sodium Magnetic Resonance Imaging". In: *Investigative Radiology* 53.9 (2018). ISSN: 0020-9996 (cit. on p. 111).

[157] Ben Ridley, Armin M. Nagel, Mark Bydder, et al. "Distribution of brain sodium long and short relaxation times and concentrations: a multi-echo ultra-high field 23Na MRI study". In: *Scientific Reports* 8.1 (2018), p. 4357. ISSN: 2045-2322. DOI: 10.1038/s41598-018-22711-0 (cit. on p. 111).

[158] Günter Steidle and Fritz Schick. "A new concept for improved quantitative analysis of reversible transverse relaxation in tissues with variable microscopic field distribution". In: *Magnetic Resonance in Medicine* 85.3 (2021), pp. 1493–1506. ISSN: 0740-3194. DOI: https://doi.org/10.1002/mrm.28534 (cit. on p. 115).

[159] Detlef Moskau. "Application of real time digital filters in NMR spectroscopy". In: *Concepts in Magnetic Resonance* 15.2 (2002), pp. 164–176. ISSN: 1043-7347. DOI: https://doi.org/10.1002/cmr.10031 (cit. on pp. 115, 122).

[160] Anne Adlung, Nadia K. Paschke, Alena-Kathrin Golla, et al. "23Na MRI in ischemic stroke: Acquisition time reduction using postprocessing with convolutional neural networks". In: *NMR in Biomedicine* 34.4 (2021), e4474. ISSN: 0952-3480. DOI: https://doi.org/10.1002/nbm.4474 (cit. on p. 116).

[161] Anne Adlung, Christian Licht, Simon Reichert, et al. "Quantification of tissue sodium concentration in the ischemic stroke: A comparison between external and internal references for 23Na MRI". In: *Journal of Neuroscience Methods* 382 (2022), p. 109721. ISSN: 0165-0270. DOI: https://doi.org/10.1016/j.jneumeth.2022.109721 (cit. on pp. 116, 125).

[162] Warda Syeda, Yasmin Blunck, Scott Kolbe, Jon O. Cleary, and Leigh A. Johnston. "A continuum of components: Flexible fast fraction mapping in sodium MRI". In: *Magnetic Resonance in Medicine* 81.6 (2019), pp. 3854–3864. ISSN: 0740-3194. DOI: https://doi.org/10.1002/mrm.27659 (cit. on p. 116).

[163] Juan Carlos Cobas and F. Javier Sardina. "Nuclear magnetic resonance data processing. MestRe-C: A software package for desktop computers". In: *Concepts in Magnetic Resonance Part A* 19A.2 (2003), pp. 80–96. ISSN: 1546-6086. DOI: https://doi.org/10.1002/cmr.a.10089 (cit. on p. 122).

[164] Christian Licht, Simon Reichert, Mark Bydder, et al. “Low-rank reconstruction for simultaneous Double-Half-Echo 23Na and undersampled 23Na Multi-Quantum Coherences MRI”. In: *Magnetic Resonance in Medicine* (Submitted on November 20, 2023) (2023) (cit. on p. 125).

[165] Simon Reichert, Dennis Kleimaier, and Lothar Schad. “Comparison of low rank compressed sensing with non-uniform undersampled non-linear FID fitting for time efficient 23Na TQTPPI measurements”. In: *Proc. Intl. Soc. Mag. Reson. Med.* 29 (2021) (cit. on p. 125).

[166] Simon Reichert, Dennis Kleimaier, and Lothar Schad. “Comparison of Double Quantum (DQ) Suppression Methods for Inversion Recovery TQTPPI (IRTQTPPI) Sequence”. In: *Proc. Intl. Soc. Mag. Reson. Med.* 30 (2022) (cit. on p. 125).

[167] Simon Reichert, Dennis Kleimaier, Vichtor D. Schepkin, and Lothar Schad. “23Na Triple Quantum (TQ) Signal Estimation from Single-Pulse Sequence with Single Quantum (SQ) Time Efficiency”. In: *Proc. Intl. Soc. Mag. Reson. Med.* 31 (2023) (cit. on p. 126).

[168] Simon Reichert, Dennis Kleimaier, Dominik Zehender, Frank G. Zöllner, and Lothar Schad. “A Novel Method to Estimate 23Na Triple Quantum (TQ) Signal: Spin Echo Sequence, Impact of Noise and Proof-of-Concept Imaging”. In: *Proc. Intl. Soc. Mag. Reson. Med.* (Submitted) (2023) (cit. on p. 126).

[169] D. Kleimaier, S. Reichert, V. D. Schepkin, and L. Schad. “Sodium TQ signal of amino acids and alpha-lactalbumin in comparison to bovine serum albumin”. In: *Proc. Intl. Soc. Mag. Reson. Med.* 29 (2021) (cit. on p. 126).

[170] C. Licht, E. Ilicak, S. Reichert, et al. “Dynamic Mode Decomposition reveals 23Na Multi-Quantum Coherences and allows incomplete RF Phase-Cycling”. In: *Proc. Intl. Soc. Mag. Reson. Med.* (Submitted) (2023) (cit. on p. 126).

[171] C. Licht, S. Reichert, G. M. Bydder, et al. “Low-rank reconstructions for simultaneous Double-Half Echo 23Na and prospectively undersampled 23Na Multi-Quantum Coherences MRI”. In: *Proc. Intl. Soc. Mag. Reson. Med.* (Submitted) (2023) (cit. on p. 126).

[172] Dominik Zehender, Simon Reichert, Frank G. Zöllner, and Lothar Schad. “Feasibility of undersampled fixed evolution time 23Na TQTPPI FID reconstruction for optimal 23Na TQ/SQ-signal estimation”. In: *Proc. Intl. Soc. Mag. Reson. Med.* (Submitted) (2023) (cit. on p. 126).

[173] Christian Licht, Simon Reichert, Jascha Zapp, et al. “Low-Rank Reconstruction for Double-Half-Echo 23Na and undersampled 23Na Multi-Quantum Coherences MRI”. In: *ISMRM 2023 Workshop on MR Imaging of X-Nuclei 23Na & Friends: From Controversies to Potential Clinical Applications Part II* (2023) (cit. on p. 126).

[174] Christian Licht, Simon Reichert, Jascha Zapp, et al. “Prospectively undersampled higher resolution 23Na Multi-Quantum Coherences MRI”. In: *ESMRMB 2023 Annual Meeting* (2023) (cit. on p. 127).

Declaration

This thesis is the result of my independent investigation under supervision. Where my work is indebted to the work or ideas of others, for example from the literature or the internet, I have acknowledged this within the thesis.

I declare that this study has not already been accepted for any degree, nor is it currently being submitted in candidature for any other degree.

I am aware that a false declaration could have legal implications.

Erklärung

Ich versichere, dass ich diese Arbeit selbstständig verfasst habe und keine anderen als die angegebenen Quellen und Hilfsmittel benutzt habe.

Heidelberg, November 20, 2023

Simon Reichert